

# DISSERTATION

## **Experimental and Numerical Gas-Side Performance Evaluation of Finned-Tube Heat Exchangers**

ausgeführt zum Zwecke der Erlangung des akademischen Grades  
eines Doktors der technischen Wissenschaften unter der Leitung von

A.o. Univ.Prof. Dipl.-Ing. Dr.techn. Karl Ponweiser

E 302

Institut für Thermodynamik und Energiewandlung

eingereicht an der Technischen Universität Wien

**Fakultät für Maschinenwesen und Betriebswissenschaften**

von

Dipl.-Ing. René Hofmann

e9525119

2340 Mödling, Neudorferstraße 56

Mödling, am 06.09.2009



#### ACKNOWLEDGEMENTS

I would like to express my sincere gratitude to A.o. Univ.Prof. Dipl.-Ing. Dr.techn. Karl Ponweiser my academic supervisor for his patient guidance, professional comments and useful critiques during the course of this dissertation. I would also like to express my deep appreciation to my Co-referent A.o. Univ.Prof. Dipl.-Ing. Dr.techn. Reinhard Willinger for his unending patience and valuable suggestions throughout this scientific work. Especially to A.o. Univ.Prof. Dipl.-Ing. Dr.techn. Heimo Walter and ObRat i.R. Dipl.-Ing. Dr.techn. Friedrich Frasz as well as to all my colleagues at the Institute for Thermodynamics and Energy Conversion thank you for your advice and assistance in keeping my progress on schedule. Furthermore, I would like to thank the technicians of the laboratory who helped me in construction and assembling the experimental rig and especially for altering the assembly many times in order to be able to examine different finned-tube arrangements.

Last but not least, I extend my thanks to my family and especially to my wife, give birth to our wonderful son, who provided endless support and encouragement to me all the time.

This work is dedicated with greatest respect to my grandfather Franz.

## Abstract

The objective of this work is to develop new heat transfer coefficient and pressure drop coefficient correlations for a heat exchanger with different numbers of consecutively arranged U-shaped finned-tubes in staggered layout, to characterize the global behavior at the gas-side (The overall heat transfer coefficients are averaged values across the entire fin surface of each tube (fin efficiency) as well as above all tubes within the bundle (average mean between inlet and outlet)). The experimental investigations at a semi-industrial scale test facility, at the Institute for Thermodynamics and Energy Conversion, were performed at different finned-tube bundle configurations. The tube bundles were arranged at equal transverse pitch, and in case of up to eight consecutively arranged tubes, with equal longitudinal pitch in staggered formation. Thus, a maximum total number of 88 tubes at different configurations was investigated. The Reynolds-Number was varied in the range between 4500 and 35000. The measurements were accomplished at the gas-side and at the water-side. The scope of a subsequently performed measurement validation should be addressed to fulfill the energy balance of the used system boundaries. The experimental setup, the measurement technique, and the measurement uncertainties are presented. As a result of measurements at different tube row configurations, a row correction factor for the heat transfer from the finned-tubes was derived. The average mean heat transfer seems to increase degresively from row to row. A comparison of the developed heat transfer and pressure drop correlations with available literature is presented.

A three dimensional steady state numerical analysis of fluid flow and heat transfer across a tube row with a periodic array of solid and segmented fins was performed. For this reason, five different models of a single row finned-tube heat exchanger, with solid and segmented circular and helical I/U-shaped fins, were developed. The thermal field has been examined for convective transport phenomena. The effect of the parametrically varied Reynolds-number to the Nusselt-number was analyzed. Especially the difference between solid and serrated fins as well as the influence at the fin surface between two adjacent fins of *I*-shape and *U*-shape was analyzed. Apart from the application of a  $k-\epsilon$  turbulence model, for modeling turbulence, a renormalization group theory (RNG) based on a  $k-\epsilon$  turbulence model was applied to resolve near wall treatment between the adjacent fins. It is intended to verify the results of the CFD-calculations within the computational model boundaries with those calculated from the measurements at the test rig, to draw any conclusions from global to local effects of conjugated heat transfer and fluid flow. Therefore, at the gas-side of the test rig, a flow rectifier and an inflow channel should provide the same inlet conditions and the investigation of an array of finned-tubes represents the periodic boundaries as in the computational domain of the simulation.

A comparison of the proposed equation for the Nusselt number with the simulation as well as most measurement results are found to be accurate within about  $\pm 15\%$ ; for the equation of the pressure drop coefficient an uncertainty of  $\pm 20\%$  may be found. A performance evaluation criterion for single-phase flows was applied to characterize the effectivity of the various finned-tube bundles (solid/segmented I/U-shaped). The result of the comparison of heat transfer data from measurements, performed on a single U-segmented finned-tube row in cross-flow with a semi-tube installed at the channel wall, and the corresponding CFD calculations is found to be in excellent agreement, with only a small deviation. A qualitative and quantitative pressure drop coefficient comparison of the experiment at 8 tube rows (evaluated for a single

tube row) with the CFD-calculation shows good agreement especially in the  $Re$ -range of about  $6000 \leq Re \leq 20000$ . At higher Reynolds numbers than 20000 up to 50000, a diverging effect was observed.

Some local effects may be indicated in the course of the investigation. The boundary layer thickness at the finned surface decreases with an increasing Reynolds number and it may be concluded that the heat transfer declines with increasing boundary layer thickness. As a result of an adverse pressure gradient, horseshoe vortex systems developed. As the investigations of the local velocity distribution indicate, no considerable difference between the segmented I-shaped fin compared to the U-shaped fin may be observed. In the course of the parameter study temperature profiles across the finned surface, circumferentially and radially averaged heat transfer coefficients across the finned surface were analyzed.

These studies, especially comparisons between measurement results at global performance and numerical investigations of local heat transfer behavior in a single finned-tube row, will provide further knowledge of the local thermal field and convective transport phenomena and will give a more complete understanding of the performance behavior.



## Kurzfassung

Das Ziel der vorliegenden Arbeit ist die Entwicklung neuartiger Korrelationen zur Berechnung des gasseitigen Wärmeübergangskoeffizienten sowie des Druckverlustkoeffizienten für Wärmeübertrager unterschiedlicher Bauart mit verschiedener Anzahl hintereinander angeordneter Rohrreihen von U-geformten segmentierten Rippenrohren in versetzter Anordnung, um das globale Verhalten auf der Gasseite zu charakterisieren (Dabei sind die Wärmeübergangskoeffizienten Mittelwerte über die Rippenoberfläche jedes Rohres (Rippenwirkungsgrad) sowie Mittelwerte über alle Rohre innerhalb des betrachteten Rohrbündels (mittlerer Wert zwischen Einlass und Auslass)). Die experimentellen Untersuchungen wurden an einem halb-industriellen Prüfstand des Institutes für Thermodynamik und Energiewandlung an Rippenrohrbündeln unterschiedlicher Konfiguration durchgeführt. Dabei wurden die Rohrbündel bei gleicher Querteilung und im Falle von bis zu acht hintereinander angeordneten Rohrreihen in versetzter Anordnung mit gleicher Längsteilung untersucht. Somit wurde eine maximale Rohranzahl von 88 Rohren experimentell vermessen. Die Reynolds-Zahl wurde dabei im Bereich von 4500 bis 35000 verändert. Alle Messungen wurden auf der Gasseite und der Wasserseite durchgeführt. Eine im Anschluss an die Messung durchgeführte Messdatenvalidierung hatte zum Ziel die Energiebilanz zwischen den betrachteten Systemgrenzen zu schließen. Die Versuchsanlage, die Messtechnik und die Messunsicherheitsberechnung sind in der vorliegenden Arbeit präsentiert. Als Ergebnis der Messungen an unterschiedlichen Rohrreihen wurde ein Abminderungsfaktor des Wärmeübergangskoeffizienten an Rippenrohren hergeleitet. Der mittlere Wärmeübergang steigt dabei scheinbar von Rohrreihe zu Rohrreihe degresiv an. Ein Vergleich der entwickelten Wärmeübergangs- und Druckverlustkorrelationen mit der Literatur wird präsentiert.

Eine drei-dimensionale stationäre numerische Berechnung der Strömung und des Wärmeübergangs über eine Rohrreihe mit einer periodischen Anordnung von glatten und segmentierten Rippen wurde durchgeführt. Zu diesem Zweck wurden fünf unterschiedliche Modelle von einem Wärmeübertrager einer Einzelrohrreihe mit glatten und segmentierten kreisförmigen und verschraubten I/U-geformten Rippen entwickelt. Das thermische Strömungsfeld wurde auf konvektive Transportphänomene untersucht. Der Einfluss der parametrisch veränderten Reynolds-Zahl auf die Nusselt-Zahl wurde analysiert. Speziell der Unterschied zwischen glatten und segmentierten Rippen, sowie der Einfluss auf die Rippenoberfläche zwischen zwei gegenüberliegenden Rippen mit I-Form und U-Form wurde untersucht. Neben dem  $k$ - $\epsilon$  Modell zur Turbulenzmodellierung, wurde das auf diesem basierende renormalization group theory (RNG)  $k$ - $\epsilon$  Turbulenzmodell angewandt, um wandnahe Effekte zwischen den Rippen schneiden zu berechnen. In dieser Arbeit sollen die Ergebnisse der CFD-Berechnung innerhalb der vorgegebenen Berechnungsgrenzen mit den berechneten Messwerten des Experiments an der Versuchsanlage verifiziert werden, um etwaige Rückschlüsse von globalem auf lokales Verhalten eines konjugierten Wärmeübergangs- und Strömungsproblems zu erhalten. Zu diesem Zweck sind an der Gasseite der Versuchsanlage Strömungsgleichrichter sowie eine Beruhigungsstrecke angeordnet, um die gleichen Einlassbedingungen wie in der Berechnung zu simulieren. Die Untersuchungen an einem Rohrbündel sollen das periodische Verhalten in der Simulationsrechnung abbilden.

Ein Vergleich der vorgeschlagenen Berechnungsgleichung für die Nusselt-Zahl mit der Simulationsrechnung sowie den meisten Messwerten zeigt, daß eine Genauigkeitsgrenze von etwa  $\pm 15\%$  eingehalten werden kann, für die Gleichung des Druckverlustkoeffizienten wurde eine

Unsicherheit von  $\pm 20\%$  ermittelt. Ein Performance-Evaluierungskriterium für Einphasenströmungen wurde angewandt um das Leistungsverhalten von verschiedenen Rippenrohrbündeln (glatt/segmentiert I/U-Form) zu bewerten. Die Ergebnisse des Vergleichs vom berechneten Wärmeübergang aus den Messwerten, ermittelt an einer querangeströmten U-segmentierten Einzelrohrreihe mit Halbrohr installiert an der Kanalwand, sowie den dazugehörigen Simulationsrechnungen mit CFD zeigen eine sehr gute Übereinstimmung mit geringer Abweichung. Ein qualitativer sowie quantitativer Druckverlustkoeffizient-Vergleich zwischen Experiment an 8 Rohrreihen (ermittelt für eine Einzelrohrreihe) und der CFD-Berechnung zeigt gute Übereinstimmung, speziell im  $Re$ -Bereich von etwa  $6000 \leq Re \leq 20000$ . Bei größeren Reynolds Zahlen als 20000 bis zu 50000 wurde abweichendes Verhalten beobachtet.

Auf einige lokale Effekte könnte im Zuge der Untersuchungen hingedeutet werden. Die Grenzschichtdicke an der Rippenoberfläche verkleinert sich mit steigender Reynolds-Zahl, wodurch darauf geschlossen werden könnte, daß der Wärmeübergang mit wachsender Grenzschichtdicke abnimmt. Die Ausbildung von Hufeisenwirbelsystemen wurde als Ergebnis eines negativen Druckgradienten beobachtet. Die Untersuchungen von lokalen Geschwindigkeitsverteilungen deuten darauf hin, daß keine beachtlichen Unterschiede zwischen segmentierten I-geformten und U-geformten Rippen beobachtet werden konnten. Im Zuge der Parameterstudien wurden Temperaturprofile über die Rippenoberflächen und umfangsmässig sowie radial gemittelte Wärmeübergangskoeffizienten über die Rippenoberflächen analysiert.

Diese Untersuchungen, speziell der Vergleich zwischen Messergebnissen bei globaler Betrachtung und numerischer Simulationsrechnungen bei lokaler Betrachtung des Wärmeübergangs an einer Einzelrohrreihe, haben zum Ziel, weitere Erkenntnisse im Bereich von konvektivem Strömungstransport sowie thermischen Effekten zu liefern, um ein besseres Verständnis des Leistungsverhaltens zu erlangen.

# Contents

<b>1. Introduction</b>	<b>1</b>
1.1. Background and Motivation . . . . .	1
1.2. State of the Art . . . . .	2
1.3. Concluding Remarks and Objectives . . . . .	13
<b>2. Experimental Techniques</b>	<b>15</b>
2.1. Experimental Apparatus . . . . .	15
2.2. Measurement Instrumentation . . . . .	18
2.3. Calibration of the Configuration . . . . .	21
2.4. Test Section . . . . .	23
2.4.1. Investigated Finned-Tubes . . . . .	24
2.4.2. Geometrical Arrangement and Configuration of Tubes in the Bundle . . . . .	27
2.5. Measurement Procedure . . . . .	31
2.6. Data Reduction . . . . .	34
2.6.1. Governing Equations for Heat Transfer . . . . .	34
2.6.2. Governing Equations for Pressure Drop . . . . .	39
2.7. Measurement Validation . . . . .	41
2.8. Calculation of the Measurement Uncertainties . . . . .	44
<b>3. Numerical Consideration</b>	<b>56</b>
3.1. Analytical Approximation of Conduction through a Finned-Tube . . . . .	56
3.2. Numerical Simulation of a Single Finned-Tube Row Heat Exchanger in Forced Convection . . . . .	61
3.2.1. Governing Equations of Fluid Flow and Heat Transfer and Turbulence Modeling for the Examined Problem . . . . .	62
3.2.2. Wall Functions . . . . .	66
3.2.3. Modeling of the Computational Domain and Grid Generation . . . . .	67
3.2.4. Boundary Conditions and Thermo-Physical Properties . . . . .	71
3.2.5. CFD-Procedure . . . . .	72

## Contents

<b>4. Experimental and Numerical Results</b>	<b>75</b>
4.1. Global Consideration of the Experimental Results . . . . .	75
4.1.1. Heat Transfer and Pressure Drop of the Investigated Tube-Bundle	75
4.1.2. Row Correction Factor . . . . .	85
4.2. Global Consideration of the Numerical Results . . . . .	89
4.3. Comparison of Experiment and CFD-Simulation . . . . .	92
4.4. Dimensional Analysis of the Investigated Heat Transfer and Pressure Drop Problem . . . . .	95
4.4.1. Correlations of Dimensionless Heat Transfer Coefficient . . . . .	96
4.4.2. Correlations of Pressure Drop Coefficient . . . . .	99
4.4.3. Data Comparison with Literature . . . . .	105
4.5. Comparison of Solid and Segmented Finned-Tubes with I-Shaped and U-Shaped Fins . . . . .	109
4.5.1. Heat Transfer Behavior . . . . .	109
4.5.2. Pressure Drop Behavior . . . . .	114
4.5.3. Performance Evaluation and Comparison Between the Applied Different Three Heat Exchangers . . . . .	117
4.6. Local Considerations of the Finned-Tube Bundle . . . . .	127
4.6.1. Fluid Flow Behavior . . . . .	127
4.6.2. Heat Transfer Behavior . . . . .	133
<b>5. Summary and Conclusions</b>	<b>143</b>
<b>A. Test facility</b>	<b>148</b>
<b>B. Thermo-Physical Properties</b>	<b>150</b>
B.1. Experiment . . . . .	150
B.2. Simulation . . . . .	150
<b>C. Geometrical Data of Investigated I-Shaped Finned-Tubes</b>	<b>153</b>

# List of Figures

1.1. Sketch of a Vertical Type Natural Circulation Heat Recovery Steam Generator. Printed with Friendly Permission of BERTSCHenergy Kessel- und Energietechnik Apparatebau, Austria . . . . .	2
1.2. Schematic Sketch of Selected Segmented Fin-Base Types . . . . .	13
2.1. Sketch of the Test Facility . . . . .	16
2.2. Sketch of the Measurement Setup . . . . .	18
2.3. Sectional Sketch of the Investigated Finned-Tube with U-Shape . . . . .	25
2.4. Contact Area of I-shaped and U-shaped Finned-Tube . . . . .	25
2.5. Sketch of the Staggered Tube Arrangement . . . . .	29
2.6. Sketch of the Tube Arrangement in Flow Direction . . . . .	30
2.7. Measurement Range of Water . . . . .	33
2.8. Relative Deviation between Counter Cross-Flow and Counter-Flow Heat Exchanger . . . . .	35
2.9. Fin-modeling for Calculation . . . . .	36
2.10. Fin-surfaces for Calculation . . . . .	37
2.11. Relative Uncertainty of the Air Mass-flow Measurement for the Full <i>Re</i> -range . . . . .	46
2.12. Relative Uncertainties of all Measured Values . . . . .	47
2.13. Relative Uncertainties of the Transferred Heat . . . . .	50
2.14. Relative Uncertainties of the Heat Transfer at the Gas-Side . . . . .	51
2.15. Relative Uncertainty of the Pressure Drop Coefficient of 8 Tube Rows . . . . .	54
2.16. Relative Uncertainties of the Finned-Tube Pressure Drop Coefficient . . . . .	55
3.1. Temperature Profile . . . . .	60
3.2. Dimensionless Velocity Profile of a Turbulent Boundary Layer in Comparison to Experimental Data, for $\kappa \approx 0.4$ and $E \approx 9.8$ taken from [65] . . . . .	67
3.3. Computational Domains of Circular Segmented Finned-Tubes . . . . .	68
3.4. Computational Domain of the Helical Segmented Finned-Tube . . . . .	69
3.5. Computational Domain of Solid Finned-Tubes . . . . .	70

## List of Figures

4.1. Heat Transfer of Segmented U-Finned-Tubes, for $Pr \approx 0.71$ , $d = 38 \text{ mm}$ , with $\pm 15\%$ Overall Relative Uncertainty . . . . .	76
4.2. Heat Transfer of Segmented U-Finned-Tubes, for $Pr \approx 0.71$ , $d = 38 \text{ mm}$ , with $\pm 15\%$ Overall Relative Uncertainty . . . . .	77
4.3. Heat Transfer of Segmented U-Finned-Tubes, for $Pr \approx 0.71$ , $d = 38 \text{ mm}$ , with $\pm 15\%$ Overall Relative Uncertainty . . . . .	79
4.4. Pressure Drop Coefficient of Segmented U-Finned-Tubes at Different Configurations, evaluated for 1 Tube Row and $d = 38 \text{ mm}$ . . . . .	81
4.5. Relative Uncertainties of Pressure Drop Coefficient at Different Tube Row Configurations at Ambient Temperature . . . . .	82
4.6. Pressure Drop Coefficient of Segmented U-Finned-Tubes, evaluated for 1 Tube Row and $d = 38 \text{ mm}$ , with $\pm 20\%$ Overall Relative Uncertainty .	83
4.7. Pressure Drop Coefficient of Segmented U-Finned-Tubes, evaluated for 1 Tube Row and $d = 38 \text{ mm}$ , with $\pm 20\%$ Overall Relative Uncertainty .	84
4.8. Pressure Drop Coefficient of Segmented U-Finned-Tubes, evaluated for 1 Tube Row and $d = 38 \text{ mm}$ , with $\pm 20\%$ Overall Relative Uncertainty .	85
4.9. Row Correction Factor $K_{N_R}$ for 8, 6, 4, 2, and 1 Tube Rows at Different $Re$ -Numbers . . . . .	86
4.10. Function $C_{N_R}$ According to FRASZ, [15] at Different $Re$ -Numbers . . . .	87
4.11. Comparison of Row Correction Factor with Literature . . . . .	88
4.12. Heat Transfer of a Single Segmented Finned-Tube Row in Cross-Flow .	89
4.13. Pressure Drop Coefficient of a Single Segmented Finned-Tube Row in Cross-Flow . . . . .	90
4.14. Heat Transfer of a Single Solid Finned-Tube Row in Cross-Flow . . . . .	91
4.15. Pressure Drop Coefficient of a Single Solid Finned-Tube Row in Cross-Flow . . . . .	91
4.16. Comparison of Experiment and <i>CFD</i> Simulation: Dimensionless Air-Side Heat Transfer Coefficient at Segmented Finned-Tubes . . . . .	92
4.17. Comparison of Experiment and <i>CFD</i> Simulation: Pressure Drop Coefficient at Segmented Finned-Tubes . . . . .	93
4.18. Comparison of Experiment and <i>CFD</i> Simulation: Dimensionless Air-Side Heat Transfer Coefficient at Solid Finned-Tubes . . . . .	95
4.19. Comparison of Experiment and <i>CFD</i> Simulation: Pressure Drop Coefficient at Solid Finned-Tubes . . . . .	96
4.20. Regression of Heat Transfer at 8 Segmented Finned-Tube Rows . . . . .	99
4.21. Comparison between $Nu$ -Correlation (4.15) and Experimental/Simulation at Segmented U/I-Shaped Finned-Tubes . . . . .	100
4.22. Deviation between $Nu$ -Correlations and Experimental Results . . . . .	101
4.23. Regression of Pressure Drop Coefficient at 8 Segmented Finned-Tube Rows . . . . .	103

## List of Figures

4.24. Comparison of Pressure Drop Coefficient Correlations with Experimental Data . . . . .	104
4.25. Comparison of Heat Transfer Corr. with Literature, Based on Geometrical Data of Helically U-shaped Finned-Tubes, $\frac{Nu_{Eq.(4.15)} - Nu}{Nu_{Eq.(4.15)}} \cdot 100\%$ . . . . .	106
4.26. Comparison of Pressure Drop Coefficient Correlation with Literature, Based on Geometrical Data of Helically U-shaped Finned-Tubes . . . . .	108
4.27. Heat Transfer at 8 Tube Rows, $Pr \approx 0.71$ , Segmented and Solid Tubes, $d_a = 38 \text{ mm}$ . . . . .	110
4.28. Comparison of Heat Transfer at 8 Tube Rows with Literature, $Pr \approx 0.71$ , $d_a = 38 \text{ mm}$ . . . . .	111
4.29. Relative Deviation of Correlations . . . . .	112
4.30. Fin Efficiency of Segmented and Solid I/U-Finned-Tubes and CFD-Simulation . . . . .	113
4.31. Comparison of Segmented and Solid I-Finned-Tubes . . . . .	114
4.32. Pressure Drop Coefficient of Different Finned-Tube Geometries, evaluated for 1 Tube Row . . . . .	116
4.33. $Nu^*/Nu$ of Investigated Sol./Seg. I/U-Shaped Fin . . . . .	118
4.34. Comparison of the Pressure Drop Coefficients ( $\xi^*/\xi$ ) . . . . .	119
4.35. $(St^*/\xi^{1/3})/(St/\xi^{1/3})$ according to [59] . . . . .	121
4.36. $(\alpha^*A^*)/(\alpha A)$ at equal $(P^*/P)$ and $(A^*/A)$ . . . . .	123
4.37. $(P^*/P)$ at equal $(\alpha^*A^*)/(\alpha A)$ and $(A^*/A)$ . . . . .	124
4.38. $(A^*/A)$ at equal $(\alpha^*A^*)/(\alpha A)$ and $(P^*/P)$ . . . . .	125
4.39. Formation of Horseshoe Vortex at the Leading Part of the Tube . . . . .	128
4.40. Calculated Possible Pathlines with Local Velocity Upstream/Downstream above Circular Segmented Fin-Surface . . . . .	128
4.41. Local Velocity Distribution in $[m/s]$ between Adjacent Circular Solid Fins in Symmetry-Plane . . . . .	130
4.42. Local Velocity Distribution in $[m/s]$ between Adjacent Circular Segmented I-Shaped Fins in Symmetry-Plane . . . . .	131
4.43. Local Velocity Distribution in $[m/s]$ between Adjacent Circular Segmented U-Shaped Fins in Symmetry-Plane . . . . .	132
4.44. Contour of the Local Temperature Distribution of the Fin and between Adjacent Circular I-Shaped Segmented Fin-Surface in Symmetry-Plane . . . . .	134
4.45. Contour of the Local Temperature Distribution of the Fin and between Adjacent Circular U-Shaped Segmented Fin-Surface in Symmetry-Plane . . . . .	135
4.46. Contour of the Local Temperature Distribution in $[K]$ at the Circular Segmented Fin-Surface . . . . .	137
4.47. Contour of the Local Temperature Distribution in $[K]$ at the Circular Solid Fin-Surface . . . . .	138
4.48. Circumferentially Averaged Heat Transfer Coefficient . . . . .	140

*List of Figures*

4.49. Relative Circumferentially Averaged Heat Transfer Coefficient . . . . .	141
4.50. Radially Averaged Heat Transfer Coefficient at Discrete Angles ( $\Delta\Theta$ ) . .	142
A.1. Finned-Tube . . . . .	148
A.2. Sketch of the Test Section . . . . .	149



## List of Tables

2.1. Specifications of the Duct Burner . . . . .	16
2.2. Specifications of the Pressure Transducers . . . . .	21
2.3. Specifications of the Investigated Finned-Tube . . . . .	26
3.1. Specifications of the Modeled Finned-Tubes . . . . .	71
4.1. Relevant Variables for Heat Transfer Specification . . . . .	97
4.2. Relevant Variables for Pressure Drop Specification . . . . .	102
4.3. Coefficients of Regressions . . . . .	102
B.1. Thermo-Physical Properties of Dry-air and Carbon Steel . . . . .	152
C.1. Specifications of Finned-Tubes taken from FRASZ-Institute of Thermody- namics and Energy Conversion . . . . .	153

# Notation

## English Symbols

Symbol	Unit	Definition
$\vec{A}$	–	Dimensional matrix
$\vec{A}_i$	m <sup>2</sup>	Cell Surface area
$a$	m	Fin spacing $a = t - s$
$A$	m <sup>2</sup>	Overall heat transfer surface area
$A_{Ch}$	m <sup>2</sup>	Cross-section of the flow channel
$A_f$	m <sup>2</sup>	Surface area of the fin face
$A_{ff}$	m <sup>2</sup>	Surface area of the projected fin face
$A_{lf}$	m <sup>2</sup>	Surface area of the segment lateral face
$A_R$	m <sup>2</sup>	Surface area of the bare tube without fins
$A_s$	m <sup>2</sup>	Surface area of the total face enlargement of the fin
$A_{sff}$	m <sup>2</sup>	Surface area of the total face enlargement of the projected fin face
$A_{stf}$	m <sup>2</sup>	Surface area of the total face enlargement of the projected tip face
$A_{tf}$	m <sup>2</sup>	Surface area of the segment tip face
$A_{tot}$	m <sup>2</sup>	Total outside surface area of the finned-tube bundle
$A_{tube}$	m <sup>2</sup>	Bare tube surface area part of the finned-tube bundle
$B$	m	Flow channel width
$b_{0.4}$	–	Coefficient
$b_s$	m	Average segment width
$C_f$	–	Volume flow number
$C_1..C_6$	–	Factors/Functions according to $ESCOA_{TM}$
$C_{NR}$	–	Fitting function to mean average row correction factor
$c_p$	J/kgK	Specific heat capacity at constant pressure
$c_v$	J/kgK	Specific heat capacity at constant volume
$C_1, C, C_h,$	–	Constant in power law on geometric parameters and tube bundle arrangement
$C_s, C_t$		
$D$	m	Total outside diameter
$d_a, d$	m	Bare tube diameter
$D_{Ch}$	m	Hydraulic diameter of flow channel

(continued)

Symbol	Unit	Definition
$D_H$	m	Hydraulic diameter
$d_i$	m	Internal bare tube diameter
$d_{nz}$	m	Nozzle diameter
$d_{Vent}$	m	Inner diameter of Venturi
$D_{Vent}$	m	Outer diameter of Venturi
$e$	%	Relative deviation
$e_F$	%	Relative error
$e$	J/kg	Specific internal Energy
$F$	–	Corrected value, determined function
$F_0$	–	Uncorrected value
$f_i$	–	Measured value
$F_{min}$	m <sup>2</sup>	Minimum net free area of tube row
$f$	–	Measured value
$f_f$	–	Fanning friction factor
$G(v)$	–	Fitting function
$h$	J/kg	Specific enthalpy
$h$	m	Average fin height
$H$	m	Flow channel height
$h(V)$	–	Side condition
$h_b$	m	Fin height minus $h_s$
$h_{red1}$	m	Reduced fin height for the radial part with the segment
$h_{red2}$	m	Reduced fin height for the radial part without the segment
$h_s$	m	Average segment height
$I_0(mr),$ $K_0(mr)$	–	Modified 0.order Bessel functions of imaginary argument
$I_1(mr),$ $K_1(mr)$	–	Modified 1.order Bessel functions of imaginary argument
$k$	W/m <sup>2</sup> K	Overall heat transfer coefficient
$k$	m <sup>2</sup> /s <sup>2</sup>	Turbulent kinetic energy
$k_{1..10}$	–	Unknown exponents
$K_{N_R}$	–	Row correction factor
$l$	m	Turbulence length scale
$L$	m	Flow channel length within the test section
$L$	m	Diagonal pitch
$L_t$	m	Average tube length
$LMTD$	K	Logarithmic mean temperature difference
$\dot{m}$	kg/s	Mass flow
$m$	1/m	Fin parameter
$m, n$	–	Exponent in power law on geometric parameters, fluid flow

(continued)

Symbol	Unit	Definition
$M_{1..6}$	–	Measurement values
$m_1$	1/m	Parameter for the fin efficiency with segment
$m_2$	1/m	Parameter for the fin efficiency without segment
$N_i$	%	Number of measurands
$N_L$	–	Number of tubes per row
$n$	–	Measurands
$n_R$	1/m	Number of fins per $m$
$n_r$	–	Number of fins
$N_R$	–	Number of tubes in flow-direction
$n_s$	–	Number of segments
$o$	–	Exponent related to fin height influence function
$O()$	–	Fin height influence function
$p$	–	Exponent related to fin thickness influence function
$p$	N/m <sup>2</sup>	Pressure
$P$	W	Pumping power
$P()$	–	Fin thickness influence function
$p_s$	N/m <sup>2</sup>	Static pressure
$p_{stat1}$	N/m <sup>2</sup>	Static pressure of gas at the channel wall
$p_{stat2}$	N/m <sup>2</sup>	Static pressure of gas in the channel center
$p_t$	N/m <sup>2</sup>	Total pressure
$p_{total}$	N/m <sup>2</sup>	Total pressure of gas in the channel center
$p_w$	N/m <sup>2</sup>	Pressure of water
$q$	–	Exponent related to fin pitch influence function
$\dot{q}$	W/m <sup>2</sup>	Heat flux
$\dot{Q}$	W	Heat transfer rate
$Q()$	–	Fin pitch influence function
$R$	–	Strain-dependent correction
$R$	J/kgK	Gas constant
$r$	m	Radius
$r_a$	m	Radius at the fin tip
$r_{ab}$	m	Radius at the fin base of the solid part of the fin
$r_{at}$	m	Radius at the fin tip of the solid part of the fin
$r_i$	m	Radius at the fin base
$r_{sb}$	m	Radius at the fin base of the segmented part of the fin
$r_{st}$	m	Radius at the fin tip of the segmented part of the fin
$s$	m	Average fin thickness
$s_{ij}$		Strain-rate tensor
$s_t$	m	Tube thickness
$t$	–	Exponent in power law on geometric parameters

(continued)

Symbol	Unit	Definition
$T$	K	Temperature
$t$	m	Fin pitch
$T^+$	–	Non-dimensional, sublayer scaled, temperature
$T_b$	K	Boundary layer temperature
$T_i$	K	Temperature at the fin base
$t_{ij}$		Viscous stress tensor
$t_l$	m	Longitudinal tube pitch
$t_q$	m	Transversal tube pitch
$T_s$	K	Average fin temperature according to $ESCOA_{TM}$
$T_{sat}$	K	Saturation temperature of water
$Tu$	%	Turbulent intensity
$u$	–	Exponent related to min. net free area influence function
$u$	m/s	Velocity component in x-direction
$u'$	m/s	Fluctuating velocity components in x, y, z-directions
$U$	m	Circumference
$U^+$	–	Non-dimensional, sublayer scaled, velocity
$u_\tau$	m/s	Friction velocity
$u_a$	m/s	Velocity of air
$u_E$	m/s	Velocity in the net free area of a tube row
$u_w$	m/s	Velocity of water
$v$	–	Exponent related to longitudinal pitch influence function
$v$	m/s	Velocity component in y-direction
$v$	m <sup>3</sup> /kg	Specific volume
$V_{1..6}$	–	Corrected measurement values
$\dot{V}_w$	Nm <sup>3</sup> /h	Volume flow of water
$w$	–	Exponent related to transversal pitch influence function
$w$	m/s	Velocity component in z-direction
$x, y, z$	–	Rectangular Cartesian coordinates
$x_b$	m	Distance of bottom flow channel wall and finned-tube
$x_t$	m	Distance of top flow channel wall and finned-tube
$y^+$	–	Non-dimensional, sublayer scaled, wall-distance
$z$	–	Number of consecutive arranged equal crossings
$Z$	–	Constant in power law on geometric parameters
$\Pi$	–	Dimensionless product

## Greek Symbols

Symbol	Unit	Definition
$\alpha, \alpha_0$	–	Inverse Prandtl number
$\alpha$	W/m <sup>2</sup> K	Heat transfer coefficient apparent
$\alpha_\infty$	W/m <sup>2</sup> K	Heat transfer coefficient at 8 or more tube rows
$\alpha_0$	W/m <sup>2</sup> K	Heat transfer coefficient external current
$\bar{\alpha}$	W/m <sup>2</sup> K	Integral mean heat transfer coefficient
$\beta$	–	Diameter ratio
$\gamma$	deg	Displacement angle of tubes
$\delta f_i$	–	Unknown systematic errors
$\Delta p$	N/m <sup>2</sup>	Pressure difference
$\Delta p_\rho$	N/m <sup>2</sup>	Pressure difference considering the density variation
$\delta$	m	Boundary layer thickness
$\delta_{ij}$	–	Kronecker delta
$\epsilon$	–	Expansion number
$\epsilon$	m <sup>2</sup> /s <sup>3</sup>	Turbulent dissipation rate
$\eta_r$	–	Fin efficiency
$\eta_{r1}$	–	Fin efficiency for the radian part with the segment
$\eta_{r2}$	–	Fin efficiency for the radian part without the segment
$\kappa$	–	Kármán's constant
$\lambda$	–	Relative surface roughness
$\lambda$	W/mK	Thermal conductivity
$\lambda_{1..6}$	–	Lagrange multiplier
$\lambda_{eff}$	W/mK	Effective thermal conductivity
$\lambda_f$	W/mK	Thermal conductivity of fin
$\lambda_t$	W/mK	Thermal conductivity of tube
$\lambda_t$	W/mK	Turbulent thermal conductivity
$\mu$	kg/ms	Dynamic viscosity
$\mu_t$	kg/ms	Turbulent or eddy viscosity
$\mu_{eff}$	kg/ms	Effective viscosity
$\nu$	m <sup>2</sup> /s	Kinematic viscosity
$\nu_{1..6}$	–	Correction factors
$\phi$	–	Relative humidity of air
$\varphi$	deg	Angle
$\rho$	kg/m <sup>3</sup>	Density
$\rho_s$	kg/m <sup>3</sup>	Density of steel
$\sigma_{M1..6}$	–	Co-variances
$\tau_{ij}$	N/m <sup>2</sup>	Reynolds stress tensor
$\tau_w$	N/m <sup>2</sup>	Wall shear stress

(continued)

Symbol	Unit	Definition
$\Theta$	deg	Angle of attack
$\Theta$	–	Correction factor
$\vartheta$	°C	Temperature
$\zeta$	–	Pressure drop coefficient
$\zeta_1$	–	Pressure drop coefficient at the flow channel wall
$\zeta_2$	–	Pressure drop coefficient in the flow channel center
$\Xi$	K	Temperature difference

## Subscripts

Symbol	Definition
–	Outlet (pressure)
+	Inlet (pressure)
0	Characteristic length at $d_a$
1	Inlet
1	Tube row number
1R	Single Tube Row
2	Outlet
8	Tube row number
$a$	Air
$a$	Outside
AC	Alternate Current
$ab$	Fin base of the solid part of the fin
AD	Analog/digital
$at$	Fin tip of the solid part of the fin
$b$	Calculation condition
$baro$	Barometer
$C$	Counter flow
$c$	Converted
$C_h, C_s, C_t$	Constants in power law on geometric parameters
CC	Counter cross-flow
CFD	Computational fluid dynamics
$Ch$	Channel
$Corr$	Correlation
$Cs$	Carbon steel
$E$	Net free area of a row
$ESCOA_{TM}$	Extended Surface Corporation of America
$exp$	Experiment
(continued)	

Symbol	Definition
$f$	Fin
$f$	Fixed, Constant
$FDBR$	Fachverband Dampfkessel-, Behälter- und Rohrleitungsbau
$FT$	Finned-tube bundle
$g$	Gas
$gf$	Gas fixed
$gm$	Gas average between inlet and outlet
$h$	Hydraulic
$HE$	Heat exchanger
$HEDH$	Heat Exchanger Design Handbook
$hy$	Hyperbola
$i$	Internal
$I$	Shape of fin
$I - fin_1$	Modeled I-shaped fin with coarse grid
$I - fin_2$	Modeled I-shaped fin with fine grid
$in$	Inlet
$I - seg$	I-shaped segmented
$l$	Loss
$lam$	Laminar
$m$	Average mean
$max$	Maximum
$meas$	Measured
$min$	Minimum
$ng$	Natural gas
$num$	Numerical
$p_1, p_2$	Measurement positions
$PEC$	Performance evaluation criterion
$po$	Power(a,b,c)
$R$	Tube Row
$r, f$	Fin
$RANS$	Reynolds-averaged Navier Stokes
$red$	Reduced
$redun$	Redundant
$RG$	Flue gas
$RNG$	Renormalization group theory
$RTD$	Resistance temperature detector
$s$	I-shaped segmented finned-tube
$sat$	Saturation
$sb$	Fin base of the segmented part of the fin

(continued)



Symbol	Definition
<i>seg</i>	Segmented
<i>sf</i>	Fin fixed
<i>simul</i>	Simulation
<i>sol</i>	Solid
<i>SST</i>	Shear stress transport
<i>st</i>	Fin tip of the segmented part of the fin
<i>stat</i>	Static
<i>STR, 1S TR</i>	Tube row with semi tube installed
<i>surf</i>	Surface
<i>t</i>	Tube
<i>tot</i>	Total
<i>TR</i>	Tube row
<i>turb</i>	Turbulent
<i>U</i>	Shape of fin
<i>U – seg</i>	U-shaped segmented
<i>Vent</i>	Venturi
<i>w</i>	Water
<i>X</i>	Cross-flow

## Dimensionless Numbers

Symbol	Definition
<i>Eu</i>	Euler number
<i>j</i>	Colburn factor
<i>Nu</i>	Nusselt number
<i>Pe</i>	Péclet number
<i>Pr</i>	Prandtl number
<i>Re</i>	Reynolds number
<i>St</i>	Stanton number

# 1. Introduction

Each individual fact, taken by itself, can indeed arouse our curiosity or our astonishment, or be useful to us in its practical applications.

*Hermann von Helmholtz*

★

## 1.1. Background and Motivation

A contribution to sustainability requires a decrease of the production of anthropogenic  $\text{CO}_2$ . This may be accomplished by the reduction of primary energy sources, which in terms calls for an improvement of the efficiency of steam generators or heat recovery steam generators (HRSG) utilized in thermal power plants. These HRSGs may be applied in combined power cycles and are located downstream of a gas turbine. Modern gas turbines are highly flexible in their mode of operation, e.g. concerning rates of start up, load changes, and shutdown, thus HRSG are forced to ensure non-restrictive operation. It is a well known fact that the heat transfer coefficient  $\alpha_0$  at the gas-side of gas/water tube heat exchangers, e.g. steam boilers or HRSG, is inherently lower than the heat transfer coefficient on the inside of the water tubes. For this reason, extended surfaces (e.g. finned-tubes) are applied to enhance heat transfer. The heat transfer between flue gas and finned-tube wall has a considerable influence on the heat flux. Thus, for a compact design, finned-tubes are applied nowadays in HRSG as bundle heating surfaces. In Figure 1.1 a sketch of a modern vertical type natural circulation HRSG is presented, where finned-tube bundles are arranged horizontally. These bundle heating surfaces may be arranged and applied as superheater, evaporator, and economizer in flow direction. Many HRSG are designed with up to 3 different pressure levels. Many possibilities for improving heat transfer on the gas-side exist. On the one hand, the heat-transferring surface may be enlarged by an arrangement of annular/helical fins or other elements. This increase of total tube surface allows the transfer of a greater amount of heat from hot gas, but the demand for smaller

## 1. Introduction

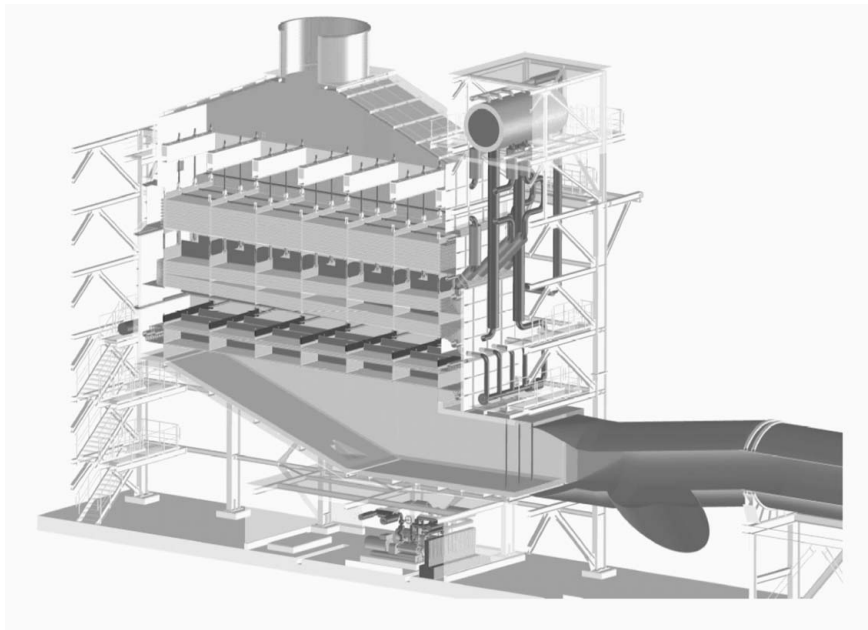


Figure 1.1.: Sketch of a Vertical Type Natural Circulation Heat Recovery Steam Generator. Printed with Friendly Permission of BERTSCHenergy Kessel- und Energietechnik Apparatebau, Austria

installation sizes requires higher density package of the tubes. In the case of applying finned-tubes, this may be achieved by smaller fin pitch with larger fin height. On the other hand, finned-tubes with segmented fins show a somewhat higher fluid flow turbulence than those with solid fins since the boundary layer has to be developed at each individual segment [14]. Staggered arrangement of the tubes in the bundle also increases heat transfer, but a higher pressure drop is caused by the resistances in the flow channel. For this reason, an overall optimization of heat exchangers comprises also the minimization of the required pumping power with the simultaneous maximization of the heat transfer rate<sup>1</sup>.

### 1.2. State of the Art

As discussed in the following, many experiments at finned-tube bundles in cross-flow have been accomplished. However, only few results specifically concern helically segmented fins. As the literature review will show, only a vanishingly small number of numerical CFD investigations especially concerned this topic, compared to fin and tube heat exchangers. In this section an overview of published researches in open literature in the field of average and local heat transfer behavior at circular/helical

---

<sup>1</sup>Some material from this Dissertation has been published by WSEAS Copyright © in 2007 and 2008.

## 1. Introduction

solid and segmented/studded finned-tubes in cross-flow is presented. It is impossible to seriously group all results of research done so far into considerable categories, because of the many different effects being investigated in parallel. However, this literature review is attempted to be globally classified into experimental and numerical investigations. Additionally, the performance evaluation of selected publications at realized tube bundles will be covered.

### **Average and Local Heat Transfer and Pressure Drop Behavior of Finned-Tubes**

**Survey of the Experimental Investigations** Experimental investigations at circular and helical solid finned-tubes have been studied extensively in literature. In this context, the work of SCHMIDT who investigated experimentally mostly annular solid finned-tube bundles, may be seen as one of the basic papers, [56]. In the exact analytical solutions the heat transfer from the fin tip is not considered. He approximated the participation of the fin tip in heat transfer by increasing the effective fin height by one-half. As a result of his investigations, SCHMIDT developed correlations for the evaluation of the dimensionless heat transfer coefficient at finned-tubes in cross-flow. The application of the well known REYNOLDS-analogy, which combines the momentum transfer with the heat transfer, applied at obstacles in cross-flow, indicates that the number of tubes arranged consecutively as well as the degree of upstream turbulence are of considerable influence to the investigated tube bundle, [56].

BRIGGS and YOUNG, [5], investigated several finned-tube configurations experimentally. The given heat transfer correlation is based on tubes varying widely with respect to fin height, fin thickness, fin spacing, and root diameter. These equations can be used for predicting six-row deep tube banks with solid fins. Additionally, pressure drop equations at different tube pitch and thus different net free fluid flow area in a tube row is presented. Contrary to SCHMIDT, who considered the ratio of the total outside surface area of the finned-tubes and the smooth-tubes in the power law (basic heat transfer equation), BRIGGS and YOUNG developed heat transfer correlations and pressure drop correlations, including specifically the impact of any geometrical parameters, namely fin spacing, fin height, fin thickness, longitudinal and transversal tube pitch, hydraulic diameter, as well as the viscosity of air.

RABAS and ECKELS, [52], investigated seven different high segmented finned-tube bundle arrangements with varying geometrical parameters at three row deep consecutive arranged finned-tubes in cross-flow. They ascertained almost equal results in heat transfer and pressure drop by comparing equilateral and diamond staggered tube arrangements. A decrease in heat transfer and pressure drop is evaluated by comparing staggered with in-line tube layouts. They stated that, compared to solid fins, the fin height of segmented fins can be greater than the maximum fin height

## 1. Introduction

because of manufacturing reasons. Such fins are easier to laser-weld due to limited stretching factors of the materials. An increasing fin height would increase the total outside surface area and, as a result, the efficiency of the heat exchanger. The gathered results are compared to studded fin tubes and to results obtained from literature, which are performed at measurements of tubes with segmented fins. The influence between in-line and staggered tube layout regarding to the pressure drop and heat transfer as a function of the tube row number is discussed. This effect seems to be stronger at tube bundles with fewer consecutive arranged tubes and decreases with increasing tube row number, [52].

Only few publications concerning fin segmentation effects exist. BREBER, [4], presents a review and evaluation of heat transfer and pressure drop predictive methods for tube bundles with studded fins with aim of a more accurate correlation. The comparison includes also equations of ESCOA<sub>TM</sub> (Extended Surface Corporation of America), WEIERMAN, WORLEY and ROSS, and MIETH. The investigations by WORLEY and ROSS are performed at tubes with a bare tube diameter of 38.1 mm, 8 row deep tube bundles, and transversal pitch ratio of 1.87 to 3.2; the gas inlet temperature ranges from 60°C to 200°C, the water inlet temperature from 10°C to 55°C. The evaluated correlations, although accomplished at studded fins but geometrically close to segmented fins, are very comparative to the finned-tubes in this actual work. Both MIETH, [45], and WEIERMAN, [72], investigated segmented finned-tube bundles and developed correlations for the calculation of heat transfer. MIETH presents a calculation method with a step by step procedure to evaluate the heat transfer at helically segmented and solid finned-tubes. For this purpose, functions dependent on appropriate physical parameters as the mass-velocity, the diameter and fin type, the temperature, and the fin correction (fin spacing, fin height, and fin thickness) are stated in form of curves and charts. No correction for the segment widths at segmental fins is made due to their small influence. MIETH states a general accuracy considering predicted distribution corrections of  $\pm 5\%$  for an optimum flue gas distribution. This overall value is affected if less than three consecutive arranged tube rows are applied, [45]. WEIERMAN's investigations are accomplished at segmented and solid finned-tubes with staggered equilateral and isosceles tube layout as well as in-line square or rectangular tube arrangement. Since more data for staggered layout is available, the author specified the smallest uncertainties for this configuration. The equations for calculating heat transfer and pressure drop include geometry correction factors as well as non-equilateral and row correction factors. These correlations use the bare tube diameter as the characteristic length for calculating  $Nu$  or  $Re$  and differentiate only slightly from the ESCOA<sub>TM</sub>-correlation stated in [16]. The coefficient 0.23 in the power-law (basic correlation) is substituted by 0.25, refer to [4]. The traditional correlations of ESCOA<sub>TM</sub> as well as the revised ESCOA<sub>TM</sub>-correlations are presented in [16]. A more recent analysis is performed by VICENTE ET AL., [43]. They accomplished a single-phase experimen-

## 1. Introduction

tal analysis of heat transfer at a helical finned-tube heat exchanger at staggered tube arrangement in industrial scale. This analysis include a comparison between the performed measurements, the traditional correlations of ESCOA<sub>TM</sub> as well as the revised ESCOA<sub>TM</sub>-correlations. A precision of approximately 96% in heat transfer (ESCOA<sub>TM</sub>-traditional and ESCOA<sub>TM</sub>-revised minimum 96.61%) and 90% in pressure drop coefficient (ESCOA<sub>TM</sub>-traditional 81.15 ÷ 94.41%, ESCOA<sub>TM</sub>-revised 85.71 ÷ 90.63%) at  $Re \geq 10000$  is evaluated. Regarding the present pressure drop analysis, VICENTE ET AL. suggest the application of ESCOA<sub>TM</sub>-traditional equations, based on WEIERMAN, [72] for designing HSFHE<sup>2</sup>, because of the security tolerance between the correlation and their measured results. Regarding the heat transfer analysis and the security tolerance, the revised equations of ESCOA<sub>TM</sub> are in better agreement with their measurements.

WEIERMAN ET AL., [73], investigated the performance of in-line and staggered tube arrangements of different types of segmented finned-tubes. All the measurements are performed at an open circuit wind tunnel, where air is forced by a centrifugal blower across the tube banks and is straightened by perforated plates and screens, to provide uniformly distributed velocity profile as well as homogeneous and isotropic turbulence. In their study WEIERMAN ET AL. used shielded thermocouples to reduce uncertainties caused by radiation and applied a hot wire anemometer for velocity measurement. Thus, a detailed study of the temperature profile and velocity profile downstream of the tube bundle is accomplished. They ascertained that in-line arrangement should only be used for special cases because of the disadvantage of possible bypass flow between the tube bundles and fin tips with relatively low temperature, because the performance of this tube arrangement is strongly dependent on the tube and layout, [73]. The temperature of the fluid stream between the transversally arranged finned-tubes is much closer to the finned surface temperature. The comparison is performed for a  $Re$ -number of 36000. On the other hand, staggered arrangement of tubes in the flow channel may cause a higher pressure drop.

Several investigations at solid and segmented finned-tubes are accomplished and numerous correlations for the prediction of heat transfer and pressure drop of segmented and solid fin tubes have been developed or may be found in NIR, [47], WALCZYK, [69], STASIULEVIČIUS ET AL., [58], KAWAGUCHI ET AL., [35], HEDH, [27], VDI, [1] and FRASZ ET AL., [13] and [15], whereas the correlations of NIR are based on a large amount of heat-transfer and pressure-drop data. These general equations are valid for segmented as well as solid fins at staggered tube layout in the  $Re$ -range of  $Re_{Nir} = 300 \div 10000$  and are within  $\pm 10\%$  agreement with most of the available data. These equations use an equivalent hydraulic diameter, but are also derived with the diameter of the fin or the bare tube as characteristic length. The correlations developed by WALCZYK ET AL. are valid for bimetallic helically extruded high finned-tubes

---

<sup>2</sup>Helically serrated finned-tube heat exchanger

## 1. Introduction

at staggered layout. These equations consider the effect caused by the geometry and layout (bare tube diameter, fin thickness, fin pitch, fin height, and transversal tube pitch) and are evaluated in agreement of  $\pm 20\%$  with correlations in literature. The bundles are arranged with 2 to 6 consecutive tubes in cross-flow. The  $Re$ -number is varied between 2000 and 10000, but the effect of the tube row numbers on the dimensionless heat transfer coefficient and pressure drop coefficient related to a single tube row in cross-flow is not distinctly observed, [69]. The results of measurement are compared with results from literature of e.g. BRIGGS and YOUNG, [5] and STASIULEVIČIUS ET AL., [58]. Geometrical effects, e.g. row effects on heat transfer and pressure drop, have been observed in literature. In addition, correction factors have been introduced and a relationship between heat transfer and pressure drop, depending on the tube row number, has been established. The influence to the heat transfer as a function of the number of tube rows at different solid and segmented finned-tube bundles, arranged consecutively, is investigated by FRASZ in [13] and [15]. The developed equation for the row correction factor is compared and found to be in good agreement with literature. Additionally, a correction factor considering the geometry for calculating the heat transfer is introduced. The exponent of the  $Re$ -number in the power law varied between 0.54 and 0.82, depending on the longitudinal and transversal tube pitch as well as the bare tube diameter of the investigated finned-tubes. KAWAGUCHI ET AL., [35], compared the performance of segmented and solid finned-tube bundles. The staggered tube arrangement is chosen in a way, that half of the tubes next to the flow channel top and the bottom lies within the insulation outside the flow duct. As a result of the measurements, heat transfer and pressure drop correlations for 3 to 6 row deep solid and segmented finned-tube bundles are evaluated. Additionally, a row correction factor in case of few consecutively arranged tubes is developed. They concluded that in case of large fin pitch segmented finned-tubes are advantageous compared to tubes with solid fins, but the friction factor increases considerable. Also the tube arrangement within the bundle features smaller influence to heat transfer and pressure drop characteristics, [35]. KAWAGUCHI ET AL. specify an accuracy level of  $\pm 5\%$  for the equations used to predict the Nusselt number and the friction factor compared to the measured results.

Different selection criteria for solid and segmented finned-tubes are discussed by REID and TABOREK, [54]. They point out the cost-effective manufacturing of segmented finned-tubes, as already mentioned by RABAS and ECKELS. The fin segmentation seems to be advantageous because of compactness, weight, and cost per unit area. In their work REID and TABOREK also suggested the density of fins per meter tube dependent on the fin-side fluid type, which varies in case of natural gas combustion between  $6 \div 8$  fins per inch. If dry air is applied the fin density increases, but for liquid oil and solid fuel combustion this value drops down rapidly, [54]. Additionally, a basic guideline of design parameters is presented. With increasing fin density the total outside pressure

## 1. Introduction

drop increases, as well as fouling. For increasing fin height the fin efficiency increases more strongly for solid fins than for segmented. It is suggested to apply solid fins if the fin height is less than 12 mm because of the advantageous application behavior<sup>3</sup>. Especially regarding cleaning and fouling behavior, solid fins provide favorable design properties. Additionally some effects concerning the fin thickness, the tube pitch, and the tube layout type are discussed. The application of segmented finned-tubes rather than solid finned-tubes may compensate an increased pressure drop by the application of fewer tube rows within the bundle at the same performance, [54].

The experimental research of STASIULEVIČIUS and SKRINSKA, [58], comprises the effect of both the mean heat transfer behavior as well as the local heat transfer behavior of staggered solid finned-tube bundles in cross-flow. The investigated *Re*-range covered 10000 ÷ 1300000. The effect of two dimensional conduction through the fin is analyzed. According to STASIULEVIČIUS and SKRINSKA, geometrical parameters are taken into account, e.g. fin height, fin pitch. Since finned-tubes are mostly used as tube bundles, certain parameters are considered, such as the transverse tube pitch and the longitudinal tube pitch as well as the specification of the tube arrangement (staggered or in-line), [14]. They found that the mode of flow over the tube bundle is reflected in the flow pattern of the boundary layer in the leading part of the fin tube up to the flow separation and the vortex generation in the tailing part of the tube. Thus the exponent of the Reynolds number in the basic equation (power law) may change its value, [58]. The heat transfer from an inner tube row within the bundle is found to be higher compared to the first tube row. The increase in heat transfer is evaluated to be higher with increasing fin pitch and decreasing fin height, but decreases with greater longitudinal tube pitch of the tube bundle. In the work of [58], the local measuring technique using a calorimeter tube with a trapezoidal fin cross-section is applied. For the determination of the local heat transfer a point measuring technique is utilized. Thus the temperature and the heat transfer coefficient distribution across the fin surface as function of the circumference and fin height are evaluated. However, only few aspects in the work of STASIULEVIČIUS and SKRINSKA regarding the structure of boundary layer development as well as the fluid flow behavior near the fin surface are analyzed in detail.

LEGKIY ET AL., [40], investigated experimentally the local heat transfer behavior of a solid finned-tube in cross-flow. For this reason 6 heat flux sensors are embedded on a fin surface and 4 thermocouples are installed. The internal tube-side is heated while the air-side is cooled. During test conditions the finned-tube is rotated axially, thus the orientation of the sensors is varied and the air-sided heat transfer coefficient around and across the finned surface is able to be evaluated. The measurement is accomplished every 9° certain rotation angle. LEGKIY ET AL. evaluated the distribution

---

<sup>3</sup>This comment may related to the diameter of the bare tube



## 1. Introduction

of local heat transfer coefficients over the circumference and along the fin height of the finned surface for two different air velocities and calculated an averaged value over the total surface. A result of this study indicates two radial heat transfer maxima, one at the base and the other at the tip of the fin, [40]. As an additional course of this study the average values are compared with literature, which are evaluated in good agreement.

SHETTY ET AL., [57], investigated the local heat transfer behavior of solid vs. segmented finned-tubes. The Laser-Doppler Velocimetry (LDV) measurement technique for the determination of local velocities as well as turbulence parameters of the fluid, including also the velocity profile in the space between adjacent fins, is applied. Additionally, a liquid crystal thermometry is applied to measure the local fin surface temperatures. For more details regarding the measurement technique it is referred to [57]. From the known mass and energy balances the local heat transfer coefficients across the fin surface as well as the radial and angular heat conductions are evaluated. For the determination of the local heat transfer coefficient, the temperature difference between fin surface and contracting air is used. As the results of the work of SHETTY ET AL. indicate, the overall heat transfer coefficients for solid and segmented finned-tubes are very similar, which may be seen on one hand as an effect of better flow distribution of segmented fins, where the boundary layer detaches and reattaches due to fin segmentation. On the other hand solid finned-tubes provide a strong angular conduction component, [57]. Thus, SHETTY ET AL. concluded that these two effects may cancel each other.

HU and JACOBI, [31], analyzed the local heat transfer behavior of single-row finned-tubes in cross-flow with the help of optical adaptation of the naphthalene sublimation technique in order to evaluate the fin efficiency. Measurements are accomplished at an open-loop wind tunnel, where downstream of honeycomb flow straighteners the velocity profile (maximum velocity  $10 \text{ m/s}$ ) is measured applying a Pitot-probe and a hot-wire anemometer. Five annular finned-tubes are arranged as a single-row heat exchanger with a bare tube diameter of  $d_a = 38.1 \text{ mm}$  and a finning diameter of  $76.2 \text{ mm}$ . A selected tube in the flow channel center contains cast naphthalene. The casting procedure is presented in [31]; any sublimation by natural convection is prevented. During test run, contour measurements every  $10^\circ$  increments and for 10 different radii are accomplished within a  $Re$ -range of 3300 to 12000. The development of boundary layer, the flow separation, tube wake regions and horseshoe vortices are observed. The authors concluded that local heat transfer behavior is significantly influenced by fin tip vortices. In their research work HU and JACOBI stated that local flow structures have any influence on the average performance. The evaluated "true" fin efficiency of local measurements is below the fin efficiency, valid for a constant heat transfer coefficient above the finned surface, according to the definition in literature; and increases

## 1. Introduction

for high  $Re$ -numbers, [31]<sup>4</sup>. Furthermore, KEARNEY and JACOBI, [36], investigated the local convective behavior and fin efficiency of in-line and staggered (equilateral triangle) finned-tubes in the second tube row, within the  $Re$ -range of 5000 to 28000. In the course of their measurements the conventional naphthalene sublimation experiment is supplemented by a laser triangulation technique, to measure the sublimation depths. During test conditions, contour measurements every  $4^\circ$  increments and for 31 different radii are performed. The evaluated row-to-row heat transfer coefficient in staggered tube formation is approximately 45% lower at the first row than at the second. For in-line arrangement this value is in the range of  $34 \div 45\%$ . But the "true" efficiencies from all the evaluated local data are correlated in very good agreement to the average values. Also the corrected values obtained by HU and JACOBI, [31], are found to be in good agreement with literature. Thus they may finally conclude, compared to earlier studies, that local variations in heat transfer do not cause any significant impact to the fin efficiency at constant heat transfer coefficient. However, the authors indicate that the effect of bundle arrangement and fin height on local and overall heat transfer behavior may be linked, [36]. Additionally, KEARNEY and JACOBI, [36], calculated average heat transfer coefficient and pressure drop coefficient correlations for in-line and staggered arranged finned-tube bundles with two consecutive rows and compared the results with equations from literature, as e.g. SCHMIDT, BRIGGS and YOUNG, and STASIULEVIČIUS.

In WEBB, [70], an excellent survey of recent developments related to air-side aspects of plate fin and circular finned-tube studies is presented. Factors such as fin spacing, fin efficiency and fin configuration may yield enhanced heat transfer. Different fin surface geometries for performance enhancement are presented. Apart from a literature review of heat transfer and pressure drop coefficient correlations, row correction factors, tube arrangements (staggered vs. in-line) as well as local effects within the tube banks are being discussed. Yet one finned-tube heat exchanger study claims to maximize the heat transfer rate while simultaneously minimizing pumping power. WEBB, [71], as well as STEPHAN and MITROVIC [59], developed criteria for the evaluation of the performance of a heat exchanger in order to quantify the heat output capacity while considering the pumping power and the overall heat exchanger size.

**Survey of the Numerical Investigations** A considerable amount of researches on numerical investigations at fin and tube heat exchangers is accomplished in literature, e.g. by KAMINSKI, [34], GEISER, [19], and JOADAR and JACOBI, [33], just to mention some of them, but only the published work of TORRESI ET AL., [64], may be found

---

<sup>4</sup>The differential equation of heat conduction in cylindrical coordinates for steady state conditions has to be resolved numerically using a finite differencing technique; the fin material is assumed to be homogeneous and isotropic, and conduction normal to surface is neglected. Afterwards the temperature distribution is numerically integrated to evaluate the "true" fin efficiency, [31].

## 1. Introduction

in open literature concerning numerical investigations at circular/helically segmented finned-tubes. This is also intended by MON, [46] in the course of the comprehensive literature review about circular solid finned-tubes under cross-flow conditions.

GEISER, [19], investigated global and local fluid flow and heat transfer effects of fin and tube heat exchangers experimentally and numerically applying the commercial software *FIDAP* at  $Re_{num} \leq 2000$  and up to approximately  $Re_{exp} \leq 30000$ . For the investigation of local transport processes due to varying geometry, e.g. tube shape, the application of a convective mass transfer method (ammonia method) is employed, where the variation of different bare tube shapes at different  $Re$ -numbers is analyzed in detail.

The air-side flow and heat transfer behavior of fin and tube heat exchangers is analyzed in detail numerically with the application of the commercial CFD code *Fluent<sub>TM</sub>* by KAMINSKI, [34]. At the internal tube-side a refrigerant is condensed. Velocity, pressure, and temperature fields in between and across the fin segments are investigated. The parameter study consists of the variation of the fin pitch, the fin thickness, diameter of tubes and pitch of tubes, arrangement and number of tube rows up to approximately  $Re_{num} \leq 2000$ . From the results of the numerical simulations, heat transfer and pressure drop correlations are developed and compared with literature. Additionally, performance evaluations for the determinations of the effectiveness of different configurations are considered, comprising the heat transfer rate vs. pumping power.

The influence of heat transfer and air-flow downstream a solid circular finned tube is investigated in [53]. This is accomplished by means of an incompressible three dimensional-unsteady laminar calculation model, applying the PISO<sup>5</sup> algorithm for pressure-velocity coupling with a second order upwinding scheme. The mean flow velocity is chosen with  $2.5 \text{ m/s}$ , the inlet gas-temperature is fixed with  $T_{in} = 293 \text{ K}$ , and the wall-temperature is assumed to be constant with  $T_{wall} = 323 \text{ K}$ , which are typical values in air-cooled heat exchanger applications. RANAGAN ET AL., [53], investigated especially variations of the local effects from the flow field, by varying the fin spacings and their impact on the heat transfer augmentation. They evaluated the pumping power for the different configurations and found an optimum fin spacing. The impact of the clearance of two adjacent fins is found to be influenced by boundary layer development.

In the numerical study of MON, [46], global and local heat transfer as well as pressure drop investigations at circular solid finned-tube banks in cross-flow are investigated. The tube banks have been arranged in staggered and in-line layout, with 2 to 6 tube row numbers placed consecutively. A finite volume method, applying a three dimensional incompressible unsteady RNG  $k - \epsilon$  turbulence model with a wall function approach, is used to determine the flow and temperature field. Air is

---

<sup>5</sup>Pressure-Implicit Splitting of Operators

## 1. Introduction

considered with an inlet temperature of  $T_{in} = 308.15$  K and the wall temperature is assumed to be constant at  $T_{wall} = 283.15$  K. All simulations are performed in the range of  $5000 \leq Re \leq 70000$ . In the course of this unsteady simulation, flow structure phenomena and temperature distributions across the fin surface and within the bundle geometry are investigated. The investigation is concerned with the influence of fin height, -thickness, -spacing, tube diameter, -arrangement and number of tubes arranged consecutively, to develop  $Nu$  and  $Eu$  correlations, [46].

TORRESI ET AL., [64], analyzed in the course of their research the performance of horizontal type HRSG by means of a three dimensional steady-state numerical simulation, which is validated with experimental data. In their work they applied also porous media zones as modeling type for comparison with real modeled segmented finned- or bare-tubes, to reduce the complexity of the fluid flow behavior. The simulations of the single finned-tube in cross-flow are proceeded with an standard  $k - \epsilon$  model with a wall function approach, and are concerned mainly with fluid flow behavior in detail at the finned surface. The  $I$ -type right and left handed helical fins with 30 segments have a thickness of  $(0.026 \times d_a)$ , a total height of  $(0.211 \times d_a + 0.342 \times d_a)$ , and a transversal tube pitch of  $(2.37 \times d_a)$ . The computational grid is realized with unstructured meshes, and no end tube effect is considered, thus the finned-tube is considered to be arranged within an infinite tube bank. In the course of the simulations, the  $Re$ -number is varied between  $20000 \leq Re \leq 1000000$ , with an inlet pitch angle of  $20^\circ$  from the horizontal direction. Additionally, the inlet yaw and pitch angles are varied, to study the flow behavior above the finned-surface by means of pressure-drop evaluation. Performing the finned-tube simulations, they found that if the transversal pitch increases, the pressure drop and the deflection of the flow decrease, [64].

A basic research of a comparison of flow interactions past a circular cylinder and a circular finned-tube is performed by LEE ET AL., [39]. The three-dimensional, time-dependent numerical investigation is accomplished at  $Re = 300$ , calculated with the bare tube diameter and constant  $Pr$ -number. A single fin is modeled and calculated geometrically periodic along the spanwise direction. The results of the time histories of the velocity components indicate a more chaotic flow behavior caused by the presence of the fin. Due to smaller Strouhal numbers at the finned-tubes, the vortex shedding process slows down. Also the mean pressure drag coefficient and the surface averaged  $Nu$ -number of the finned-tube are smaller than compared with the smooth tube. However, due to greater total outside surface area, the overall heat transfer of the finned-tube is evaluated to be twice of the smooth cylinder, [39]. LEE ET AL. ascertained that the flow physics past the finned-tube show substantially different behavior compared to the smooth cylinder. It is denoted that the effect of fin spacing causes important influences on the formation of the flow-structure which affects the local and global heat transfer performance, [39].

## 1. Introduction

JANG ET AL., [32], compared steady state experimental and numerical results established from an investigated circular solid finned-tube heat exchanger with up to four consecutive arranged tube rows at staggered layout under dry and wet conditions within  $Re$ -number of approximately  $1500 \leq Re \leq 8000$ . The energy balance at measurements between air-side and tube-side is fulfilled within 3% under dry and 7% under wet conditions. For evaluating the average dimensionless heat transfer coefficient and pressure drop coefficient, average mean values for the fluid properties between inlet and outlet are associated for the evaluation. In the laminar numerical consideration the fluid is assumed as incompressible with constant fluid properties. The outlet of the computational domain is located seven diameters downstream from the last tube row. For the boundary condition of the computational domain of the three-dimensional numerical model, JANG ET AL. associated symmetry planes and the wall temperature is assumed to be constant. The local heat transfer coefficient is evaluated with the temperature difference between fin surface wall and local bulk average mean temperature of fluid. For meshing the computational domain, a multi-block system is used and a grid independence study is applied between three different grid systems, where the relative error of local pressure and temperature is calculated with less than 1%. The heat transfer and pressure drop results under wet conditions are 20% and 15% higher than for the dry bundle. A comparison with literature, especially with BRIGGS and YOUNG, [5], shows good agreement. From the numerical considerations JANG ET AL., [32], analyzed quite a difference in flow patterns between the mid plane of two adjacent fins and near the fin surface. As stated in the research work, a greater backflow area in the wake of the tube is observed in the mid-plane than near the fin surface. Also the temperature differences are evaluated differently for each tube row, compare with the work of MON. Another result is the dimensionless heat transfer coefficient integrated along the radii, which decreases with increasing circumferential flow angle around the tube, as a result of increasing boundary layer. A comparison within the gathered experimental and numerical results show a good agreement especially for the pressure drop behavior of the finned-tube bundle. But a comparison of the calculated heat transfer coefficients from the numerical considerations with the experimental data may be overestimated by 20% to 30%.

In [61], heat transfer from a cylinder in cross-flow is numerically investigated. Two dimensional steady state and unsteady simulations are compared with experimental results from literature by applying unmodified  $k - \omega$  SST<sup>6</sup> and modified  $k - \omega$  turbulence models. The investigations are performed for a  $Re$ -range of 7190 up to 50350 and a free stream temperature of 310°C. The unsteady simulations satisfactorily showed vortex shedding behavior. SZCZEPANIK K. ET AL. found that a comparison of the evaluated time averaged  $Nu$  numbers with the results obtained from steady state

---

<sup>6</sup>Shear Stress Transport

simulations, in their different turbulence models, do not account for any significant benefits in predicting heat transfer behavior from the tube, [61].

### 1.3. Concluding Remarks and Objectives

As discussed in the literature review of experimental techniques and numerical investigations above, heat transfer and pressure drop equations are functions depending on the one hand on geometrical parameters, e.g. fin height, fin pitch, fin thickness, fin width, and tube layout as well as tube pitch, and on the other hand on fluid properties as well as variables of state, etc. Finned-tubes as they are applied in a HRSG feature in principle geometrically a similar design. As REID and TABOREK in [54] stated, due to manufacturing reasons, a simple flat metal strip is cost effectively fixed around the bare tube, which is also denoted as *I* foot fin rather than the *L* foot fin type. Many different fin types of helically finned-tubes are well known, see Figure 1.2. These are the plain and crimped fin type, the G-base, the I-base and the recently applied U-base fin type, integral type and spirally wound finned-tubes and many more; for more details refer to literature. Because of the L-shaped and U-shaped fins an optimum contact area exists between fin and bare tube. As a result of this, L-shaped and U-shaped finned-tubes may be designed for maximization of the heat transfer properties. All these fin types may be found in literature, but apparently most available heat transfer and pressure drop correlations in literature are evaluated for solid finned-tubes with L-shaped and I-shaped fins.

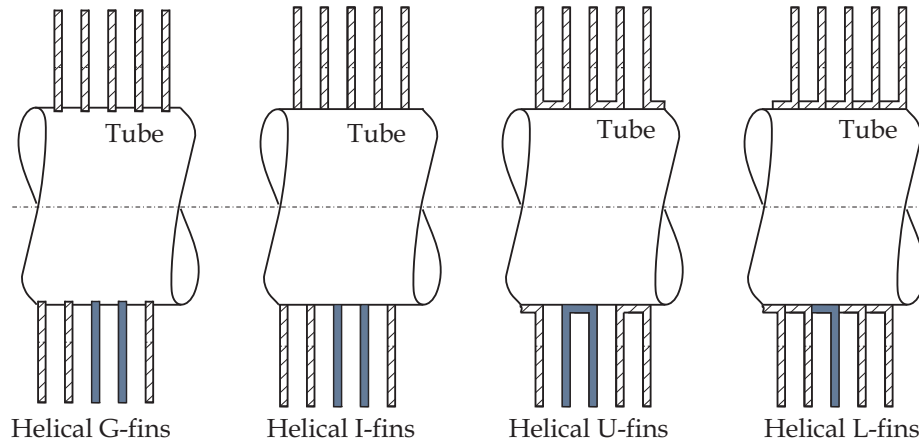


Figure 1.2.: Schematic Sketch of Selected Segmented Fin-Base Types

However, only few equations exist for finned-tubes with segmented fins. To the author's knowledge, no correlation is developed in open literature which accounts for the U-shape of segmented finned-tubes. Strictly speaking, all these correlations are measured at different conditions and definition regions for  $Re$  and  $Pr$ -numbers and

## 1. Introduction

with different geometries. Most of the above introduced correlations are found in the Section *Results*, in terms of a literature-comparison with the developed equations in this work. In order to calculate from these developed correlations the averaged heat transfer coefficient of an applied finned-tube bundle at real industrial applications according to the laws of heat conduction and heat convection, a so-called well known "fin efficiency" as a reduction coefficient (or temperature dependent performance value) has to be considered, which is introduced in Section *Data Reduction*. The overall heat transfer coefficients as required for the design of heating surface bundles in HRSG are averaged values across the entire fin surface of each tube (fin efficiency) as well as above all tubes within the bundle (average mean between inlet and outlet).

The objective of this work is to develop new heat transfer coefficient and pressure drop coefficient correlations for a heat exchanger with different numbers of consecutively arranged U-shaped finned-tubes in staggered layout, applicable for industrial scale, for the characterization of the global behavior at the gas-side. All investigations are accomplished at hot conditions, so that the effect of the pressure recovery through the tube bundle has to be considered, as well as ambient temperature conditions without any pressure recovery. The measurements are accomplished at the gas-side and at the water-side. The scope of a subsequently performed measurement validation should be addressed to fulfill the energy balance of the used system boundaries. As a result of measurements at different tube row configurations, a row correction factor for the heat transfer from the finned-tubes will be derived.

Furthermore, a three dimensional steady state numerical analysis of fluid flow and heat transfer above a solid and segmented finned-tube will be performed. For this reason, five different models of a single row finned-tube heat exchanger, with solid and segmented circular and helical I/U-shaped fins, are developed. It is intended to verify the results of the CFD-calculations within the computational model boundaries with those calculated from the measurements at the test rig, to draw any conclusions from global to local effects of conjugate heat transfer and fluid flow. Especially the difference between solid and serrated fins as well as the influence at the fin surface between two adjacent fins of *I*-shape and *U*-shape is analyzed. These studies, especially comparisons between measurement results at global performance and numerical investigations of local heat transfer behavior in a single finned-tube row, will provide further knowledge of the local thermal field and convective transport phenomena and will give a more complete understanding of the performance behavior.

Consequently to the fact that the choice of different correlations at the gas-sided mass flow inlet and outlet influences the design properties of a HRSG, a comparison of the developed heat transfer and pressure drop correlations with available literature is indispensable.

## 2. Experimental Techniques

Knowledge is the daughter of experiment.

*Leonardo da Vinci*

★

### 2.1. Experimental Apparatus

All experiments were carried out in a test rig at the laboratory of the Institute for Thermodynamics and Energy Conversion of the Vienna University of Technology. This experimental apparatus in semi-industrial scale has been built up to perform measurements of heat transfer and pressure-drop on tube bundles in cross-flow; a sketch is shown in Figure 2.1. Large parts of the description and methods have been taken from [14], [75]. The test facility allows measurement at Reynolds numbers in the range between 4500 and 35000<sup>1</sup>. This equals a flue gas mass-flow at the inlet of 0.6 to 4.5 kg/s.

The finned-tube bundle is admitted with hot gas of up to 400°C, which is generated by combustion of natural gas and air. Air at ambient conditions is sucked from the inside of the laboratory building by means of a radial fan. The fan is powered by a 90 kW three-phase alternator motor. The volume flow measurement of combustion air is performed using two different nozzles. In the range of high Reynolds numbers of about  $13000 < Re < 35000$ , a Venturi nozzle and in the range of  $4500 < Re < 15000$  at low Reynolds numbers, a smaller ISA 1932 inlet nozzle is applied.

Following that, the air is redirected in a connecting-section with a bend, and flows through a variable inlet guide vane, which is implemented in front of the radial fan. The radial fan can produce a maximum pressure height of 5000 Pa and generates 45000 Nm<sup>3</sup>/h at 3500 Pa. The air is directed through a 2500 mm long diffuser to the natural-gas burner. The subsonic diffuser allows static pressure recovery by reducing the fluid kinetic energy and thus increasing efficiency of operation of the apparatus [62]. The burner is designed as a duct-burner, drawing its combustion air partly from

---

<sup>1</sup>Herein the Reynolds number is calculated with the bare tube diameter of the investigated tube.



## 2. Experimental Techniques

the process air through ductings. The specifications are listed in Table 2.1. Maximum burner power is 1160 kW. The overpressure of approximately 60 – 80 mbar of gas in the duct-burner is necessary for a constant flue-gas flow through the experimental rig. The natural gas in the gas-pipe therefore has to be compressed, starting from approximately 15 mbar, by using a side-channel compressor with bypass control. The natural-gas flows to the burner through a safety system with pressure switch and magnetic valves. Firing is initiated by an ignition burner with high voltage pulse. The flame is controlled by means of a flame detector with ionization. Any temperature regulation is achieved through adjustable regulators, which control a gas adjustment valve.

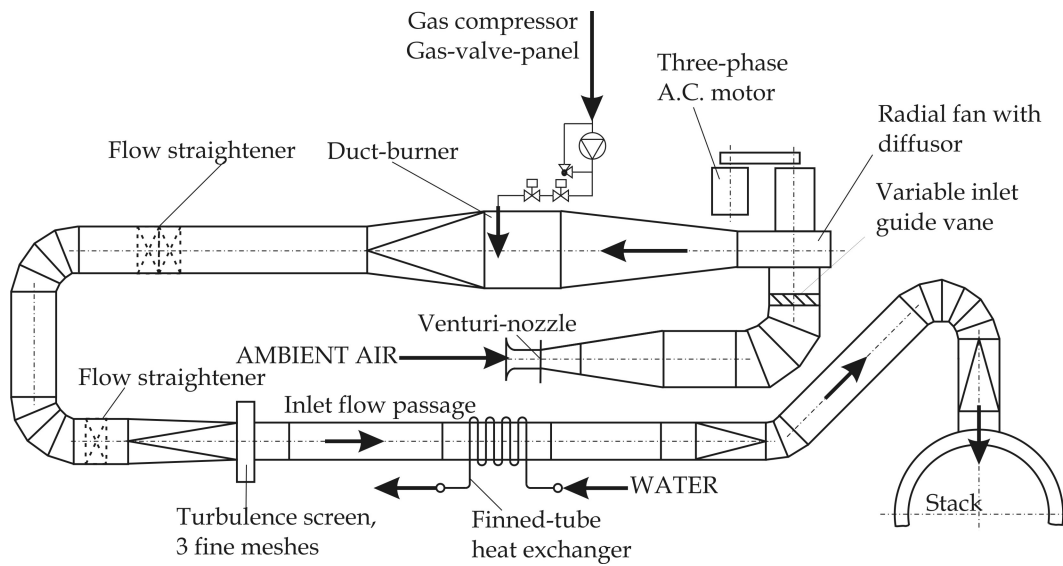


Figure 2.1.: Sketch of the Test Facility

Table 2.1.: Specifications of the Duct Burner

Manufacturer	<i>Flameco Eclipse</i>
Type	<i>TAH 400</i>
Maximum Temperature	<i>400°C</i>
Mass-flow of air	<i>3 kg/s</i>
Maximum burner power	<i>1160 kW</i>
Type of gas	<i>Natural gas</i>
Pressure of gas	<i>15 mbar / max. 150 mbar</i>
up-/downstream of compressor	

## 2. Experimental Techniques

Following that, the flue-gas is accelerated as it flows from a rectangular cross-section of  $1000 \times 750 \text{ mm}$  to a circular one within a diameter of  $600 \text{ mm}$ . This contraction causes a more uniformly distributed fluid flow and lowers the turbulence intensity [62]. In the circular tube two flow straightener applications are installed. Downstream of two  $90^\circ$  bends with turning vanes, there is an additional straightener application, followed by a transition piece to a rectangular cross-section,  $500 \text{ mm}$  in width and approximately  $1000 \text{ mm}$  in height. Therein turbulence screens, consisting of three fine-wire meshes in close arrangement, made of metal, are installed to rectify and/or straighten the flow. These screens are plain and mounted in normal direction to the fluid flow. The U-shaped layout of the test rig is necessary due to length restrictions placed by the experimental laboratory. Downstream of the flow straightener, which rectifies the vortices, caused by redirecting pipes, a  $500 \text{ mm}$  long adjustment-channel follows, which adapts the height of the experimental channel to the required value between  $900 \text{ mm}$  and  $1000 \text{ mm}$ . To avoid stall, the angle between the flow direction and the adjustment axis must be kept below  $7^\circ$ , [62]. Following that, a  $2250 \text{ mm}$  inflow (inlet)-channel is arranged, which serves to calm down the turbulent flow. The finned-tube heat exchanger with a tube length of approximately  $500 \text{ mm}$  is installed into a  $1500 \text{ mm}$  channel section. Downstream of this testing channel, a  $1500 \text{ mm}$  outlet-channel with the same cross-section is arranged. Then a further adjustment-channel follows with a  $500 \times 1000 \text{ mm}$  rectangular cross-section. Finally, a connecting-piece to a circular cross-section with a diameter of  $500 \text{ mm}$  is installed, which ends up in a steel tube stack, into which flue gases are conducted.

To dissipate the transferred heat from the finned-tube heat exchanger at the water-side, a cooling water cycle is installed. The columns are connected to the collectors in parallel at the water side. Each tube layer is therefore mounted to the flow-pipe and a return-pipe. The hot water from the return collector is recirculated through pipings to a closed circuit cooler with two ventilating fans, and is installed at the laboratory roof. Therefrom the water flows into a water tank. This water is recirculated to the finned-tube heat exchanger in the test-section with the help of a cooling water circulating pump with a pumping head of  $34 \text{ m}$  and a maximum volume flow of  $15 \text{ m}^3/\text{h}$ . The volume flow of water can be varied for each individual tube configuration in the range between  $\dot{V}_w = 1.1 \text{ m}^3/\text{h}$  and  $14.1 \text{ m}^3/\text{h}$ . An even cooling water flow distribution in the tubes is achieved by orifices installed downstream of the inlet collector. The diameter of these 11 nozzles is  $d_{nz} = 5.9 \pm 0.15 \text{ mm}$ . Thus, the velocity of water can be varied in the range between about  $u_w = 0.15 \text{ m/s}$  and  $0.5 \text{ m/s}$  for the individual setup. Additionally, a second cooling water circulating pump is installed to ascertain the minimal velocity of water for fully developed turbulent flow conditions inside of the finned-tubes. The system pressure of  $p_w = 2.7 \text{ bar}$  at the water-side is equalized with the use of a compensator reservoir of  $80 \text{ l}$ . For safety reasons, a pressure relief valve NW 32 with an actuation pressure of  $3 \text{ bar}$  is installed. A water treatment unit

## 2. Experimental Techniques

provides a complete demineralization of the used water to avoid incrustation and deposit of boiler scale.

All hot parts of the test facility are insulated using a 70 mm layer of mineral wool, an additional 50 mm layer of glass wool, and a layer of 1 mm aluminum foil as a finish to prevent or reduce heat loss. Instead of the glass wool, a 35 mm layer of ceramic wool is applied directly on the hot parts for the insulation of the test section. The cooling water collectors and the inlets as well as the outlets of the tube-bundle are insulated using polyurethane foam. For more detailed basic information about construction design it is also referred to [44], [14], and Appendix A.

### 2.2. Measurement Instrumentation

The experimental investigation requires a number of measurements to be taken simultaneously in order to evaluate and determine the amount of transferred heat as well as gas-side pressure drop. A diagram of the measurement application is presented in Figure 2.2.

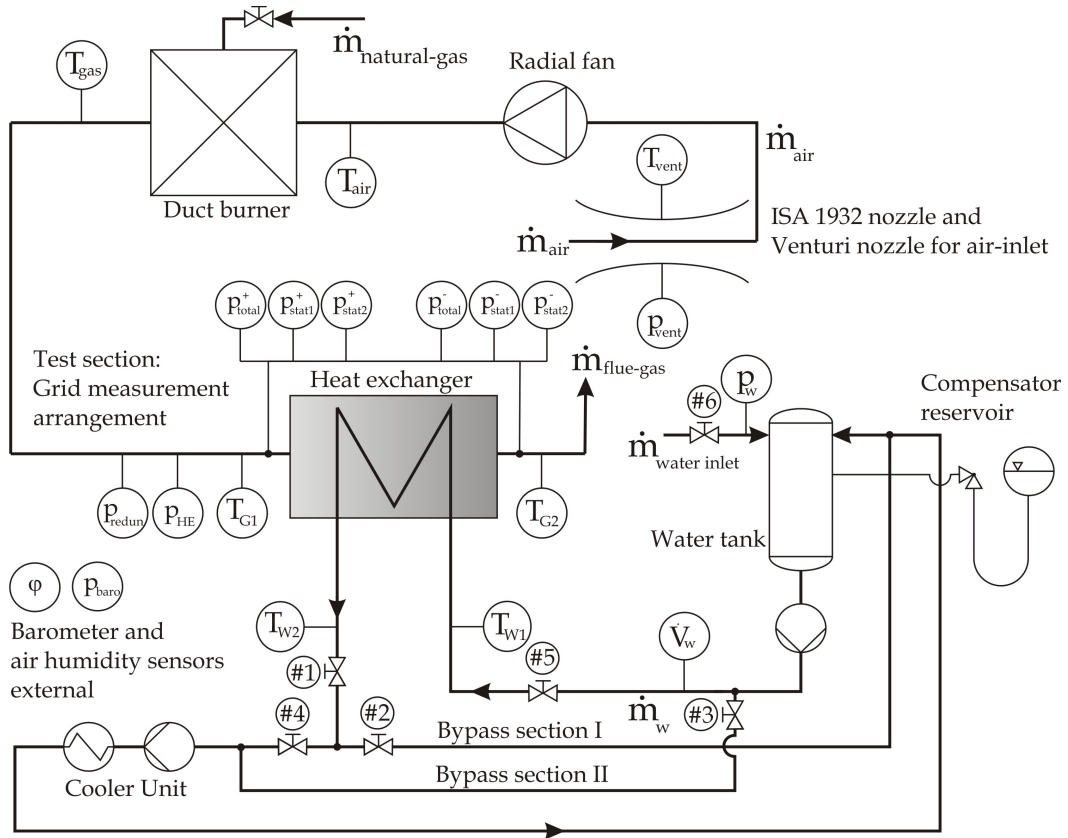


Figure 2.2.: Sketch of the Measurement Setup

## 2. Experimental Techniques

Some parts of the description can also be found in [75], but attention has to be paid to the various specifications. The temperatures at the water-side are measured in every tube (layer #1 to #11, see Figure 2.5 and Figure 2.6) at the inlet and at the outlet using Pt-100 RTDs (resistance temperature detectors), so that fringe effects can be ascertained for tubes near the channel-wall and thus be considered in the evaluation. Generally, the applied RTDs are very accurate and stable with a resolution of 0.1 K. At tube bundle configurations with 4, 6, and 8 consecutively arranged tubes, temperature measuring points are placed also at intermediate tubes rows. Thus, a total number of 28 RTDs are applied. The sensors are directly immersed in the water and sealed by screw joints [14]. All RTDs have a  $25\mu A$  power supply (IEX 0). The lead length is greater than 3 m. To compensate for this lead resistance in order to increase accuracy, a 4-wire technology measurement method is applied. One pair of wires carries the current through the RTD; the other pair senses the voltage across the RTD. Because of very small current flows through the sensing wires, the lead resistance error is negligible. The measured temperature signals from the Pt-100 sensors are transferred to two analog/digital converters (TBX-68T) with terminals for 14 analog inputs. Following those converters, two 24-bit high precision data acquisition devices (NI PCI-4351) convert the electrical voltages into temperature signals.

Gas temperatures are measured using *NiCr – Ni* thermocouples (type "K"). 8 thermocouples are mounted in form of  $(2 \times 4)^2$ , related to the flow cross-section, in front of and behind the heating surface of the heat exchanger in a certain distance for each individual tube configuration, to obtain a grid measurement. The electronic compensation for reference points is achieved by software. All "K"-thermocouples are connected to two modules (PAD-CB-K-P). Following a data acquisition unit (DEWE-BOOK), equipped with modules (PAD-TH8-P), all signals are processed to a serial input (RS-232) and transferred to a PC. In order not to significantly affect the flow pattern and a fast temperature responding behavior, the diameter of these thermocouples is chosen to be only 1.5 mm. To reduce any influences caused by thermal radiation (temperature difference between the first/last finned-tube row and the channel wall and/or flue gas respectively), all temperature sensors were adjusted into the far side of the tube and aligned in flow direction. Additionally three *NiCr – Ni* thermocouples measure the air-temperature at the Venturi nozzle and downstream of the fan as well as the gas-temperature of the duct-burner.

The volume-flow of water is measured using a calibrated hot water meter with an electronic sensor and an external power supply of 220 V (SCHINTZL IWUS 1). Beyond this, a 24 V pulse amplifier is connected, which transforms an electric current of 0 – 20 V, using a demodulator. This corresponds to a volume flow of 0 – 15 m<sup>3</sup>/h. A

---

<sup>2</sup>Two thermocouples are arranged at the sidewall near the bottom and two near the top of the flow-channel wall

## 2. Experimental Techniques

resistance of  $100\ \Omega$  converts this value to a voltage of  $0 - 2\ V$  for further processing to a data acquisition system (DAQ), using a connector block (SCB-100 100-Pin shielded) in single-referenced mode. The voltages are recorded with a 16-bit high-speed voltmeter unit (NI PCI-6031E). The humidity of air is measured by means of an electronic humidity sensor, and transformed to the same high-speed voltmeter unit.

The volume-flow of air is measured by determining the pressure difference up-/downstream of the nozzle and the barometric pressure in front of the inlet. The used pressure transducers, of the manufacturer Honeywell ©, especially feature stable transfer behavior and precise linearity. The pressure difference at the utilized Venturi nozzle is measured using two different piezo-resistive pressure sensors: a digital Honeywell precision pressure transducer (DPVENT) and a Furness Controls digital micro-manometer (MICROMANO) especially for the lower  $Re$ -range. Applying the ISA 1932 inlet nozzle, an analog Honeywell micro-switch series 160 (DPDUESE) is used. Barometric pressure (BARO) is measured using a digital Honeywell precision barometer. For detecting the absolute pressure in the combustion channel (PWT), an analog Honeywell micro-switch series 160 is applied.

The static pressure differences at the air-side of the finned-tube bundle (DV1-D) are measured in front of and behind the heating surface of the heat exchanger, to obtain a grid measurement using a Honeywell digital precision pressure transducer. Therefore, small boreholes are placed at four positions, top, bottom, and the side channel walls, to average the pressures in a closed circular Teflon coated pipe. Additionally, the static (DV2-A) and the total (DVT) pressure differences in the channel center are measured using a United Sensor pitot-static pressure probe TM-US-PAE18M and analog Honeywell micro-switches. A redundant pressure transducer (DPREDUN) is installed at the test section inlet against outage of PWT. All specifications of the applied pressure transducers are given in Table 2.2. The accuracy is related to full scale (FS). The supply voltage of all analog pressure transducers is supplied using a constant-voltage source (LTRONIX B 703 DT) of  $8\ V$ . Any voltage fluctuation is compensated with the reference voltage, using a monitoring program. The voltage output of  $1 - 6\ V$  of each individual transducer is sampled with a 16-bit high-speed voltmeter unit (NI PCI-6031E).

The measured values are transmitted to the process computer using measurement value periphery by National Instruments and the LabView 7E program system. Every 30 seconds a complete loop is performed by the generated program. This contains the time for the sampling rate of the signals and a time delay. The program processes all sampled measurement signals automatically. For this purpose, polynomials for the specific heat capacities of flue-gas and the thermo-physical properties of gas are used, see FDBH-Handbook [9]. The thermo-physical properties of water are implemented

## 2. Experimental Techniques

Table 2.2.: Specifications of the Pressure Transducers

Fabrication	Notation	Accuracy	Range
Honeywell PS 162PC01D	PWT	$\pm 0.15\%$	$0 \div 69 \text{ mbar}$
Honeywell PS 164PC01D37	DV2-A	$\pm 0.25\%$	$0 \div 25 \text{ mbar}$
Honeywell PS 163PC01D36	DPREDUN	$\pm 0.25\%$	$-12.5 \div 12.5 \text{ mbar}$
Honeywell PS 163PC01D75	DPDUESE	$\pm 0.25\%$	$-6.35 \div 6.35 \text{ mbar}$
Honeywell PS 164PC01D37	DVT	$\pm 0.25\%$	$0 \div 25 \text{ mbar}$
FURNESS CONTROLS FCO12	MICROMANO	$\pm 2 \text{ Pa}(FS)$	$0 \div 200 \text{ Pa}$
Honeywell PPT0001DWW2VB	DV1-D	$\pm 0.05\%$	$-69 \div 69 \text{ mbar}$
Honeywell PPT0001DWW2VB	DPVENT	$\pm 0.05\%$	$-69 \div 69 \text{ mbar}$
Honeywell HPB200W2D-B-A	BARO	$\pm 0.4 \text{ hPa}(FS)$	$0 \div 25 \text{ mbar}$

according to [23]. This is completed using a C-subroutine programming language. If the water temperature and pressure are known, the density, specific enthalpy, dynamic viscosity, thermal conductivity, and the *Pr*-number are calculated automatically using the steam table, [75]. The polynomials for the thermal conductivity of fin and tube material are implemented using diagrams from literature, [42]. The influence of the air-humidity to the partial pressure of water vapor is considered by a correction of the density variation at the flue-channel inlet, using the ANTOINE-equation. After an input of all geometrical data from the heat exchanger, the iterative calculation of the dimensionless heat transfer coefficient and the pressure drop coefficient is performed automatically. For investigation purposes, diagrams indicate a steady state condition of the water/gas temperatures, if the transferred energy difference between water- and gas-side is lower than 5%. All continuously measured and calculated data is saved to a data-file in table form. The test facility is operated only through the screen displays; no other instruments are necessary.

### 2.3. Calibration of the Configuration

All measurement systems for the determination of pressure, temperature, volume flow of water as well as air, and the humidity have to be calibrated before application.

**Resistance Temperature Detectors and Thermocouples** Since the calculation of the transferred heat starts from the water-side and is performed in the direction of the gas-side, especially the temperature of water has to be measured very precisely. For investigation purposes, the temperature measurement is arranged at the tube inlet and outlet in a way that simply temperature differences are measured at the water-side of a single tube and thus the relative measurement error will be reduced. For a pre-

## 2. Experimental Techniques

cise measurement and determination of the dimensionless heat transfer number, all  $Pt - 100$  should lie within a range of  $\pm 0.5^\circ\text{C}$  relative deviation. Thus, it is possible to calibrate all RTDs together in a water bath. The tank is insulated using a layer of ceramic wool. A mixer application ensures an even temperature distribution within the water bath. All 28 temperature sensors and a reference thermometer are mounted at the cover of the tank in a plate with small bore-holes in a certain distance and immerse into the water at equal height. As reference thermometer a 1/10  $Pt - 100$  DIN 385 is used. Applying an electrical heater, the temperature is elevated in steps of  $5^\circ\text{C}$ , starting from about  $0^\circ\text{C}$  up to  $100^\circ\text{C}$ . To reach the lower temperature bound, crashed ice of distilled water is used. Each step is temperature stabilized for 15 minutes. Afterwards, to avoid hysteresis effects, the water is cooled down to ambient temperature. The whole calibration process has to be repeated. After calculation from the deviations of each RTD, compared to the reference thermometer, fitting functions with an exponent of  $3^{\text{rd}}$ -order magnitude are implemented into the measurement program. For the calibration of the 11 thermocouples, a field-calibrator unit (JOFRA Model 600S) is applied. All temperature sensors and the reference thermocouple were calibrated together using fine quartz-sand for an equal temperature distribution within the immersion shell. The relative uncertainty of the reference thermocouple should lie within  $\pm 3^\circ\text{C}$ . The calibration procedure starts from ambient temperature and elevates stepwise in  $25^\circ\text{C}$  increments up to  $450^\circ\text{C}$ . Fitting functions with an exponent of  $4^{\text{th}}$ -order magnitude are calculated for all thermocouples.

**Pressure Transducers** Although the analog pressure transducers were pre-calibrated (linearized and temperature compensated) by the manufacturer, an additional calibration process is performed. This is done by means of a pressure calibrating device (Meriam Instruments MERI-CAL II). To ensure highest accuracy, an external pump with a turning wheel is utilized and a deairing valve ensures initial conditions. To minimize all measurement uncertainties it is important to achieve a steady state to reduce all dynamics of the air column inside, which causes oscillations and pulsations within the pipe. A representative number of measurement points, depending on the measurement range of the pressure transducer, are taken. Fitting functions with an exponent of  $2^{\text{nd}}$ - or  $3^{\text{rd}}$ -order magnitude are calculated for all analog pressure switches.

**Venturi Nozzles at the Air-Side** As already mentioned above, two different instruments are applied to measure the volume flow of air at the inlet. This is done to reduce the measurement uncertainties of the determined volume flow at the lower measurement boundary, because the pressure drop above the inlet nozzle rises with a smaller diameter and same pressure height of the radial fan. The venturi nozzle for higher  $Re$ -Numbers of about  $13000 < Re < 35000$  is constructed with a rectangular cross-section. This does not conform to the European standard [8]. Thus, the flow coefficient for the nozzle was evaluated individually in an empirically way by FRASZ [14]

## 2. Experimental Techniques

and GASTEIGER [17]. The narrowest nozzle cross-section is  $0.1789 \text{ m}^2$ . The pressure drop coefficient is derived iteratively from the pressure drop equation of BERNOULLI for incompressible flow of gases, because at the inlet an almost constant temperature and thus  $\rho = \text{const.}$  can be assumed. The flow coefficient is defined by

$$\zeta_{Vent} = 1.788 + \left( 1.11 \log \frac{Re_a}{10^6} \right). \quad (2.1)$$

Therein the  $Re$ -Number is calculated with a hydraulic diameter of the rectangular flow cross-section  $D_{Vent}$ , the velocity of air  $u_a$  is calculated due to pressure-drop above the nozzle, and it is assumed that all thermo-physical properties at the inlet are evaluated for humid air. In [17] a velocity profile and a turbulent intensity at the outlet of the venturi nozzle is ascertained. For an average flow velocity of  $10 \text{ m/s}$ , a turbulent intensity of about  $6 - 8\%$  is determined. The ISA 1932 inlet nozzle for low Reynolds numbers of about  $4500 < Re < 15000$  is designed according to the European standard [8]. The narrowest inlet nozzle cross-section is applied with  $0.0452 \text{ m}^2$ .

**Flow-Meter at the Water-Side** The hot water-meter is calibrated using high precision flow control unit (FLUXUS ADM 6725) applying the well established ultrasonic flow measuring method.

### 2.4. Test Section

The heat exchanger consists of a rectangular sheet-steel channel in which bare-tubes or finned-tubes are arranged horizontally with a given transversal and longitudinal pitch. The free channel width is fixed with  $500 \text{ mm}$  and the channel height is  $975 \text{ mm}$ . The advantage of the removable channel piece is the comparatively easy reassembling. As described also in [14], the tubes of  $600 \text{ mm}$  length are constructed in a way that fins are arranged on a length of  $495 \text{ mm}$ . The additional approximately  $50 \text{ mm}$  at each tube end are smooth. The bare tubes, which remain after the fins at the tube ends are cut off, offer the advantage of an assembling through the sidewalls of the heat exchanger. This in turn provides a complete sealing, using asbestos-substitute cord rings and conical thrust washers on the outside of the flow-channel. All connecting pipes between the single tube rows are arranged within the insulation at the outside of the channel, [14]. This is the only arrangement allowing exact measurement of heat transfer at the small test section width of the tube banks. Measurements are thus not influenced by any bypass flow through the space for the bends. The connecting bends have been soft soldered together, using conventional copper fittings, as these maintain their dimensions well<sup>3</sup>. This provides an easy mounting, and O-rings are used to achieve a tight seal with the finned-tubes. At the tube end, the water-tubes

---

<sup>3</sup> $T_{w_{max}} = T_{sat}|_{2.7 \text{ bar}}$



## 2. Experimental Techniques

are equipped with soldered pipe connections of brass with O-ring grooves, in which these copper fittings are mounted. The whole construction is fixed together using steel profiles, which are mounted at the outside of the test-channel. A detailed construction drawing is presented in the Appendix in Figure A.2. As seen, the heat exchanger is operated in counter cross-flow. In case of investigating less than eight tube rows arranged consecutively, the perforated plate is sealed with a steel sheet by means of inert-gas-shielded arc welding.

Apart from the possibilities of the heating techniques, the complete thermal simulation is applied. Here, all tubes are heated and temperature sensors are placed in every tube at the inlet and outlet of the water-side<sup>4</sup>. Thermocouples are placed at the inlet and the outlet of the gas-side. The flow temperature is defined as the arithmetic mean gas-temperature at the inlet and the outlet of the bundle [58]. Generally, the measurement uncertainty is higher and the accuracy is lower than when applying the local thermal simulation method. Here, the measuring tube (calorimeter) is heated, whereas the remaining tubes in the bundle are unheated. The main advantage is the small temperature difference between the calorimeter tube wall that influences the temperature of the flow at the inlet and the outlet [58].

Two possibilities exist for calculating the heat transfer coefficient from row to row. The first one is the measurement of the water temperatures at 8 staggered arranged tubes with RTDs installed at intermediate tube rows. The alternative is the measurement of different row-configurations. In each individual case, the tube-surface temperature has to be calculated. As the results show, it is more difficult to determine exactly the temperatures of two consecutive tube rows, especially of intermediate ones. Thus, different tube configurations are investigated.

### 2.4.1. Investigated Finned-Tubes

The investigated U-shaped finned-tubes of the company *Rosink Apparate- und Anlagenbau, Germany* are kindly provided by the company *BERTSCHenergy Kessel- und Energietechnik Apparatebau, Austria*. The profile of the helical finned-tube used is depicted in a schematic sketch in Figure 2.3. Therein the fin pitch  $t$  is  $\frac{1}{n_R}$ ,  $b_s$  is the average segment width,  $h_s$  the average segment height,  $h_b$  the fin height minus  $h_s$ ,  $s$  the average fin thickness,  $h$  the average fin height,  $s_t$  the tube thickness, and  $D = d_a + 2h$ , with  $d_a$  as the bare tube diameter.

The geometrical data of the tube and the arrangement in the test channel is summarized in Table 2.3. The geometrical dimensions of the investigated tubes are equal to real industrial scale. Some special fin details are depicted in Appendix A. Figure 2.4 shows the different fin types and the differences in contact area schematically.

The diverse geometry and a higher thermal input to the fin or tube produces a

---

<sup>4</sup>Also in some tubes of an inner row; at least in a single tube of each row, in case of more than two tube rows arranged consecutively

## 2. Experimental Techniques

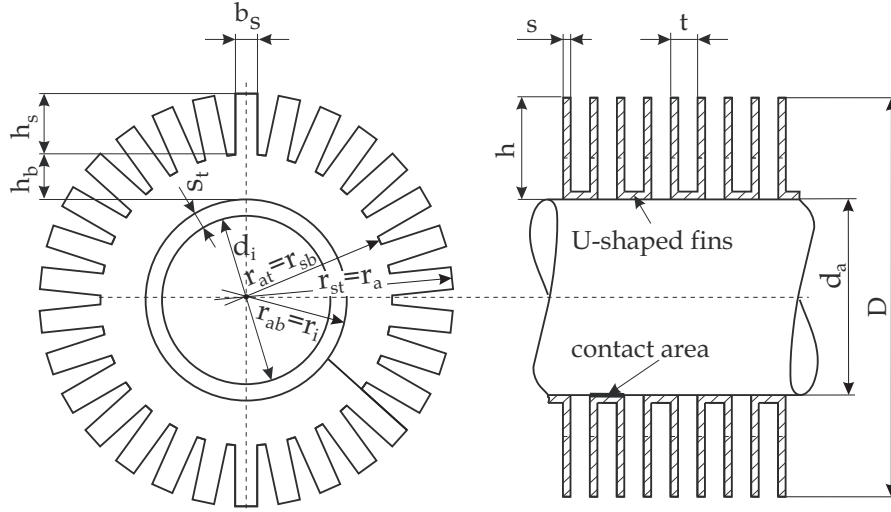


Figure 2.3.: Sectional Sketch of the Investigated Finned-Tube with U-Shape

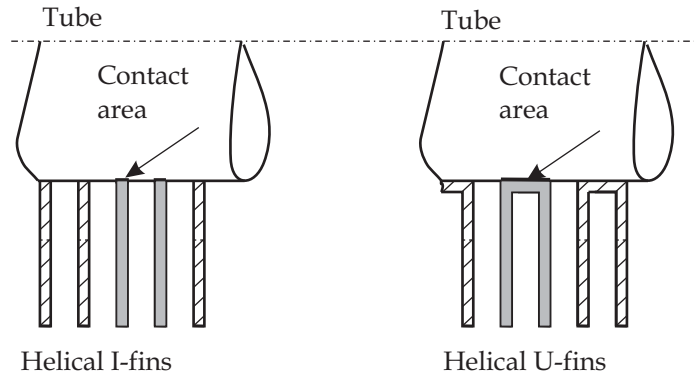


Figure 2.4.: Contact Area of I-shaped and U-shaped Finned-Tube

difference in heat conduction amount. The main idea of the U-shaped finned-tube is a larger contact area between fin and tube than with I-shaped fins. Throughout a larger fin base, enough space for laser welding manufacturing is available [14]. The closer fin spacing opportunities allow a higher total outside surface area at equal fin height. U-shaped fins in turn provide the construction possibility of equal or smaller installation size and weight of the heat exchanger. If the fin height at equal number of fin per  $m$  is enlarged, the pressure drop tend to be larger. This assumption requires as a prerequisite, that the longitudinal and transversal tube pitch is unvaried, which equals the test conditions. The temperatures are almost equal in these considerations. The smaller projected minimum net free area between the tubes causes a higher pressure

## 2. Experimental Techniques

Table 2.3.: Specifications of the Investigated Finned-Tube

Fin Geometry	Notation	U-shaped segmented
Bare tube diameter	$d_a, d$	38.0 mm
Tube thickness	$s_t$	3.2 mm
Number of fins per m	$n_R$	295 1/m
Average fin height	$h$	20.0 mm
Average fin thickness	$s$	0.8 mm
Average tube length	$L_t$	495 mm
Average segment width	$b_s$	4.3 mm
Average segment height	$h_s$	11.5 mm
Number of segments	$n_s$	30
Number of tubes in flow-direction	$N_R$	8, 6, 4, 2, 1
Number of tubes per row	$N_L$	11
Longitudinal tube pitch	$t_l$	79 mm
Transversal tube pitch	$t_q$	85 mm
Outside surface area for 8 tube rows	$A_{tot}$	84.48 m <sup>2</sup>
for 6 tube rows	$A_{tot}$	63.36 m <sup>2</sup>
for 4 tube rows	$A_{tot}$	42.24 m <sup>2</sup>
for 3 tube rows	$A_{tot}$	21.12 m <sup>2</sup>
for 1 tube row	$A_{tot}$	10.56 m <sup>2</sup>
Fin material		DC 01
Tube material		St35.8
Net free area of tube row	$F_{min}$	0.2292 m <sup>2</sup>

drop. This can be seen as follows:

$$\Delta p_{FT} = N_R \tilde{\xi} \frac{\rho_{gm} u_E^2}{2} \quad (2.2)$$

with

$$u_E = \frac{\dot{m}_g}{F_{min} \rho_{gm}} . \quad (2.3)$$

According to few selected literature, where investigations and analysis are performed by [14], [70], [52], [35], [13], [73], [72], and [54], it follows that finned-tubes with segmented fins show a somewhat higher heat transfer and thus turbulence than those with smooth fins, since the development of a laminar boundary layer has to be renewed at each individual segment. Heat will be transferred especially convectively at low velocities between the adjacent fins. This effect may also be enhanced if the fins are helically arranged around the bare tube. The upstream fluid flow of

## 2. Experimental Techniques

the first tube row is comparable to a flow over a single tube in cross-flow. The second tube row lies in the wake region of the first tube row. These vortices, caused by tube arrangements, are in partial responsible for heat transfer enhancement. Thus, the convective heat transfer from the fluid to the tube-surface is enhanced. Likewise a staggered formation instead of in-line arrangement of the tubes within the bundle increases turbulence, but also causes a higher pressure drop as the measurement results show [14], [52], [35], [13], [73], and [72], just to mention some of them. At equal installation size, an increase of the heat transfer surface area, and thus of the heat transfer rate, is only achieved at the expense of an increase in pressure drop. On the other side, an increase of the total outside surface area, by means of e.g. the fin pitch or the fin height, of a finned-tube heat exchanger provides specific parameters to enhance the heat transfer rate at the gas-side.

### 2.4.2. Geometrical Arrangement and Configuration of Tubes in the Bundle

The characteristics of the dimensionless heat transfer coefficient  $Nu$  and the dimensionless pressure drop coefficient  $\zeta$  of finned-tubes within a bundle is noticeably influenced by the tube arrangement. Apart from the possibilities of staggered or in-line tube configuration, KUNTYSH and STENIN [38] investigated partly staggered layouts. They examined five tube arrangements. Starting from an in-line tube line-up, the last layout, an equilateral triangular pitch is reached by rotating all consecutively arranged tubes by a certain angle, beginning with the first tube row. The heat transfer shows to be maximum at an angle of about  $24^\circ$ . It was found that the thermal performance is about 5% smaller for equilateral triangular pitch ( $30^\circ$ ) than at the intermediated position with the maximum effectiveness. Regardless of the different tube arrangements, the first tube rows in these investigations yield to the same heat transfer intensity. These results are found applying the total and the local modeling technique.

In this actual study, all test series are performed at finned-tube bundles with staggered formation. Apart from equilateral triangular pitch, studied in literature (e.g. [73]), the investigated tube arrangement is isosceles triangular pitch, which is the most examined layout in scientific open literature. The certain displacement angle is  $\gamma = 28.28^\circ$ . In Figure 2.5, a schematic sketch of six consecutive tube rows in staggered tube formation is depicted. The columns are connected to the collectors in parallel and consist of 11 horizontal tube layers each. The heat exchanger is operated in counter-crossflow. The tube bundles are assembled in 2, 4, 6, or 8 consecutive rows or as a single tube row. All investigated tube banks have the same transversal and the same longitudinal pitch. To measure heat transfer at a lower number of consecutive rows than 8, the tubes were removed from the downstream of the test channel. Measurements for a single tube row were only possible due to modification of the test rig, because the system is only designed for an even number of tube rows. In case of investigating fewer tube rows than 6, any occurrence of a detrimental bypass flow, as a result of the staggered formation in the flow channel, through the otherwise empty

## 2. Experimental Techniques

space must be prevented. This effect increases especially with a single tube row configuration. The effect of any bypass flow can be assessed with the distances  $x_t$  at the top and  $x_b$  at the bottom of the flow duct, which are approximately  $x_t \approx 7 \text{ mm}$  and  $x_b \approx 50 \text{ mm}$ , see Figure 2.5 and Figure 2.6. Thus, a bypass flow of roughly 6 – 8% is calculated. This effect can be seen in the energy balance, which is barely fulfilled. To reduce the flow bypassing effect, a semi-tube has to be installed at the bottom of the channel wall. However, the disadvantage is a very complicated construction design at the tube water-side. Because of this, the semi-tube does not participate in heat transfer and thus is not taken into account for calculations. However, the semi-tube is seen as a resistance, which reduces the effective minimum net free area in a tube row.

## 2. Experimental Techniques

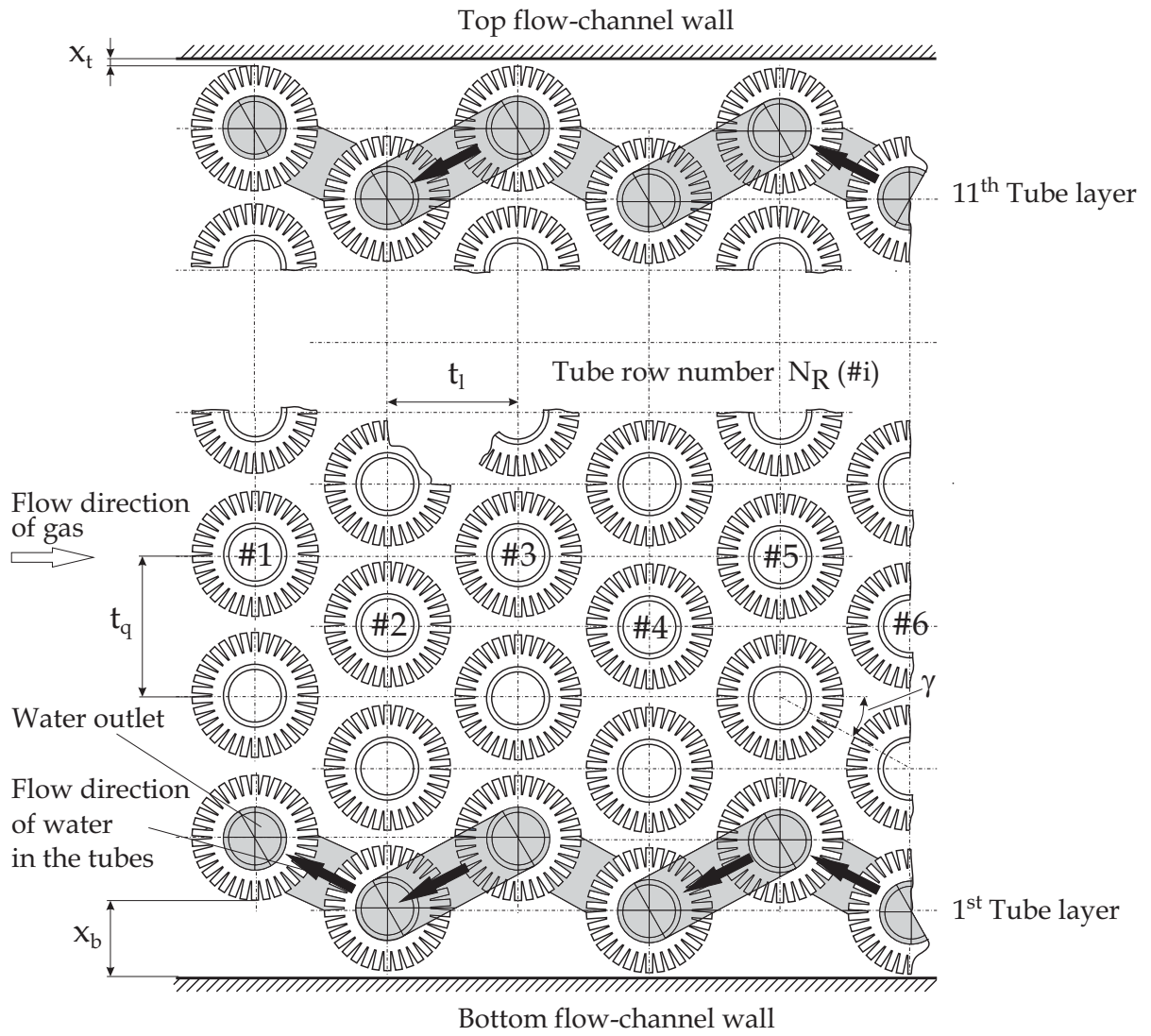


Figure 2.5.: Sketch of the Staggered Tube Arrangement

## 2. Experimental Techniques

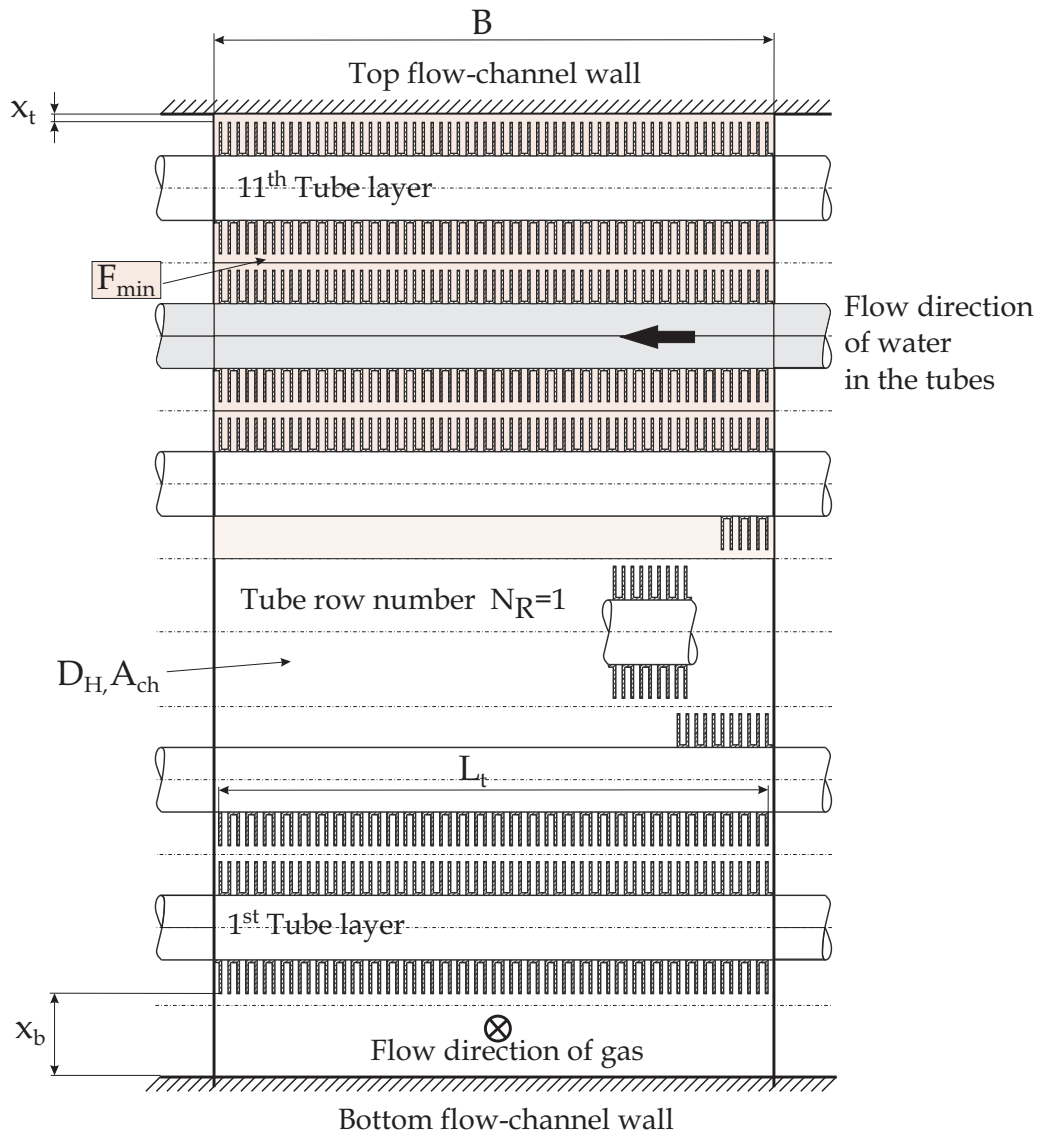


Figure 2.6.: Sketch of the Tube Arrangement in Flow Direction

### 2.5. Measurement Procedure

All measurements in the test rig are performed to get information about heat transfer and pressure drop behavior of serrated helical finned-tubes of U-shaped geometry. It is also intended to get some information especially about the influence of the tube row number in flow direction upon the heat transfer intensity. The selected measurement range at the gas-side for  $Re$  as mentioned above is comparable to realize industrial application conditions (as it occur in a HRSG). The following preliminary tests and measurements at different configurations of tubes were performed:

- Preliminary tests at the unloaded channel
- Preliminary tests at solid and segmented finned-tubes
- Experimental rig configuration tests
- Measurements at 8, 6, 4, and 2 consecutively arranged finned-tube rows
- Measurements at 1 heated finned-tube row with 7 consecutively arranged unheated rows
- Measurements at 1 finned-tube row with/without a semi-tube installed at the channel-wall
- Temperature dependence and stability tests

*Preliminary tests at the unloaded channel* are attempted to validate the pressure drop coefficient due to friction of the test section walls. For this purpose the analog pressure transducers (DV2-A, DVT) and the high precision digital micro-manometer (MICROMANO) are installed. Since the velocity of flue gas is low and the length of the measurement section rather small, compared to the hydraulic diameter of the cross-section, the estimated pressure drop will also be very low. This circumstance amplifies a very high measurement uncertainty of the measurement instrumentation. Two test runs are accomplished at ambient conditions. In the analysis of the measured values, the density  $\rho$  is assumed to be constant. The dynamic portion of the pressure drop is very small. Hence, it is neglected in further calculations. The principal arrangement of the measurement positions  $P1$ ,  $P2$  is presented in the Appendix A.2 qualitatively.

Generally, the micro-manometer tends to have a more uniform pressure drop characteristic than the piezo-resistive pressure transducer, because of its lower measurement uncertainty. But especially at low  $Re$ -numbers, in case of small pressure differences, the measurement systems DV2-A and DVT lead to very high measurement uncertainties. Any conclusion about the pressure drop coefficient, calculated from DV2-A and DVT, are therefore be to neglected. Also, any conclusion about the pressure drop coefficient, calculated from the micro-manometer, is limited to the range between  $1.85 \times 10^5 < Re < 4.25 \times 10^5$ .



## 2. Experimental Techniques

The shear stress between the channel wall and fluid along the wall causes a pressure drop. It is assumed that all properties of state, i.e. density  $\rho$ , temperature  $T$ , pressure  $p$ , and the specific internal energy as well as the specific enthalpy are constant across the cross-section of the flow channel. The relative surface roughness is evaluated from the pressure drop coefficient of a channel with rectangular cross-section due to friction with the well known equation

$$\lambda = 2\Delta p_{Ch}\rho \frac{D_{Ch}}{L} \left( \frac{A_{Ch}}{\dot{m}_g} \right)^2. \quad (2.4)$$

Following the measurement results, a typical relative surface roughness (hydraulic smooth tubes  $\lambda = 0.02 \div 0.03$ ) for the inlet/outlet tube and the test channel is assessed. For all investigations, the pressure drop coefficient of the test channel due to friction is correlated, implementing the KONAKOV-equation [37]. This equation is valid for turbulent flow conditions in the range between  $10^4 < Re_{Ch} < 10^6$  and is defined as follows:

$$\lambda = \frac{1}{(1.8 \log(Re) - 1.5)^2}. \quad (2.5)$$

All finned-tube test cases with different tube bundle configurations have the same upstream pressure drop measurement position of  $\approx 190 \text{ mm}$  in front of the first finned-tube row and downstream measurement position of  $\approx 1250 \text{ mm}$  from the test channel inlet, see Figure A.2.

**Experimental rig configuration tests** are performed at solid finned-tubes with a bare tube diameter of  $31.8 \text{ mm}$  and segmented finned-tubes as specified in Table 2.3. This was inevitable to verify the energy balance between the water/gas-side and to determine all heat losses as well as the operation of the test rig. A full stabilization of a single measurement point, starting from a cold test rig and considering the warm-up phase, takes about 2 – 3 hours; under operating conditions about 90 minutes. After the expiration of this time, the measurement point at steady state conditions is recorded and the program loop is repeated about 25 times. The air-flow is regulated with a frequency converter beyond the three phase AC motor and an inlet guide vane. The most effective handling of the test run is to start from high frequency with low temperatures and a fully open inlet guide vane down to low frequency with high temperatures and a nearly closed vane. Each complete measurement at different configurations was performed twice, to ascertain the reproducibility and repeatability conditions as well as to lower any measurement uncertainties. In case of investigating tube rows fewer than 6, the water-velocity and the water-temperatures are limited, because the mass-flow of water has to be lowered down as a result of the small test section width and the small temperature differences between the inlet and the outlet. Thus, the uncertainty of the calculated transferred heat will be reduced. The heat transfer at the water side is calculated, using the well known equation of GNIELINSKI in [1], which is valid at constant wall-temperature and constant heat flux. From the region of validity of this

## 2. Experimental Techniques

equation, the minimum water temperature boundary can be calculated. The lower and upper boundary of the water-velocity is limited due to technical reasons of the cooling water circulating pump. The boiling temperature of water at 2.7 bar ascertains the upper temperature boundary. These conditions restrict the measuring area for all different test configurations and are presented in Figure 2.7.

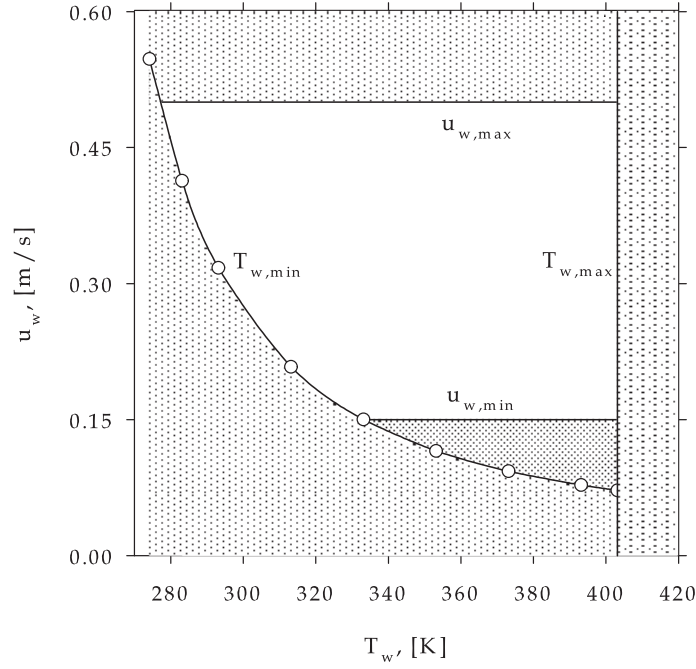


Figure 2.7.: Measurement Range of Water

All setting parameters during a test run, the average mean values, the standard deviations of the measurement values, the thermo-physical properties, the geometrical dimensions, and the used materials are the certain condition to characterize explicitly all gathered information about convective-, conductive heat transfer, and fluid flow within the measurement range.

*The measurements at different finned-tube configurations* are intended to investigate the effect of heat transfer enhancement at different tube row numbers, arranged in flow direction. Also effects, caused by different fin-heights and number of fins per  $m$ , as well as the differences of solid and segmented fins will be analyzed. The comparison is done by means of the obtained measurement results and those performed by FRASZ [14]. This study is especially emphasized to obtain new results about a single U-shaped fin-tube row under cross-flow conditions and to calibrate the following CFD calculations.

## 2. Experimental Techniques

*Temperature dependence tests* are carried out to declare the stability of the obtained measurement point regarding the  $Re$ -number, as well as the evaluation and measurement validation process.

### 2.6. Data Reduction

In this chapter the equations for calculating the dimensionless heat transfer coefficient and the pressure drop coefficient are derived. As presented in [28], [30], and [29] particular specific assumptions are made for the analyzed segmented fins.

#### 2.6.1. Governing Equations for Heat Transfer

Generally, the method for calculating global heat transfer at finned-tubes is common practice and is taken from [22], [14], and [1]. The dimensionless heat transfer coefficient  $Nu$  of a finned-tube at the gas-side is usually correlated semi-empirically, using dimensionless numbers  $Re$  and  $Pr$ . These functions have a strong monotonic characteristic and thus can be piecewise approximated to a power-law function within the scope of validity, and are well known as NUSSELT-Equation [21]. The selection of the characteristic length for the  $Re$ -number is rather nonuniform. In open literature, the bare tube diameter [58], [14], [56], [16], [72], and [1] the average mean fin-diameter, the equivalent in area diameter [9], and the hydraulic diameter [47] are used as reference parameters, just to mention a few of them. In this work, the bare tube diameter for the characteristic length is used, though the heat exchange is not described exactly.

To evaluate the air-sided heat transfer behavior of finned-tubes, the transferred heat has to be determined. This is done by use of energy balances, ascertained with the 1<sup>st</sup>-law of thermodynamics for stationary flow processes. The heat flow due to the change of enthalpy of the water and gas in the heat exchanger can be determined from the measurements. In case of negligible heat loss from the test section surface, the transferred energy of water and gas must be equal.

$$\dot{Q} = \dot{m}_w (h_{w2} - h_{w1}) = \dot{m}_g c_{p_g} (T_{g1} - T_{g2}) \quad (2.6)$$

First, the logarithmic mean temperature difference  $LMTD$  has to be ascertained for the different configurations. According to [67], the  $LMTD$  for a counter cross-flow heat exchanger is calculated with

$$LMTD_{CC,z} = \sqrt[z]{LMTD_X} (LMTD_C)^{1-\frac{1}{z}}. \quad (2.7)$$

Therein,  $z$  is the number of consecutively arranged equal crossings. In case of  $z = 1$ , Equation (2.7) changes into the formula for cross-flow heat exchangers

$$LMTD_X = \Theta (\vartheta_{g1} - \vartheta_{w1}). \quad (2.8)$$

## 2. Experimental Techniques

The correction factor  $\Theta$  defines the balance or imbalance of the heat exchanger, using the ratio of the capacity rates. If  $z \rightarrow \infty$ , Equation (2.7) is reduced to

$$LMTD_C = \frac{(\vartheta_{g1} - \vartheta_{w2}) - (\vartheta_{g2} - \vartheta_{w1})}{\ln \left( \frac{\vartheta_{g1} - \vartheta_{w2}}{\vartheta_{g2} - \vartheta_{w1}} \right)}. \quad (2.9)$$

Equation (2.9) is the *LMTD*-equation of a counter-flow heat exchanger. In Figure 2.8 the relative deviations between the Equations (2.7) to (2.9) as a function of  $N_R$  are demonstrated. The average mean value shows a very slight increase of the calculated uncertainty  $e$  (rel. deviation), if Equation (2.9) is used for the different heat exchanger configurations. An average mean error maximum of 3% is calculated. The difference between counter-flow and counter cross-flow in the formula for the calculation of the logarithmic mean temperature difference is decreasing with an increasing number of consecutive tube rows. Therefore, in this study for all tube row configurations, the *LMTD* is calculated using Equation (2.9) for counter-flow heat exchangers.

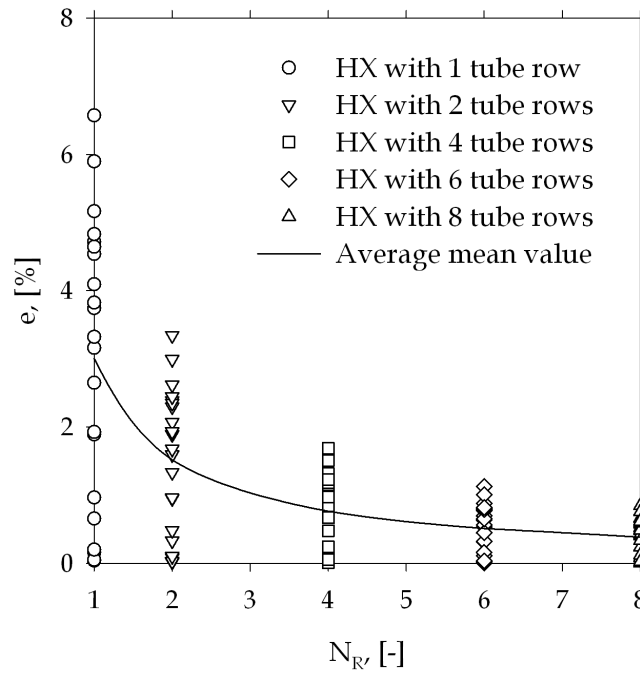


Figure 2.8.: Relative Deviation between Counter Cross-Flow and Counter-Flow Heat Exchanger

The total outside surface area  $A_{tot}$  of the finned-tubes is calculated non-helicly and the fin is modeled with an *I*-shape, see Figure 2.9. The fin steel-strip consists of

## 2. Experimental Techniques

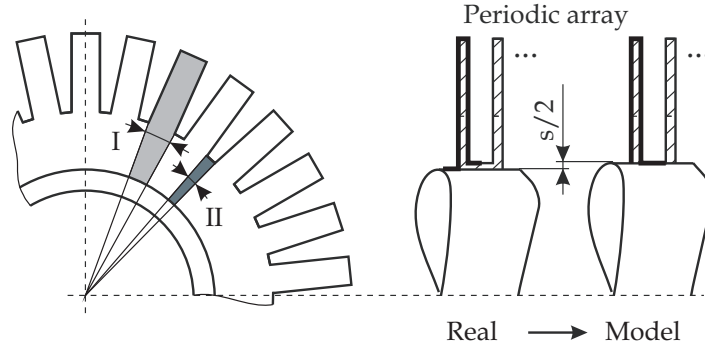


Figure 2.9.: Fin-modeling for Calculation

the solid part and the segmented part. During production process, the fin is wound around a boiler tube in a helical manner and is stretched at the outside and slightly compressed at the inside in circumferential direction. Yet, for a more precise approximation, also the lengthening piece between the segments of the projected fin face and circumferential face is considered. Nevertheless, all dimensions of the geometry are seen as an average mean measurement value of the 88 finned-tubes. Thus,  $A_{tot}$  is expressed as

$$\left. \begin{aligned} A_{tot} &= n_r (A_{tube} + A_f) \\ &= n_r (A_{tube} + A_{ff} + A_{tf} + A_{lf} + A_s) \\ &= n_r (A_{tube} + A_{ff} + A_{tf} + A_{lf} + A_{sff} + A_{stf}) \end{aligned} \right\} \quad (2.10)$$

where  $A_{tube}$  is the face of the free bare tube and  $A_f$  the fin face.  $A_{ff}$  is the projected fin face,  $A_{tf}$  is the segment tip face,  $A_{lf}$  is the segment lateral face, and  $A_s$  is the total face enlargement of the fin. This increase in size is grouped into the projected fin face  $A_{sff}$  and tip face  $A_{stf}$ . These considerations are defined for a single fin and tube in a periodic array, as shown in Figure 2.10.

With the data from Table 2.3 as depicted in Figure 2.3 it follows:

$$\left. \begin{aligned} \frac{A_{tot}}{n_r} &= [(d_a + s) \pi (t - s)] + \\ &2 \left[ \frac{\pi}{4} \left( (d_a + 2h_b)^2 - (d_a + s)^2 \right) + n_s b_s (h - h_b) \right] + \\ &n_s s b_s + \\ &2 n_s s (h - h_b) + \\ &2 n_s h_b \sin \left( \frac{\pi}{2 n_s} \right) \sqrt{h_b^2 - \left( h_b \sin \left( \frac{\pi}{2 n_s} \right) \right)^2} + \\ &2 n_s s h_b \sin \left( \frac{\pi}{2 n_s} \right) \end{aligned} \right\} \quad (2.11)$$

## 2. Experimental Techniques

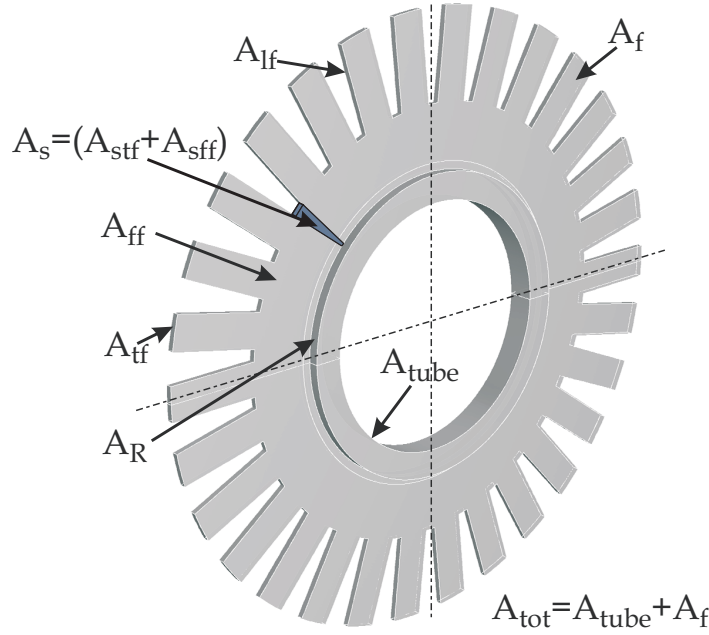


Figure 2.10.: Fin-surfaces for Calculation

The heat transfer coefficient at the internal side of the tube, as mentioned above, can be calculated with the knowledge of all data at the water-side. Combining the energy balance with the law of FOURIER, the overall heat transfer coefficient  $k$  is expressed with

$$k = \frac{\dot{Q}}{A_{\text{tot}} LMTD} = \frac{1}{\frac{1}{\alpha} + \frac{A_{\text{tot}}}{A_{\text{R}}} \left( \frac{d_a + s}{2\lambda_t} \ln \frac{d_a + s}{d_i} + \frac{d_a + s}{d_i \alpha_i} \right)}. \quad (2.12)$$

The apparent heat transfer coefficient  $\alpha$  at the gas-side is defined, using the logarithmic mean temperature difference, the geometry, and the fluid properties. This calculation scheme equals those mentioned in [73], [1], and [22]. To calculate the actual heat transfer coefficient at the finned-tube "surface"<sup>5</sup>, a reduction coefficient – so-called fin efficiency – is defined, according to [56]. This fin efficiency is calculated according to the laws of heat conduction and is restricted to uniformly distributed heat transfer coefficient across the fin surface and thermal insulation at the surface of the segmented section, see also [14]. To define fin efficiency, the segmented finned-tube is divided into two parts.  $\eta_{r1}$  (I) includes the radial part, starting at the fin-base and ending at its tip.  $\eta_{r2}$  (II) is the fin efficiency for the radial part of the fin without the segment. This is presented in Figure 2.9. Under the assumption of given reduced fin

<sup>5</sup>Substantially, this assumption quantifies the fin-part and the tube-part

## 2. Experimental Techniques

height  $h_{red1}$  and  $h_{red2}$  it follows that

$$\eta_{r1} = \frac{\tanh(m_1 h_{red1})}{m_1 h_{red1}}, \quad (2.13)$$

$$\eta_{r2} = \frac{\tanh(m_2 h_{red2})}{m_2 h_{red2}}, \quad (2.14)$$

with

$$m_1 = \sqrt{\frac{2\alpha_0}{\lambda_f s} \frac{b_s + s}{b_s}}, \quad (2.15)$$

$$m_2 = \sqrt{\frac{2\alpha_0}{\lambda_f s}}, \quad (2.16)$$

as fin-efficiency parameters. Herein,  $\lambda_f$  is the thermal conductivity of the fin material and  $b_s$  the segment width. The reduced fin height is calculated according to the method of SCHMIDT [56], [13], and [14] separately for the radial part with and without the segment. To define for this case  $h_{red1}$  and  $h_{red2}$  a Taylor series expansion of the linear terms, which is accurate enough, is used and expressed as follows:

$$h_{red1} = h_b \left( 1 + 0.35 \ln \left( \frac{d_a + 2h_b}{d_a} \right) \right) + \left( h_s + \frac{s}{2} \right) \quad (2.17)$$

$$h_{red2} = \left( h_b + \frac{s}{2} \right) \left( 1 + 0.35 \ln \left( \frac{d_a + 2h_b}{d_a} \right) \right). \quad (2.18)$$

This approach for evaluating fin efficiency of the segmented finned-tube shows good agreement compared to literature e.g. [72], [16]. To consider the effect of heat transfer from the fin tip, the effective fin height is increased by one half of its thickness, according to literature e.g. [58] uses the approach of STYRIKOVICH. If Equations (2.15) and (2.16) are applied to (2.13) and (2.14) with (2.17) and (2.18), overall fin efficiency  $\eta_r$  calculates as follows

$$\eta_r = \eta_{r1} \frac{d_a + h_b}{d_a + 2h_b} + \eta_{r2} \frac{h_b}{d_a + 2h_b}. \quad (2.19)$$

With the developed fin efficiency, the current (external) heat transfer coefficient at the surface is determined iteratively by

$$\alpha_0 = \frac{\alpha A_{tot}}{A_{tube} + \eta_r A_f}. \quad (2.20)$$

Using the characteristic length  $d_a + s$  of the modeled I-fin (real U-shaped fin), the dimensionless number  $Nu_0$  is calculated using the established equation

$$Nu_0 = \frac{\alpha_0 (d_a + s)}{\lambda_{gm}}. \quad (2.21)$$

## 2. Experimental Techniques

Special care has to be taken of the choice to substitute the fluid properties. The dimensionless groups include all fluid properties, which are temperature dependent and thus it has to be distinguished if the wall temperature or the average mean temperature of the flue-gas is to be set [14]. By taking into account the average mean boundary layer temperature at the gas-side

$$T_b = \frac{T_w + T_{gm}}{2}, \quad (2.22)$$

the Nusselt number states

$$Nu_b = Nu_0 \frac{\lambda_{gm}}{\lambda_b}. \quad (2.23)$$

The *Pr*-Number at the gas-sided average mean boundary layer temperature is defined as follows:

$$Pr = \mu_b \frac{c_p}{\lambda_b}. \quad (2.24)$$

The average velocity of the fluid flow in this work is defined with the projected minimum net free area between the investigated tubes, see Figure 2.6.

$$F_{min} = H B - N_L \left( (d_a + s) L_t + 2 \left( \frac{L_t}{a + s} \right) s h \right) \quad (2.25)$$

In case of a half tube installed at the channel wall,  $F_{min}$  changes to

$$F_{min} = H B - N_L \left( (d_a + s) L_t + 2 \frac{L_t}{a + s} s h \right) - \left( \frac{d_a + s}{2} L_t + \frac{L_t}{a + s} s h \right). \quad (2.26)$$

The Reynolds number is calculated according to [14] with

$$Re_b = \frac{\dot{m}_{RG} (d_a + s) T_{gm}}{F_{min} \mu_b T_b}. \quad (2.27)$$

### 2.6.2. Governing Equations for Pressure Drop

The total pressure drop of the finned-tube and the channel is obtained by

$$\Delta p = \Delta p_{FT} + \Delta p_{Ch}, \quad (2.28)$$

where  $\Delta p$  is the measured pressure difference between the inlet and outlet of the test section above a length of 1040 mm. These measurement positions are presented in Figure A.2.  $\Delta p_{FT}$  is the pressure drop of the finned-tube bundle (inserts, resistances in the flow channel) and  $\Delta p_{Ch}$  is the pressure drop calculated with Equation (2.4).

By considering the pressure variation as a result of the temperature change above the bundle, the total pressure drop coefficient for the serrated tube bundle in the test section is calculated with

$$\xi_{N_R} = \left[ \Delta p + \underbrace{\left( \frac{\dot{m}_g}{F_{min}} \right)^2 \left( \frac{1}{\rho_{g1}} - \frac{1}{\rho_{g2}} \right)}_{\text{density variation}} \right] \frac{2}{\rho_{gm} u_E^2} - \lambda \frac{L_{Ch}}{D_{Ch}} \left( \frac{u_E}{w_{Ch}} \right)^2. \quad (2.29)$$



## 2. Experimental Techniques

The pressure drop coefficient due to friction of the channel is correlated approximative using Equation (2.5), as verified before. All properties for the physical quantities are based on the arithmetic mean temperature of hot gas between inlet ( $T_{g1}$ ) and outlet ( $T_{g2}$ ). The flue-gas cools down along the way through the heat exchanger. Thus, the volume and the velocity are reduced. The flue-gas density rises if the temperature is lowered. The pressure variation as a result of velocity change is seen from the momentum balance for a horizontal channel with  $\rho(x) \neq \text{const.}$  as follows [51], [50], [41]:

$$\frac{1}{\rho(x)} \frac{dp}{dx} + \frac{d}{dx} \left( \frac{u^2}{2} \right) = 0. \quad (2.30)$$

If  $\frac{dp}{dx} = \text{const.}$  and  $\rho(x)$  is known, then Equation (2.30) changes after reordering and integration into:

$$\begin{aligned} \frac{1}{\rho(x)} \frac{dp}{dx} &= - \frac{d \left( \frac{u^2}{2} \right)}{dx} \\ - \int_1^2 d \left( \frac{u^2}{2} \right) &= \frac{u_{g1}^2 - u_{g2}^2}{2} \end{aligned}$$

with

$$\begin{aligned} \frac{dp}{dx} \int_1^2 \frac{dx}{\rho(x)} &= \frac{dp}{dx} \int_1^2 v(x) dx \\ &\approx \frac{dp}{dx} \left[ \frac{v_{g1} + v_{g2}}{2} \right] L \\ &= \frac{dp}{dx} \frac{1}{2} \left[ \frac{1}{\rho_{g1}} + \frac{1}{\rho_{g2}} \right] L \end{aligned}$$

Thus, (2.30) simplifies to

$$\frac{u_{g1}^2 - u_{g2}^2}{2} \frac{1}{L} = \frac{1}{2} \left[ \frac{1}{\rho_{g1}} + \frac{1}{\rho_{g2}} \right] \frac{\Delta p_\rho}{L}.$$

After rewriting and introducing the mass balance,  $\Delta p_\rho$  can be expressed as:

$$\Delta p_\rho = \left( \frac{\dot{m}_g}{F_{min}} \right)^2 \left[ \frac{1}{\rho_{g1}} - \frac{1}{\rho_{g2}} \right]. \quad (2.31)$$

This term considers the density change due to a temperature variation. In case of cooling, the term is positive (pressure recovery) and negative for heating. To compensate for all side effects, all pressure drop measurements are performed additionally at ambient temperatures without heat exchange through the heating surface. Then the density between inlet and outlet is almost equal ( $\rho_1 \approx \rho_2$ ) and Equation (2.30) is

## 2. Experimental Techniques

reduced to the BERNOULLI-equation for incompressible flows. The pressure drop of the inserts (tube bundle) becomes

$$\Delta p_{FT} = N_R \xi \frac{\rho_{gm} u_E^2}{2},$$

using the afore mentioned Equation. The velocity within the minimum net free area of a tube row  $u_E$  is defined by

$$u_E = \frac{\dot{m}_g}{F_{min} \rho_{gm}},$$

if Equation (2.3) is recalled. Finally, the *average* pressure drop coefficient of a single tube row is determined with

$$\xi_{1R} = \frac{\xi_{N_R}}{N_R}. \quad (2.32)$$

This relationship is shown in section 4.1.1 and is performed according to well established literature e.g. [58], [73], and [14].

### 2.7. Measurement Validation

The measurements are accomplished at the gas-side and at the water-side. Apart from describing the functional connections of the measurements, the scope of the validation should be addressed to fulfill the energy balance of the used system boundaries. Each heat transfer measurement series is performed to attempt high accuracy. To obtain precise heat transfer correlations, each calculated point is validated after measurement. The applied data validation model, shown in [28], was introduced by TENNER, KLAUS, and SCHULZE [63]. This curve-fitting technique utilizes equations for mass and energy balances as well as measurement value equations. The basic concept of the validation is to use all measurement values with their variances and co-variances in such a way that all calculated "true" measurement values fulfill the auxiliary conditions. This criterion, developed by [63], is adopted to the applied measurement process as follows: The energy balance Equation (2.6) is determined and its conditions must be met. With the unknown measurement values for the variables  $\dot{m}_w$ ,  $\dot{m}_g$ ,  $T_{w1}$ ,  $T_{w2}$ ,  $T_{g1}$ , and  $T_{g2}$ , these equations change to:

$$\dot{Q} = M_1 c_{p_w} (M_2 - M_3) \quad (2.33)$$

and

$$\dot{Q} = M_4 c_{p_g} (M_5 - M_6). \quad (2.34)$$

The measured values with their uncertainties

$$\mathbf{M} = (M_1, M_2, \dots, M_6), \quad (2.35)$$

do not fulfill the side conditions. For this reason, all values  $\mathbf{M}$  are supplemented with correction factors. Thus, the true values are:

$$\mathbf{V} = \mathbf{M} + \mathbf{v}. \quad (2.36)$$

## 2. Experimental Techniques

The correction factors  $\nu$  are determined in such a way, that equation (2.37) reaches a minimum and the side condition (2.39) is equal to zero. According to the method of least squares, Equation (2.37) with the empiric inverse matrix for the co-variance reads as

$$G(\nu) = \nu^T \sum M^{-1} \nu \mapsto \text{Min}. \quad (2.37)$$

It is attempted to investigate steady state conditions. Thus, the temperature difference between flue-gas and channel wall is nearly equal. Also the temperature difference between the fin tip and flue-gas is very small. The adjacent fins do have also nearly the same temperature distribution above the surface. Thus, the portion of radiant heat transfer is very small and is therefore to be neglected in the further calculation of gas-sided heat transfer coefficient.

The heat losses through the channel wall are evaluated according to [1]. The heat flow is calculated according to the laws of convection and conduction. The convective heat transfer coefficient at the internal side of the test channel wall is known. The layers of the channel wall, the ceramic wool, the mineral wool, and the aluminum foil are considered in the evaluation of the heat conduction. At the outside of the channel wall, the heat transfer coefficient is calculated separately according to the laws of heat transfer at horizontal and vertical plates under natural convection. The surface temperature is estimated and measured to have a maximum of  $T_{surf} = 60^\circ\text{C}$ . Inside the laboratory building, the temperature has ambient conditions. The finally calculated heat losses are very small, which leads to the conclusion that the resistive layers of the isolations from the test channel wall are very effective. Since the heat loss through the channel wall is rather small compared to the transferred heat by means of the heat exchanger, the energy balance becomes

$$\dot{Q}_w + \dot{Q}_g + \underbrace{\dot{Q}_l}_{\dot{Q}_l < \dot{Q}} = 0 \quad (2.38)$$

Thus, the side condition is

$$h(V) = 0. \quad (2.39)$$

After combining equation (2.37), (2.39) and using the LAGRANGE multiplier

$$\lambda = (\lambda_1, \lambda_2, \dots, \lambda_6), \quad (2.40)$$

it follows:

$$G(V, \lambda) = (V - M)^T \sum M^{-1} (V - M) + 2\lambda^T h(V) \mapsto \text{Min}. \quad (2.41)$$

It can be assumed that all measured values are independent, so the matrix of the

## 2. Experimental Techniques

co-variances according to [63] and [60] changes into

$$\sum_{i=1}^6 M_i = \begin{vmatrix} \sigma_{M_1}^2 & 0 & 0 & 0 & 0 & 0 \\ 0 & \sigma_{M_2}^2 & 0 & 0 & 0 & 0 \\ 0 & 0 & \sigma_{M_3}^2 & 0 & 0 & 0 \\ 0 & 0 & 0 & \sigma_{M_4}^2 & 0 & 0 \\ 0 & 0 & 0 & 0 & \sigma_{M_5}^2 & 0 \\ 0 & 0 & 0 & 0 & 0 & \sigma_{M_6}^2 \end{vmatrix}.$$

The variance of a random variable is a measure of a statistical dispersion from the mean value. For the weighting function, the relative uncertainty is considered. After combining the inverse co-variance matrix

$$\sum_{i=1}^6 M_i^{-1} = \begin{vmatrix} \frac{1}{\sigma_{M_1}^2} & 0 & 0 & 0 & 0 & 0 \\ 0 & \frac{1}{\sigma_{M_2}^2} & 0 & 0 & 0 & 0 \\ 0 & 0 & \frac{1}{\sigma_{M_3}^2} & 0 & 0 & 0 \\ 0 & 0 & 0 & \frac{1}{\sigma_{M_4}^2} & 0 & 0 \\ 0 & 0 & 0 & 0 & \frac{1}{\sigma_{M_5}^2} & 0 \\ 0 & 0 & 0 & 0 & 0 & \frac{1}{\sigma_{M_6}^2} \end{vmatrix}$$

with equation (2.41), it follows that

$$G(V, \lambda) = \frac{(V_1 - M_1)^2}{\sigma_{M_1}^2} + \frac{(V_2 - M_2)^2}{\sigma_{M_2}^2} + \dots + \frac{(V_6 - M_6)^2}{\sigma_{M_6}^2} + 2\lambda [V_1 c_{p_w} (V_2 - V_3) - V_4 c_{p_g} (V_5 - V_6)] \mapsto Min. \quad (2.42)$$

The minimum of  $G(V, \lambda)$  is evaluated by calculus of variations. This is done by means of partial derivations with respect to the true values and the LAGRANGE multiplier. A determined non-linear system of equations for 7 variables is obtained. The solutions to this system are the 6 validated measurement values and the LAGRANGE multiplier  $\lambda$ . This process validation method is also standardized by VDI 2048, applied e.g. for nuclear power plants. Most of the validation procedures are applied for stationary conditions, as presented in this study. But also in applied thermodynamic processes, a dynamic behavior often occurs. In open literature online-validation models for transient behavior can be found for these applications.

After applying the criterion of data validation, all measured values can be developed into correlations for the prediction of the Nusselt number. According to the method of dynamic similarity, an objective function for  $Nu$  may be defined as follows:

$$Nu = f(Re, Pr). \quad (2.43)$$

## 2. Experimental Techniques

Following dimensional analysis, the simplest form of the power law for the heat transfer correlation, without any term related to the characteristic length for the consideration of geometry parameters, would be achieved.

$$Nu = CRe^m Pr^n \quad (2.44)$$

$C$  and  $m$  are functions of geometrical parameters, whereas  $n$  depends on fluid properties. In this study, all  $Nu$ -Correlations are calculated at constant  $Pr$  values<sup>6</sup>.

### 2.8. Calculation of the Measurement Uncertainties

For the analysis of measurements, an uncertainty calculation is a sufficient condition. According to *DIN 1319*, [7], [20], and [3], the propagation of uncertainties is calculated. A measured value is usually subdivided into the true value, the systematic error, and the random error. This assumption takes into account that rough errors are prevented and thus are avoided. Systematic errors are signed values, which can be corrected or detected by the change of the measurement procedure or by the use of a more precise measurement instrumentation itself. The systematic errors are composed additively by the known and the unknown systematic errors. Random errors are not deterministically detectable or influenced. These uncertainties are in principle not avoidable, but straggling if a statistic measurement is repeated under identical conditions. For this purpose, random errors can be reduced, if the number of recorded measurands of the same measurement values is increased under repeatability conditions. It is not possible for every test case to distinguish between a random error or an unknown systematic error [7]. To quantify the random errors or unknown systematic errors, the methods of statistical mathematics are applied. All measured uncertainties for the applied system are well known and can be quantified with the law of uncertainty propagation.  $F$  is the determined function of the  $n$  measurands or measured values  $f_i$ . The measured values are independent of each other. Attention has to be paid to this, because a compensation of the individual calculated mean error could be initiated. Thus, the mean uncertainty with the unknown systematic errors  $\delta f_i$  is expressed in form of a "square addition" according to the law of propagation of the uncertainty with

$$\delta F = \pm \sqrt{\sum_{i=1}^n \left( \frac{\partial F}{\partial f_i} \right)^2 \delta f_i^2} . \quad (2.45)$$

The uncertainty is defined by the absolute error, with the same unit of the measurand. The relative error is the uncertainty related to the result of the measurement (FS).

---

<sup>6</sup>It is assumed that the condition of air as transfer medium in this study is almost constant ( $Pr = const.$ )

## 2. Experimental Techniques

The relative error of a product of two or more values is calculated geometrically.

$$e_F = \frac{\delta F}{F_0} 100 \quad [\%] \quad (2.46)$$

The input quantities for the unknown systematic errors of the different measurement systems are taken from the manufacturer or were estimated regarding to the used measurement instrumentation as empirical values. Apart from the validity of the law of uncertainty propagation of GAUSS for random errors, the evaluation of the unknown systematic errors is sufficiently accurate in the industrial measuring method for a confidence interval of 95% [3]. In this section, the calculation procedure of the error propagation is indicated, to evaluate the true values for the heat transfer coefficients as well as for the pressure drop coefficients.

- **The relative uncertainty of the flow measurement (DIN 1952):**

The mass flow of air is a function of the temperature, the pressure in front of the nozzle, as well as the pressure drop according to the velocity change and is defined as follows:

$$\dot{m}_a = f(p_a, \Delta p_{Vent}, T_a) \quad (2.47)$$

The relative measurement uncertainty of the air mass-flow is defined in [7] and [8] can be expressed as a function in form of:

$$e_{\dot{m}_a} = f(e_{C_f}, e_\epsilon, e_{D_{Vent}}, e_{d_{Vent}}, \beta, e_{\Delta_{Vent}}, e_{p_{baro}}, e_{\rho_a}(R_{RG}, p_{baro}, T_a)) \quad (2.48)$$

with

$$\beta = \frac{d_{Vent}}{D_{Vent}}$$

Herein, the unknown systematic errors or relative errors are estimated or specified by the manufacturer or the DIN standard with

$$\left. \begin{aligned} e_{C_f} &= \pm 0.8973 \% \\ e_\epsilon &= \pm 2 \frac{\Delta p_{Vent}}{p_{baro}} \% \\ e_{D_{Vent}} &= \pm 0.4 \% \\ e_{d_{Vent}} &= \pm 0.07 \% \\ e_{AD} &= \pm 0.05 \% \\ \delta \Delta p_{Vent} &= \pm 1.71 \text{ Pa} \\ \delta p_{baro} &= \pm 427.107 \text{ Pa} \\ \delta R_{RG} &= \pm 2.88 \frac{\text{J}}{\text{kgK}} \\ \delta T_a &= \pm 3 \text{ K} \end{aligned} \right\} .$$

## 2. Experimental Techniques

Applying the law of error propagation to the mass flow measurement of air at 8 consecutively arranged tube rows, the uncertainties calculate as follows: the results show a disproportionate increase at low  $Re$ -numbers ( $Re < 14000$ ) if the Venturi nozzle is applied over the entire  $Re$ -range, which is presented in Figure 2.11. The average error of the mass flow measurement of air is lower than  $\pm 3\%$ . At  $Re = 10000$  the uncertainty is nearly about  $\pm 10\%$ , and extrapolated for  $Re < 7000$  about  $\pm 15\%$ . Thus, at low  $Re$ -numbers, an ISA 1932 inlet nozzle is applied with almost linear measurement uncertainty distribution of approximately  $\pm 3\%$  within the entire  $Re$ -range. In addition, at low  $Re$ -numbers, while using the Venturi nozzle, the already mentioned micro-manometer (meter scale  $19.99 \text{ mmH}_2\text{O}$ ) is applied to reduce these measurement uncertainties. In Figure 2.12(a) the relative uncertainties for the mass flow of air  $e_{\dot{m}_a}$ , structured according to their size above the total number of measurements  $N_i$  in %, are presented. As it is shown, the uncertainty is lower than  $\pm 3\%$  for 90% of the measured values.

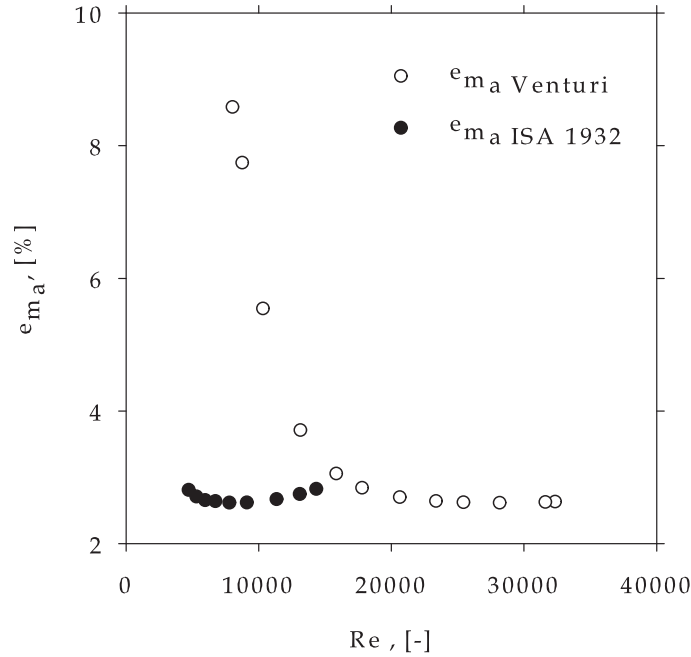
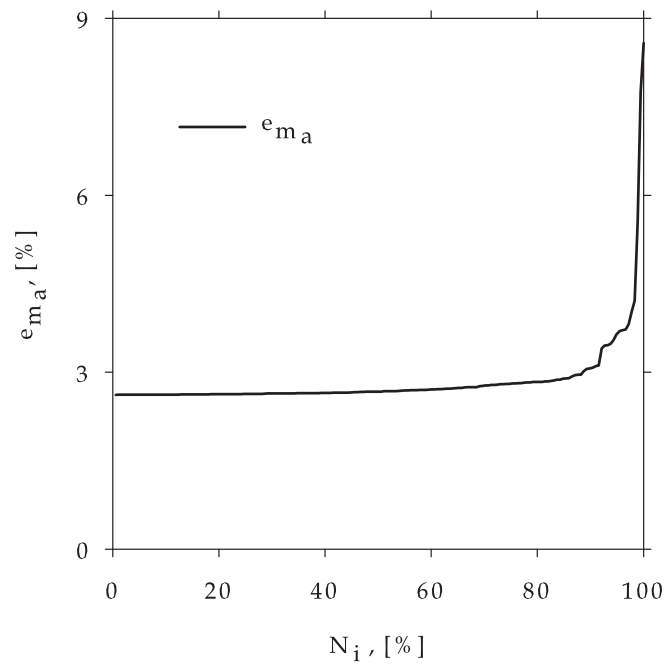


Figure 2.11.: Relative Uncertainty of the Air Mass-flow Measurement for the Full  $Re$ -range

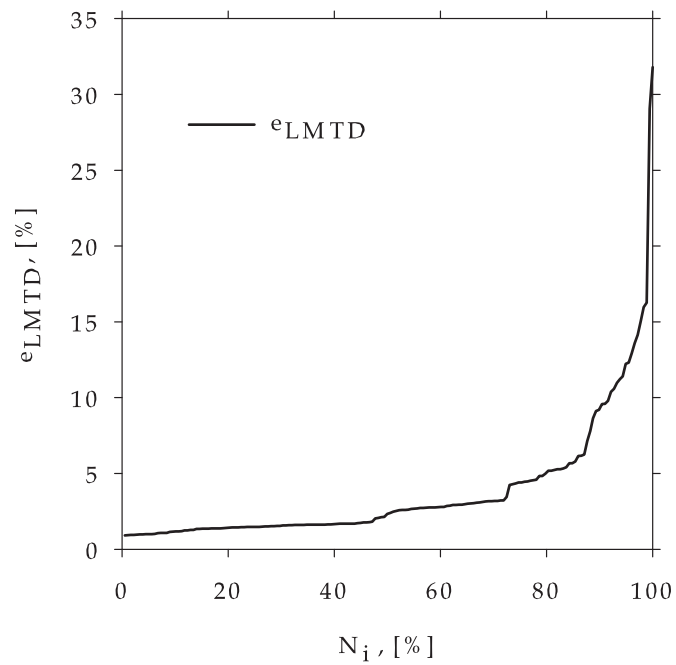
- **The uncertainty of the gas-sided heat transfer coefficient:**

The apparent heat transfer coefficient at the gas-side is determined with Equation (2.12). It can be expected that  $\alpha_i \gg \alpha$ . As an approximative estimation it is assumed that the second term (\*) in the denominator is rather small compared to

## 2. Experimental Techniques



(a) Mass Flow of Air



(b) Logarithmic Mean Temperature Difference

Figure 2.12.: Relative Uncertainties of all Measured Values



## 2. Experimental Techniques

$\frac{1}{\alpha}$ , thus the formula for calculating used in the law of error propagation reduces to:

$$k = \frac{\dot{Q}}{A_{tot}LMTD} = \frac{1}{\frac{1}{\alpha} + \underbrace{\frac{A_{tot}}{A_R} \frac{d_a + s}{2\lambda_t} \ln \frac{d_a + s}{d_i}}_{(* < \frac{1}{\alpha}) \rightarrow 0} + \underbrace{\frac{A_{tot}}{A_R} \frac{d_a + s}{d_i \alpha_i}}_{(\alpha_i >>) \rightarrow 0}}$$

Since the gas-sided apparent heat transfer coefficient is a function of

$$\alpha = f(A_{tot}, LMTD, \dot{Q}), \quad (2.49)$$

with

$$\dot{Q} = \dot{Q}_w = \dot{Q}_g, \quad (2.50)$$

the uncertainties for  $LMTD$  and  $\dot{Q}$  have to be evaluated separately. Thus, for the considered objective functions it follows:

$$\left. \begin{aligned} LMTD &= f(T_{g1}, T_{g2}, T_{w1}, T_{w2}) \\ \dot{Q}_w &= f(\dot{m}_w, c_{pw}, T_{w1}, T_{w2}) \\ \dot{Q}_g &= f\left(\dot{m}_g \left(e_{C_f}, e_{D_{Vent}}, e_{d_{Vent}}, \beta, e_{\Delta_{Vent}}, e_{p_{baro}}, e_{\rho_a} (R_{RG}, p_{baro}, T_a)\right), c_{pg}, T_{g1}, T_{g2}\right) \end{aligned} \right\} \quad (2.51)$$

In Figure 2.12(b) the graph of the relative uncertainties of  $LMTD$  is displayed. 80% of the measurands have an uncertainty lower than  $\pm 5\%$  and 90% of the values are within  $\pm 10\%$ . This indicates a low dispersion of the individual gas and water temperatures, which is important for a low uncertainty of the heat transfer coefficient. The mass flow of water  $\dot{m}_w$  was unvaried at each individual configuration during the measurement procedure. However, the measured values cause small straggling, so this part is also considered in the error propagation at the water-side. Since the mass flow of natural-gas  $\dot{m}_{ng}$  is rather small, compared to the mass flow of air  $\dot{m}_a$ , the calculated relative uncertainties from Equation (2.48) are implemented component-wise for evaluating the relative heat flow uncertainties at the gas-side. The unknown errors are estimated with

$$\left. \begin{aligned} \delta T_{g1} &= \pm 3 \text{ K} \\ \delta T_{g2} &= \pm 3 \text{ K} \\ \delta T_{w1} &= \pm 0.5 \text{ K} \\ \delta T_{w2} &= \pm 0.5 \text{ K} \\ e_{\dot{m}_w} &= \pm 1 \% \\ e_{c_{pw}} &= \pm 0.0035 \% \\ \delta \dot{m}_g &= \pm e_a m_g \frac{\text{kg}}{\text{s}} \quad \text{with } m_a \approx m_g \\ e_{c_{pg}} &= \pm 0.025 \% \end{aligned} \right\}.$$

## 2. Experimental Techniques

In Figures 2.13(a) and 2.13(b), the structured relative uncertainties of the transferred heat are presented. Both graphs were calculated using the objective function (2.51). As seen, for 80% of all measured values at individual configurations, the relative uncertainty evaluates for  $e_{\dot{Q}_g} \approx \pm 15\%$  and for  $e_{\dot{Q}_w} \approx \pm 12\%$ . The minimum uncertainty for both cases is about  $\pm 5\%$ . Apart from the calculated uncertainties, it is important to have a more precise determination of the measured values at the water-side, since this is responsible for the evaluated heat transfer coefficient.

After applying the law of uncertainty propagation, by evaluating the partial derivations with respect to  $LMTD$ ,  $\dot{Q}_w$  or  $\dot{Q}_g$ , the uncertainty of the apparent heat transfer coefficient is determined with

$$\delta\alpha = \pm \sqrt{\left(\frac{\partial\alpha}{\partial\dot{Q}_{g/w}}\right)^2 \delta\dot{Q}_{g/w}^2 + \left(\frac{\partial\alpha}{\partial LMTD}\right)^2 \delta LMTD^2}. \quad (2.52)$$

In Figure 2.14 the structured relative uncertainties of the apparent heat transfer coefficient are presented. The result of the total measurements indicates that approximately 80% of the measurands have a relative uncertainty laying within  $\pm 15\%$ .

- **The uncertainty of the gas-sided pressure drop coefficient:**

The mean velocity of the flue-gas is a function of:

$$u_E = f(\dot{m}_g, \rho_{gm}, F_{min}) \quad (2.53)$$

With the specified errors

$$\left. \begin{aligned} \delta F_{min} &= \pm 0.001146 \text{ m}^2 \\ \delta \dot{m}_g &= \pm e_{\dot{m}_a} \dot{m}_g \frac{\text{kg}}{\text{s}} \end{aligned} \right\},$$

it follows for the uncertainty of the flue-gas velocity:

$$\delta u_E = \pm \sqrt{\left(\frac{\partial u_E}{\partial \dot{m}_g}\right)^2 \delta \dot{m}_g^2 + \left(\frac{\partial u_E}{\partial \rho_{gm}}\right)^2 \delta \rho_{gm}^2 + \left(\frac{\partial u_E}{\partial F_{min}}\right)^2 \delta F_{min}^2} \quad (2.54)$$

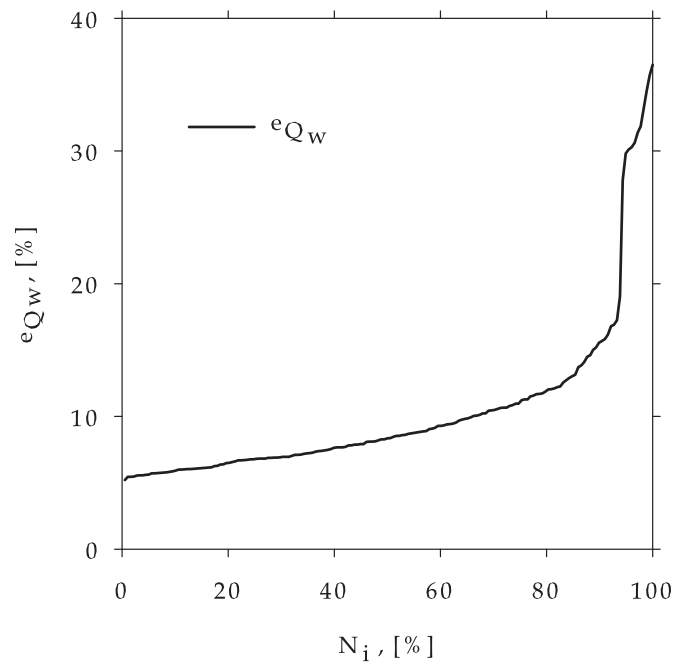
In the uncertainty calculation, the density at the inlet and at the outlet of the test section is considered separately. The average mean value is evaluated with

$$\rho_{gm} = \frac{\rho_{g1} + \rho_{g2}}{2}. \quad (2.55)$$

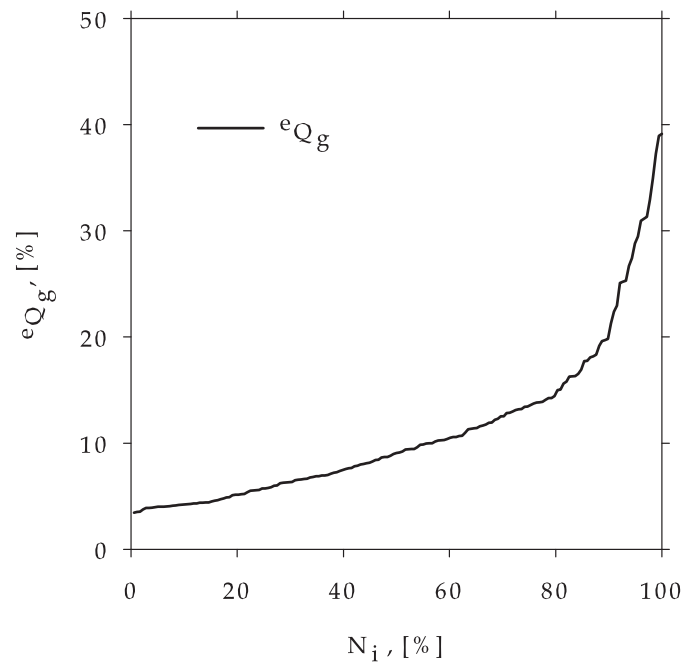
If it is assumed that

$$\rho_{g1/2} = f(R_{RG}, T_{g1/2}, p_{PWT}) \quad (2.56)$$

## 2. Experimental Techniques



(a) Heat Flow of Water



(b) Heat Flow of Flue-Gas

Figure 2.13.: Relative Uncertainties of the Transferred Heat

## 2. Experimental Techniques

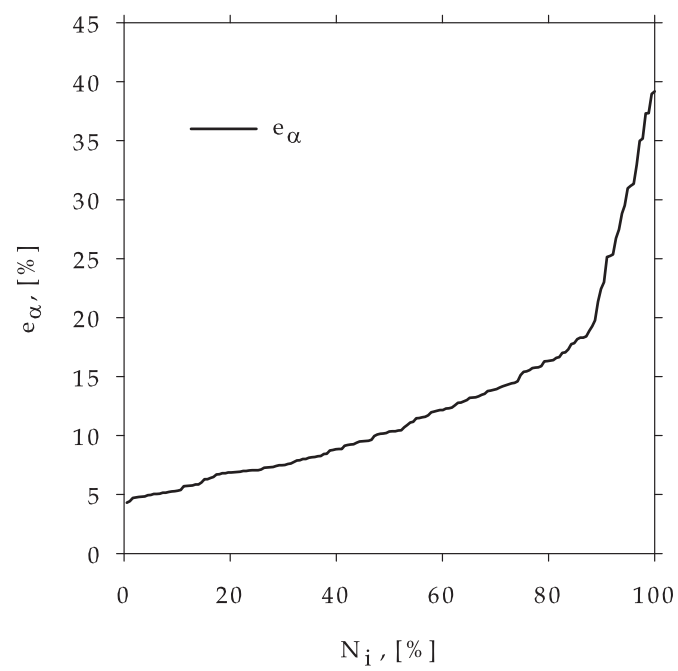


Figure 2.14.: Relative Uncertainties of the Heat Transfer at the Gas-Side

## 2. Experimental Techniques

with

$$\left. \begin{aligned} e_{R_{RG}} &= \pm 1 \% \\ e_{P_{WPT}} &= \pm 0.15 \% \\ \delta p_{baro} &= \pm 427.107 \text{ Pa} \\ \delta T_{g1} &= \pm 3 \text{ K} \\ \delta T_{g2} &= \pm 3 \text{ K} \end{aligned} \right\},$$

the uncertainty becomes

$$\delta \rho_{g1/2} = \pm \sqrt{\left(\frac{\partial \rho_{g1/2}}{\partial R_{RG}}\right)^2 \delta R_{RG}^2 + \left(\frac{\partial \rho_{g1/2}}{\partial p_{PWT}}\right)^2 \delta p_{PWT}^2 + \left(\frac{\partial \rho_{g1/2}}{\partial T_{g1/2}}\right)^2 \delta T_{g1/2}^2}. \quad (2.57)$$

The pressure drop uncertainty of the unloaded channel is evaluated with the equation according to KONAOKOV and expressed in form of:

$$\left. \begin{aligned} \lambda &= f(Re) \\ Re &= f(\dot{m}_g, A_{Ch}, \mu_{gm}) \end{aligned} \right\} \quad (2.58)$$

Following the calculation procedure for the uncertainty propagation with

$$e_{\mu_{gm}} = \pm 0.5 \%,$$

the estimated relative uncertainty for the channel Reynolds number is  $e_{Re_{Ch}} \approx \pm 0.7\%$ <sup>7</sup> and for  $\lambda$  a very small value of  $e_\lambda = \pm 0.15 - 0.2\%$  is evaluated. The relative uncertainty for the pressure drop of the tube bundle is calculated with the knowledge of Equation (2.29) and is defined as a function as follows:

$$\xi_{N_R} = f(\Delta p_{1/2}, \dot{m}_g, \rho_{g1}, \rho_{g2}, \rho_{gm}, u_E, \lambda, F_{Min}, D_{Ch}, L_{Ch}, A_{Ch}) \quad (2.59)$$

The influence, caused by the geometrical dimensions, is very small and can thus be neglected in further evaluations. For hot test conditions, the density variation effect to the relative measurement uncertainty is also considered, thus the mean density is calculated separately. With the relative uncertainties for the applied pressure transducers, given in Table 2.2, and an estimated  $A/D$  converting uncertainty as well as the uncertainties for the individual values as stated above, the law of error propagation for the pressure drop uncertainty measured at the channel wall (1) and channel center (2) is finally specified with

$$\begin{aligned} \delta \xi_{N_R}^2 &= \left(\frac{\partial \xi_{N_R}}{\partial \dot{m}_g}\right)^2 \delta \dot{m}_g^2 + \left(\frac{\partial \xi_{N_R}}{\partial \Delta p_{1/2}}\right)^2 \delta \Delta p_{1/2}^2 + \left(\frac{\partial \xi_{N_R}}{\partial \rho_{g1}}\right)^2 \delta \rho_{g1}^2 + \\ &+ \left(\frac{\partial \xi_{N_R}}{\partial \rho_{g2}}\right)^2 \delta \rho_{g2}^2 + \left(\frac{\partial \xi_{N_R}}{\partial \rho_{gm}}\right)^2 \delta \rho_{gm}^2 + \left(\frac{\partial \xi_{N_R}}{\partial u_E}\right)^2 \delta u_E^2 + \left(\frac{\partial \xi_{N_R}}{\partial \lambda}\right)^2 \delta \lambda^2. \end{aligned} \quad (2.60)$$

<sup>7</sup>The index indicates the characteristic length

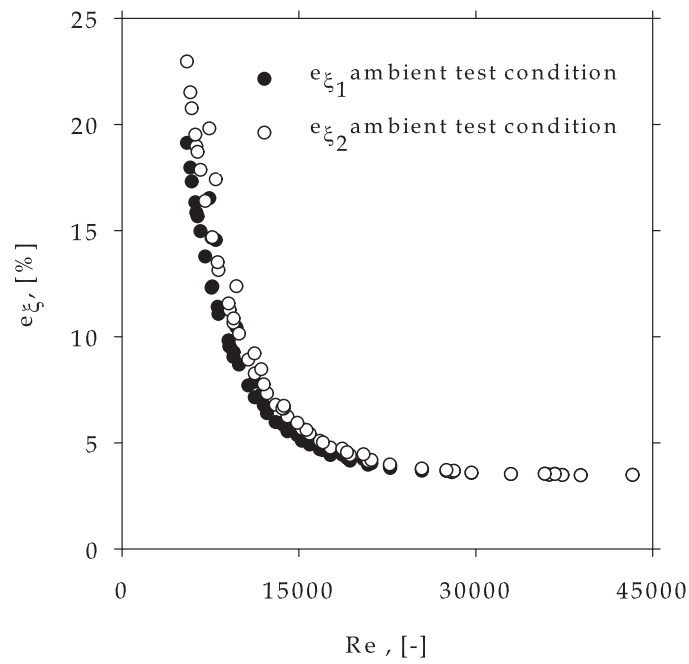
## 2. Experimental Techniques

As the evaluated relative uncertainties in Figures 2.15(a) and 2.15(b) show, exemplary for 8 tube row configuration, for  $Re > 15000$  a constant value of approximately  $\pm 5\%$  is to be expected. Especially for  $Re < 15000$  down to the lower measurement range, the relative uncertainties show a disproportional increase. This is caused by small pressure differences between test section inlet and outlet. As seen between measurements, performed at ambient conditions as well as hot test conditions, no considerable difference is noticeable. Generally, the error propagation performed for the pressure transducer at the channel wall results in lower relative uncertainties than at the channel center, as seen. In Figures 2.16(a) and 2.16(b), the structured relative uncertainties of the pressure drop coefficients are presented. 80% of the evaluated uncertainties of the pressure drop coefficient measured from the pressure drop at the channel wall are between  $\pm 15 - 20\%$ . The propagation of the uncertainties performed for the channel center are between  $\pm 20 - 25\%$ . Any occurring differences between the results of ambient and hot condition may be interpreted by the total number of measurands. Especially the pressure drop influence at low  $Re$ -number is investigated at ambient conditions. Thus, considerably more measured points are performed at  $Re < 15000$ .

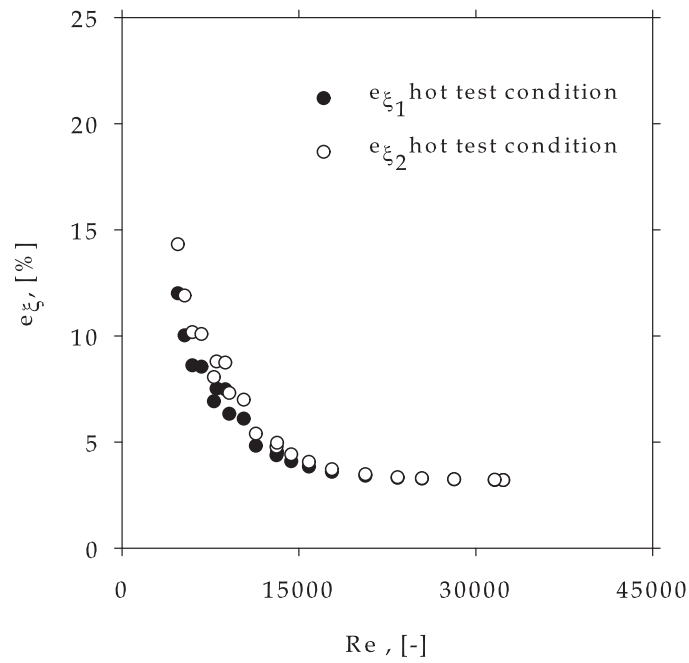
Finally, it may be agreed that the relative uncertainties for the pressure drop coefficient, evaluated for the channel wall and channel center, for 80% of the measurands are  $\pm 20\%$ .

The application of the law of propagation of uncertainty according to the measuring section is emphasized to give an association or insight to the size of the measured quantities.

## 2. Experimental Techniques



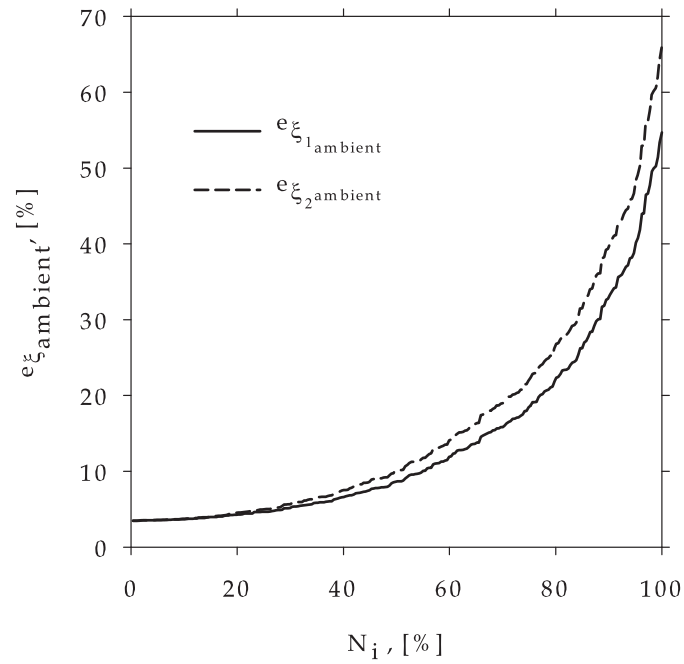
(a) Pressure Drop Coefficient at Ambient Conditions



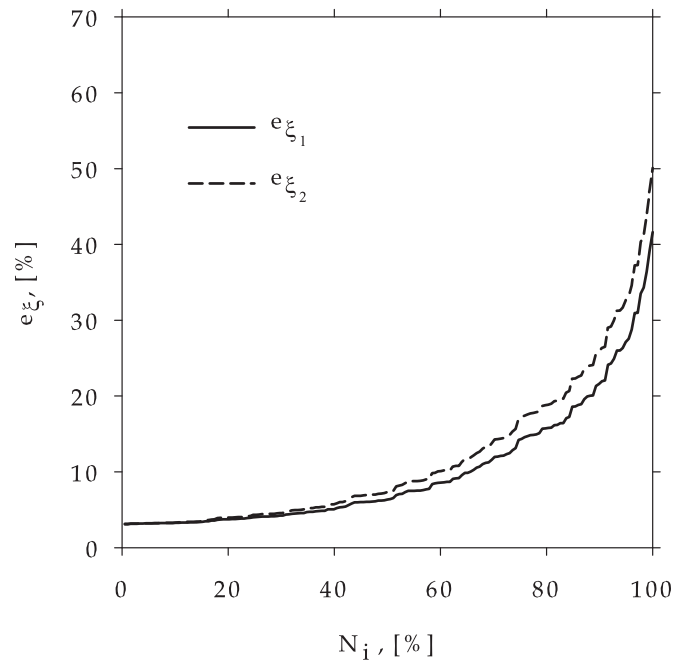
(b) Pressure Drop Coefficient at Hot Conditions

Figure 2.15.: Relative Uncertainty of the Pressure Drop Coefficient of 8 Tube Rows

## 2. Experimental Techniques



(a) Pressure Drop Coefficient at Ambient Conditions



(b) Pressure Drop Coefficient at Hot Conditions

Figure 2.16.: Relative Uncertainties of the Finned-Tube Pressure Drop Coefficient



### 3. Numerical Consideration

Determine that the thing can and shall be done, and then we shall find the way.

*Abraham Lincoln*

★

#### 3.1. Analytical Approximation of Conduction through a Finned-Tube

The determination of heat transfer above a complex finned-surface is rather complicated due to the fact of a non-uniform temperature distribution over the fin. Thus, the heat transfer coefficient  $\alpha(r, \varphi) \neq \bar{\alpha}$ , is a function of  $r$  and  $\varphi$ , where  $\bar{\alpha}$  is the integral mean heat transfer coefficient. These effects in combination with the fluid flow are denoted as forced convection problem. In the following, an analytical survey of the temperature distribution above a surface with solid and segmented fins, simply in form of a conduction problem without any convection will be discussed. While research into certain problem areas is performed, the mentioned list makes no claim of being complete. The temperature gradient in a circumferential fin has been investigated in detail by e.g. ILL'IN & STYRIKOVICH, GARDNER, KRISCHER & KAST cited in [58], and by [44]. Fin efficiency problems, as a result of the temperature distribution above a segmented fin, were analyzed by e.g. [26], [24] and [25]. The following solid fin considerations are based on [44]. To calculate the interactions between the distribution of the heat transfer coefficient and temperature, the differential equation of heat conduction in cylindrical coordinates for steady state conditions has to be resolved, which is defined as follows:

$$\frac{\partial^2 T}{\partial r^2} + \frac{1}{r} \frac{\partial T}{\partial r} + \frac{1}{r^2} \frac{\partial^2 T}{\partial \varphi^2} + \frac{2\alpha(r, \varphi)}{\lambda_{fs}} (T_{gm} - T) = 0 \quad (3.1)$$

The factor 2 considers both fin sides for heat charging rates. The thermal conductivity  $\lambda_{ri}$ , the temperature at the fin base  $T_i$ , and the fluid temperature  $T_{gm}$  are assumed

### 3. Numerical Consideration

to be constant as simplifying conditions [44]. Since this elliptic inhomogeneous linear partial differential equation has only solutions for a certain  $\alpha$ -distribution, a constant heat transfer coefficient  $\bar{\alpha}$  above the fin surface is assumed. In the following considerations the mean heat transfer coefficient  $\bar{\alpha}$  is replaced by  $\alpha$  for the purpose of convenience. Further assumptions are: No internal heat sources, homogeneous fin material, no thermal resistance between fin and tube, and negligible temperature gradient in perpendicular direction of the fin according to [58]. Considering these assumptions Equation (3.1) leads to:

$$\frac{d^2 \Xi}{dr^2} + \frac{1}{r} \frac{d\Xi}{dr} - m^2 \Xi = 0 \quad (3.2)$$

This is the well known BESSEL differential equation, with  $\Xi = T_{gm} - T$ ,  $m = \sqrt{2\alpha/\lambda_{fs}}$ , and  $\alpha(r, \varphi) = \bar{\alpha} = \alpha_0$ . The general solution of this equation are the modified zero-order BESSEL functions of the imaginary argument

$$\Xi(mr) = \Phi_1 I_0(mr) + \Psi_1 K_0(mr). \quad (3.3)$$

Considering the boundary conditions at the fin base <sup>1</sup>(no thermal resistance)

$$T|_{r=r_i} = T_i \quad (3.4)$$

and at the fin tip <sup>2</sup>(no heat exchange with the surrounding fluid)

$$\left. \frac{dT}{dr} \right|_{r=r_a} = 0, \quad (3.5)$$

the coefficients  $\Phi_1$  and  $\Psi_1$  are defined as follows:

$$\left. \begin{aligned} \Phi_1 &= \frac{K_1(mr_a)(T_{gm} - T_i)}{I_0(mr_i)K_1(mr_a) + I_1(mr_a)K_0(mr_i)} \\ \Psi_1 &= \frac{I_1(mr_a)(T_{gm} - T_i)}{I_0(mr_i)K_1(mr_a) + I_1(mr_a)K_0(mr_i)} \end{aligned} \right\}. \quad (3.6)$$

Consequentially, the temperature distribution above a solid fin can be expressed with

$$T(r) = T_{gm} - \frac{I_0(mr)K_1(mr_a) + I_1(mr_a)K_0(mr)}{I_0(mr_i)K_1(mr_a) + I_1(mr_a)K_0(mr_i)} (T_{gm} - T_i). \quad (3.7)$$

If heat exchange from the fin tip should be considered, the fin height is to be enlarged by one half of the fin thickness, as mentioned above, see [58], [14].

To calculate the temperature profile for a segmented finned-tube while considering the afore mentioned restrictions, the following approach according to [24], [25], and [26] is chosen. Herein, the fin is sub-divided into the annular section  $r_{ab} \leq r \leq r_{at}$  and

---

<sup>1</sup> $r_i \equiv d_a/2$

<sup>2</sup> $r_a \equiv D/2$

### 3. Numerical Consideration

the segmented section  $r_{sb} \leq r \leq r_{st}$ , where  $r_{at} = r_{sb}$ , see Figure 2.3. For the annular part of the considered fin, Equation (3.2) is used. For the segmented part, the Equation of a plane fin according to literature, is used:

$$\frac{d^2 \Xi}{dr^2} - m^2 \Xi = 0 \quad (3.8)$$

After substituting  $\Xi = u$  for the annular part and  $\Xi = v$  for the segmented part, Equations (3.2) and (3.8) are transformed into

$$\left. \begin{aligned} u_{rr} + \frac{1}{r}u_r - m^2 u &= 0 \\ v_{rr} - m^2 v &= 0 \end{aligned} \right\}. \quad (3.9)$$

The general solution of the BESSEL differential equation has been already evaluated, refer to Equation (3.3). The fundamental solution of the homogeneous differential equation of second order for the segmented part reads as

$$\Xi(mr) = \Phi_2 e^{mr} + \Psi_2 e^{-mr}. \quad (3.10)$$

The boundary conditions at the fin base (no thermal resistance), and at the fin tip (no heat exchange with the surrounding fluid) are

$$\left. \begin{aligned} T|_{r=r_{ab}} &= T_{ab} \\ \frac{dT}{dr}|_{r=r_{st}} &= 0 \end{aligned} \right\}; \quad (3.11)$$

and the intermediate connecting conditions [25], [24] are

$$\left. \begin{aligned} T|_{r=r_i} &= T_{at} = T_{sb} \\ \frac{dT}{dr}|_{r=r_{at}} &= \frac{dT}{dr}|_{r=r_{sb}} \end{aligned} \right\}. \quad (3.12)$$

If the substituted boundary conditions for this case

$$\left. \begin{aligned} u|_{r=r_{ab}} &= \Xi_{ab} \\ u|_{r=r_{at}} &= v|_{r=r_{sb}} \\ \frac{d}{dr}u|_{r=r_{at}} &= \frac{d}{dr}v|_{r=r_{sb}} \\ \frac{d}{dr}v|_{r=r_{st}} &= 0 \end{aligned} \right\} \quad (3.13)$$

are considered, the coefficients  $\Phi_1$ ,  $\Psi_1$ ,  $\Phi_2$ , and  $\Psi_2$  evaluate as follows, compare

### 3. Numerical Consideration

with [25], [24]:

$$\left. \begin{aligned} \Phi_1 &= \frac{(T_{gm} - T_i)}{\Omega} [-K_0(mr_{at}) e^{mr_{at}} e^{-mr_{st}} + K_0(mr_{at}) e^{-mr_{at}} e^{mr_{st}} - \\ &\quad - K_1(mr_{at}) e^{mr_{at}} e^{-mr_{st}} - K_1(mr_{at}) e^{-mr_{at}} e^{mr_{st}}] \\ \Psi_1 &= \frac{(T_{gm} - T_i)}{\Omega} [-I_0(mr_{at}) e^{mr_{at}} e^{-mr_{st}} - I_0(mr_{at}) e^{-mr_{at}} e^{mr_{st}} - \\ &\quad - I_1(mr_{at}) e^{mr_{at}} e^{-mr_{st}} - I_1(mr_{at}) e^{-mr_{at}} e^{mr_{st}}] \\ \Phi_2 &= \frac{(T_{gm} - T_i)}{\Omega} [-e^{-mr_{st}} (I_0(mr_{at}) K_1(mr_{at}) + I_1(mr_{at}) K_0(mr_{at}))] \\ \Psi_2 &= \frac{(T_{gm} - T_i)}{\Omega} [-e^{mr_{st}} (I_0(mr_{at}) K_1(mr_{at}) + I_1(mr_{at}) K_0(mr_{at}))] \end{aligned} \right\}, \quad (3.14)$$

with

$$\Omega = -I_0(mr_{ab}) K_0(mr_{at}) e^{mr_{at}} e^{-mr_{st}} + I_0(mr_{ab}) K_0(mr_{at}) e^{-mr_{at}} e^{mr_{st}} - \\ - I_0(mr_{ab}) K_1(mr_{at}) e^{mr_{at}} e^{-mr_{st}} - I_0(mr_{ab}) K_1(mr_{at}) e^{-mr_{at}} e^{mr_{st}} + \\ + I_0(mr_{at}) K_0(mr_{ab}) e^{mr_{at}} e^{-mr_{st}} - I_0(mr_{at}) K_0(mr_{ab}) e^{-mr_{at}} e^{mr_{st}} - \\ - I_1(mr_{at}) K_0(mr_{ab}) e^{mr_{at}} e^{-mr_{st}} - I_1(mr_{at}) K_0(mr_{ab}) e^{-mr_{at}} e^{mr_{st}} \quad (3.15)$$

Finally, the temperature distribution above a segmented fin is described with:

$$T(r) = \begin{cases} T_{gm} - [\Phi_1 I_0(mr) + \Psi_1 I_0(mr)] & r_{ab} \leq r \leq r_{at} \\ T_{gm} - [\Phi_2 e^{mr} + \Psi_2 e^{-mr}] & r_{sb} \leq r \leq r_{st} \end{cases} \quad (3.16)$$

This temperature profile is valid for fins with thermal insulation at the tip and side section in perpendicular direction of the segment, as well as for a uniformly distributed heat transfer coefficient over the fin surface. To account for the portion of heat transfer from the side surfaces of the segmented section, an analytical model was evaluated by [26], which is considered therein with

$$m_{seg} = \sqrt{\frac{2\alpha \left(1 + \frac{s}{b_s}\right)}{\lambda_f s}}. \quad (3.17)$$

In Figure 3.1 the temperature profiles for a segmented and a solid finned-tube, specified with the geometrical parameters from Table 2.3, are presented. The graphs are calculated for constant  $\alpha = 87.95 \text{ W/m}^2\text{K}$ ,  $\lambda_f = 52.7 \text{ W/mK}$ ,  $T_{gm} = 363.26 \text{ K}$ , and  $T_i = 342.12 \text{ K}$ . As seen, starting from the same fin-base temperature, the segmented fin has a lower fin-tip temperature.

### 3. Numerical Consideration

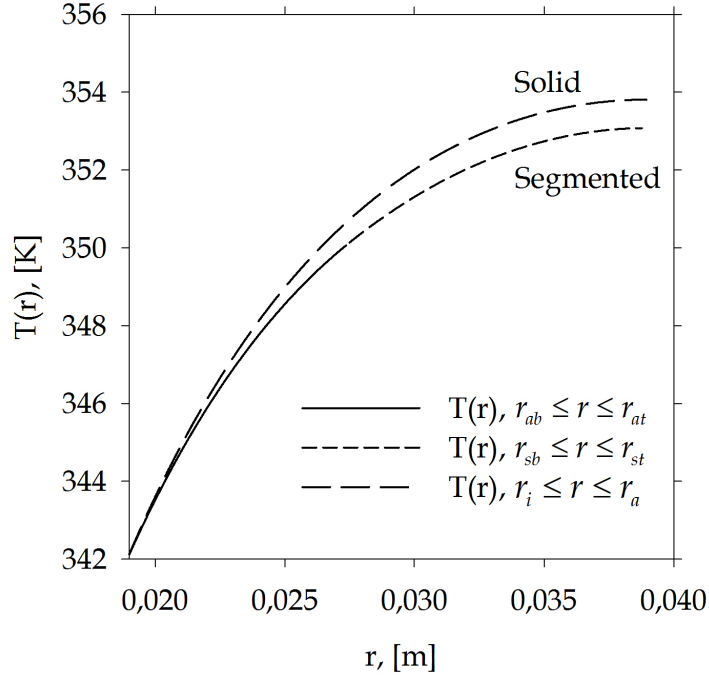


Figure 3.1.: Temperature Profile

Using the general definition of the fin efficiency, [58],

$$\eta_r = \frac{\int_{r_i}^{r_a} \int_0^{2\pi} (T_{gm} - T(r)) \alpha r dr d\phi}{(T_{gm} - T_i) \int_{r_i}^{r_a} \int_0^{2\pi} \alpha r dr d\phi}, \quad (3.18)$$

values of  $\eta_r$  for the segmented fins and for the solid fins with same fin height may be evaluated. Measurements at U-shaped segmented, at I-shaped segmented, and I-shaped solid finned-tubes have shown that fin efficiency decreases with increasing mass flow under cross-flow conditions. Thus it may be concluded that fin efficiency is highly dependent on the conduction through the fin. For more detail regarding fin efficiency research, it is referred to literature. An analytical study about fin efficiencies of solid finned-tubes has been performed by GARDNER, cited in [58]. Fin efficiencies for segmented finned-tubes were analyzed extensively by [24], [25], and [26]. Based on e.g. [72], fin efficiency pre-calculations are suggested analytically as well as by use of Nomograms.

### 3. Numerical Consideration

Yet, to account for the effect of a non-uniform temperature distribution and thus heat transfer coefficient distribution across the fin surface,  $\alpha$  has to be considered as a function of  $r$  and  $\varphi$ , being  $\alpha(r, \varphi) \neq \bar{\alpha}$ . For this case, an approximate solution has to be evaluated for Equation (3.1). Among the possible resolutions, the method of Ritz was analyzed in [44] for specific individual cases. The object is to find a linear-combination of basis functions for the temperature distribution, with coefficients from Ritz' linear system of equations. For an arbitrary  $\alpha$  distribution, the integrals have to be resolved numerically, [44].

Furthermore, to account for the heat transfer distribution above finned-tubes in cross-flow, as in laboratory test conditions, the heat conduction through the fins has to be supplement with a forced convection problem. In this study, the conjugate heat transfer considerations between fluid and wall are performed by means of a *CFD* analysis, which is calibrated and validated by test series, accomplished at the laboratory. Especially the theoretical considerations include a comparison of the global heat transfer- and pressure drop behavior from the experiments, with the results gathered from the numerical analysis, which are investigated for global and local phenomena at a single finned-tube row. Local effects viz. flow phenomena (secondary flows e.g. vortex, separation problems) and conjugate heat transfer (i.e. coupled conductive and convective heat transfer and temperature distribution) above a helical and circular finned-surface have therefore be analyzed.

#### 3.2. Numerical Simulation of a Single Finned-Tube Row Heat Exchanger in Forced Convection

Numerical calculation, especially when applying the finite volume method, is a sophisticated possibility to model forced convection problems. These results may be helpful to gain some insight into flow distribution, which influences pressure drop and heat transfer at various operating conditions. Since finned-tube heat exchangers consist of rather complex geometry, this knowledge may be useful to modify several individual geometrical parameters for a heat transfer enhancement optimization.

Judging from the literature review presented in Section 1.2 it is an appropriate assumption to predict fluid flow phenomena and convective heat transfer, using three dimensional steady state *CFD* simulations, performed at a single finned-tube row or at tube bundles in cross-flow under forced convection based on two-equation turbulence models. In this work, single row finned-tube heat exchanger in cross-flow, with solid and segmented fins, are investigated, whereas the fins are arranged circularly or helically around the bare tube. The effect of the parametrically varied Reynolds-number<sup>3</sup> in the range of  $3500 \leq Re \leq 35000$  to the Nusselt-number and the pressure drop coefficient is analyzed. Especially the difference between solid and serrated fins

---

<sup>3</sup>For this case the characteristic length is  $d_a$

### 3. Numerical Consideration

is considered. For modeling turbulence, a renormalization group theory (RNG)  $k$ - $\epsilon$  turbulence model with enhanced wall functions is applied to resolve near wall treatment between the adjacent fins. All investigations are performed under hot and ambient conditions. It is intended to calibrate the global results of the *CFD*-calculation with those calculated from the measurement at the test rig. Therefore, a flow rectifier and an inflow channel at the gas-side should provide the same inlet conditions and the investigation of an array of finned-tube layers represents the periodic boundaries as in the computational domain of the simulation. Apart from these global investigations, local transfer behavior of the thermal field is examined for convective transport phenomena.

#### 3.2.1. Governing Equations of Fluid Flow and Heat Transfer and Turbulence Modeling for the Examined Problem

Applying the finite volume method, the governing equations for the "exact" conservation of mass, momentum and energy are defined according to [74], [66], and [65]. The mass conservation for incompressible fluid under steady state conditions is described with the convective term in Cartesian coordinates

$$\frac{\partial u_i}{\partial x_i} = 0. \quad (3.19)$$

The NAVIER-STOKES equations at steady state conditions for incompressible flow without any gravity-force in tensor notation reads as

$$\underbrace{u_j \frac{\partial u_i}{\partial x_j}}_{\text{Convective}} = \underbrace{-\frac{1}{\rho} \frac{\partial p}{\partial x_i}}_{\text{Pressure Gradient}} + \underbrace{\frac{1}{\rho} \frac{\partial t_{ij}}{\partial x_j}}_{\text{Diffusive}}, \quad (3.20)$$

whereas in case of isotropic fluids, for the viscous stress tensor  $t_{ij}$  when introducing the strain rate tensor  $s_{ij}$  it follows:

$$t_{ij} = 2\mu s_{ij} = \mu \left( \frac{\partial u_i}{\partial x_j} + \frac{\partial u_j}{\partial x_i} \right). \quad (3.21)$$

From the first law of thermodynamics the energy equation is derived as the net rate of increase of energy, which equals the net rate of heat added to fluid plus the net rate of work done on fluid<sup>4</sup>, [66]. For incompressible flow under steady state conditions the energy equation reads as

$$\frac{\partial (u_i [\rho e + p])}{\partial x_i} = \frac{\partial}{\partial x_i} \left( \lambda \frac{\partial T}{\partial x_i} \right). \quad (3.22)$$

---

<sup>4</sup>Considering the fluid flow, the thermal energy is much higher than the kinetic and the potential energy. Therefore, the balance equation for the thermal energy is simplified.

### 3. Numerical Consideration

No viscous dissipation terms occur in the energy conservation, since viscous heating is neglected due to its low effect, [10]. For the special case of incompressible fluid it is

$$\left. \begin{aligned} e &= c_v T \\ h &= e + \frac{p}{\rho} = c_p T \end{aligned} \right\}, \quad (3.23)$$

thus, for ideal gas, the energy equation can be converted into a temperature equation

$$\rho c_p \frac{\partial (u_i T)}{\partial x_i} = \frac{\partial}{\partial x_i} \left( \lambda \frac{\partial T}{\partial x_i} \right). \quad (3.24)$$

For the solid part (i.e. tube and fin), the left hand side of Equation (3.24) equals 0. In three dimensions the flow field is described with five PDE's<sup>5</sup>. For incompressible flow, without any density variation, there is no linkage between the energy equation and the mass- and the momentum equations, where the energy equation is solved additionally, if a conjugate heat transfer problem is to be considered, refer to [66].

The finned-tubes in cross-flow under consideration are investigated in a *Re*-range of unstable or turbulent flow regime. The flow character becomes highly chaotic and shows random nature. Due to highly complex turbulent motions, the mass, momentum and heat is very advantageously exchanged. Reynolds decomposition enables it to quantify these velocities by assuming a steady mean value (time averaged) superimposed by a random fluctuating part. Introducing the turbulent fluctuations for the mean flow equations, the complete set of PDE's with the REYNOLDS-AVERAGED NAVIER-STOKES equations for incompressible flow reads as

$$\left. \begin{aligned} \frac{\partial U_i}{\partial x_i} &= 0 \\ \rho U_j \frac{\partial U_i}{\partial x_j} &= -\frac{\partial P}{\partial x_i} + \frac{\partial}{\partial x_j} \left( 2\mu S_{ji} - \rho \overline{u'_j u'_i} \right) \\ \frac{\partial (U_i [\rho E + P])}{\partial x_i} &= \frac{\partial}{\partial x_i} \left( \lambda_{eff} \frac{\partial T}{\partial x_i} \right) \end{aligned} \right\} \quad (3.25)$$

Herein,  $\lambda_{eff} = \lambda + \lambda_t$  is the effective thermal conductivity and  $\lambda_t$  is the turbulent conductivity, [10]. As stated above, the mean flow behavior is affected by velocity fluctuations, which cause additional stresses to the fluid, the Reynolds stresses. These stresses have to be considered in turbulent *CFD* codes. The symmetric Reynolds stress tensor  $\tau_{ij}$  is defined, [74],

$$\tau_{ij} = -\rho \overline{u'_j u'_i} \quad (3.26)$$

---

<sup>5</sup>Partial Differential Equations



### 3. Numerical Consideration

Generally, RANS turbulence models are based on the mean flow quantities and are defined by one length scale (and one time scale). As a result of Reynolds averaging, six new unknown quantities are generated. With the five unknown mean-flow properties, there are 11 unknown ones. To handle this closure problem, the BOSSINESQ eddy-viscosity<sup>6</sup> approximation is introduced, which is applied in eddy-viscosity-models, e.g. two-equation models as for example  $k - \epsilon$ ,  $k - \omega$ , or RNG  $k - \epsilon$ .

$$\tau_{ij} = -\rho \overline{u'_j u'_i} = \mu_t \left( \frac{\partial U_i}{\partial x_j} + \frac{\partial U_j}{\partial x_i} \right) - \frac{2}{3} \rho k \delta_{ij} \quad (3.27)$$

Herein, the viscosity  $\mu$  in NEWTON's law is replaced by the turbulent or eddy viscosity  $\mu_t$ <sup>7</sup>. In case of isotropic flow conditions for the specific turbulent kinetic energy follows:

$$k = \frac{1}{2} \overline{u'_i u'_i} = \frac{3}{2} \overline{u'^2_i} \quad (3.28)$$

For the applied two-equation turbulence model RNG  $k - \epsilon$ , two additional equations, one for the specific turbulent kinetic energy and one for the rate of dissipation, have to be solved. As described in [18] and [48], the Renormalization Group Theory (RNG) modeling of turbulent flows by ORSZAG and YAKHOT applies statistical perturbation methods to organize the solution of the NAVIER-STOKES equations of the dynamics from the mean flow quantities. Also, this theory allows to interpolate into low Reynolds number regions [18]. The RNG theory gives values for the closure coefficients. The mathematic is highly difficult to comprehend, thus in the following the governing  $k$ - and  $\epsilon$ -relations, the eddy viscosity, and the closure coefficients which can be found in open literature, [74], [18], [66] are just stated:

$$\left. \begin{aligned} \mu_{eff} &= \mu + \mu_t \\ \mu_t &= \rho C_\mu \frac{k^2}{\epsilon} \\ U_j \frac{\partial k}{\partial x_j} &= \frac{\partial}{\partial x_j} \left[ \frac{\mu_{eff} \alpha_k}{\rho} \frac{\partial k}{\partial x_j} \right] + \frac{\tau_{ij}}{\rho} \frac{\partial U_i}{\partial x_j} - \epsilon \\ U_j \frac{\partial \epsilon}{\partial x_j} &= \frac{\partial}{\partial x_j} \left[ \frac{\mu_{eff} \alpha_\epsilon}{\rho} \frac{\partial \epsilon}{\partial x_j} \right] + C_{\epsilon 1} \frac{\epsilon}{k} \frac{\tau_{ij}}{\rho} \frac{\partial U_i}{\partial x_j} - C_{\epsilon 2} \frac{\epsilon^2}{k} \end{aligned} \right\}, \quad (3.29)$$

<sup>6</sup>The presumption is that an analogy between viscous stress and Reynolds stress on the mean flow exists [66]

<sup>7</sup>In the term of the turbulent pressure, the KRONECKER-delta is defined with ( $\delta_{ij} = 1$  if  $i = j$  and  $\delta_{ij} = 0$  if  $i \neq j$ ) for the correct results of the Reynolds stresses.

### 3. Numerical Consideration

$$\left. \begin{aligned} C_{\epsilon 2} &\equiv \tilde{C}_{\epsilon 2} + \frac{C_{\mu} \lambda^3 \left(1 - \frac{\lambda}{\lambda_0}\right)}{1 + \beta \lambda^3} \\ \lambda &\equiv \frac{k}{\epsilon} \sqrt{2 S_{ij} S_{ij}}, \quad S_{ij} = \frac{1}{2} \left( \frac{\partial U_i}{\partial x_j} + \frac{\partial U_j}{\partial x_i} \right) \\ \frac{\mu}{\mu_{eff}} &= \left| \frac{\alpha - 1.3929}{\alpha_0 - 1.3929} \right|^{0.6321} \left| \frac{\alpha + 2.3929}{\alpha_0 + 2.3929} \right|^{0.3679} \\ C_{\epsilon 1} &= 1.42, \quad \tilde{C}_{\epsilon 2} = 1.68, \quad C_{\mu} = 0.085 \\ \beta &= 0.012, \quad \lambda_0 = 4.38 \end{aligned} \right\} \quad (3.30)$$

where  $C_{\epsilon 2}$  contains the rate of strain and  $S_{ij}$  is the mean-rate-strain tensor. Generally, the conservation equations (3.29) under steady state conditions are constructed as follows [66]: the first term on the left-hand side represents the convective transport of  $k$  or  $\epsilon$ , the first term on the right side stands for the diffusive transport, the second for the rate of production and the third term for the rate of destruction of  $k$  or  $\epsilon$ . Herein, the inverse Prandtl numbers  $\alpha$ ,  $\alpha_0$  are evaluated with the help of the heat transport relation, which was derived analytically, [18], [10]. The well reported difficulty of the application from standard  $k - \epsilon$ -models at near wall regions, adopted in a wide Reynolds range from low to high  $Re$ -numbers, and flows with rapid rate of strains as well as stream curvature will be compensated or have a positive impact imposed by a strain-dependent correction term in the  $\epsilon$ -equation, [65], [18]:

$$R = \frac{C_{\mu} \lambda^3 \left(1 - \frac{\lambda}{\lambda_0}\right)}{1 + \beta \lambda^3} \quad (3.31)$$

To choose the same or almost equal inlet conditions for the simulation as in the laboratory test rig, preliminary estimations at smooth and finned-tubes with a coarse computational grid are performed, where the boundary conditions for the inlet are varied. Fluent © provides different options for the specification method, containing explicit  $k$  and  $\epsilon$  or by recalculating from the doubles of the turbulent intensity and hydraulic diameter, or the length scale, or the viscosity ratio, [10].

$$\left. \begin{aligned} k &= \frac{3}{2} (u_{in} Tu)^2 \\ \epsilon &= C_{\mu}^{3/4} \frac{k^{3/2}}{l} \end{aligned} \right\} \quad (3.32)$$

The difficulty in the equation of the rate of dissipation arises for the choice of an appropriate length scale <sup>8</sup>. Thus, for a first examination three different configurations of the solid finned-tube for  $l$  with 0.1%, 0.4%, and 1% of the transversal tube pitch as

<sup>8</sup>Some first basic examinations are performed in case of smooth tubes at constant inlet velocity of  $u_{in} = 7 \text{ m/s}$ , where the characteristic length was varied in between the hydraulic channel diameter, the bare tube diameter, and the transversal tube pitch.

### 3. Numerical Consideration

well as applying the hydraulic channel diameter at hot and ambient conditions were calculated. Also the influence on the flow field at high  $Tu = 10\%$  and low  $Tu = 1\%$  for the velocity at the inlet of the computational domain of  $u_{in} = 5 \text{ m/s}$  and  $u_{in} = 7 \text{ m/s}$  is investigated. All CFD-calculations were performed applying ANSYS, Fluent 6.3.26 ©, providing a near wall modeling with enhanced wall functions [10]. In all calculations the incompressible ideal gas law is applied, where the density of the fluid depends only on the operating pressure and not on the local relative pressure field, and is evaluated using the ideal gas law.

#### 3.2.2. Wall Functions

The considered wall-bounded flow within the computational domain is influenced by the presence of the given solid fin structures. To save computational requirements, a wall function approach was applied. Here, the near-wall region close to a solid boundary is not solved explicitly but is "formulated" using an empirically-determined relation, serving the basis for boundary conditions of momentum, energy, and turbulence quantities. At the wall surface, the no slip condition has to be fulfilled. Generally, standard  $k - \epsilon$  models are valid at high  $Re$ -numbers and low viscous stresses. However, close to the wall, the influence of viscous stresses rises against turbulent Reynolds stresses, thus these empirically-developed wall functions are employed.  $y^+$  is the dimensionless orthogonal distance to the wall and  $U^+$  is the non-dimensional scaled velocity parallel to the wall and is defined with

$$\left. \begin{aligned} y^+ &= \frac{u_\tau y}{\nu} \\ U^+ &= \frac{U}{u_\tau} \end{aligned} \right\} \quad (3.33)$$

where,  $u_\tau = \sqrt{\frac{\tau_w}{\rho}}$  and  $\tau_w$  are the wall friction velocity and the wall shear stress, respectively. Close to the wall a linear relationship between  $y^+$  and  $U^+$  is observed. Outside of this so-called viscous sublayer, the velocity profile can be described by a log-law, named log-law-layer. This is depicted in Figure 3.2, taken from [65], where experimental data is compared to these empirically-determined functions. The region in between these two layers is often called buffer layer or blending region, from about  $y^+ \approx 5$  to  $y^+ \approx 30$ , and the range of validity is varying from author to author [10], [66], [65].

As already mentioned above, a result of these complex geometries with their dense grids (up to 6 grid points  $\hat{a}$  fin thickness) yield to small values of  $y^+$ . Thus, enhanced wall functions are used for near-wall treatment. This "single-wall-law" can be applied throughout the fully turbulent region, the blending region, and the viscous sublayer, by blending the linear and logarithmic laws, [10], [65]. Similar to a  $U^+$ -profile, the thermal wall functions are developed; both laws can be defined in form of a blending

### 3. Numerical Consideration

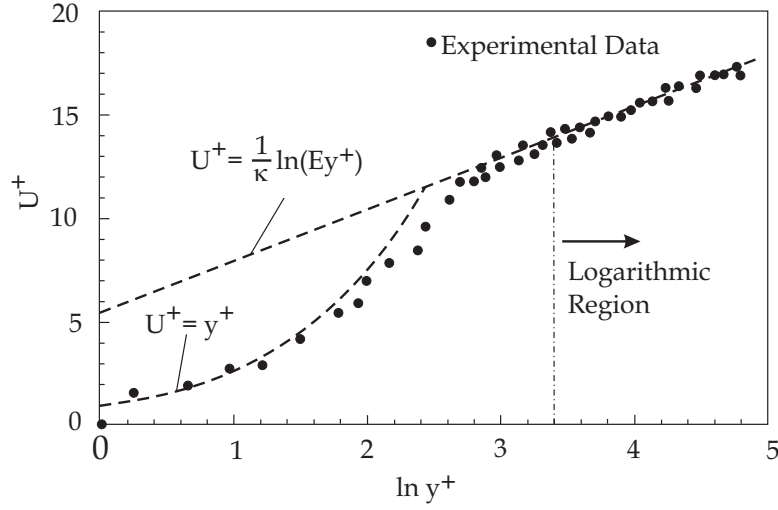


Figure 3.2.: Dimensionless Velocity Profile of a Turbulent Boundary Layer in Comparison to Experimental Data, for  $\kappa \approx 0.4$  and  $E \approx 9.8$  taken from [65]

function as defined in, [10] or [65]:

$$\left. \begin{aligned} U^+ &= e^{\Gamma_1} U_{lam}^+ + e^{\frac{1}{\Gamma_1}} U_{turb}^+ \\ T^+ &= e^{\Gamma_2} T_{lam}^+ + e^{\frac{1}{\Gamma_2}} T_{turb}^+ \end{aligned} \right\} \quad (3.34)$$

#### 3.2.3. Modeling of the Computational Domain and Grid Generation

Five different models with solid and segmented fins were developed. For the investigation of segmented fin-tubes, three different domains were generated, whereas two models are constructed to analyze especially the effect of circular segmented  $I$  and  $U$ -shaped fin geometries. The  $U$ -shaped fin model sketch is depicted in Figure 3.3(a) and 3.3(c). As seen, the computational domain consists of two half adjacent finned-tubes with two fin pitches. One fin pitch consists of the  $U$ -shaped part of the fin and the other consists of the bare tube part. For saving computational calculation time, the numerical analysis can be limited to a single fin pitch, using symmetry and/or periodic sections, as performed in [33], [39], [53], [64], [32], [34], and [46]. Thus, symmetries of the fins were utilized by adopting symmetry conditions through the mid plane of the fins at  $s/2$ . The generated model of the  $I$ -shaped fin is presented in Figure 3.3(b) and 3.3(c). As seen, due to symmetries of the geometry, only a single fin pitch is considered here. To account for any velocity distribution and thus momentum as well as heat transfer effects in  $z$ -direction, periodic boundaries were applied, passing through the mid plane at the half fin spacing between two adjacent fins. To obtain the same behavior as in the test rig, the effect of the symmetry of 11 tube layers was chosen as symmetry condition, which was adopted on the top and bottom of the computational

### 3. Numerical Consideration

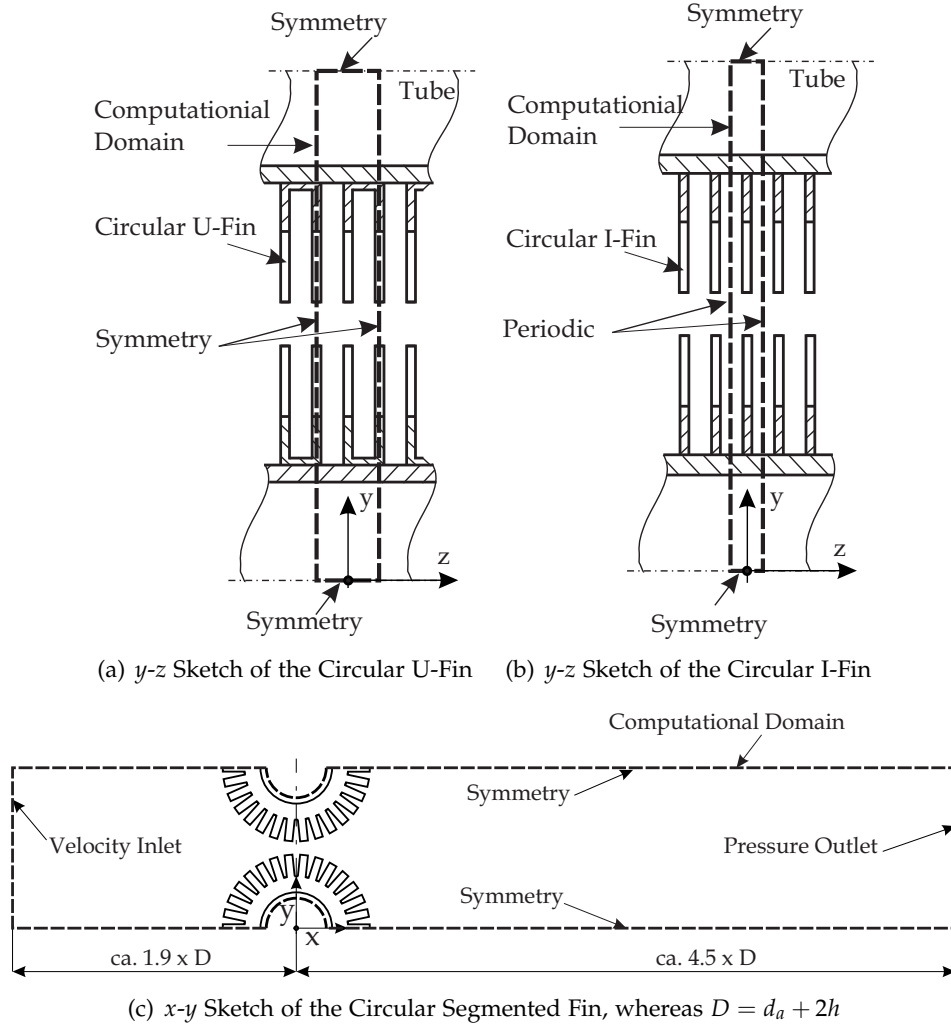


Figure 3.3.: Computational Domains of Circular Segmented Finned-Tubes

domain for all models. To investigate the influence between circular and helical fins on the fluid flow in  $z$ -direction and thus heat transfer augmentation, an additional model was developed applying helically segmented fins. For the discretization of the spiral fins, periodic conditions were applied on the left and right hand side of the domain, seen from the flow  $x$ -direction above the finned-tube bundle, see Figures 3.4(a) to 3.4(c). As seen, due to complex geometry, a single tube was considered to build a "unitary cell". The upstream and downstream region is located in a certain distance, to avoid possible side effects, [46] [53], and [64]. The "measurement" planes in the domain for temperature and pressure determination are located at equal distance compared to the experiments.

The modeling of the solid finned-tubes was performed in the same manner accord-

### 3. Numerical Consideration

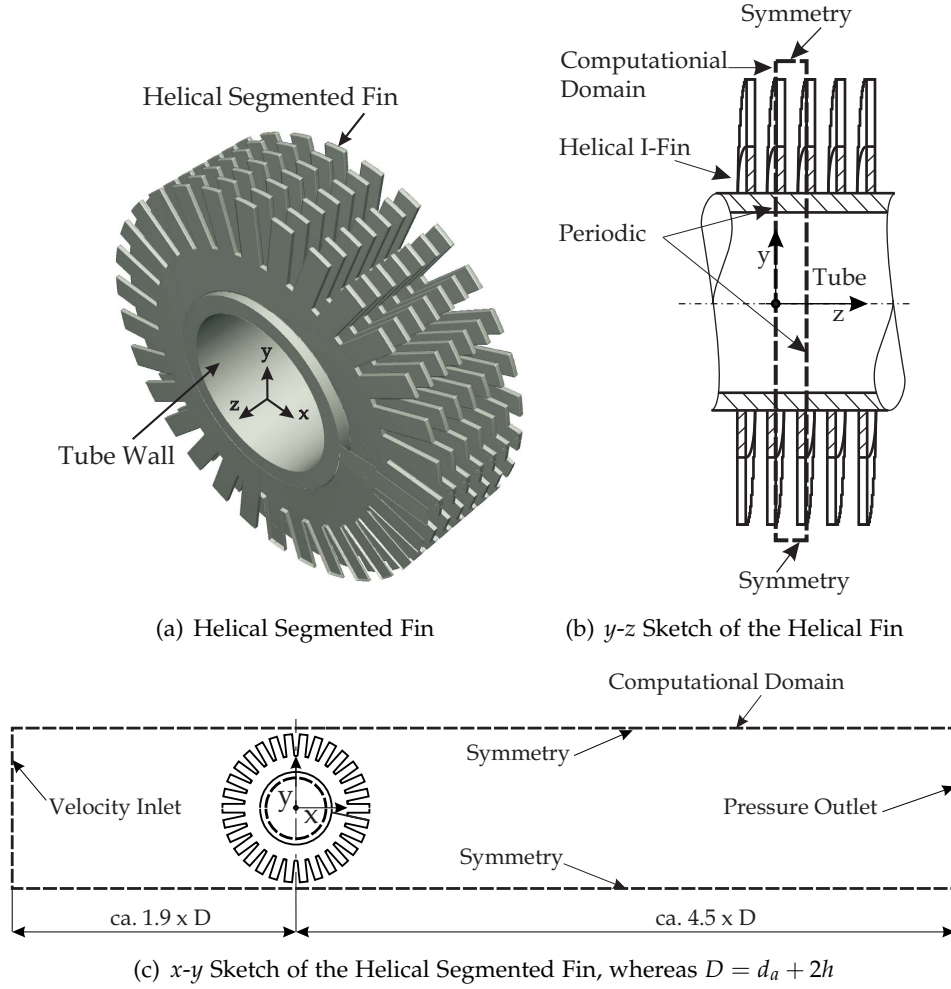


Figure 3.4.: Computational Domain of the Helical Segmented Finned-Tube

ing to the segmented fins. Due to simpler geometry of the solid fins, the computational domain consists of two half tubes each for both cases, circular and helical; refer to Figures 3.5(a) to 3.5(c).

Starting from a single bare tube in cross-flow, the computational domain was discretized stepwise until the circular and helical solid or segmented finned-tube model was able to be meshed. Therefore, the domain<sup>9</sup> was split up into several parts of simple descriptive geometries and meshed each separately.

In Table 3.1 the different specifications of the models, numbers of employed volume blocks, and total numbers of cells for meshing the solid part as well as the fluid part of the domain are given.

<sup>9</sup>I.e. fins, tube, fluid between fin and tube, inlet region, and outlet region

### 3. Numerical Consideration

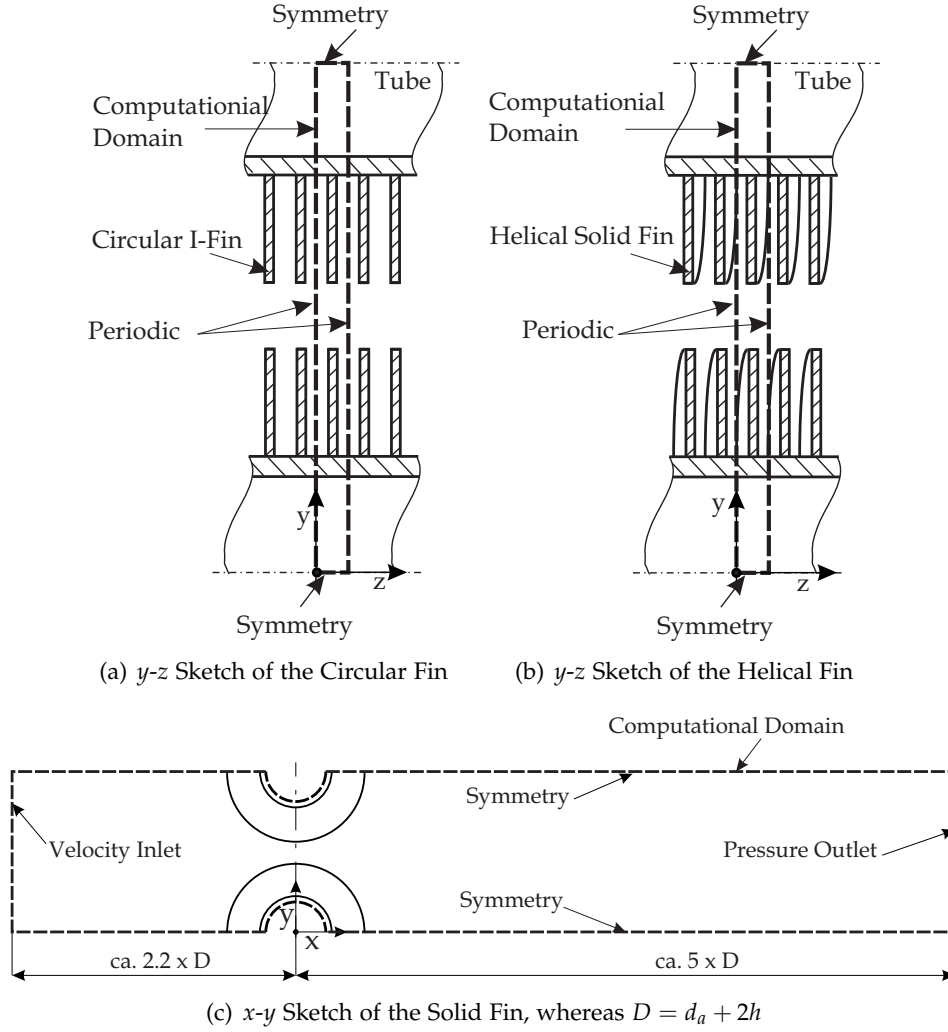


Figure 3.5.: Computational Domain of Solid Finned-Tubes

The grid was generated, combining block-structured and unstructured meshes in Cartesian coordinate systems. For the inflow and outflow region structured meshes with the so-called "coopering" constructing scheme were applied, to obtain well distributed flow conditions. The desired number of nodes and spacing of grid points is applied to several fin-tube parts of the complex geometries. At near wall regions, quadrilateral cells, so-called "boundary layers", are constructed around all circular finned-tubes. As a result of the small fin thickness and large finning diameter, huge aspect ratios will arise. To reduce this effect and for modeling of heat conduction through the solid material, up to 6 grid points are used to discretize the fin thickness. Additionally, the first cell heights in the solid and fluid regions were chosen to be

### 3. Numerical Consideration

Table 3.1.: Specifications of the Modeled Finned-Tubes

Notation	I-fin segmented circular	U-fin segmented circular	I-fin segmented helical	I-fin solid circular	I-fin solid helical
$d_i$ [mm]	31.6	31.6	31.6	32.8	32.8
$d_a$ [mm]	38.8	38/38.8	38.8	38	38
$b_s$ [mm]	4.3	4.3	4.3	—	—
$h_s$ [mm]	11.44	11.43	11.44	—	—
$s$ [mm]	0.8	0.8	0.8	1.0	1.0
$h$ [mm]	19.6	19.6	19.6	15	15
$D$ [mm]	78	78	78	68	68
$B_{Ch}$ [mm]	3.39	6.80	3.38983	3.623	3.623
$H_{Ch}$ [mm]	85	85	85	85	85
$a$ [mm]	2.59	2.60	2.58983	2.623	2.623
Volume Blocks — #	48	23	54	20	12
Cells — # [in 1000]	2.153	3.904	6.617	3.357	3.120

almost similar, for preventing numerical problems<sup>10</sup>. To reproduce the periodic effect of the helically segmented fin tube, the minimum solid fin thickness in the model starts from  $\approx 0.04$  mm. Since the condition of the dimensionless wall distance for standard wall functions between the adjacent fins could not be met ( $y^+ > 30$ , logarithmic law of the wall) [74], enhanced wall functions were applied to the model, [10]. Thus a high number of cells was needed and a large computational effort is involved for the simulation of these complex geometries, associated with these dense grids. All simplifications and assumptions for modeling in regard to saving computational time, and thus differences between the model and the realistic measured object, will be covered by evaluation and should have sparse consequence to the gained results of the numerical simulations. A rather large number of dense and coarse grids were pre-constructed. The modeling of the computational domain and the grid generation were performed by means of the commercial software ANSYS Gambit 2.3.16 ©.

#### 3.2.4. Boundary Conditions and Thermo-Physical Properties

Elliptic problems require boundary conditions for each boundary of a calculation area, to evaluate the mass, momentum and heat transfer. The upstream inlet condition was chosen as "velocity inlet" with a turbulent intensity of  $Tu = 5$  % and a given temperature of  $T_{in} = 480$  K. The constant inlet velocity is assumed to be uniformly

<sup>10</sup>Before exporting the mesh file for calculations, the grid cells were checked for aspect ratios and skewing.



### 3. Numerical Consideration

distributed with just an  $x$ -component in flow direction. In the course of the parameter variation, the inlet velocity ranges from  $0.8 \text{ m/s}$  to  $13 \text{ m/s}$ . In this study, only the fluid at the air-side was modeled and the boundary conditions from the water-side were implemented. For hot conditions, the free stream temperature at the internal tube-side was defined to be constant at  $T_w = 330 \text{ K}$  with an appropriate heat transfer coefficient of  $\alpha_i = 3860 \text{ W/m}^2\text{K}$  of the adjacent fluid inside the tube, reads as thermal convection condition, which is common practice - refer to literature [46], [53]. The water-temperature and the inlet/outlet gas-temperatures will be finally inserted into Equation (2.9) for heat transfer evaluation. Considering this modeling technique, the estimated error as a result of the constant temperature and heat transfer coefficient at the water side will be small<sup>11</sup>. The advantage of this boundary condition type is that a wall temperature is obtained for a given free stream inlet temperature and the material of the finned-section. At the wall the no-slip-condition for the velocity is ascertained. For the downstream outlet boundary a "pressure outlet" condition was chosen to an ambient static pressure of about  $1.013 \text{ bar}$ . The density variation, as mentioned above, in Fluent © is evaluated using the incompressible ideal-gas law, since the pressure variations are small enough but the flow is temperature dependent, [10]. The effect of gravity was neglected. Orthogonal to symmetry conditions, no heat flux and momentum will be transferred, [46]. For CPU-cost reasons as mentioned above, periodic and symmetry conditions are ascertained. In case of periodicity, the conditions from the left finned-tube wall are reflected to the right wall, assuming an infinite sequence of fin-arrays. For modeling the heat transferring medium, dry-air is assumed and for the solid material i.e. fin and tube, carbon steel ( $St 35.8$ ) was chosen. The user defined thermo-physical "material" properties of dry-air and the solid material are stated in the Appendix B.1.

#### 3.2.5. CFD-Procedure

Two major aspects are mainly responsible for an appropriate *CFD* calculation result, that is convergence and grid independence, [66]. In this section some computational parameters for the performed *CFD* calculations will be discussed.

- **Control- and Relaxation Parameters**

As far as it was possible in the scope of this work, especially with these complex geometries, a grid independency study was performed. For this purpose, the variation of the mass-averaged outlet temperature downstream of the tubes within the flow channel for a constant inlet velocity was judged for the stability of the obtained overall Nusselt number.

A double precision pressure-based solver was selected for heat transfer problems of incompressible flow, where the scaled residuals can fall high orders of magnitude. In case of conjugate problems involving high thermal conductivity ratios

---

<sup>11</sup> $\alpha_i \gg \alpha$

### 3. Numerical Consideration

between solid and fluid as well as the generated grids provide high-aspect-ratios, the option of the double-precision solver, implemented in Fluent ©, provides higher accuracy and convergence, [10].

For solving the convective and conductive problem at helically segmented fins, an explicit under-relaxation for the temperature was implemented. Since high skewed meshes in regions of small fin-endings ( $\approx 0.04 \text{ mm}$ ) at the periodic boundaries are expected, this technique will provide improved convergence. Here, the under-relaxation factor for the energy is set to 1 and the under-relaxation factor for the temperature was chosen with 0.5. The under-relaxation factor controls the transport variable temperature by restricting 50% change from the determined value from previous iteration to the current iteration, [65]. Additionally, the influence of the secondary gradients<sup>12</sup> due to tetrahedral grid at some wall regions was lowered, as they are used as corrective terms for the accuracy of a solution, [11]; these meshes were calculated applying the node-based averaging scheme, since this is more accurate for unstructured meshes. All these refinements are very time consuming but will enhance the obtained results of the calculation procedure.

The linkage between pressure and velocity was applied using the *SIMPLE*-scheme, [49], as well as refer to literature e.g. [66] and [65]. But so far, the Péclet number accounts for the convective and diffusive transport. In case of a real heat conduction problem, a central differencing scheme would be appropriate ( $Pe \ll$ ). In this work, the portion of convective flow behavior is large compared to diffusive effect<sup>13</sup>, thus the discretization of the differential equations was implemented by means of upwinding schemes for the pressure-velocity coupling. All calculations were started with the first-order upwinding scheme, since this was observed to provide faster convergence. After about 1000 to 1500 iterations the modulus was switched to second-order upwind- or in some cases to third-order *MUSCL*-schemes<sup>14</sup>, for better accuracy<sup>15</sup> rather than faster convergence. But the choice for an adequate discretization scheme depends on the different computational domains of the solid and segmented finned-tubes. All in all between 7000 and 12000 iterations were necessary until the termination criterion was finally reached.

- **Convergence Check of the Solutions**

A lot of factors indicate if a solution of a *CFD* calculation will converge, but it

---

<sup>12</sup>Those gradients are also responsible for computing secondary diffusion terms and velocity derivatives, [10]

<sup>13</sup>If the Péclet number becomes very large, thus any dependency of the flow upon downstream locations is rather small

<sup>14</sup>Monotonic upwind scheme for conservation laws

<sup>15</sup>Due to the fact of high velocity gradients in the channel near two adjacent fins, to avoid numerical diffusion, [10]

### 3. Numerical Consideration

is difficult to judge this criterion. For the pressure-based algorithm, the scaled residuals<sup>16</sup> have to decrease in the orders of at least 3 magnitudes, and the energy residuals must decrease at least 6 orders magnitude, [10]. For an appropriate solution with acceptable accuracy, deep convergence is thus required. The convergence check was done by means of scaled residuals and outlet temperature monitoring (being a relevant quantity). Additionally, the overall heat and mass balances were checked. A solution seemed to be converged, if the plotted curves are flattened, which indicates that the solution is no longer changing with ongoing iteration, as provided in [12].

Parallel computing is applied and a simulation was stopped if either steady or periodic behavior of the residuals undergo the termination criterion. Finally it has to mentioned that in the course of this parameter study a total number of 80 useful *CFD* calculations for solid and segmented finned-tubes were accomplished.

---

<sup>16</sup>In Fluent © the residuals are scaled with a scaling factor, i.e. representative of the flow rate [10]

## 4. Experimental and Numerical Results

To raise new questions, new possibilities,  
to regard old problems from a new angle,  
requires creative imagination and marks real  
advance in science.

*Albert Einstein*

★

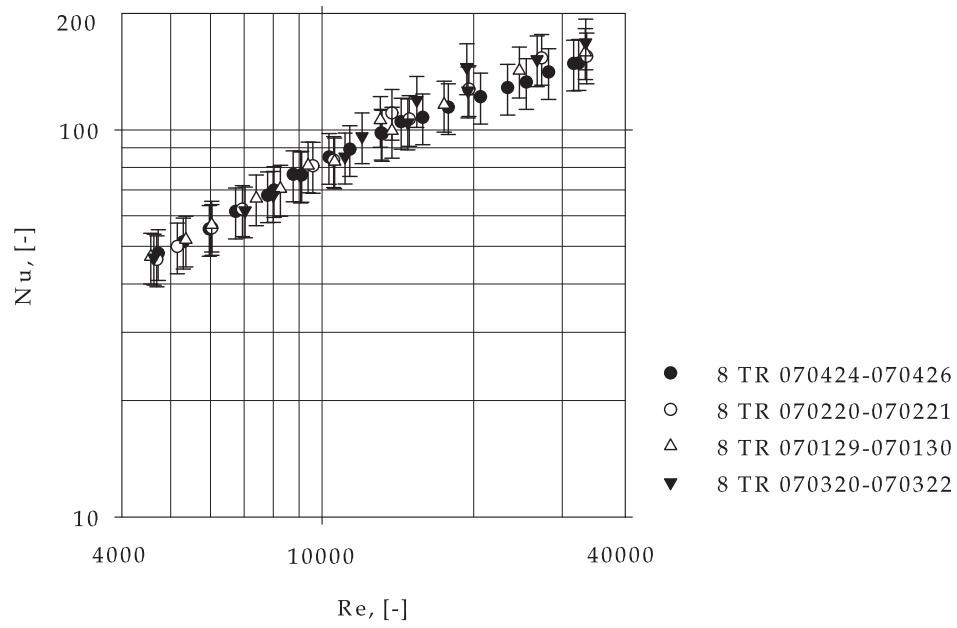
In the first part of this section, the global results evaluated from the experimental investigations at different tube configurations as well as from numerical analysis are presented. Afterwards, a row correction factor, as a result of turbulent flow conditions of consecutively arranged tube rows is determined. With the help of dimensional analysis, correlations for the prediction of heat transfer and pressure drop coefficients are derived. A comparison of the considered different finned-tube types with correlations from open literature is presented. Finally, the performance of the investigated finned-tube bundles is analyzed, applying the theory of the Performance Evaluations Criterion (PEC), suggested by WEBB, [71] as well as STEPHAN and MITROVIC [59]. The second part mainly discusses local phenomena due to fluid flow, heat convection and conduction.

### 4.1. Global Consideration of the Experimental Results

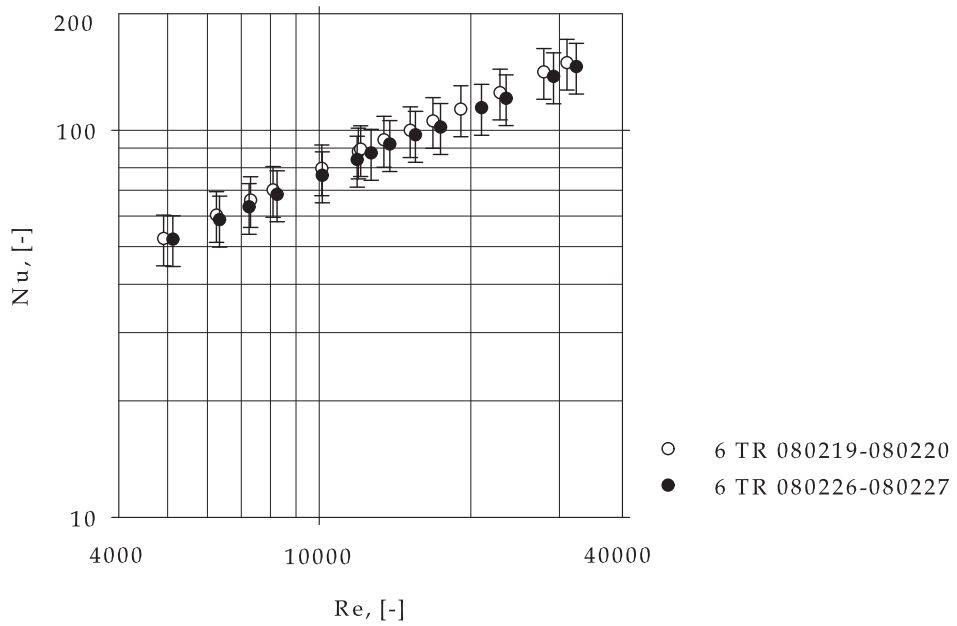
#### 4.1.1. Heat Transfer and Pressure Drop of the Investigated Tube-Bundle

The following Figures 4.1(a) to 4.3(b) present the calculated dimensionless heat transfer coefficient from the measured results as function of the Reynolds number for a representative number of measured points within the  $Re$ -range at 8, 6, 4, and 2 U-segmented finned-tube rows in staggered arrangement and for a single tube row as well as special configurations. In these diagrams an overall error bar of  $\pm 15\%$  is marked, which is calculated to include about 80% of all measured results. The date of series of measurement and the row configuration is shown in the legends of the graphs.

#### 4. Experimental and Numerical Results



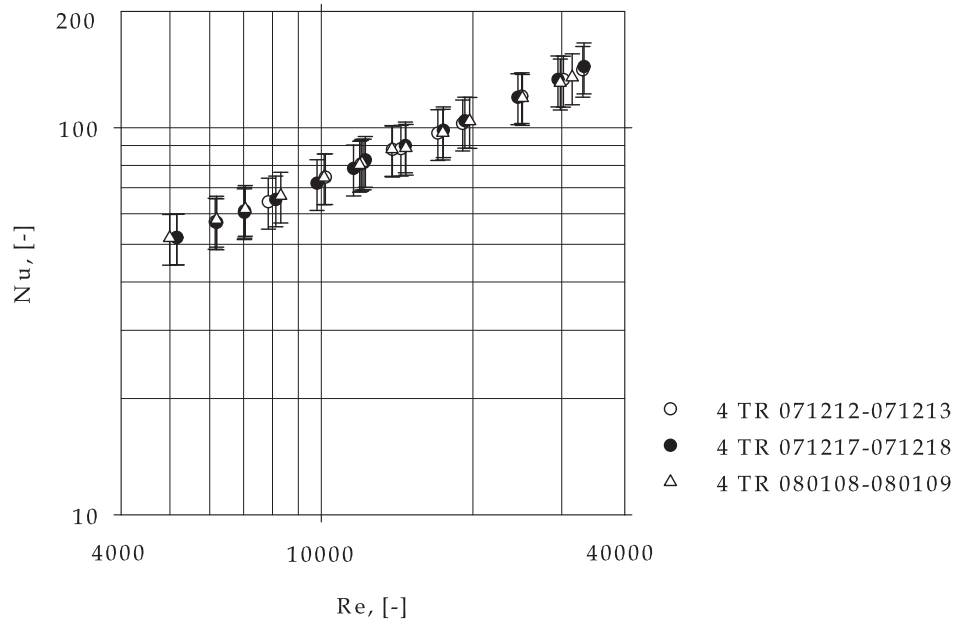
(a) 8 Consecutive Rows



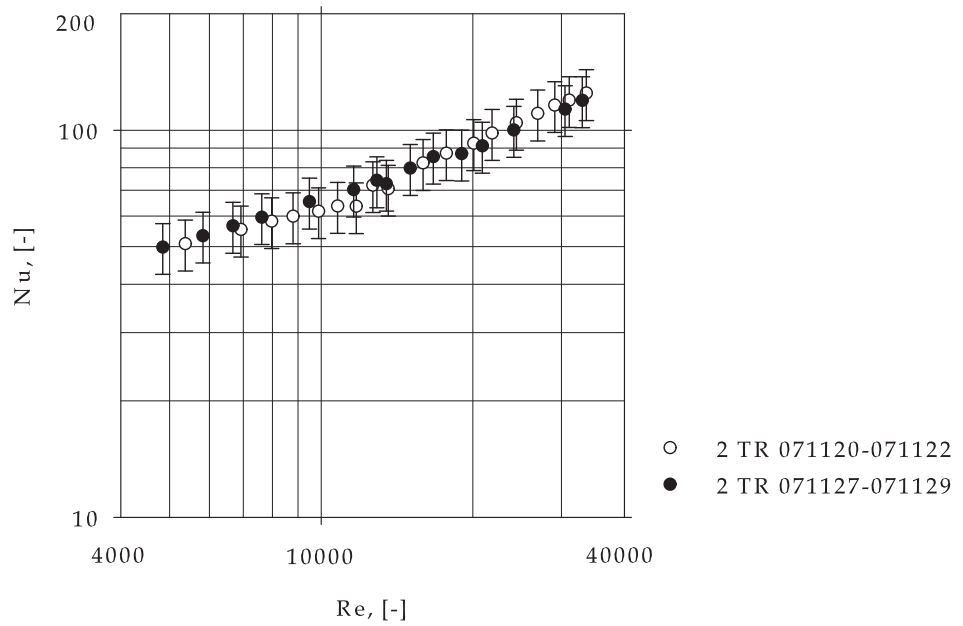
(b) 6 Consecutive Rows

Figure 4.1.: Heat Transfer of Segmented U-Finned-Tubes, for  $Pr \approx 0.71$ ,  $d = 38 \text{ mm}$ , with  $\pm 15\%$  Overall Relative Uncertainty

#### 4. Experimental and Numerical Results



(a) 4 Consecutive Rows



(b) 2 Consecutive Rows

Figure 4.2.: Heat Transfer of Segmented U-Finned-Tubes, for  $Pr \approx 0.71$ ,  $d = 38 \text{ mm}$ , with  $\pm 15\%$  Overall Relative Uncertainty

#### 4. Experimental and Numerical Results

As seen, the heat transfer coefficient increases with an increasing number of tube rows. The  $Nu$ -number tends to be constant above 8 tube rows, compare Figure 4.1(a) and 4.1(b). The exponents for the Nusselt correlations<sup>1</sup> vary roughly from about 0.46 to 0.62 for the individual row configurations. This variation may be caused by the pressure difference measurement uncertainty of the mass flow of air at low  $Re$ -Numbers as well as the temperature measurement uncertainty between inlet and outlet at the water-side and/or gas-side, especially for a lower number of tube rows.

Since two or even only one tube row occur sometimes in a bundle of heat recovery steam generators, heat transfer equations for one tube row are required. Thus, investigations are emphasized for single row configurations. The difficulty of these arrangements is the small temperature difference at the water side<sup>2</sup>, considering a minimum water velocity to fulfill turbulent flow conditions within the water-tubes. At the gas-side, a possible bypass effect due to staggered tube layout occurs, see Figure 2.5. All these effects increase the measurement uncertainty.

In Figure 4.3(a) the calculated  $Nu$ -numbers at a single tube row configuration as function of the  $Re$ -number are shown. As seen, at about  $Re > 10000$ , a possible bypass flow takes place. This reduces the effective transferred heat, which leads to a smaller exponent in the power-law for higher  $Re$ -numbers. As mentioned above, to reduce the flow bypassing effect, a semi-tube is installed at the bottom of the channel wall, reducing the effective minimum net free area in a tube row. This influence can be seen in the results of measurements at a single tube row with a semi-tube installed at the channel-bottom in Figure 4.3(b), denoted as "1S TR". Thus, at  $Re > 10000$ , the bypass flow is reduced and the power law shows a nearly linear correlation in the double-logarithmic diagram. For  $Re < 9000$  a higher measurement uncertainty between the two series of measurements may be ascertained, due to effects as mentioned above. The scatter plot, denoted with "1 + 7", presents measurements at 1 heated finned-tube row with 7 consecutively arranged unheated rows. As seen, this arrangement leads to slightly higher heat transfer than for a single tube row in cross-flow, which can be seen as an impact of blockage from the unheated tubes of the downstream, causing a reflux or reverse transport.

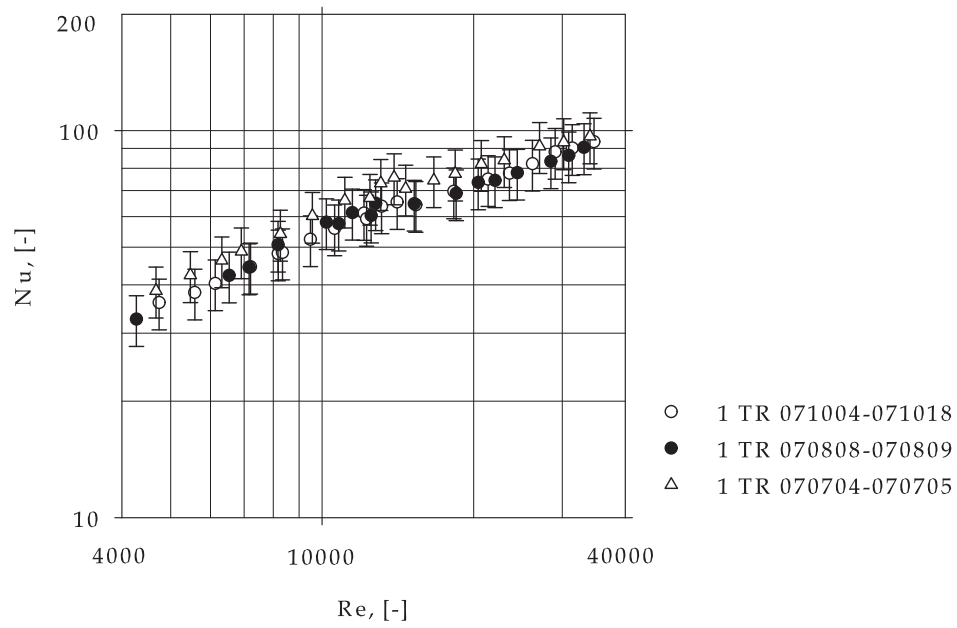
In Figures 4.4(a) and 4.4(b), the pressure drop coefficient evaluated for a single tube row (single resistance) from different investigated tube layouts in staggered arrangements is shown. Besides investigations at augmented temperature conditions, all presented pressure drop coefficient measurements are performed at ambient conditions, to reduce any effects caused by pressure recovery. The index of  $\zeta_i$  indicates the position of the pressure difference measurement up- and downstream of the investigated tube bundle. "1" ( $\zeta_1$ ) is calculated from the static pressure differences at the channel wall of the air-side at the finned-tube bundle, where "2" ( $\zeta_2$ ) is calculated from pressure differences in the center of the flow channel. A considerable amount of measured points

---

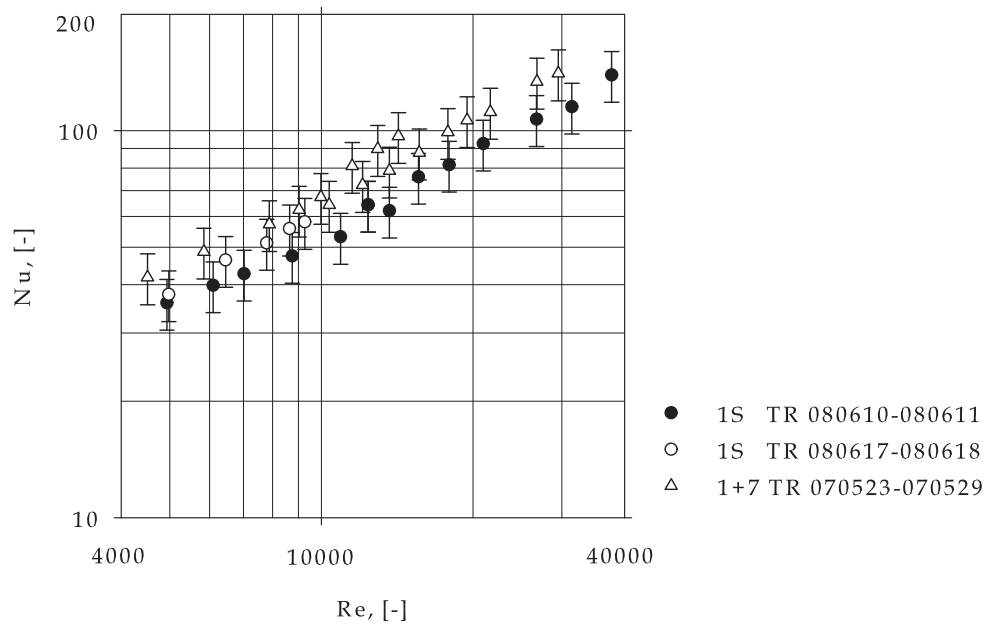
<sup>1</sup> $Nu = f(Re, Pr)$

<sup>2</sup>only a single equal crossing of the flow-channel width of about 500 mm

#### 4. Experimental and Numerical Results



(a) Single Tube Row



(b) Special Configurations

Figure 4.3.: Heat Transfer of Segmented U-Finned-Tubes, for  $Pr \approx 0.71$ ,  $d = 38 \text{ mm}$ , with  $\pm 15\%$  Overall Relative Uncertainty



#### 4. Experimental and Numerical Results

in the  $Re$ -range of about  $5000 < Re < 50000$  is accomplished. The evaluation for a single row is performed according to Equation (2.32)<sup>3</sup>, because especially for high  $Re$ -numbers no considerable difference within the obtained results may be observed. This seems to be particularly valid for  $\zeta_2$  in the whole  $Re$ -range. For  $Re > 15000$  the pressure drop coefficient of the different finned-tube bundle configurations has the same characteristics in the center as at the wall of the flow-channel, while for  $Re < 10000$  great uncertainty is revealed for the small pressure difference for U-shaped segmented finned-tubes. As shown in Figures 4.4(a) and 4.4(b) for  $Re > 15000$ , a small increase takes place, then, at  $Re \approx 35000$  up to the upper Reynolds boundary of measurement, the pressure drop coefficient tends to show a constant value. In the channel center, no flow separation or any bypass flow can be detected.

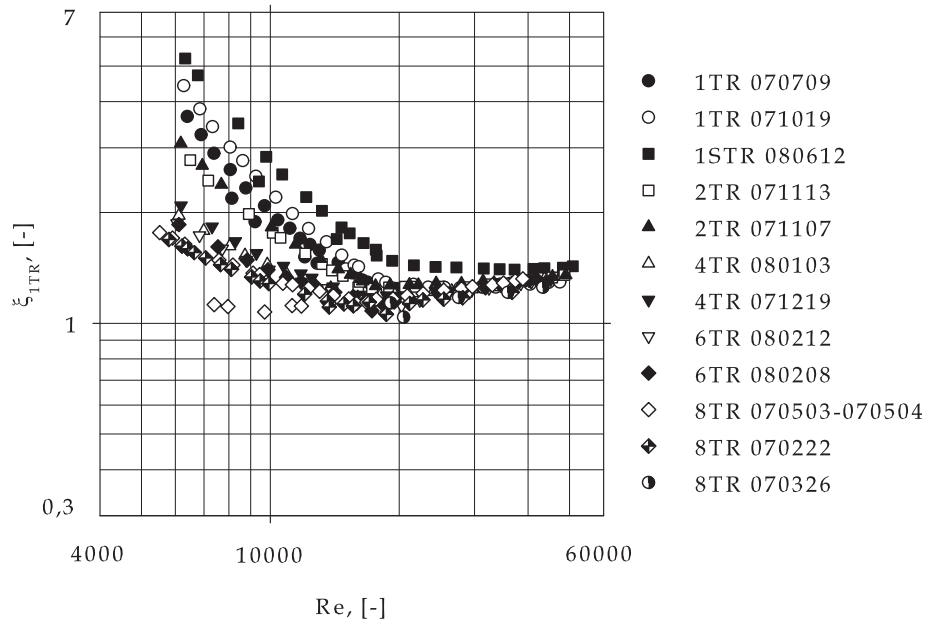
On the other hand, the evaluation of  $\zeta_1$  at the channel wall increases for low  $Re$ -numbers. This effect may be caused by any bypass flow between tubes and test channel i.e. top, bottom, and two side walls and could be explained as follows: In the immediate area of the upstream bore hole at the channel bottom for the pressure measurement the local velocity increases, while the local static pressure reduces in case of isothermal flow conditions. To reduce this effect, a semi-tube is installed. But the influence of the semi-tube on the pressure drop at the channel wall position at same installation size indicates also an increase of the pressure drop coefficient, which could be caused by any flow reflux in front of the first tube row. Due to less net free area in a tube row,  $u_E$  in Equation (2.3) is influenced and thus the pressure drop in Equation (2.2). However, this would indicate also a considerable influence (bypass flow) from the side channel walls, which can be explained by the necessary space for the double helix of the U-shaped fin as well as insufficient alignment of the tubes next to the flow-channel wall. Furthermore, the effect reduces, as the number of consecutively arranged tubes increases, which operates like natural flow resistances, see Figure 4.4(a).

An uncertainty calculation gives information of the estimated relative uncertainty as function of consecutive tube row numbers and  $Re$ -range. As presented in Figures 4.5(a) and 4.5(b), a high uncertainty is expected for a single tube row as well as a single tube row with a semi-tube at the channel wall, as a result of the very small pressure drop differences. As the number of longitudinally arranged tubes increases, the relative uncertainty decreases. A comparison of  $\zeta_1$  and  $\zeta_2$ , evaluated from measurements at 8 consecutively arranged tube rows shows, no significant difference between the flow-channel wall and center is observed. This is depicted in Figures 4.6(a) to 4.8 with an overall error bar of  $\pm 20\%$ . Considering all these facts mentioned above, significant difference among pressure drop coefficients for higher number of consecutively arranged tube rows is not expected. Thus it can be agreed that the pressure drop of the investigated tube bundles at position "1" or "2" shows same tendencies for a high number of consecutively arranged tubes. Hence, for further considerations, the pressure drop coefficient  $\zeta_{1,2}$  at 8 tube rows, evaluated for a single tube row, is chosen.

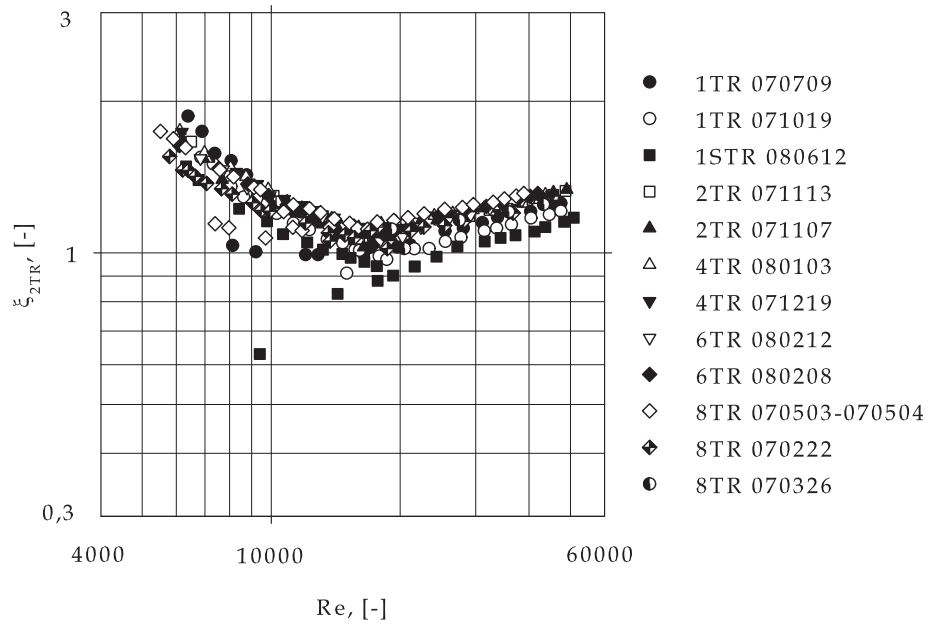
---

<sup>3</sup>mean average pressure drop

#### 4. Experimental and Numerical Results



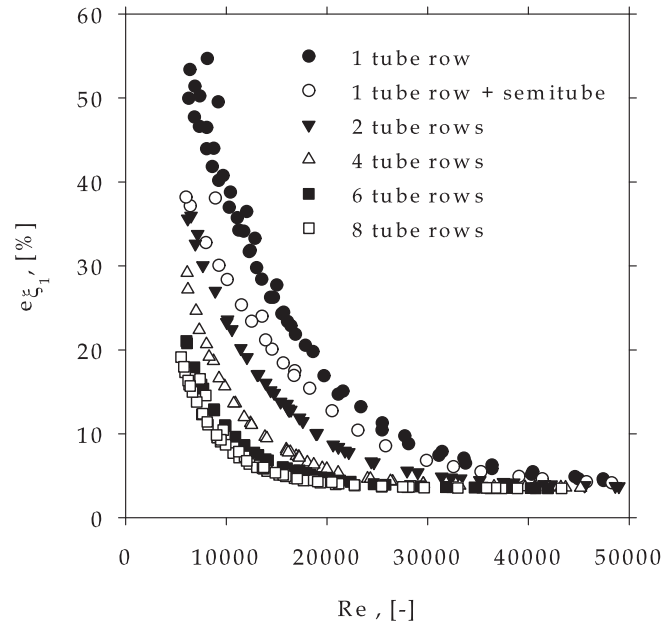
(a) At the Channel Wall



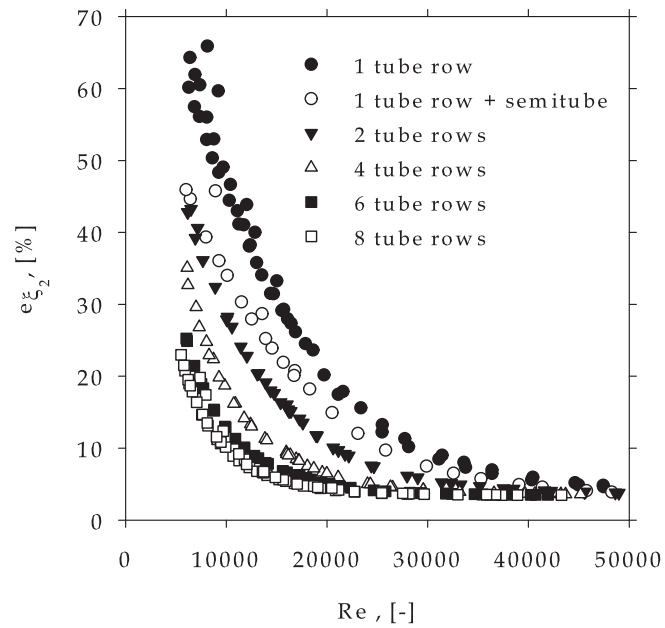
(b) In the Channel Center

Figure 4.4.: Pressure Drop Coefficient of Segmented U-Finned-Tubes at Different Configurations, evaluated for 1 Tube Row and  $d = 38 \text{ mm}$

#### 4. Experimental and Numerical Results



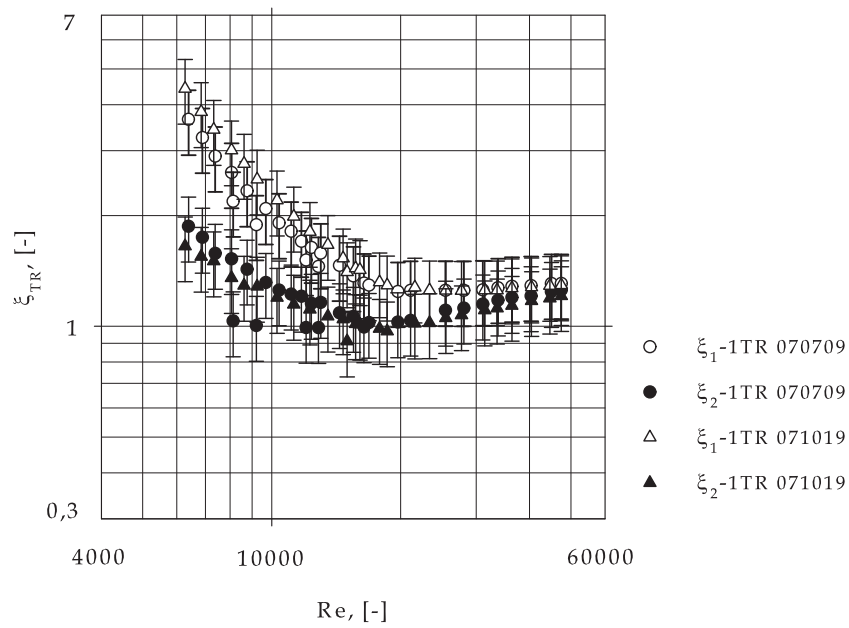
(a) At the Channel Wall



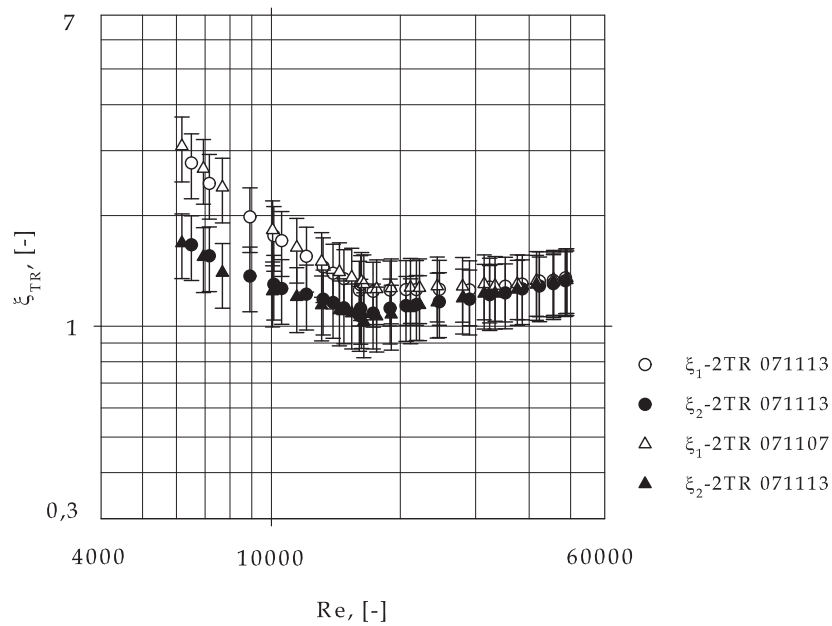
(b) In the Channel Center

Figure 4.5.: Relative Uncertainties of Pressure Drop Coefficient at Different Tube Row Configurations at Ambient Temperature

#### 4. Experimental and Numerical Results



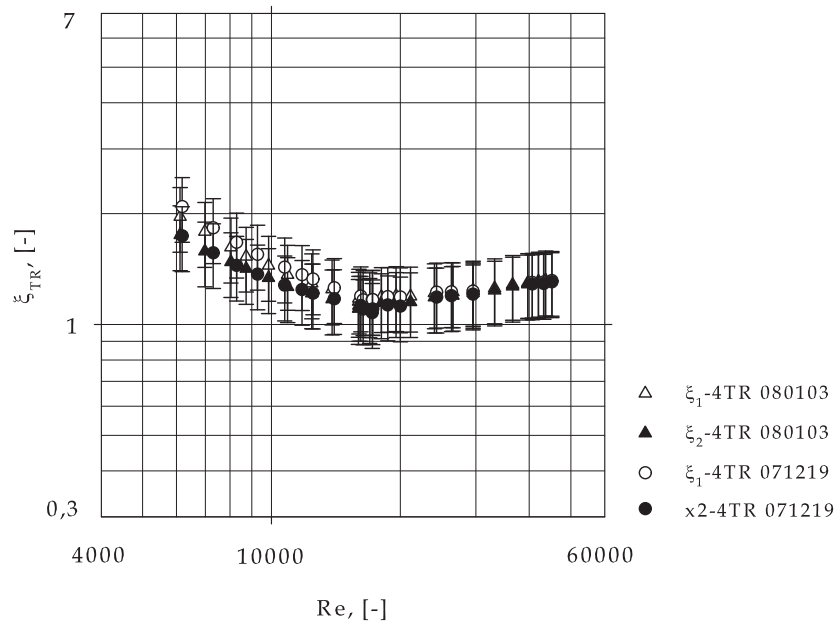
(a) Single Tube Row



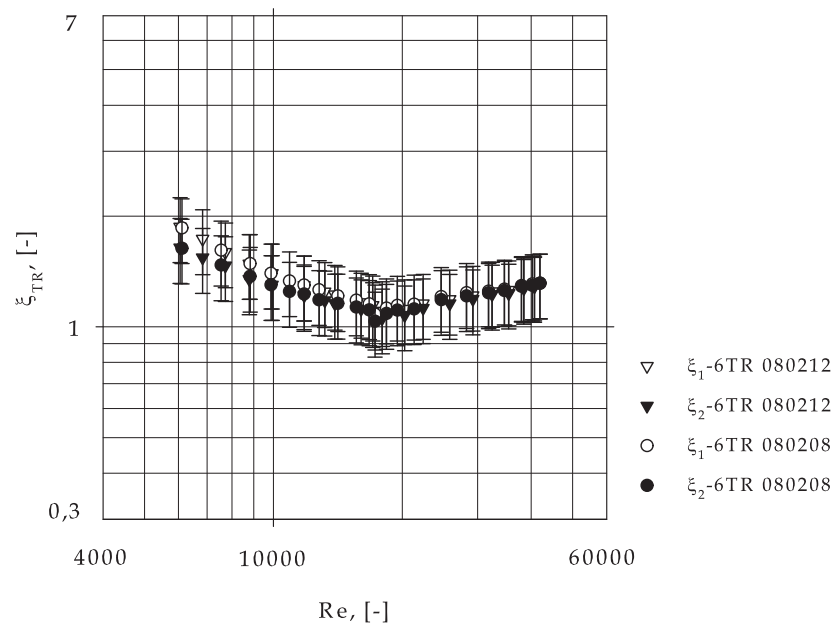
(b) 2 Consecutive Rows

Figure 4.6.: Pressure Drop Coefficient of Segmented U-Finned-Tubes, evaluated for 1 Tube Row and  $d = 38 \text{ mm}$ , with  $\pm 20\%$  Overall Relative Uncertainty

#### 4. Experimental and Numerical Results



(a) 4 Consecutive Rows



(b) 6 Consecutive Rows

Figure 4.7.: Pressure Drop Coefficient of Segmented U-Finned-Tubes, evaluated for 1 Tube Row and  $d = 38 \text{ mm}$ , with  $\pm 20\%$  Overall Relative Uncertainty

#### 4. Experimental and Numerical Results

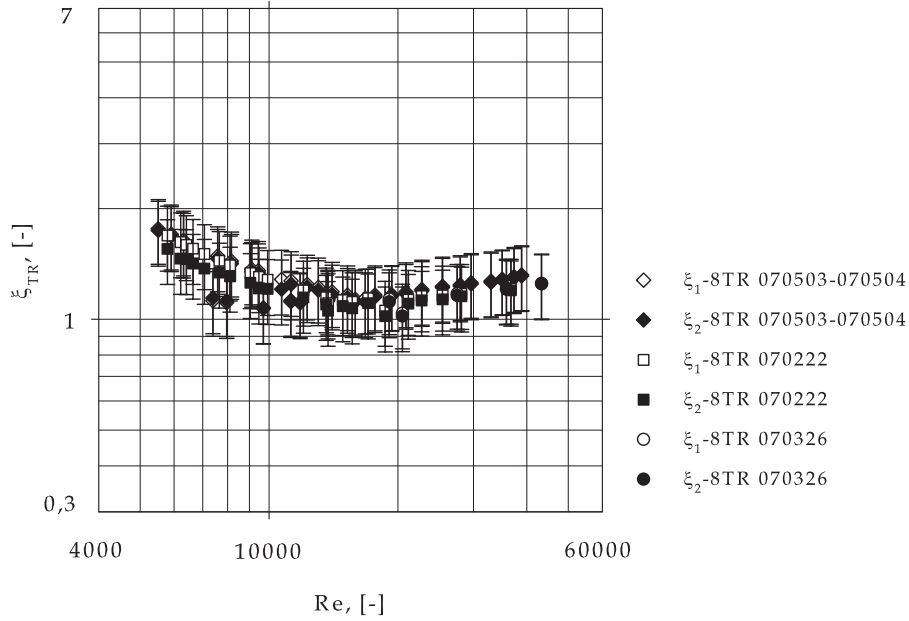


Figure 4.8.: Pressure Drop Coefficient of Segmented U-Finned-Tubes, evaluated for 1 Tube Row and  $d = 38 \text{ mm}$ , with  $\pm 20\%$  Overall Relative Uncertainty

##### 4.1.2. Row Correction Factor

Finned-tube bundles in HRSG are very often utilized with only a few consecutive tube rows in cross-flow. As tests have shown, the heat transfer coefficient of heat exchangers with staggered tube layout varies with the number of consecutive tube rows and increases with the number of tube rows arranged in cross-flow, until an almost constant value is achieved. According to literature, this varies from 4 to 12 tube rows, see e.g. [58], [46], [68], [14], [35], and [72]. Investigations at segmented finned-tubes, presented in e.g. [29], [16], and [15] have shown, that for common tube arrangements in HRSGs, this critical value can be confined with about 8 to 10 tube rows for an appropriate approximation. Yet, there is no agreement between individual authors on the tube row number at which the heat transfer coefficient remains constant.

The most formulas for calculating heat transfer at finned-tubes are generally valid for a certain minimum number of consecutive tube rows and indicate a critical value of equal or more than 8 rows in flow direction. As analyzed above, the pressure drop coefficient, evaluated for a single tube row, on the other hand shows no distinctive dependence on the number of consecutive rows in cross-flow<sup>4</sup>.

In this section, a row correction factor as a function of the Reynolds number and

<sup>4</sup>Considering the evaluated measurement uncertainty

#### 4. Experimental and Numerical Results

the number of tube rows, at smaller numbers of U-segmented finned-tube rows than 8 with staggered layout is derived for a representative number of measured points within the  $Re$ -range. The correction could be applied both for tube rows with solid and segmented fins, [13]. This reduction of the heat transfer coefficient of a small tube row number in relation to the value  $\alpha_\infty$  (heat transfer coefficient for 8 or more consecutively arranged tube rows) for different constant  $Re$ -Numbers is shown in Figure 4.9. Additionally, an average mean value for each row configuration is calculated (solid line in the diagram). As seen, between low  $Re$ -numbers (7000) and high  $Re$ -numbers (30000), this reduction varies in the range of about  $\pm 15\%$ . The heat transfer increases from row-to-row degressive, i.e. first to second row about 13.3%, second to fourth row about 10.9%, and fourth to sixth row about 5.5%.

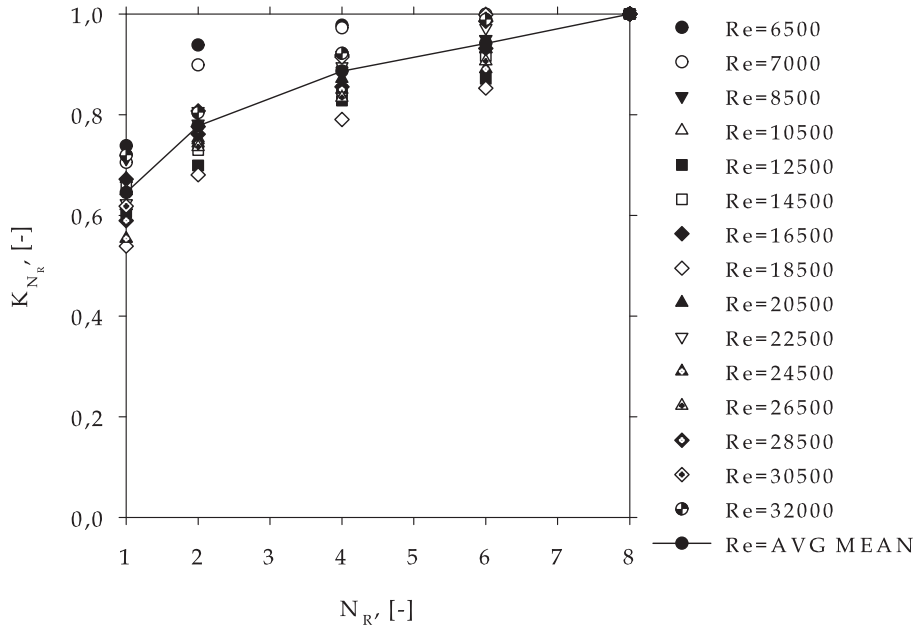


Figure 4.9.: Row Correction Factor  $K_{N_R}$  for 8, 6, 4, 2, and 1 Tube Rows at Different  $Re$ -Numbers

The evaluation of the row correction factor is performed according to the calculation procedure presented in [15]. Thus, the correction is suggested to be evaluated with

$$K_{N_R} = \frac{Nu_\infty}{Nu_1}^{-C(N_R)} \quad (4.1)$$

#### 4. Experimental and Numerical Results

and the exponent

$$C(N_R) = \frac{\ln \left[ \frac{Nu_8}{Nu_{N_R}} \right]}{\ln \left[ \frac{Nu_8}{Nu_1} \right]}. \quad (4.2)$$

In Figure 4.10, the function  $C(N_R)$  above the tube row number is depicted. Generally, this method is coupled with the relation  $[Nu_8/Nu_1]$ , considering the longitudinal and transversal tube pitch.

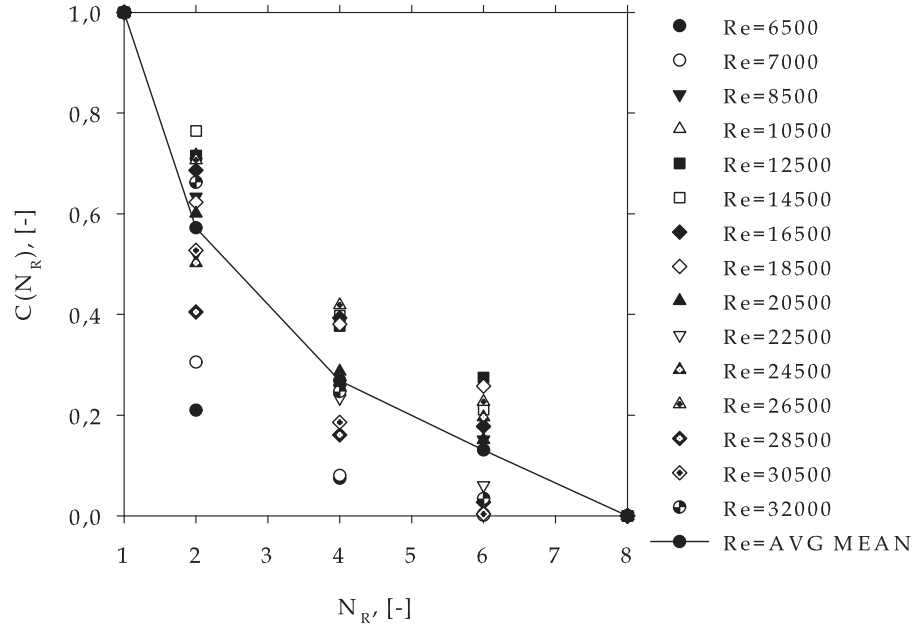


Figure 4.10.: Function  $C_{N_R}$  According to FRASZ, [15] at Different  $Re$ -Numbers

In Figure 4.11 the mean average values of  $K_{N_R}$  are compared with literature. Depending on the longitudinal pitch  $t_l$ , the heat transfer coefficient differs for various tube bundles. Thus, different values of  $K_{N_R}$  for a single tube row are obtained, compare values of e.g. STASIULEVICIUS [58] and FRASZ [15]. Considering this effect, WEIERMAN [72] and ESCOA<sub>TM</sub> in [16], stated their reduction coefficient in dependence of  $t_l/t_q$ . The coefficient of [58] was developed from measurements at solid finned-tubes. A very good agreement can be found for the values of the U-segmented finned-tubes and the correlation of FRASZ [15], which is valid for staggered tube layout with a bare tube diameter of 38 mm and the same tube pitch as in this work, denoted as Frasz<sub>1</sub>. Additionally, a more general equation is stated in [13], denoted Frasz<sub>2</sub> in the diagram. As seen, there ought to be a good congruence between the performed measurements



#### 4. Experimental and Numerical Results

and selected literature.

According to [15] and [29], the Nusselt number  $Nu_0^5$  for  $N_R$  consecutive tube rows,

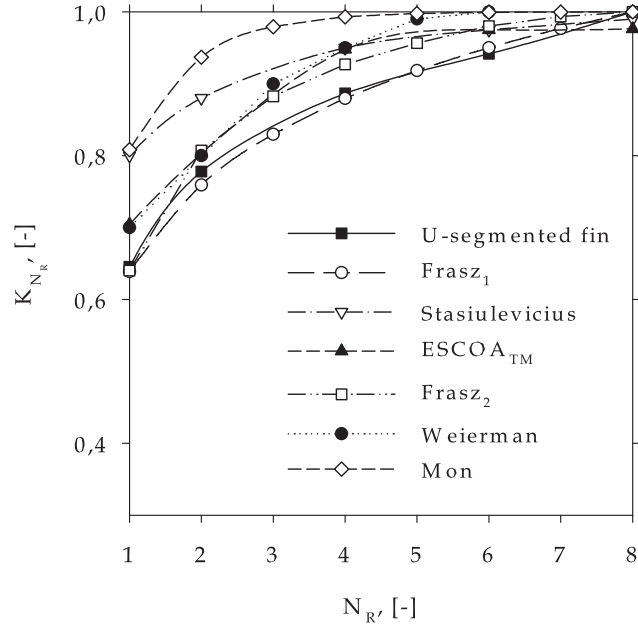


Figure 4.11.: Comparison of Row Correction Factor with Literature

with  $N_R$  less than 8 of the investigated U-fin tubes, is suggested to be correlated as follows:

$$\left. \begin{aligned} Nu_{0,N_R} &= Nu_{0,\infty} K_{N_R} \\ K_{N_R} &= 1 - 0.392 \log \left( \frac{N_{R,\infty}}{N_R} \right) \end{aligned} \right\}, \quad (4.3)$$

where  $\infty$  at  $N_R = 8$ .

---

<sup>5</sup>Calculated with the bare tube diameter

## 4.2. Global Consideration of the Numerical Results

The evaluation of the Nusselt number and the pressure drop coefficient is based on the calculation scheme exemplified in sections 2.6.1, 2.6.2, and 3.2.4. Therein the mass-averaged temperature  $T_{g2}$  at the "measuring" position is implemented, which is evaluated in Fluent © with

$$T_{g2} = \frac{\int T \rho \vec{u} d\vec{A}}{\int \rho \vec{u} d\vec{A}} = \frac{\sum_{i=1}^n T_i \rho_i \vec{u}_i \vec{A}_i}{\sum_{i=1}^n \rho_i \vec{u}_i \vec{A}_i} . \quad (4.4)$$

In Figure 4.12 the heat transfer results of the segmented finned-tube for global consideration are shown. The obtained values of the Nusselt number in case of the circular U-shaped fin, applying the RNG  $k - \epsilon$  and the standard  $k - \epsilon$  turbulence model are almost similar. No significant difference between the U-shaped and I-shaped modeled fin was analyzed within these global results. But the gathered values of the helical I-finned-tube *CFD*-model clearly shows a slight heat transfer enhancement compared to circular finned-tubes. This may be seen as an affect of the inclination of the spiral fin to the flow direction, which causes a velocity in  $z$ -coordinate and thus a fluid flow in normal direction of the fin.

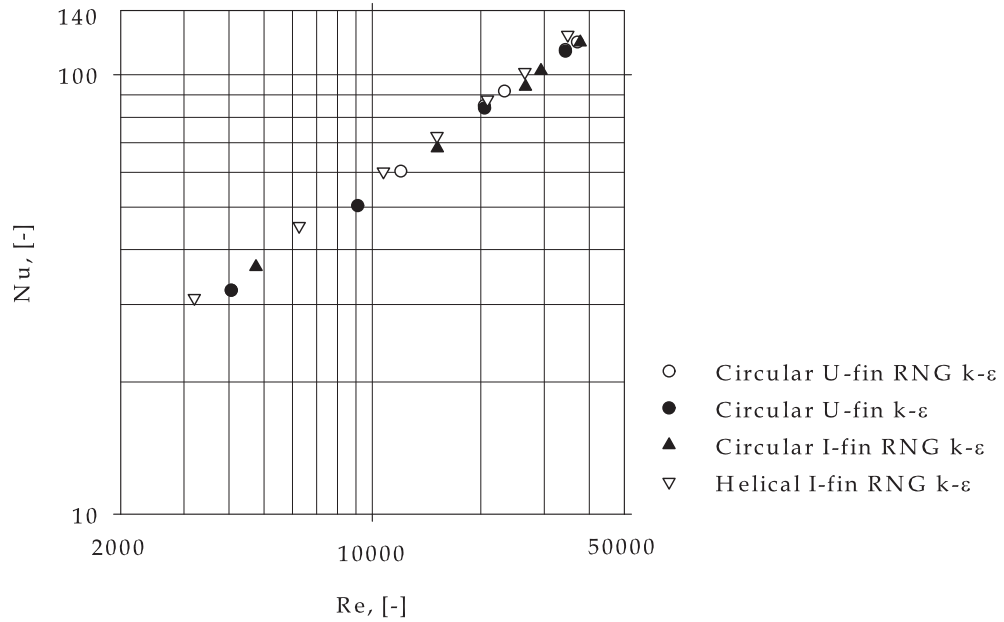


Figure 4.12.: Heat Transfer of a Single Segmented Finned-Tube Row in Cross-Flow

#### 4. Experimental and Numerical Results

However, this influence is low if the number of fins per meter is high, as it is the case in this study. Analogous to the temperature evaluation, the mass-averaged static and total pressure at the upstream and the downstream position of the investigated finned-section are defined as follows

$$p_{1,2} = \frac{\int p \vec{u} d\vec{A}}{\int \rho \vec{u} d\vec{A}} = \frac{\sum_{i=1}^n p_i \rho_i \vec{u}_i \vec{A}_i}{\sum_{i=1}^n \rho_i \vec{u}_i \vec{A}_i}, \quad (4.5)$$

but incompressible flow conditions are assumed. On the other hand, to overcome this flow transport in z-direction in case of the helically wound fin *CFD*-model, the pressure drop increases; compared to the circular fin. This is presented in Figure 4.13. As shown in the graph, the evaluated pressure drop coefficient for this single tube row bundle  $\xi_{1R}$  provides almost the same values for the circular fin models. For high *Re*-numbers, a difference between the RNG *k* –  $\epsilon$  and the standard *k* –  $\epsilon$  turbulence model is indicated to be observed. The global behavior of heat transfer

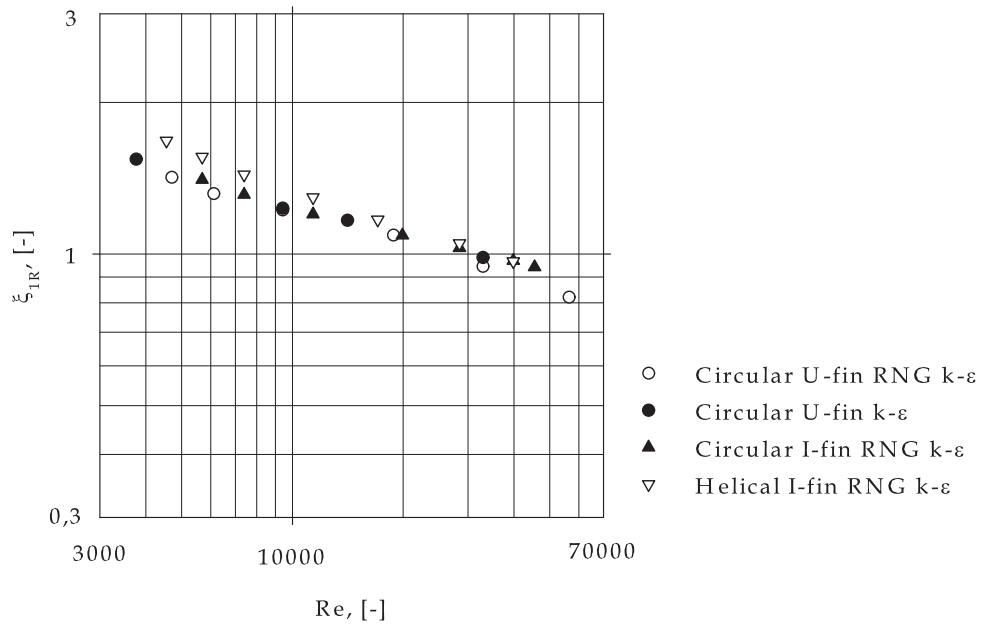


Figure 4.13.: Pressure Drop Coefficient of a Single Segmented Finned-Tube Row in Cross-Flow

from the solid finned-tube is shown in Figure 4.14. Between the analyzed helical and circular fin type no considerable difference can be observed. Yet, a slight variation in the evaluated Nusselt number between the circular model, applying a coarse grid,

#### 4. Experimental and Numerical Results

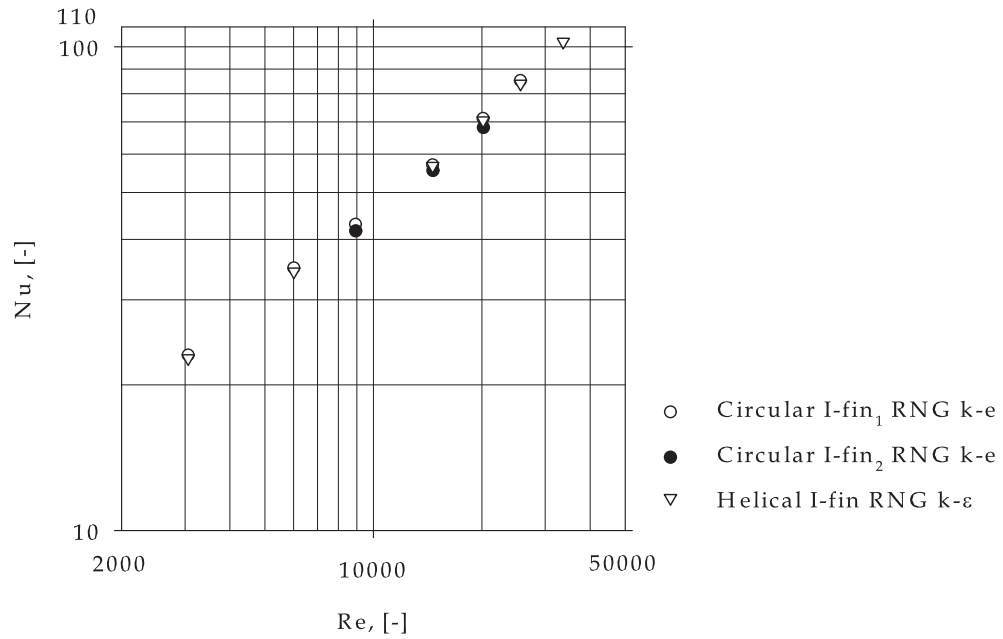


Figure 4.14.: Heat Transfer of a Single Solid Finned-Tube Row in Cross-Flow

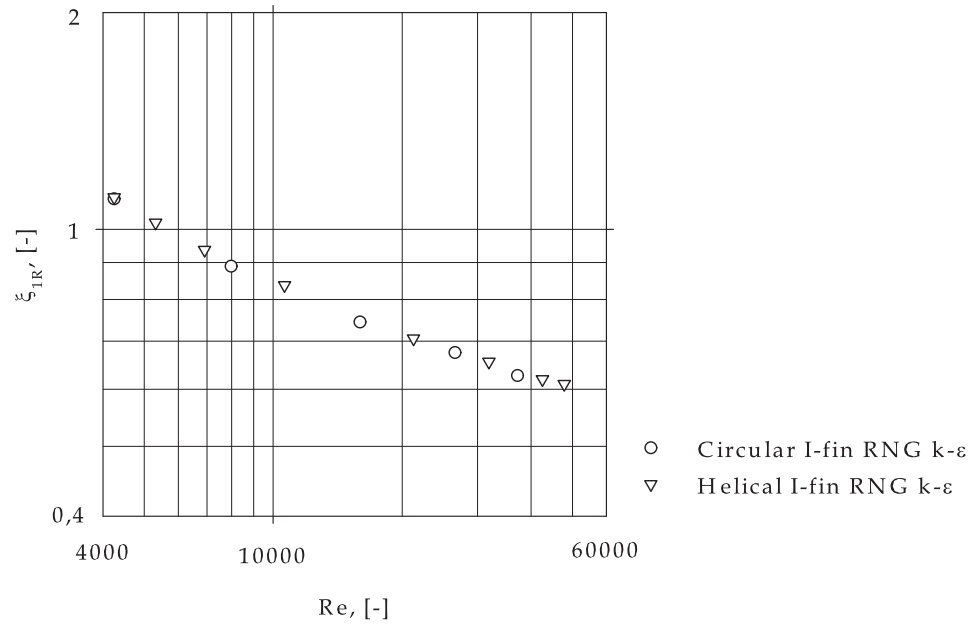


Figure 4.15.: Pressure Drop Coefficient of a Single Solid Finned-Tube Row in Cross-Flow

#### 4. Experimental and Numerical Results

which is denoted with  $\bullet$  and the same model applying a fine grid, denoted with  $\circ$ , can be observed. Generally, by comparing the dimensionless heat transfer coefficient within the analyzed  $Re$ -range in Figures 4.12 and 4.14, a heat transfer enhancement is achieved applying segmented finned-tubes with the same bare tube diameter as solid ones, although the fin height is different between the two  $CFD$ -models and the larger the fin height is, the smaller the heat transfer may be<sup>6</sup>. In Figure 4.15 the pressure drop coefficient for the different solid finned-tube models is depicted. For these cases, no difference may be evaluated within the  $Re$ -range of the generated  $CFD$ -models of the numerical simulation.

### 4.3. Comparison of Experiment and CFD-Simulation

The comparison of all gathered heat transfer data from measurements, performed on a single U-segmented finned-tube row in cross-flow, and the corresponding  $CFD$  calculation is presented in Figure 4.16. As seen, the calculated data set is within a narrow

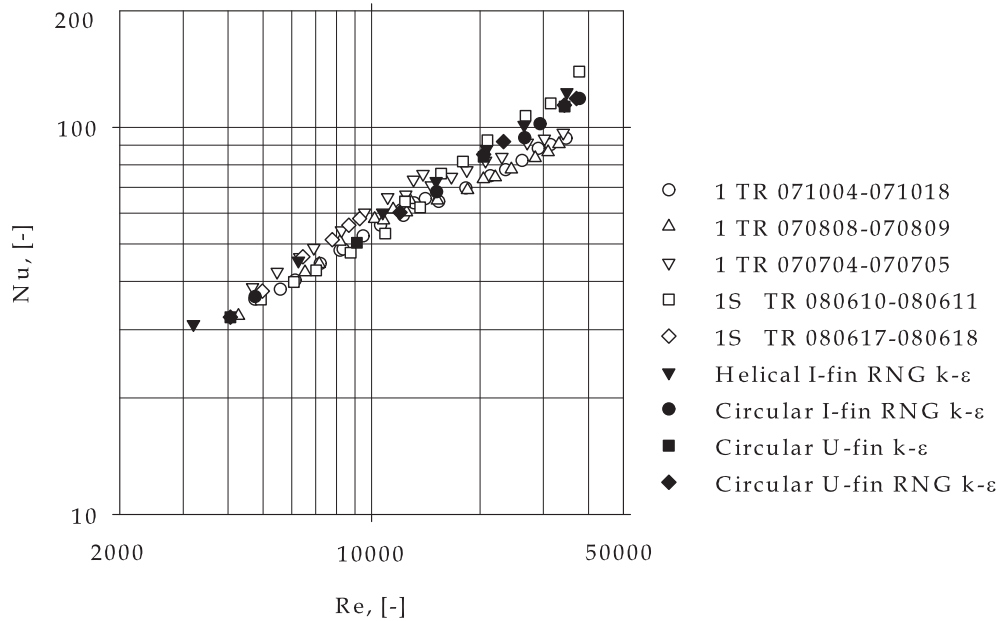


Figure 4.16.: Comparison of Experiment and  $CFD$  Simulation: Dimensionless Air-Side Heat Transfer Coefficient at Segmented Finned-Tubes

range<sup>7</sup> and arranged along a virtual straight line in the double logarithmic diagram

<sup>6</sup>As an effect from heat conduction considering the fin efficiency

<sup>7</sup>Within the calculated relative uncertainty of the heat transfer coefficient of the experiment

#### 4. Experimental and Numerical Results

with approximately same gradient. Comparing the evaluated Nusselt numbers from the measurements at a single tube row with a semi-tube installed at the channel wall<sup>8</sup>, denoted with "1S TR" and the simulation of helically wound finned-tube shows qualitatively an excellent agreement, with a small deviation. For completeness reasons, all performed simulations are considered here for a comparison with experiments. But again, no significant difference within the evaluated relative uncertainty range of  $\pm 15\%$  between circular simulations and experiment may be found.

A qualitative and quantitative pressure drop coefficient comparison of the experiment at 8 tube rows (evaluated for a single tube row) with the *CFD*-calculations shows good agreement especially in the  $Re$ -range of about  $6000 \leq Re \leq 20000$ , refer to Figure 4.17. Here, the evaluated pressure drop coefficients of measurement and simulation are quite close together, while for higher Reynolds numbers than 20000 up to 50000 a diverging effect seems to be detected. Also, for  $Re \leq 6000$  the values for the pressure drop calculated from the simulation are smaller than those obtained from the measurement. Generally, the calculated  $\xi$  from the *CFD*-simulations of the helical fin-tube shows better agreement with measurement than the circular ones.

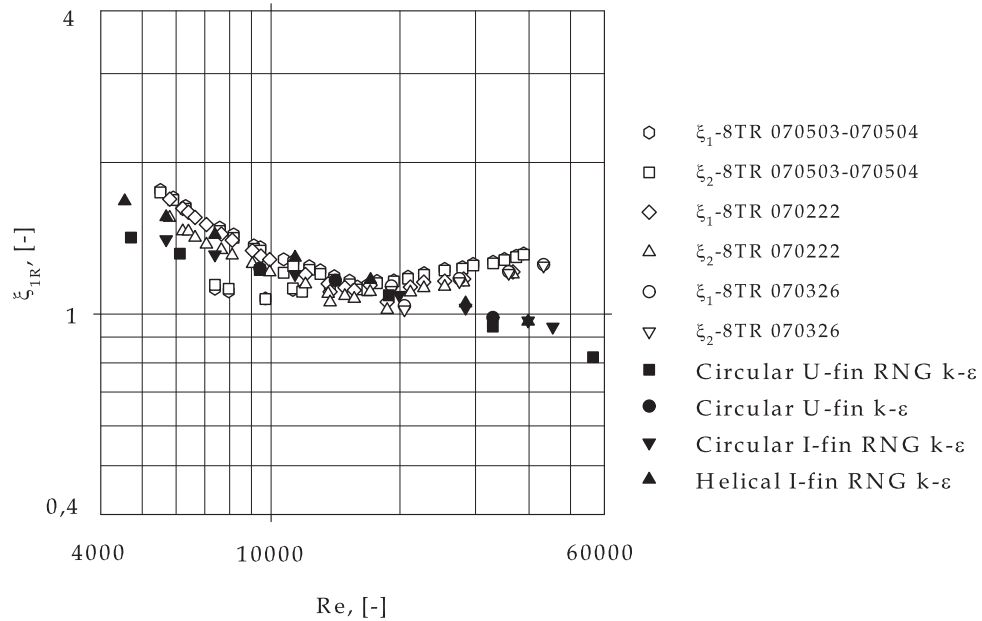


Figure 4.17.: Comparison of Experiment and *CFD* Simulation: Pressure Drop Coefficient at Segmented Finned-Tubes

In the steady-state *CFD*-simulations no inclination and deformation of the individ-

<sup>8</sup>This provides almost same effect to symmetry boundaries of the computational domain

#### 4. Experimental and Numerical Results

ual fin segments from the steel strip, see Figure A.1(b), due to manufacturing, and no especially chosen surface roughness for the fin and the tube (hydraulic smooth) is considered, which occurs at the finned-tube in reality. The contact face between fin and tube is assumed to provide no thermal resistance (perfectly welded) and the tube in the channel is arranged exactly, facing fin tip on fin tip in transversal direction, as well as no bypass effect is considered due to periodic or symmetry calculation boundary conditions. Additionally, it should be mentioned that the "evaluation" plane of the gathered results from simulation is placed as accurately as possible to the real measurement plane. Possible fluid flow effects, as flow separation and periodic repeating (oscillating) effects have not been detected in the applied measurement technique at 8 tube row configuration. By taking into account all the afore mentioned effects, it could be concluded that the obtained results from the comparison of all gathered data, considering the relative measurement uncertainty of the experiments, show good agreement.

A comparison of the *CFD*-calculations and measurements performed at 8 consecutive staggered arranged spiral solid finned-tube rows is depicted in Figure 4.18. All measurement values of this configuration with the transversal and longitudinal tube pitch, bare tube diameter, and fin geometry, being equal in this work, are taken from FRASZ, refer to Table C.1. For the evaluation of the heat transfer at a single tube row, the row correction factor  $K_{N_{R,(Frasz1)}} \approx 0.638$  was chosen, see Figure 4.11. As seen in Figure 4.18, a good congruence can be found between the obtained results. Yet in the whole *Re*-range, the *CFD*-calculations would predict slightly higher dimensionless heat transfer coefficients than the evaluated measurement values; and this effect is increased if the difference of  $F_{min}$  between simulation and measurement is considered. However, this corresponds to the pressure drop coefficient comparison, depicted in Figure 4.19. Generally, the simulation results tend to have lower pressure drop coefficients than the measurements. In the evaluation of the pressure drop coefficient, the minimum net free area between a tube row has to be considered. In case of the calculated results from the measurement this is evaluated with  $F_{min,meas} = 0.23421 \text{ m}^2$ . On the other hand, due to symmetry and periodic boundary conditions of the computational domain, the net free projected flow area is calculated with  $F_{min,CFD} = 0.20361 \text{ m}^2$ , which has a relative difference of about 13%. As seen in the diagram, both the converted pressure drop measurements <sup>9</sup> from measurement at augmented temperature conditions at the channel wall  $\zeta_1$  as well as in the flow channel center  $\zeta_2$  show high scattering. The non validated converted results from measurement at ambient temperature conditions show less scattering, but high deviations compared to simulations especially at low Reynolds numbers. It should also be mentioned here that all converted results do not reflect exactly the measurement conditions, thus carefulness when judging the obtained results has to be paid. Additionally, for comparison rea-

<sup>9</sup>Conversion for both, the *Re*-number  $Re_0$  as well as the pressure drop coefficient  $\zeta$

#### 4. Experimental and Numerical Results

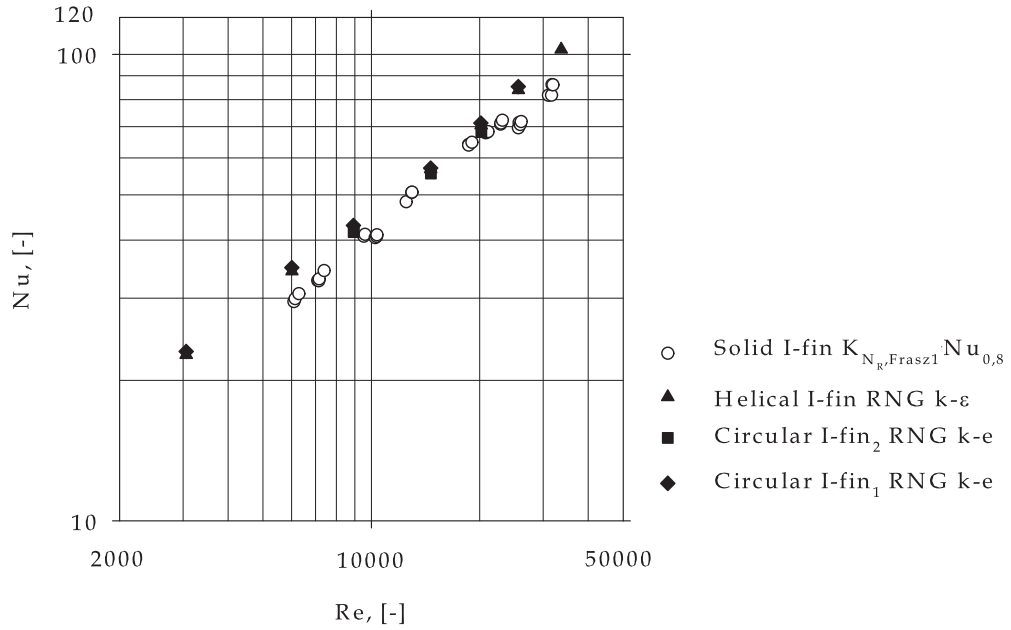


Figure 4.18.: Comparison of Experiment and CFD Simulation: Dimensionless Air-Side Heat Transfer Coefficient at Solid Finned-Tubes

sons, a correlation of FRASZ [14] is considered here, which is a modified form of the equation of STASIULEVICIUS [58], valid for solid spiral finned-tubes. As a comparison of this equation with literature in [14] shows, the evaluated pressure drop coefficients are situated in the upper range among the other calculated values of  $\zeta$ . Considering the fact of the relative difference of  $F_{min}$  between the simulation and measurement, any possible solutions of the CFD calculations could be placed among the results obtained from the  $\zeta$ -correlation of FRASZ.

#### 4.4. Dimensional Analysis of the Investigated Heat Transfer and Pressure Drop Problem

Similarity of physical phenomena is a powerful approach to model the behavior of e.g. heat transfer and fluid flow at finned-tubes in cross-flow in forced-convection. Dimensional analysis provides a mathematical modeling method to formulate the characteristics of an equation for complex quantities of engineering applications. The basis of this approach is the BUCKINGHAM II-Theorem, which provides the potentiality to characterize a complex physical behavior, using a finite number of non-dimensional products.



#### 4. Experimental and Numerical Results

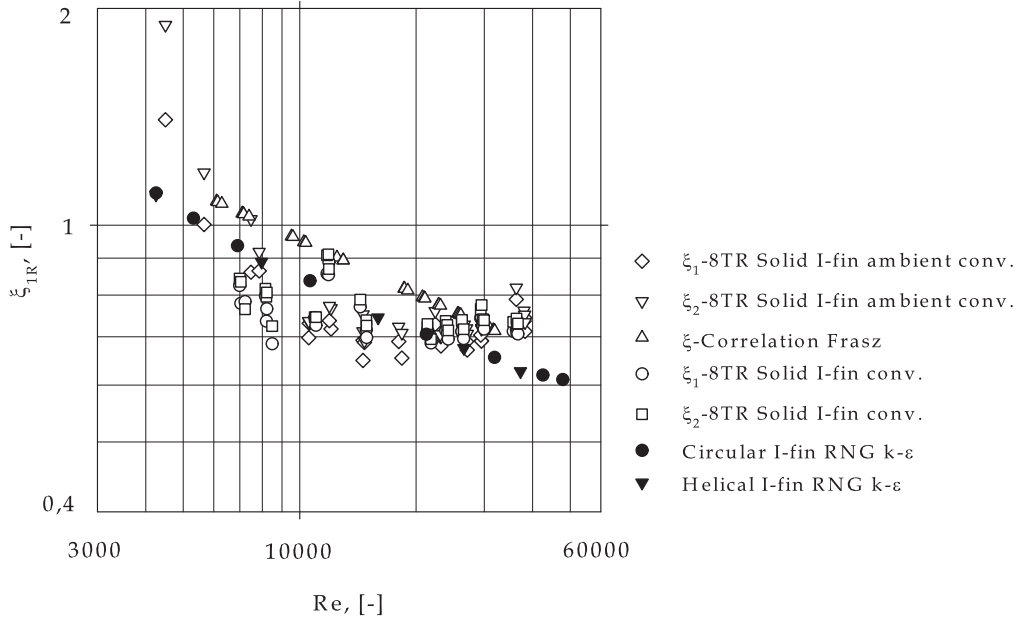


Figure 4.19.: Comparison of Experiment and *CFD* Simulation: Pressure Drop Coefficient at Solid Finned-Tubes

##### 4.4.1. Correlations of Dimensionless Heat Transfer Coefficient

In the following the gas-flow is considered at steady state conditions and assumed to be incompressible. Here, for the heat transfer examination, all thermo-physical properties are related to the average mean temperature between inlet and outlet  $\vartheta_{gm}$ . The initial step of the dimensional analysis is the characterization of the relevant variables describing the investigated problem, according to [41]. For this case, the heat transfer coefficient as function of

$$\alpha_{gm} = f(\lambda_{gm}, u_{gm}, \rho_{gm}, \nu_{gm}, c_{p_{gm}}, d_a, h, s, t) \quad (4.6)$$

is considered. In Table 4.1, the units of the 10 relevant variables (parameters) are specified, with their 4 individual base units. The rank of the dimensional matrix  $A$  calculates for 6 dimensionless power products, describing the heat transfer behavior of the finned-tube in forced convection. Applying the  $\Pi$ -Theorem, the given problem states as follows:

$$F(\Pi_1, \Pi_2, \Pi_3, \Pi_4, \Pi_5, \Pi_6) = 0, \quad (4.7)$$

with

$$\Pi = \alpha_{gm}^{k_1} \lambda_{gm}^{k_2} u_{gm}^{k_3} \rho_{gm}^{k_4} \nu_{gm}^{k_5} c_{p_{gm}}^{k_6} d_a^{k_7} h^{k_8} s^{k_9} t^{k_{10}}. \quad (4.8)$$

#### 4. Experimental and Numerical Results

Table 4.1.: Relevant Variables for Heat Transfer Specification

Variable	Unit	Specification	M	L	T	$\Theta$
Heat Transfer Coefficient	$\frac{kg}{s^3K}$	$\alpha_{gm}$	1	0	-3	-1
Thermal Conduction	$\frac{kgm}{s^3K}$	$\lambda_{gm}$	1	1	-3	-1
Gas Velocity	$\frac{m}{s}$	$u_{gm}$	0	1	-1	0
Density	$\frac{kg}{m^3}$	$\rho_{gm}$	1	-3	0	0
Kinematic Viscosity	$\frac{m^2}{s}$	$\nu_{gm}$	0	2	-1	0
Specific Heat Capacity	$\frac{m^2}{s^2K}$	$c_{p_{gm}}$	0	2	-2	-1
Tube Diameter	$m$	$d_a$	0	1	0	0
Average Fin Height	$m$	$h$	0	1	0	0
Average Fin Thickness	$m$	$s$	0	1	0	0
Fin Pitch	$m$	$t$	0	1	0	0

The solution of the system of equations

$$A \cdot [k_1, k_2, k_3, k_4, k_5, k_6, k_7, k_8, k_9, k_{10}]^T = \mathbf{0}, \quad (4.9)$$

with

$$A = a_{jk} \begin{cases} k = 1, \dots, n = 10 \\ j = 1, \dots, m = 4 \end{cases}, \quad (4.10)$$

are the exponents in Equation (4.7). The 6 dimensionless products for the given problem are

$$\begin{aligned} \Pi_1 &= \frac{\alpha_{gm} d_a}{\lambda_{gm}} = Nu & \Pi_4 &= \frac{h}{d_a} \\ \Pi_2 &= \frac{u_{gm} d_a}{\nu_{gm}} = Re & \Pi_5 &= \frac{s}{d_a} \\ \Pi_3 &= \frac{\rho_{gm} \nu_{gm} c_{p_{gm}}}{\lambda_{gm}} = Pr & \Pi_6 &= \frac{t}{d_a} \end{aligned} \quad (4.11)$$

Thus, Equation (4.7) is evaluated with:

$$F_n(\alpha_{gm}, \lambda_{gm}, u_{gm}, \rho_{gm}, \nu_{gm}, c_{p_{gm}}, d_a, h, s, t) \Leftrightarrow F\left(Nu, Re, Pr, \frac{h}{d_a}, \frac{s}{d_a}, \frac{t}{d_a}\right) \quad (4.12)$$

Hence follows the  $Nu$ -number at finned-tubes in cross-flow, which is correlated in formulation of a power law with terms related to the characteristic length for the consideration of geometry parameters; compare with Equation (2.44).

$$Nu = C Re^m Pr^n \left(\frac{h}{d_a}\right)^o \left(\frac{s}{d_a}\right)^p \left(\frac{t}{d_a}\right)^q \quad (4.13)$$

#### 4. Experimental and Numerical Results

Considering the two different geometries of the I/U-shaped segmented finned-tubes (for specification see Tables 2.3 and C.1), the following approach gives

$$Nu = C O \left( \frac{h}{d_a} \right) P \left( \frac{s}{d_a} \right) Q \left( \frac{t}{d_a} \right) Re^m Pr^n = C_1 Re^m Pr^n, \quad (4.14)$$

where

$$\left. \begin{aligned} O \left( \frac{h}{d_a} \right) &= C_h \left( \frac{h_{I/U}}{d_a} \right)^{-0.007} \approx C_h \\ P \left( \frac{s}{d_a} \right) &= C_s \left( \frac{s_{I/U}}{d_a} \right)^{0.008} \approx C_s \\ Q \left( \frac{t}{d_a} \right) &= C_t \left( \frac{t_{R,I/U}}{d_a} \right)^{0.026} \approx C_t \end{aligned} \right\}$$

are extended factors in the correlation, supplementing the influence of  $h$ ,  $s$ , and  $t$ . In Figure 4.20 the evaluated results of measurement at segmented I-shaped as well as U-shaped finned-tubes and the calculated regressions are presented. As seen in the diagram, the calculated overall regression including I-shaped and U-shaped finned-tubes is slightly different compared to the regression with the approach evaluated according to Equation (4.13). Two different geometries are considered for calculating the correlations  $O$ ,  $P$ , and  $Q$ , therefore these functions do not account exactly for its influence. As evaluated, the exponent in the geometry functions  $O$ ,  $P$ , and  $Q$  is very small, thus the effect of these additional terms is not of real significance and is therefore neglected. However, by comparing  $C_1$  of both correlations it can be seen that the  $Nu$ -number difference between this two equations is roughly  $\approx 5\%$ .

In order to have a better agreement at measurement and simulation, the heat transfer at segmented finned-tubes at staggered layout at constant  $Pr$  is suggested to be empirically correlated with the following equation:

$$Nu_{0,N_R} = 0.36475 \cdot Re^{0.6013} Pr^{1/3} \left[ 1 - 0.392 \log \left( \frac{N_{R,\infty}}{N_R} \right) \right], \quad (4.15)$$

within the range of validity

$$\left. \begin{aligned} Pr &\approx 0.71 \\ 4500 &\leq Re \leq 35000 \\ 15.5 \text{ mm} &\leq h \leq 20 \text{ mm} \\ 0.8 \text{ mm} &\leq s \leq 1.0 \text{ mm} \\ 1/295 &\leq t \leq 1/276 \text{ fins/m} \\ 1 &\leq N_R \leq 8 \end{aligned} \right\}.$$

A comparison of the proposed equation for the Nusselt number and the simulation as well as most measurement results are found to be accurate within about  $\pm 15\%$ , as presented in Figure 4.21.

#### 4. Experimental and Numerical Results

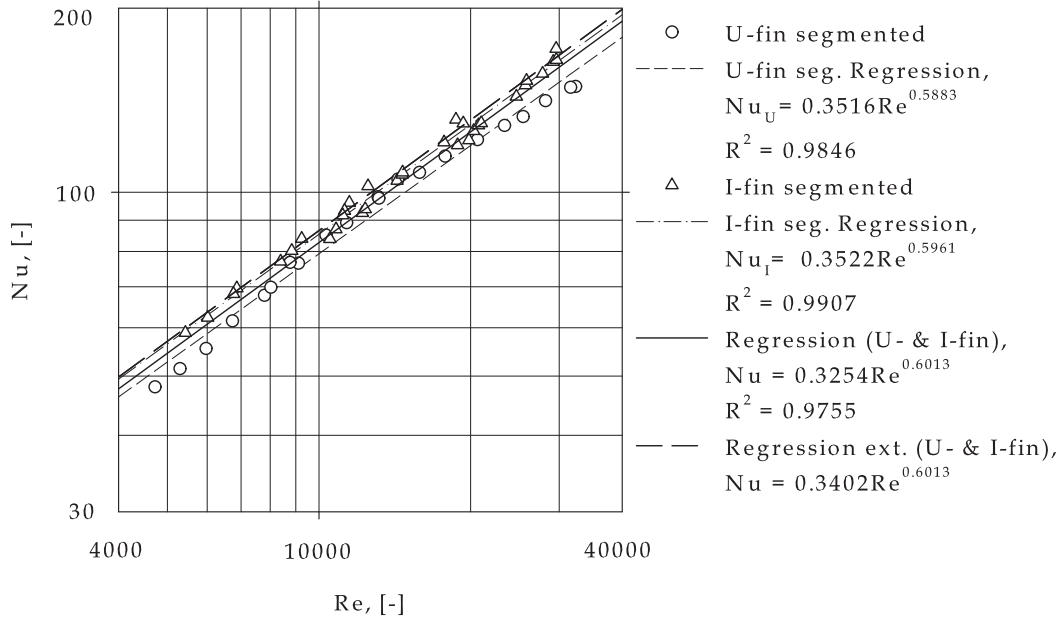


Figure 4.20.: Regression of Heat Transfer at 8 Segmented Finned-Tube Rows

The deviation between 50% of all measurement results and Equation (4.15) are correlated within  $\pm 5\%$ , 80% of all measurement results are within  $\pm 10\%$ , and 90% are within  $\pm 15\%$ , see Figure 4.22.

##### 4.4.2. Correlations of Pressure Drop Coefficient

Between momentum transfer and heat transfer an analogy exists. The formulation of these interactions between friction and convection of a flow in a tube is described by the REYNOLDS-analogy, which is based on measurements at turbulent flow conditions. The momentum and heat transfer are related using the following equation, which was first introduced by REYNOLDS as stated in [21] and reads as

$$\frac{\dot{q}}{\rho u_{\tau} c_p \vartheta} \equiv \frac{\alpha}{\rho u_{\tau} c_p} \equiv \frac{Nu}{Re Pr} \equiv St = \frac{\tau_w}{\rho u_{\tau}^2}. \quad (4.16)$$

Therein,  $\dot{q}$  is the heat flux,  $\tau_w$  the wall shear stress and  $\alpha$  the external heat transfer coefficient, valid near the wall. Introducing the fanning friction factor  $f_f$ , which is widely-used in American literature, according to [21], gives

$$St = \frac{\xi}{8} = \frac{f_f}{2}. \quad (4.17)$$

#### 4. Experimental and Numerical Results

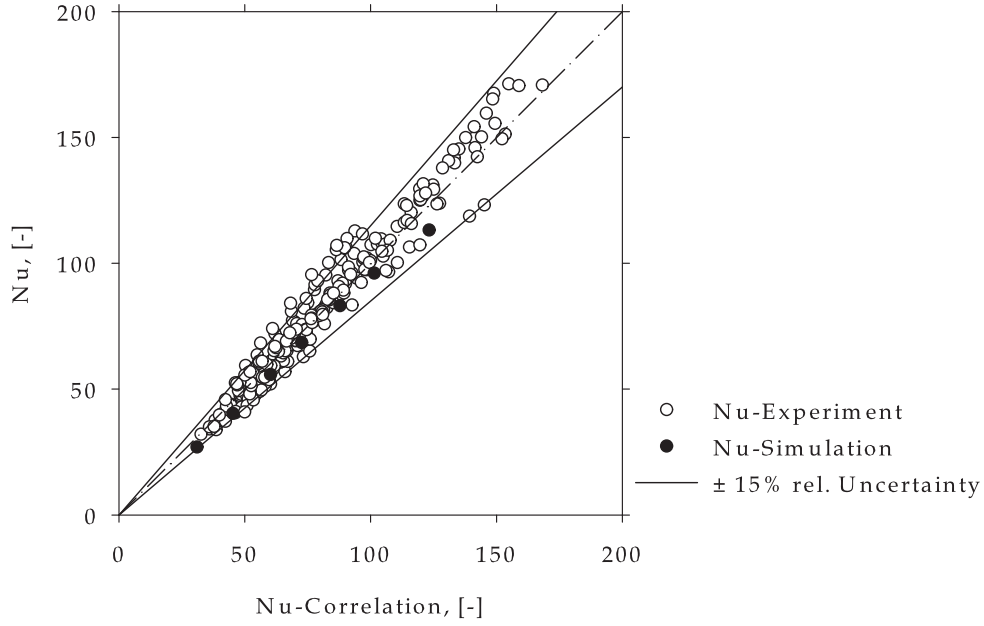


Figure 4.21.: Comparison between  $Nu$ -Correlation (4.15) and Experimental/Simulation at Segmented U/I-Shaped Finned-Tubes

An approximate combination<sup>10</sup> with limited range of validity of the dimensionless groups  $StPr^{2/3}$ <sup>11</sup>, well known in literature e.g. [71], [2], is denoted as the COLBURN-factor  $j$ , which applies the analogy from heat, momentum, and mass transfer, and is valid for turbulent flow conditions (approximately  $Pr > 0.7$  and  $Re > 10000$ ). This analogy may also be found in literature as the modified REYNOLDS-analogy or CHILTON-COLBURN-analogy. For the description of the pressure drop behavior of finned-tubes in cross-flow, all relevant variables have to be defined, [41]. Thus, the pressure drop coefficient is a function of

$$\xi = g(u_E, v_{gm}, F_{min}, t_l, t_q, d_a). \quad (4.18)$$

In Table 4.2, the units of the 7 input parameters are specified. Considering 2 individual base units, the rank of the dimensional matrix  $A$  calculates for 5 dimensionless power products.

For the given problem, the  $\Pi$ -Theorem states as follows

$$G(\Pi_1, \Pi_2, \Pi_3, \Pi_4, \Pi_5) = 0, \quad (4.19)$$

<sup>10</sup>This analogy will be later on used for the performance evaluation of different heat exchangers

<sup>11</sup>Is equal to  $\frac{Nu}{RePr^{1/3}}$

#### 4. Experimental and Numerical Results

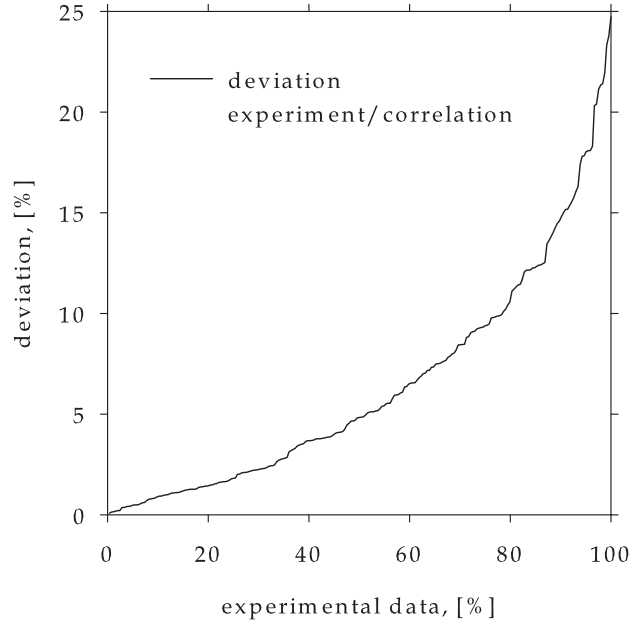


Figure 4.22.: Deviation between  $Nu$ -Correlations and Experimental Results

with

$$\Pi = u_E^{k_1} \nu_{gm}^{k_2} F_{min}^{k_3} t_l^{k_4} d_a^{k_5} \zeta^{k_6}. \quad (4.20)$$

Using the system of equations

$$\mathbf{A} \cdot [k_1, k_2, k_3, k_4, k_5, k_6, k_7]^T = \mathbf{0}, \quad (4.21)$$

with

$$\mathbf{A} = a_{jk} \begin{cases} k = 1, \dots, n = 7 \\ j = 1, \dots, m = 2 \end{cases}, \quad (4.22)$$

the 5 dimensionless products may be defined with:

$$\begin{aligned} \Pi_1 &= \frac{u_E d_a}{\nu_{gm}} = Re & \Pi_3 &= \frac{F_{min}}{d_a^2} \\ \Pi_2 &= \zeta & \Pi_4 &= \frac{t_l}{d_a} \\ & & \Pi_5 &= \frac{t_q}{d_a} \end{aligned} \quad (4.23)$$

Furthermore, the pressure drop of finned-tubes in cross-flow is evaluated with:

$$G_n(\zeta, u_E, \nu_{gm}, F_{min}, t_l, t_q, d_a) \Leftrightarrow G\left(Re, \zeta, \frac{F_{min}}{d_a^2}, \frac{t_l}{d_a}, \frac{t_q}{d_a}\right) \quad (4.24)$$

#### 4. Experimental and Numerical Results

Table 4.2.: Relevant Variables for Pressure Drop Specification

Variable	Unit	Specification	M	L	T	$\Theta$
Gas Velocity	$\frac{m}{s}$	$u_E$	0	1	-1	0
Kinematic Viscosity	$\frac{m^2}{s}$	$\nu_{gm}$	0	2	-1	0
Net Free Area of Tube Row	$m^2$	$F_{min}$	0	2	0	0
Longitudinal Tube Pitch	$m$	$t_l$	0	1	0	0
Transversal Tube Pitch	$m$	$t_q$	0	1	0	0
Tube Diameter	$m$	$d_a$	0	1	0	0
Pressure Drop Coefficient	1	$\zeta$	0	0	0	0

Finally, the pressure drop coefficient may be correlated in its general formulation with 5 dimensionless products in form of:

$$\zeta_{N_R} = N_R Z Re^t \left( \frac{F_{min}}{d_a^2} \right)^u \left( \frac{t_l}{d_a} \right)^v \left( \frac{t_q}{d_a} \right)^w, \quad (4.25)$$

where  $t_l$ ,  $t_q$ , and  $F_{min}$  are considered to account for the geometrical arrangement of the tubes within the bundle.

Both, the I-shaped and the U-shaped finned-tube bundles are arranged at equal longitudinal and transversal tube pitch. As later on presented, the measurements at I-shaped finned-tubes in the range of low  $Re$ -numbers exhibit high measurement uncertainties, see Figure 4.32(a). Thus, a specific correlation is developed simply for measurement results at U-shaped finned-tube bundles; the approach states as follows:

$$\zeta_{N_R} = N_R Z Re^t = N_R \left[ a_{hy} + \frac{b_{hy}}{Re} + \frac{c_{hy}}{Re^2} \right] = N_R [a_{po} + b_{po} Re^{c_{po}}]. \quad (4.26)$$

The evaluated coefficients of the correlations are given in Table 4.3.

Table 4.3.: Coefficients of Regressions

Function	Shortcut	a	b	c
Hyperbola	hy	1.3550	-7189.7055	55970438.4750
Power(a,b,c)	po	1.1321	148575379605.4982	-3.0312

In Figure 4.23 all results of measurements at ambient temperature conditions as well as the calculated regressions within the investigated  $Re$ -range are presented. As seen, the overall regressions are slightly different at high  $Re$ -numbers, but in better

#### 4. Experimental and Numerical Results

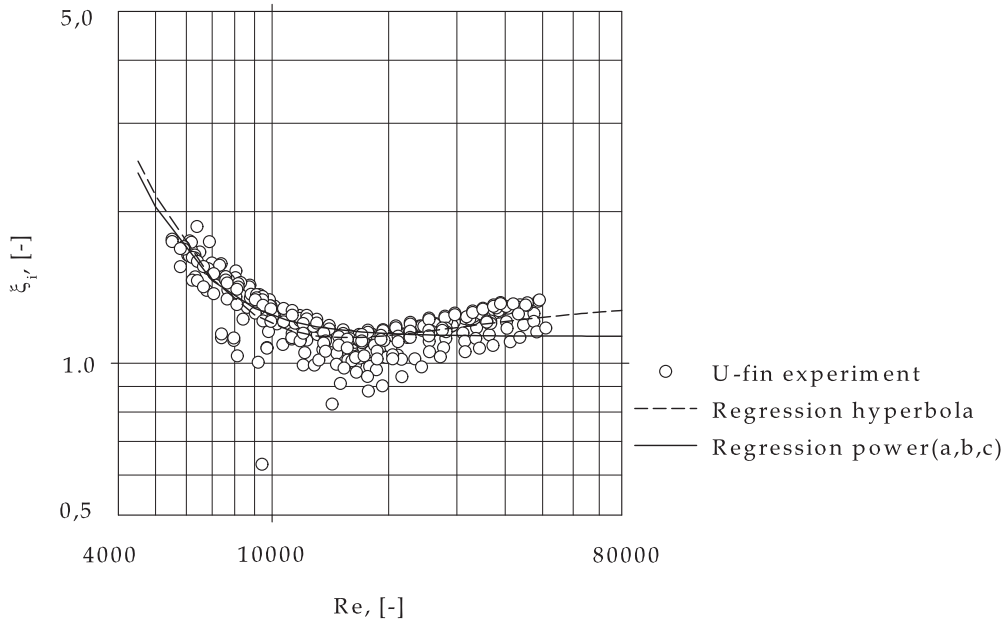
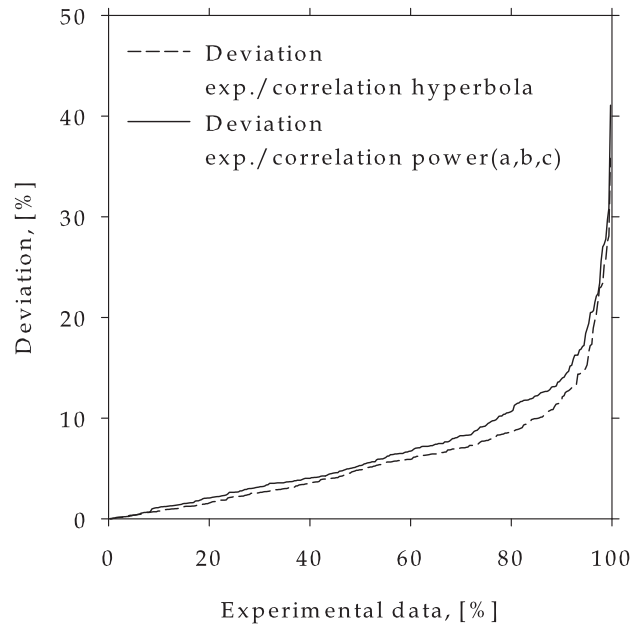


Figure 4.23.: Regression of Pressure Drop Coefficient at 8 Segmented Finned-Tube Rows

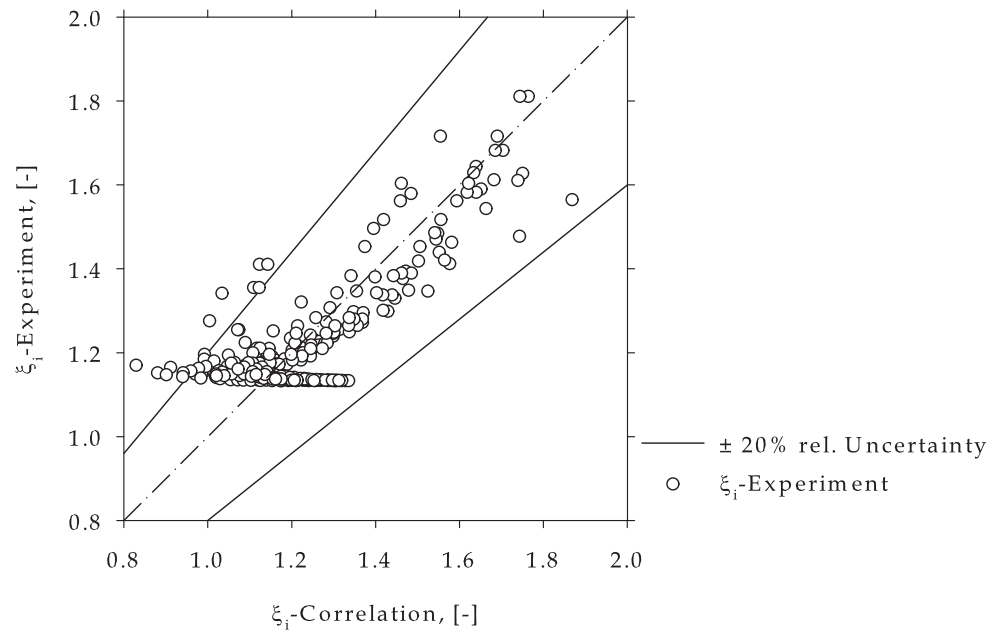
agreement to literature an improved power law approach is chosen rather than a hyperbola function. A comparison of the measurement/correlation deviations from the hyperbola and power law function shows no significant difference, see Figure 4.24(a). The average deviation between 50% of all measurement results and both correlations, Equation (4.26), is evaluated within approximately  $\pm 5\%$ , 80% of all measurement results are within about  $\pm 10\%$ , and 90% are within  $\pm 13\%$ . It is suggested to empirically correlate the pressure drop coefficient from a tube bundle, valid for a single tube row at segmented finned-tubes within the  $Re$ -range of  $4500 \leq Re \leq 50000$ , using the improved power law function. A comparison of the proposed equation and most experimental results are found to be accurate within about  $\pm 20\%$ , as presented in Figure 4.24(b).



#### 4. Experimental and Numerical Results



(a) Deviation between  $\xi$ -Correlations and Experimental Results



(b)  $\xi$ -Comparison between Correlation (4.26) and Experiment

Figure 4.24.: Comparison of Pressure Drop Coefficient Correlations with Experimental Data

#### 4.4.3. Data Comparison with Literature

The correlations developed above (Equation (4.15) and (4.26)) are valid in general for segmented fin tubes in cross-flow at staggered layout. Figures 4.25(a) and 4.25(b) show a comparison of the heat transfer with literature based on a tube bundle, utilizing eight tube rows; the geometrical data is taken from Table 2.3. Apart from the fact to keep exactly the range of validity of each individual equation in the course of the comparison, some correlations are developed for solid finned-tubes. Hence, this comparison should present more or less a qualitative as well as quantitative survey. All of these correlations along with their scope of validity are described in open literature. Most correlations in literature are related to the bare tube diameter. If the wetted length, equivalent diameter in volume, or hydraulic diameter is used as the characteristic length, both the  $Nu$ -number and the  $Re$ -number have to be converted.

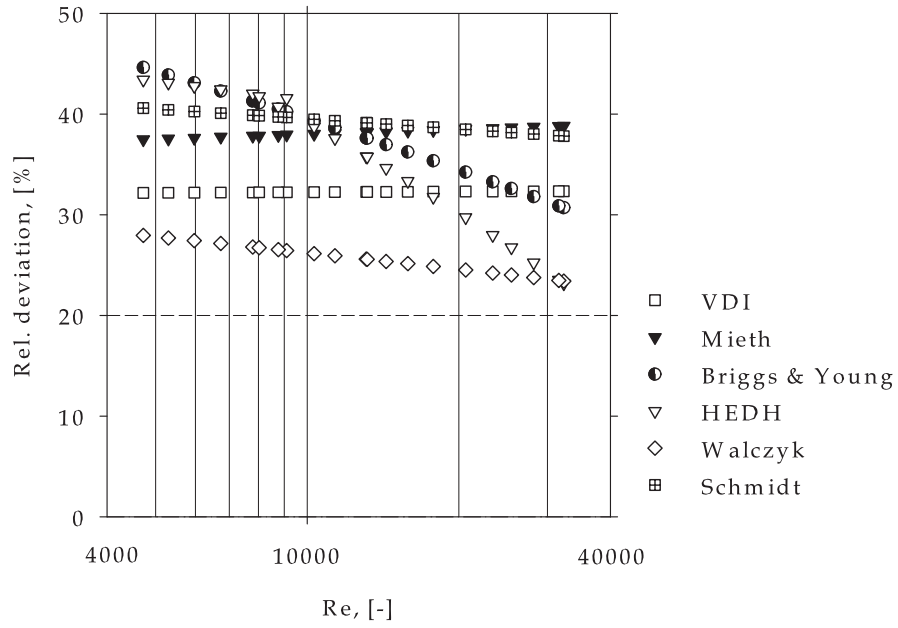
Generally, by comparing the developed correlation with literature of solid finned-tubes, see Figure 4.25(a), higher Nusselt numbers are expected. According to SCHMIDT [56], in terms of significance, the bare tube diameter as the characteristic length for determining heat transfer is taken into account. The correlation is evaluated from a large number of test cases, mostly with annular solid fins, which leads to lower heat transfer coefficients than with spiral fins. This heat transfer correlation is valid for an evaluated measurement uncertainty of about  $\pm 25\%$ ,  $1000 \leq Re \leq 40000$ ,  $5 \leq \frac{A_{tot}}{A_t} \leq 12$ , and  $N_R \geq 3$  consecutively arranged tube rows. As remarked in [14] and [56] in this case  $A_{tot}$  is the entire gas-affected heating surface per  $m$  tube;  $A_t$  represents the heating surface of the bare tube per  $m$ . More or less the equations of BRIGGS & YOUNG [5], WALCZYK [69], VDI [1], HEDH [27], and MIETH [45] according to [4] are apparently valid for solid fins. Thus, a difference in heat transfer between solid and segmented fins of roughly 20% is expected, see Section 4.5.1, which may be interpreted by comparing Figure 4.25(a) and 4.25(b). The correlation of the VDI Heat atlas, 10<sup>th</sup> edition, [1], seems to be valid for solid as well as segmented fins and for  $N_R \geq 4$  consecutively arranged tube rows. In case of  $N_R = 3$  tube rows the constant  $C$  in the power law evaluates for 0.36, and if  $N_R = 2$  the constant follows to 0.33. This heat transfer correlation is valid for an evaluated measurement uncertainty of about  $\pm 10\%$  to  $\pm 25\%$ ,  $1000 \leq Re \leq 100000$ ,  $5 \leq \frac{A_{tot}}{A_t} \leq 30$ . Further details are found in [1].

In open literature just a few equations are explicitly defined to be valid for segmented fins, e.g. WEIERMAN [72], KAWAGUCHI [35], and ESCOA<sub>TM</sub>/ESCOA<sub>TM</sub>-REVISED in [16]. By comparing these results with Equation (4.15), a smaller relative deviation of approximately  $\pm 20\%$  is found. However, the correlations of KAWAGUCHI [35] and Ross in [4]<sup>12</sup> would pronounce effective higher heat transfer at high  $Re$ -numbers. The relative deviation of the ESCOA<sub>TM</sub>-correlation is more or less constant ( $\approx 10\%$ ) within

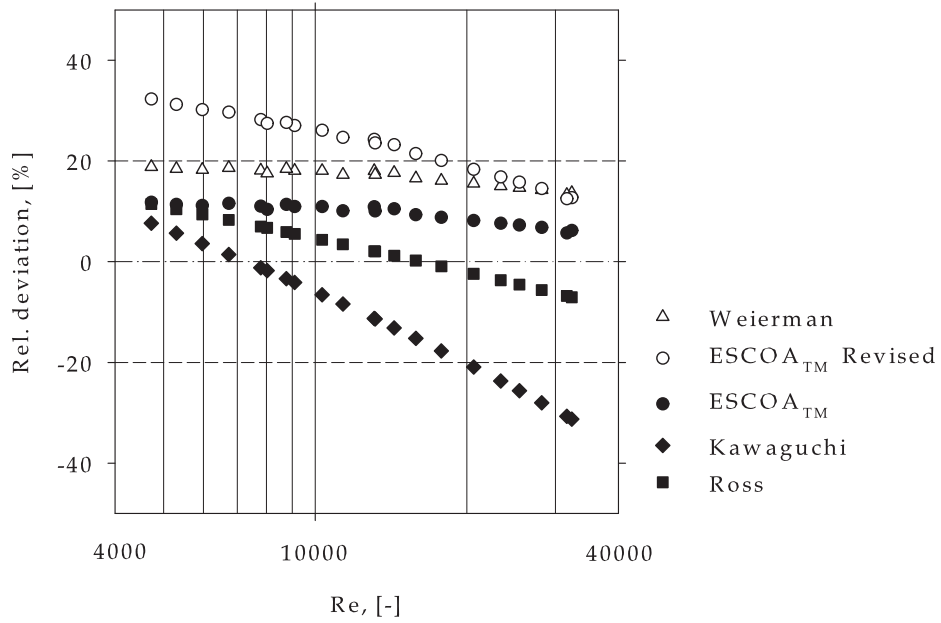
---

<sup>12</sup>Ross' equation is based on stud fins

#### 4. Experimental and Numerical Results



(a) VDI [1], Mieth [45], Briggs & Young [5], HEDH [27], Walczyk [69], and Schmidt [56]



(b) Weierman [72], ESCOA<sub>TM</sub>/ESCOA<sub>TM</sub> – Revised in [16], Kawaguchi [35], and Ross in [4]

Figure 4.25.: Comparison of Heat Transfer Corr. with Literature, Based on Geometrical Data of Helically U-shaped Finned-Tubes,  $\frac{Nu_{Eq.(4.15)} - Nu}{Nu_{Eq.(4.15)}} \cdot 100\%$

#### 4. Experimental and Numerical Results

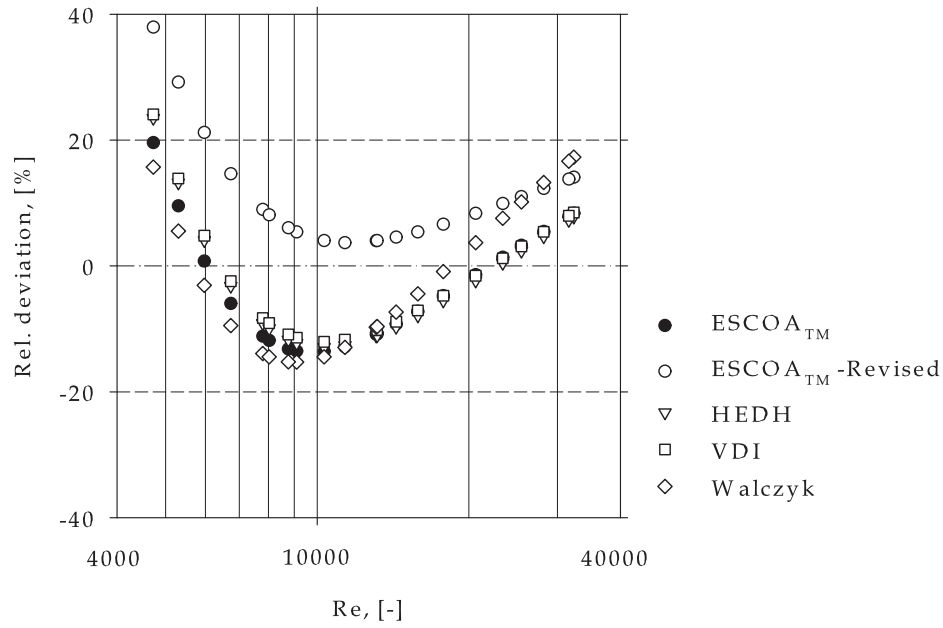
the investigated  $Re$ -range, indicating approximately the same gradient. The basis of these equations are measurements performed by e.g. WEIERMAN, [72]. The heat transfer equations of WEIERMAN [72] show an evaluated measurement uncertainty of about  $\pm 10\%$  for segmented fin tubes in an equilateral staggered layout; the friction factor equations exhibits an expected accuracy of  $\pm 15\%$ . The range of validity as far as known may be defined according to [72] with:

$$\left. \begin{array}{l} \approx (2000 \leq Re \leq 500000) \\ 9.5 \text{ mm} \leq h \leq 38.1 \text{ mm} \\ 0.9 \text{ mm} \leq s \leq 4.2 \text{ mm} \\ 1 \leq t \leq 7 \text{ fins/inch} \end{array} \right\}.$$

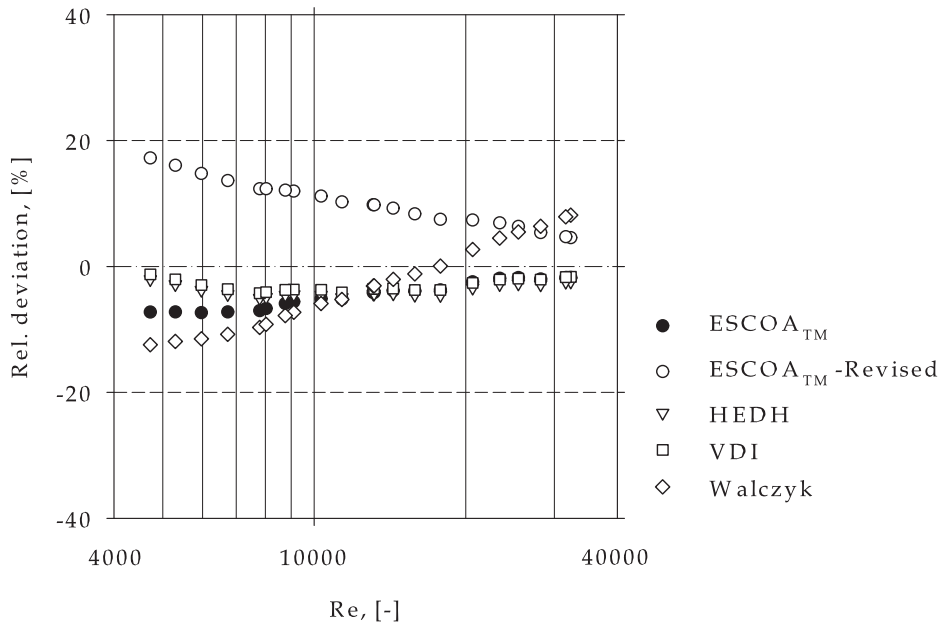
As Figure 4.25(b) shows, the results of Equation (4.15) with the pronounced measurement uncertainty lie within the range of the other correlations for segmented finned-tubes.

The global behavior of the pressure drop coefficient, evaluated for a single tube in cross-flow, is presented in Figures 4.26(a) and 4.26(b). The evaluated relative deviations of pressure drop coefficient data is within about  $\pm 20\%$ ; this equals the calculated overall measurement uncertainty. As presented, a comparison of Equation (4.26) with literature shows a tendency towards higher deviations at lower  $Re$ -numbers. The calculated values of WALCZYK [69], HEDH [27], and VDI [1], valid for solid fins, show slightly higher deviations than the correlations of ESCOA<sub>TM</sub>/ESCOA<sub>TM</sub>-REVISED in [16], being valid for segmented fins. Within the investigated  $Re$ -range the ESCOA<sub>TM</sub>-REVISED-correlation would indicate lower  $\zeta$ . Generally, all correlations attribute the same characteristics. Especially between literature and simulation of the helically segmented finned-tubes a good agreement can be found.

#### 4. Experimental and Numerical Results



(a) Relative Deviation of  $\frac{\xi_{exp} - \xi}{\xi_{exp}} \cdot 100\%$



(b) Relative Deviation of  $\frac{\xi_{simul} - \xi}{\xi_{simul}} \cdot 100\%$

Figure 4.26.: Comparison of Pressure Drop Coefficient Correlation with Literature, Based on Geometrical Data of Helically U-shaped Finned-Tubes

## 4.5. Comparison of Solid and Segmented Finned-Tubes with I-Shaped and U-Shaped Fins

### 4.5.1. Heat Transfer Behavior

As presented in [28], in this section a literature study is performed, focusing especially on selected correlations of WEIERMAN [72] or ESCOA<sub>TM</sub> (traditional), [16]<sup>13</sup>. For a comparison of solid and segmented I-shaped finned-tubes and U-shaped segmented finned-tubes the measurement data performed at I-shaped fins are taken from FRASZ, for specification refer to Table C.1, where the data validation is succeeded in the same manner as in case of U-shaped finned-tubes. According to the power law, the correlation of ESCOA<sub>TM</sub> for external heat transfer at finned-tubes with segmented fins in staggered tube arrangement is given in [16] and/or [14] and reads as

$$\begin{aligned} Nu_0 &= RePr^{1/3} \left( \frac{T_{gm}}{T_s} \right)^{1/4} \left( \frac{d_a + 2h}{d_a} \right)^{1/2} C_1 C_3 C_5 \\ &= \frac{1}{4} Re^{0.65} Pr^{1/3} \left( \frac{T_{gm}}{T_s} \right)^{1/4} \left( \frac{d_a + 2h}{d_a} \right)^{1/2} C_3 C_5. \end{aligned} \quad (4.27)$$

The factors  $C_1$ ,  $C_3$ , and  $C_5$  consider the  $Re$ -number, the geometry, the arrangement, and the tube row number, respectively. For the definition of  $C_3$  ( $C_{3_{seg}}$  or  $C_{3_{sol}}$ ), and  $C_5$  see literature, e.g. [16] or [14]. In case of solid finned-tubes,  $C_{3_{sol}}$  is applied in the place of  $C_3$  for the calculation, otherwise for segmented fins,  $C_{3_{seg}}$  is used. The limitations of each of these functions can be found in e.g. [16] or [14]. As already denoted above in the basic Equation (4.27), according to WEIERMAN the coefficient 0.25 is substituted by 0.23, see [72] and [4]. Figure 4.27 shows the dimensionless heat transfer coefficient for a representative number of validated measured points within the  $Re$ -range of segmented and solid finned-tubes at 8 row configuration in staggered arrangement. As seen, the heat transfer of the segmented I-shaped finned-tube is somewhat higher than that for the U-shaped finned-tube. The evaluated regressions of the segmented U-shaped and the I-shaped finned-tubes show almost equal gradients. The exponents for the Nusselt correlations of all three different fin types vary from approximately 0.58 to 0.62. This variation may be caused by the pressure difference measurement uncertainty of the mass flow of air at low  $Re$ -numbers as well as the temperature measurement uncertainty, see the uncertainty calculation in section 2.8. The overall heat transfer of the solid finned-tubes is inherently smaller. This may be caused by the effect of lower turbulences between the tubes. All I-shaped finned-tubes (i.e. solid and segmented) have almost the same fin height and the same transversal and longitudinal tube pitch. Thus, there is no effect of a greater overall heat transfer caused by the larger surface. Figure 4.28 depicts a comparison of the measured results with ESCOA<sub>TM</sub>-correlation.

<sup>13</sup>GANAPATHY states in his book two different versions of equations, namely "traditional ESCOA<sub>TM</sub>" and "revised ESCOA<sub>TM</sub>" correlations, distinguishing in the factors of  $C_i$

#### 4. Experimental and Numerical Results

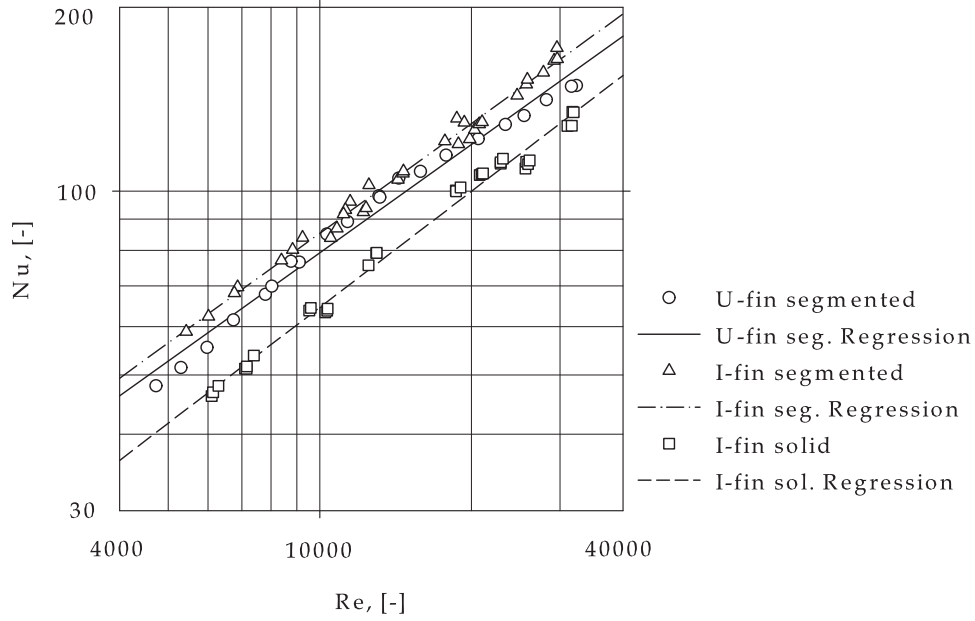


Figure 4.27.: Heat Transfer at 8 Tube Rows,  $Pr \approx 0.71$ , Segmented and Solid Tubes,  $d_a = 38 \text{ mm}$

Fin segmentation intrinsically increases heat transfer. The measured results for the solid finned-tubes show good agreement with the correlation from literature. The equations of WEIERMAN [72] and ESCOA<sub>TM</sub> [16] states a measurement uncertainty of about  $\pm 10\%$  in case of staggered tube layout. Thus, especially the results of the segmented U-shaped finned-tubes concur well with literature. Since in Equation (4.27)

$$Nu_0 = f(Re_0, Pr, T_g, T_s, d_a, h, t, s, t_l, t_q, N_R) \quad (4.28)$$

and heat conduction through the tube and the fin varies for the two geometries, the equation for the Nusselt number has to be modified to reflect the same conditions. This objective function depends on parameters such as dimensionless groups, temperatures and geometry.  $C_5$  does not change in value due to equal transversal and longitudinal pitch as well as fixed tube row numbers. Each point in the diagram is obtained at different temperatures. For further calculations, a new fixed average reference temperature for gas and fin has to be set and all values have to be interpolated for equal  $Re$ -numbers. The reference Nusselt number between the segmented U-fin

#### 4. Experimental and Numerical Results

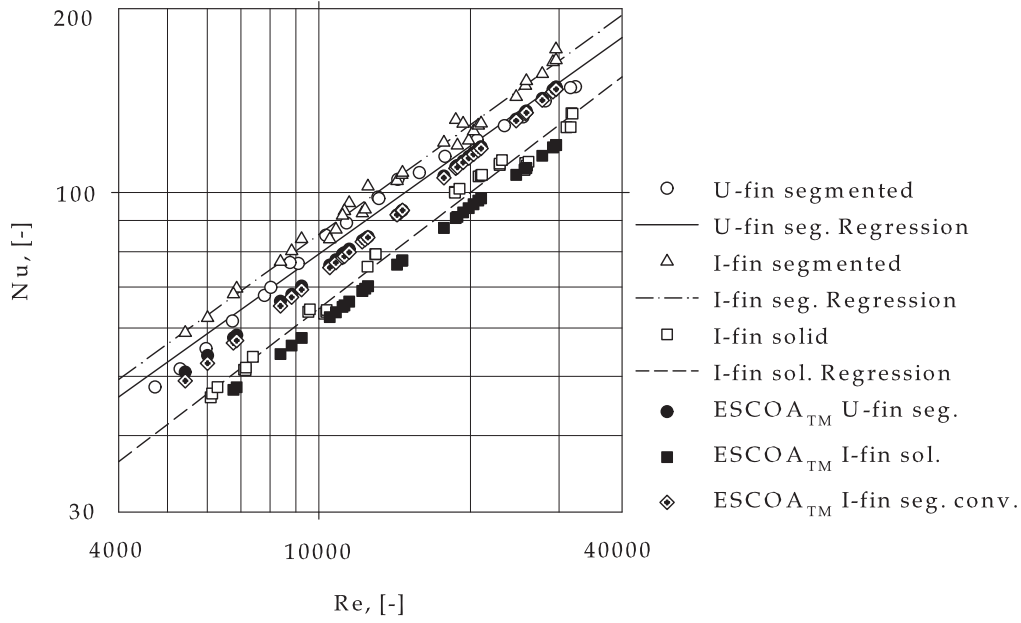


Figure 4.28.: Comparison of Heat Transfer at 8 Tube Rows with Literature,  $Pr \approx 0.71$ ,  $d_a = 38 \text{ mm}$

and I-fin then becomes

$$Nu_c = Nu_U \frac{\left(\frac{T_{gf}}{T_{sf}}\right)^{1/4}}{\left(\frac{T_{gm}}{T_s}\right)^{1/4}} \sqrt{\frac{d_a + 2h_I}{d_a + 2h_U} \frac{C_{3I}}{C_{3U}}} . \quad (4.29)$$

$C_3$  directly influences heat transfer.  $C_{3I}$  and  $C_{3U}$  are functions with the negative factor  $h/(t-s)$  in the exponent, see [16]. The influence of the factor  $h/(t-s)$  on heat transfer is of interest. A comparison among segmented fins reveals the following: if equation (4.29) is applied to Equation (4.27) for the individual case, the factor  $h/(t-s)$  for U-shaped fins and for I-shaped fins may be evaluated. If the exponent  $h/(t-s)$  decreases,  $C_3$  increases up to approximately 5 ÷ 7%, and thus overall heat transfer rises for the two different segmented types, depending on an evaluated overall average reference temperature for gas and fin and if the influence of the geometry is considered. Figure 4.29 shows the relative deviation of the evaluated  $Nu$ -numbers, based on the  $ESCOA_{TM}$ -correlation of the measured values of the three tested geometries (marked with  $\triangle$ ,  $\square$ , and  $\circ$ ) within the investigated  $Re$ -range. All points marked with  $\blacktriangle$  in the diagram represent values for the relative deviation of the compared Nusselt numbers of U-shaped fin geometry with the I-shaped fin tubes of the exact measurement



#### 4. Experimental and Numerical Results

temperatures. To eliminate this deviation, a comparison with equal average reference temperatures is performed. The points marked with  $\bullet$  in Figure 4.29 represent these evaluated values for the relative deviation of the compared Nusselt numbers for the U- and I-fin geometry with average temperatures. All  $Nu$ -correlations are calculated at approximately constant  $Pr$  values. The Prandtl number represents the thermo-physical properties. In the case of air as heat transfer medium, the thermal boundary layer is thicker than the boundary layer of fluid flow. Because of the very small variation of  $Pr$  under test conditions, this influence shall be neglected for further considerations in this work.

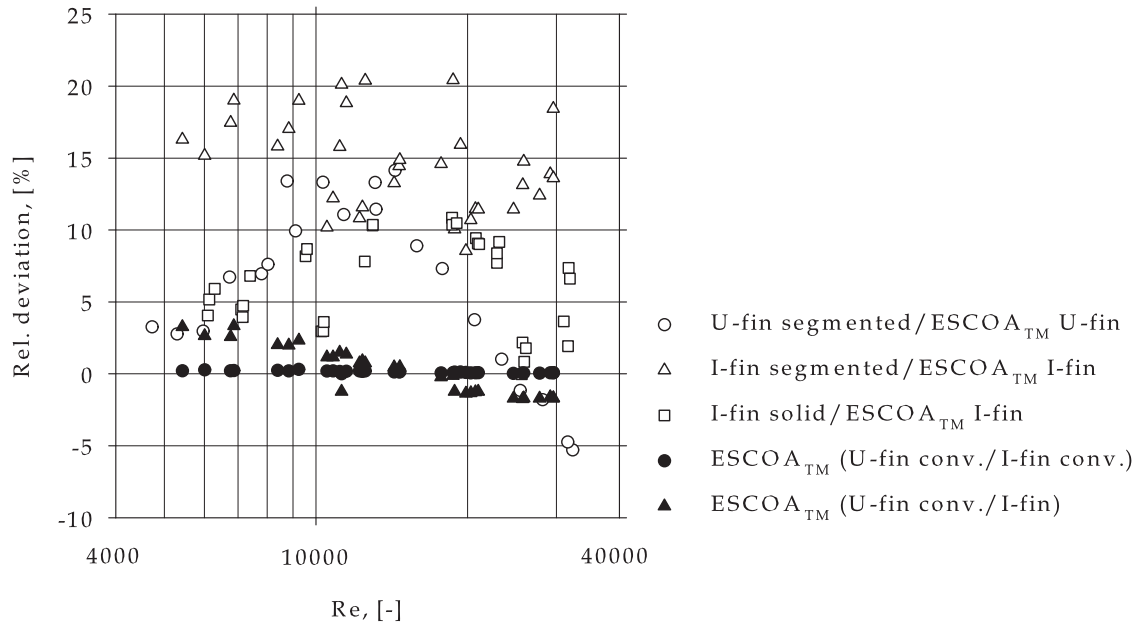


Figure 4.29.: Relative Deviation of Correlations

As expected, the dimensionless heat transfer coefficient declines with increasing fin height and fin pitch. Specifically, in view of WEIERMANS correlations, fin height does not very strongly influence overall heat transfer, evaluated in [14]. Yet with increasing fin height, the total external heating surface also increases. There might be a gain from the heating surface as  $h$  is increased. The volumetric specific heat output of a heat exchanger with a U-shaped finned-tube bundle of the same longitudinal and transversal pitch, same number of tubes, smaller fin pitch and greater fin height is improved than that of an I-shaped finned-tube bundle of the same installation size but with greater fin pitch. As the literature study shows, an enhanced effect on heat transfer with variation of the fin height is expected, see also [14]. A maximum fin height and the

#### 4. Experimental and Numerical Results

minimum fin pitch result from limitations, such as the need to avoid fouling, posed in finned-tube production by the kind of fuel used (liquid, solid or gaseous). REID and TABOREK, [54], recommended fin densities in relation to fuel type, refer to section 1.2. The influence of the fin height to the heat transfer is presented in Figure 4.30. As a comparison between the measured results at segmented fin types shows,  $\eta_r$  decreases with increasing fin height and increasing Reynolds number. From the measured results it may be interpreted that fin efficiency of solid fin-tubes evaluates for higher values. The difference between measurement and *CFD*-simulation does not exceed about 7%, but generally the evaluated results of the numerical calculation would predict higher values, as presented in the linear-logarithmic axis diagram.

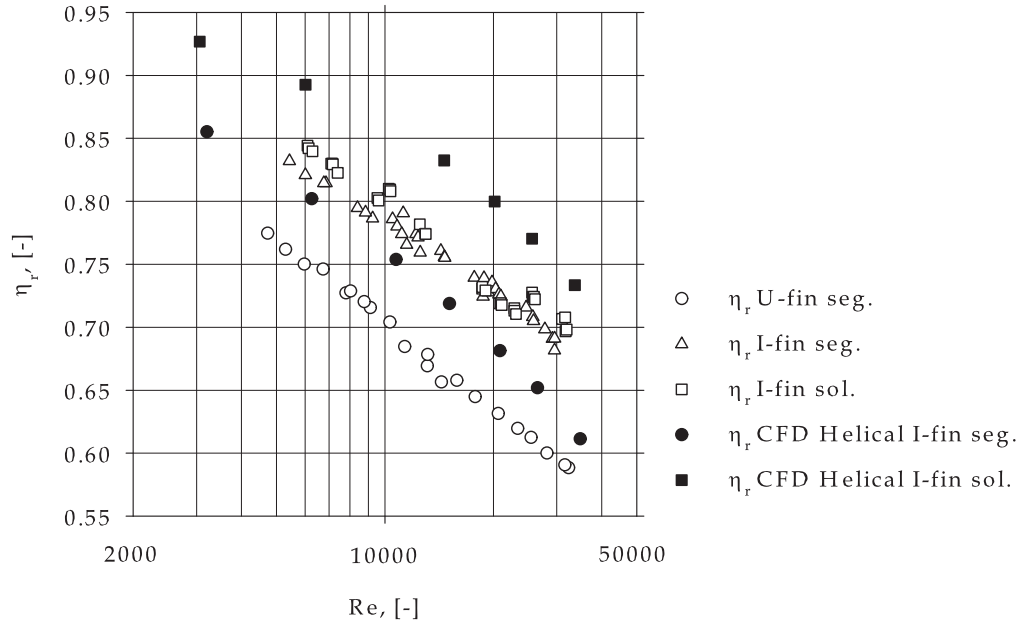


Figure 4.30.: Fin Efficiency of Segmented and Solid I/U-Finned-Tubes and *CFD*-Simulation

Using the exponent  $h/(t-s)$ , a comparison between almost equal segmented and solid I-shaped finned-tubes (the fin height varies 0.5 mm) shows an increase of the function  $C_3$ . Therefore,  $C_{3_{sol}}$  in the equation for solid finned-tubes and in case of segmented fins  $C_{3_{seg}}$  is considered, see for definition [16]. In Figure 4.31, this comparison of  $Nu$  at segmented and solid I-shaped finned-tubes is depicted for selected 13 validated measurement points in the middle  $Re$ -range. For a given fin height at  $h/(t-s) = 5.718$  a scatter plot, marked with  $\square$ , is shown. This variation may be attributed to measurement uncertainty when calculating the heat transfer rate. The calculated average mean value for a comparison of the two different fin types, marked

#### 4. Experimental and Numerical Results

in the diagram with  $\blacktriangle$ , shows good predictive capability for the increase in heat transfer rate according to Equation (4.27), [28]. A comparison of the segmented and solid

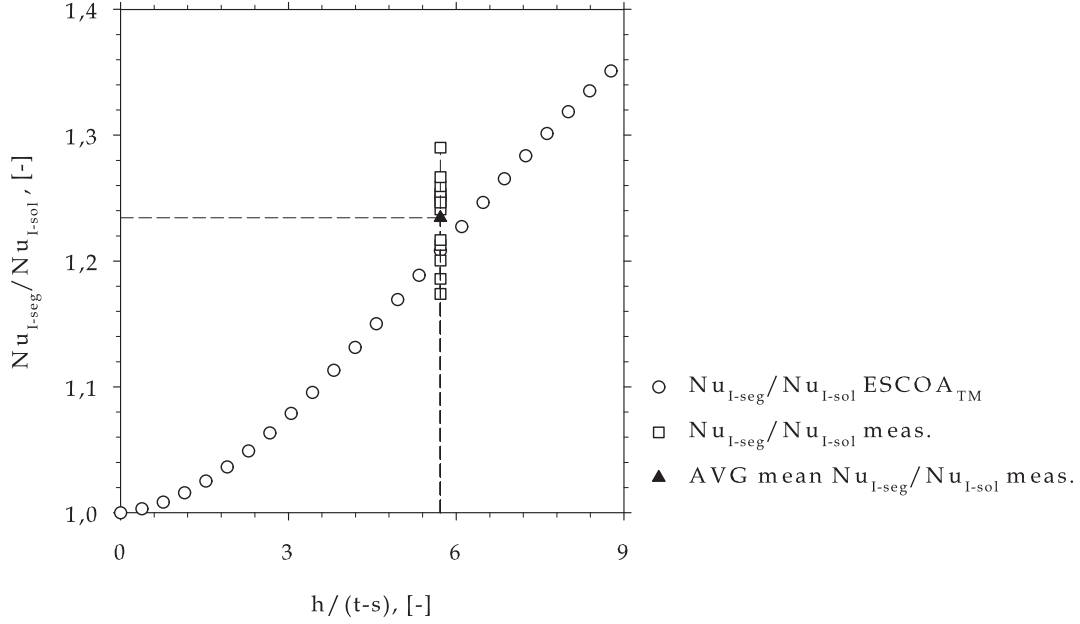


Figure 4.31.: Comparison of Segmented and Solid I-Finned-Tubes

finned-tubes shows explicitly, a higher overall dimensionless heat transfer coefficient for 8 segmented finned-tube rows in staggered arrangement of roughly 24%. This enhancement is comparable to REID and TABOREK, [54]. They concluded that fin segmentation increases turbulences and improves the gas penetration to the fin root area, causing a higher heat transfer coefficient of as much as 20% compared to solid fins.

##### 4.5.2. Pressure Drop Behavior

According to ESCOA<sub>TM</sub> the pressure drop coefficient correlation, given in [16] and/or [14], reads as

$$\xi = 4f_f = 4 \left( \frac{d_a + 2h}{d_a} \right)^{1/2} C_2 C_4 C_6 . \quad (4.30)$$

The factor  $C_2$  accounts for the  $Re$ -number,  $C_4$  considers the geometry and arrangement, and  $C_6$  includes the arrangement and the tube row number. For detailed definition of  $C_2$ ,  $C_4$ , and  $C_6$ , see literature. A comparison of the three heat exchanger geometries is

#### 4. Experimental and Numerical Results

only possible for same conditions. The objective function

$$\zeta = f(Re_0, N_R, d_a, h, t, s, t_l, t_q) \quad (4.31)$$

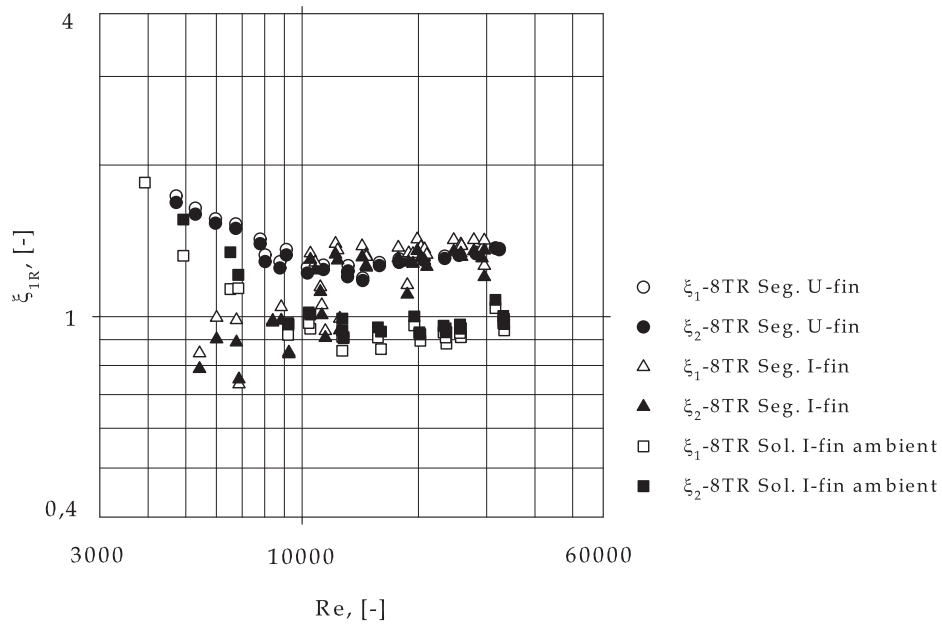
accounts for dimensionless groups, tube row numbers and the geometry. Equation (4.31) does not account for any effect caused by different gas temperatures and fin temperatures. A theoretical conversion function of the pressure drop could be stated if same flow conditions are assumed. The difference of  $F_{min}$  between segmented U-fin and I-fin is  $\approx 1.5\%$ ; the difference between segmented I-fin and solid I-fin due to almost equal tube geometry is very small with  $\approx 0.65\%$ . A conversion of  $\zeta_c$  may be defined as follows:

$$\zeta_c = \zeta_U \sqrt{\frac{d_a + 2h_I}{d_a + 2h_U} \frac{C_{4_I}}{C_{4_U}}}. \quad (4.32)$$

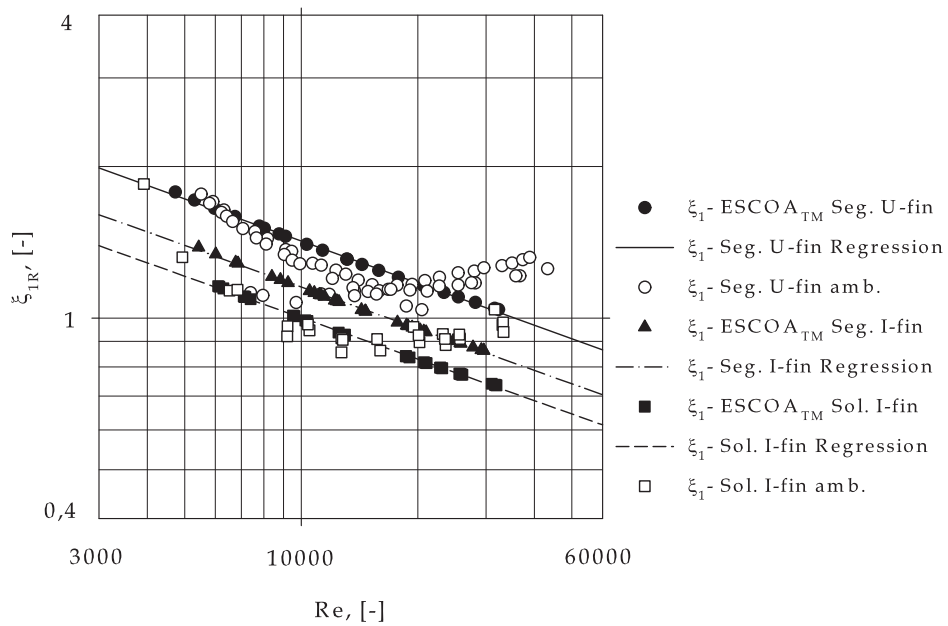
In Figure 4.32(a), the pressure drop coefficient at 8 tube rows for all tube bundles in staggered arrangement, evaluated for a single row in cross-flow, is shown. Aside from measurements at solid finned-tubes with ambient test conditions ( $\square, \blacksquare$ ), all values at U-shaped fins ( $\circ, \bullet$ ) and at I-shaped fins ( $\triangle, \blacktriangle$ ) performed at augmented temperatures, are evaluated with Equation (2.29)<sup>14</sup>. At  $Re > 10000$  the pressure drop coefficient of the three different tube bundles has the same characteristics. For  $Re < 10000$  great scattering is revealed among the data evaluated from tests at segmented I-shaped finned-tubes. At solid finned-tubes, a data comparison between tests performed at ambient and augmented temperatures shows a similar trend at low  $Re$ -numbers, see Figure 4.19. Unfortunately, no data at ambient test conditions from segmented I-shaped finned-tubes is available. However, this effect could not be observed within the gathered data from the U-shaped finned-tubes, compare Figures 4.32(a) and 4.32(b). For  $Re > 15000$ , a small increase takes place, then, at  $25000 < Re < 35000$ , the pressure drop coefficient tends to show a constant value for all bundles with equal  $t_l$  and  $t_q$ . This increase at certain  $Re$ -numbers can be found as well in literature e.g. BROCKMANN [6], and seems to be dependent on the tube pitches and arrangements, among other influences. The measured pressure drop of the U-shaped finned-tubes shows very good congruence and the same gradient of the correlation in literature (ESCOA<sub>TM</sub>) especially in the range of  $5500 < Re < 15000$ , refer to Figure 4.32(b). Applying the ESCOA<sub>TM</sub>-correlation for evaluation gives lower values of  $\zeta_{1R_{I-seg}}$  than  $\zeta_{1R_{U-seg}}$ , which could be seen as a slight difference of  $u_E$  for the individual case. The pressure drop at the solid test tubes is somewhat higher within the measured  $Re$ -range than calculated with Equation (4.30), but the evaluated results of the I-shaped fins at ambient test conditions reveal high measurement uncertainties at very low  $Re$ -numbers. The influence of fin height on the pressure drop at same installation size

<sup>14</sup>The black/white color of the symbols in the Figures distinguishes between the measurement position

#### 4. Experimental and Numerical Results



(a) Comparison of Measurement



(b) Comparison with Literature

Figure 4.32.: Pressure Drop Coefficient of Different Finned-Tube Geometries, evaluated for 1 Tube Row

#### 4. Experimental and Numerical Results

indicates an increase of the pressure drop coefficient with increasing  $h$  according to the analysis above<sup>15</sup>. This matches review stated in literature [14].

Although the fin height and fin thickness as well as fin pitch vary among the different tested segmented geometries, the net free area in a tube row is nearly the same in each case. Thus, a significant difference among the measured pressure drop coefficients is not expected. This seems not to be valid for the solid fin type. Following the procedure performed for the heat transfer analysis above, an influence of the factor  $h/(t-s)$  on the pressure drop coefficient may be found. In case of U-segmented fins the average mean value of  $h/(t-s)$  evaluates for approximately  $7 \div 7.7$ ; for I-fin the factor  $h/(t-s)$  becomes roughly  $6 \div 6.8$ . This variation in case of e.g. the U-fin type depends on the applied  $\zeta$ , calculated from measurement or with the  $ESCOA_{TM}$ -correlation, where the influence of fin height is neglected. As the overall heat transfer for solid fin tubes is about 20% lower than for segmented fin tubes, the pressure drop shows the same tendencies.

##### 4.5.3. Performance Evaluation and Comparison Between the Applied Different Three Heat Exchangers

A comparison of the dimensionless heat transfer coefficient and the pressure drop coefficient gives an indicator of the overall thermal effectiveness of a heat exchanger. Specifically, the pressure drop characteristic and the heat transfer characteristic are indirectly proportional, see the  $Nu$  and  $\zeta$  evaluations above. Following these expertises, enhanced heat transfer using finned-tubes is only achieved by means of an increase in pressure drop. The objective is to identify a Reynolds number/range for the "best effectiveness point/range". In Figure 4.33, the ratio of Nusselt numbers of tubes with I-shaped and U-shaped fins is shown. The segmentation of the fin may be seen to increase the dimensionless heat transfer coefficient within the investigated Reynolds range, as the comparison with solid fins shows. For  $Re < 10000$  and  $Re > 20000$ , this effect is even more significant. Moreover, a comparison of segmented I-shaped and U-shaped finned-tubes reveals superior results using I-shaped fins with a fin height of 15 mm, refer to Figure 4.33. But, at  $10000 < Re < 20000$  no significant difference between those two fin-types may be detected, even the fin height varies about 4.5 mm.

A comparison of the pressure drop coefficients gives information about the required pumping power. Figure 4.34(a) shows explicitly the demand of a higher pumping power if applying fins with segmentation. In case of low Reynolds numbers, both, the solid and segmented fin-types indicate almost equal pressure drop, at approximately equal  $F_{min}$ . Apart from the solid finned-tubes, a comparison of the two different segmented tubes at  $Re > 15000$  may be interpreted to have almost equal  $\zeta$ , refer to Figure 4.34(b). At  $Re < 15000$  the heat exchanger applied with I-shaped fins reveals supe-

---

<sup>15</sup>Due to less net free area in a tube row, which influences  $u_E$  and thus the pressure drop

#### 4. Experimental and Numerical Results

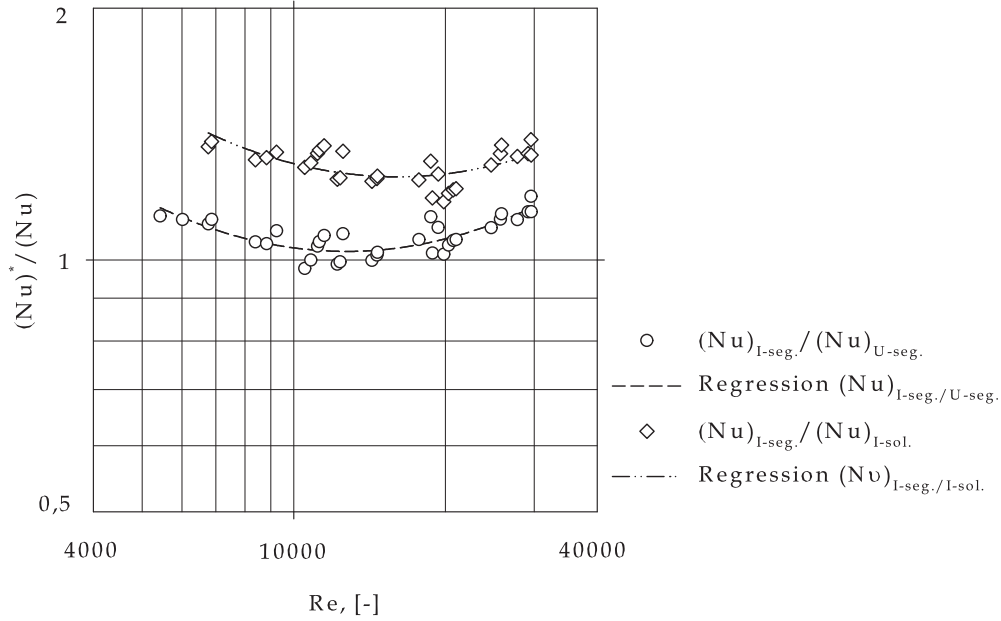


Figure 4.33.:  $Nu^*/Nu$  of Investigated Sol./Seg. I/U-Shaped Fin

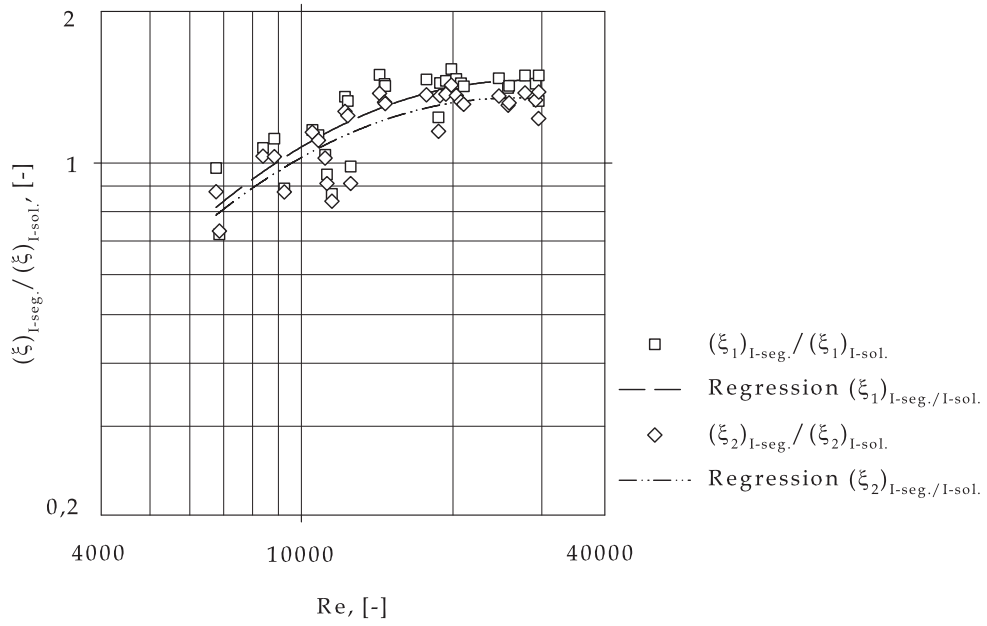
rior results. This effect is even more significant for low Reynolds numbers. However, at low  $Re$ -numbers, the measurement results of the I-shaped segmented finned-tubes exhibit high uncertainties, see Figure 4.32(a).

Speaking in terms of heat exchanger effectiveness investigation ("optimization"), an integral evaluation has to be applied, including heat transfer, pressure drop, and heat exchanger size or weight. As presented in [28], the three different fin types are compared in order to identify best performance. Several criteria for the evaluation of the performance of a heat exchanger can be found in literature, e.g. [58], [59], and [71]. As STEPHAN and MITROVIC stated in [59], for the evaluation of different tubes, as well as in general for different geometrical arrangements of heat exchangers, heat transfer rate is related to pumping power, or more generally formulated:

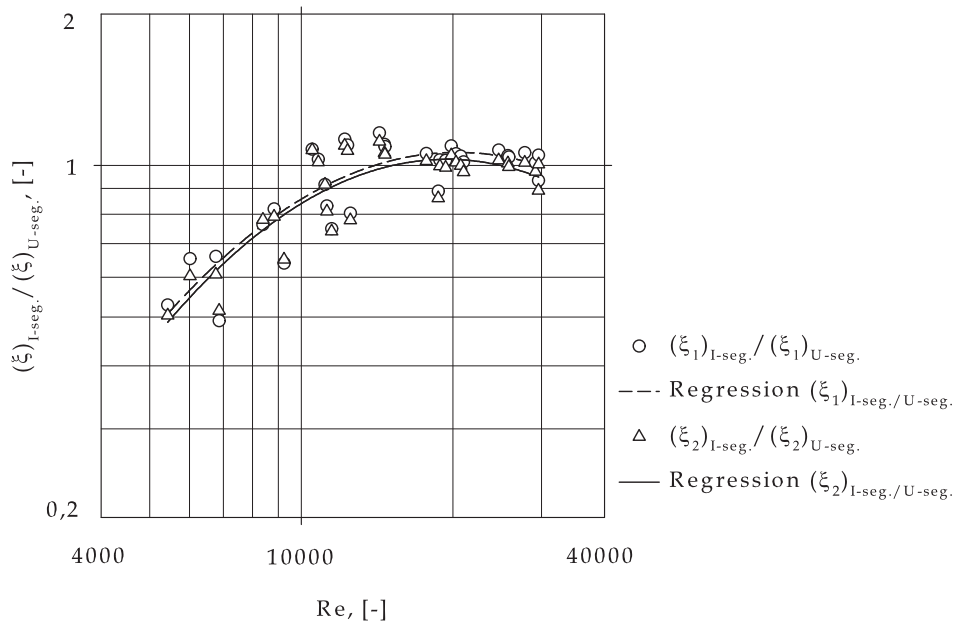
$$\left( \frac{St^*}{\xi^{*1/3}} \right) / \left( \frac{St}{\xi^{1/3}} \right) = f(Re, geometry). \quad (4.33)$$

STEPHAN and MITROVIC suggested for the evaluations approximate constant values as the ratio between flow cross-sectional area and total outside surface area, all properties of state, and the logarithmic temperature difference. This may be interpreted as a restriction, but makes these bulky equations more easy to handle. A comparison of solid and segmented I-shaped finned-tubes reveals improvement applying segmented fins rather than solid ones, see Figure 4.35(a). This characteristic especially increases

#### 4. Experimental and Numerical Results



(a) Comparison of Seg./Sol. I-Shaped Fins



(b) Comparison of Seg. I/U-Shaped Fins

Figure 4.34.: Comparison of the Pressure Drop Coefficients  $(\xi^*/\xi)$



#### 4. Experimental and Numerical Results

for  $Re < 10000$ . For  $Re > 15000$  the  $(St^*/\xi^{*1/3}) / (St/\xi^{1/3})$  ratio tends to display a constant value of 1.2. This equals the value calculated using Equation (4.27). However, at low  $Re$ -numbers, this effect reveals superior results. A comparison of the different segmented finned-tubes is presented in Figure 4.35(b). The heat transfer rate at segmented I-shaped and U-shaped fins increases for  $Re < 10000$  and  $Re > 20000$ . This effect is more pronounced for low  $Re$ -numbers. Between  $10000 < Re < 20000$ , no significant difference may be identified.

GEISER, [19], adopted the criterion suggested in [59] by means of fin efficiency to consider the conduction within the fin. By way of example, the performance evaluation criteria (PEC) suggested and derived by WEBB, applicable for single-phase laminar or turbulent flows in tubes or normal to tube banks, [71], is adopted and applied here and reads in its general definition

$$\frac{(\alpha^* A^*)/(\alpha A)}{(P^*/P)^{1/3}/(A^*/A)^{2/3}} = \frac{j^*/j}{(\xi^*/\xi)^{1/3}} = \frac{(St^* Pr^{*2/3})/(St Pr^{2/3})}{(\xi^*/\xi)^{1/3}}. \quad (4.34)$$

The terms on the left side of this equation,  $(\alpha^* A^*)/(\alpha A)$ ,  $(P^*/P)^{1/3}$  and  $(A^*/A)^{1/3}$ , are part of the COLBURN-factor ratio for heat transfer and the pressure drop ratio, whereby the Stanton number at the average mean gas temperature is defined as follows<sup>16</sup>:

$$St = \frac{j}{Pr^{2/3}} = \frac{\alpha}{\rho_{gm} c_{p_{gm}} u_{gm}}. \quad (4.35)$$

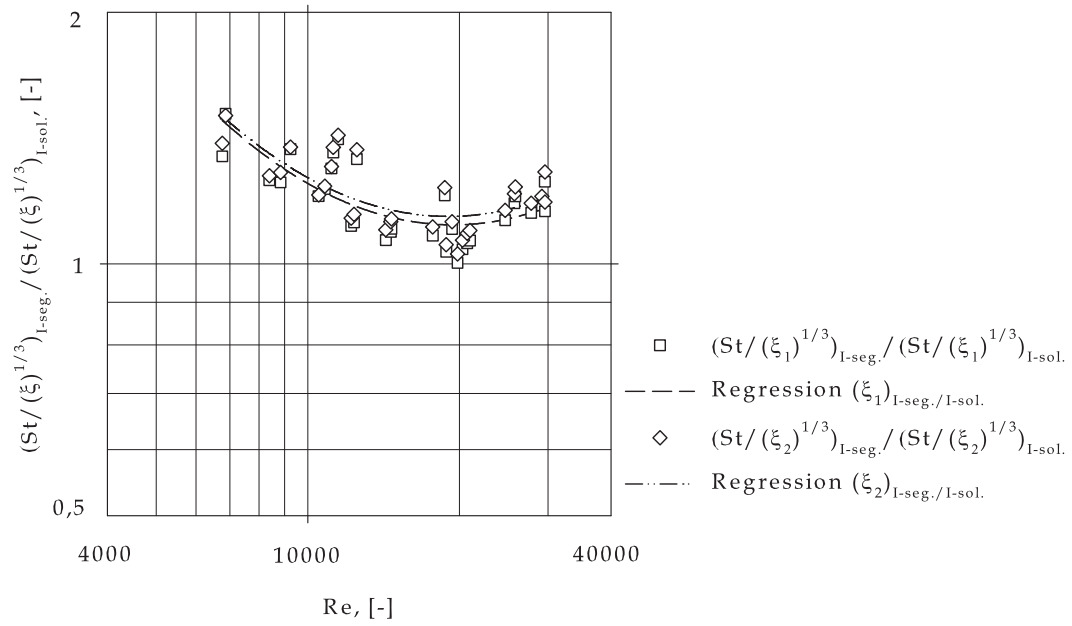
For judging these PEC, the heat exchanger flow rate, the flow frontal area, the heat transfer surface area, and the heat transfer coefficient have to be specified according to [71]. The differences between the three fin types, i.e. the net free flow area between the tubes, the heat transfer coefficient at the internal tube side, and the internal diameter of the tubes as well as the tube wall thickness, are neglected due to their small variation. The three different possibilities described by this criterion state as follows:

1. **MAX** $(\alpha^* A^*)/(\alpha A)$ :  
maximizing the heat transfer rate for equal pumping power  $(P^*/P)$  and equal overall surface area  $(A^*/A)$ ;
2. **MIN** $(P^*/P)$ :  
minimizing the pumping power for equal heat transfer rate  $(\alpha^* A^*)/(\alpha A)$  and equal heat transfer surface area  $(A^*/A)$ ;
3. **MIN** $(A^*/A)$ :  
minimizing the overall heat exchanger size for equal pumping power  $(P^*/P)$  and equal heat transfer rate  $(\alpha^* A^*)/(\alpha A)$ .

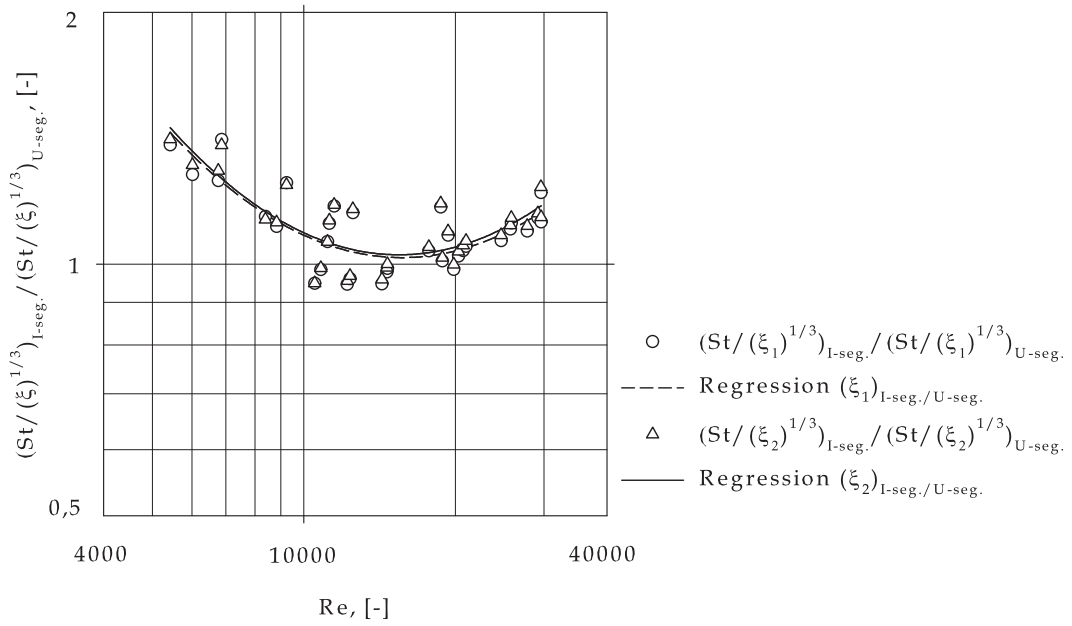
---

<sup>16</sup>This criterion applied here accounts only for the fin sided thermal resistances

#### 4. Experimental and Numerical Results



(a) Comparison of Seg./Sol. I-Shaped Fins



(b) Comparison of Seg. I/U-Shaped Fins

Figure 4.35.:  $(St^*/\xi^{*1/3})/(St/\xi^{1/3})$  according to [59]

#### 4. Experimental and Numerical Results

##### 1. Maximizing the heat transfer rate:

It is assumed that the investigated heat exchanger has equal pumping power and equal overall heat exchanger surface at equal overall heat exchanger size. At equal installation size, an increase of the heat transfer surface area, and thus of the heat transfer rate, is only achieved at the expense of an increase in pressure drop. Optimizing the heat exchanger by means of the performance criterion entails maximizing the heat transfer rate while simultaneously minimizing pressure drop and heat exchanger size. The heat transfer rate for segmented I-shaped fins increases significantly for  $Re < 10000$  similar to the applied theory of STEPHAN and MITROVIC, [59], as the comparison between solid and segmented finned-tubes shows, Figure 4.36(a). Equal behavior may be found by comparing I-shaped and U-shaped finned-tubes, refer to Figure 4.36(b).

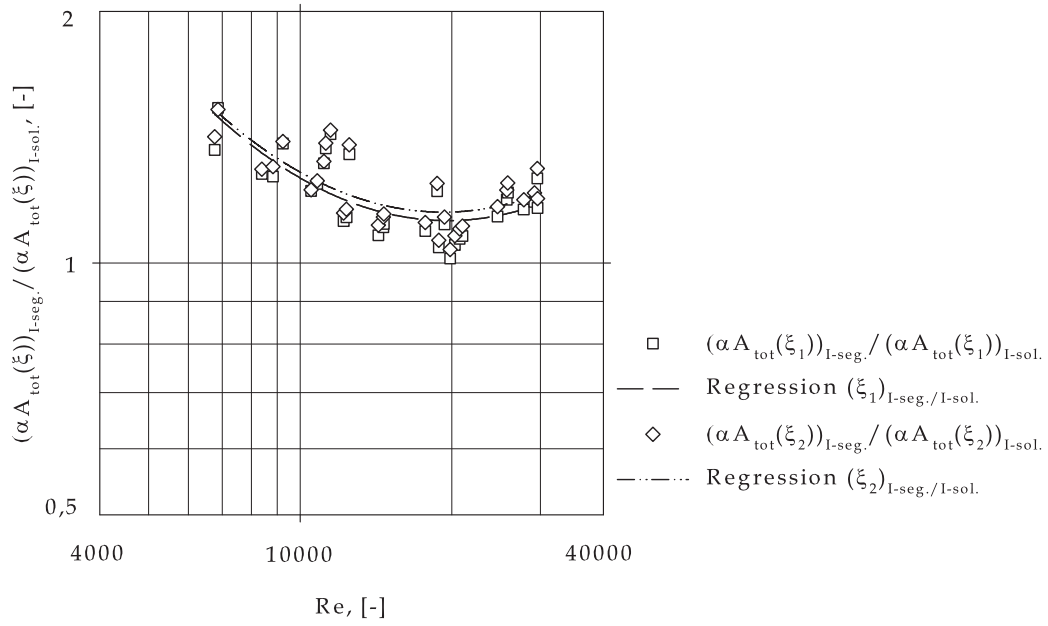
##### 2. Minimizing the pumping power:

In case of equal heat transfer rate and equal total heat transfer surface area of the two compared systems, the pumping power  $P$  tends to a minimum. The pumping power (Figure 4.37(a)) of the segmented I-shaped finned-tubes is lower for  $Re < 10000$  and  $Re > 20000$ . At  $Re \approx 20000$  the pumping power is almost the same as with solid finned-tubes. All solid finned-tubes show higher  $P$ . This kind of tube has a relatively low  $h$  and almost equal  $A_{sol}$  compared to  $A_{seg}$ . Satisfying condition "(2.)" at equal  $(\alpha^* A^*)/(\alpha A)$  and  $(A^*/A)$  results in an increase in pumping power. This effect might be intensified by the high measurement uncertainty at low  $Re$ -numbers, as mentioned above. A comparison of all segmented finned-tubes under condition "(2.)" is seen in Figure 4.37(b). At  $Re < 10000$  and  $Re > 20000$ , pumping power decreases for all tubes. In the range of  $10000 < Re < 20000$ , pumping power displays the same characteristic curve for both, segmented U-shaped and I-shaped finned-tubes. The small difference resulting from the varying net free area in tube rows with these tube geometries was neglected.

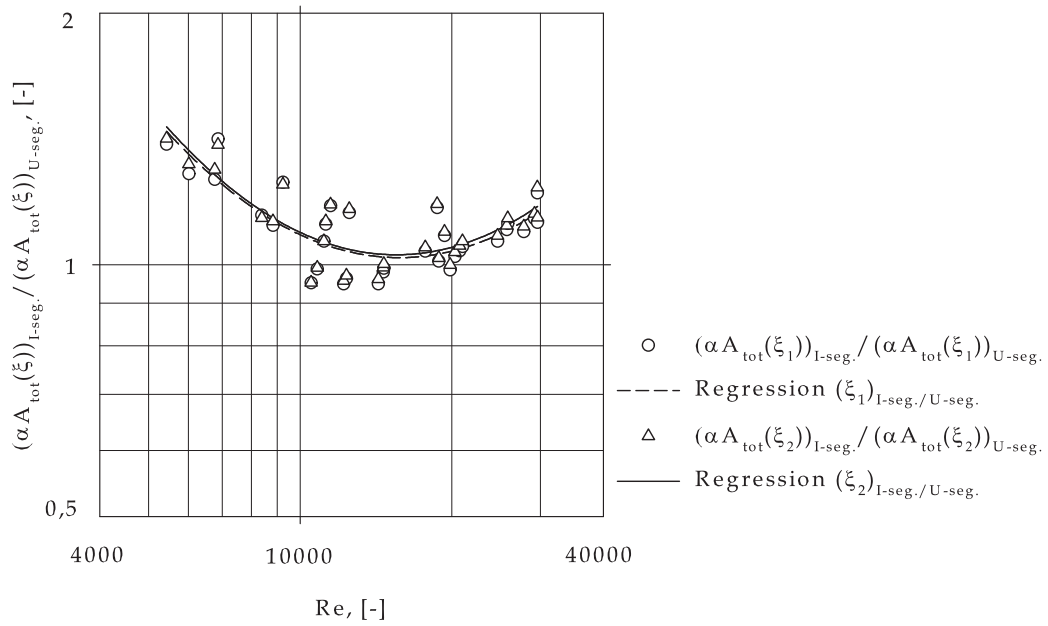
##### 3. Minimizing the overall heat exchanger size:

The ratios of the heat transfer rate and pumping power are assumed to be 1. The two I-shaped finned-tube bundles are considered first: In Figure 4.38(a), the ratio of the total outside surface area of the bundles is presented. To enhance heat transfer, it is necessary to enlarge the tube surface area and/or improve heat conduction. Within the investigated Reynolds range, an enhanced system is achieved using a solid finned-tube, if equal  $(P^*/P)$  and  $(\alpha^* A^*)/(\alpha A)$  can be assumed. All segmented I-shaped finned-tubes would require less space than U-shaped finned-tubes. Yet this result is obtained only for the same tube pitch. The  $\alpha$  values of the two heat exchangers vary only little. On the other hand, the U-shaped tube is applied with a larger fin height at smaller fin thickness, provid-

#### 4. Experimental and Numerical Results



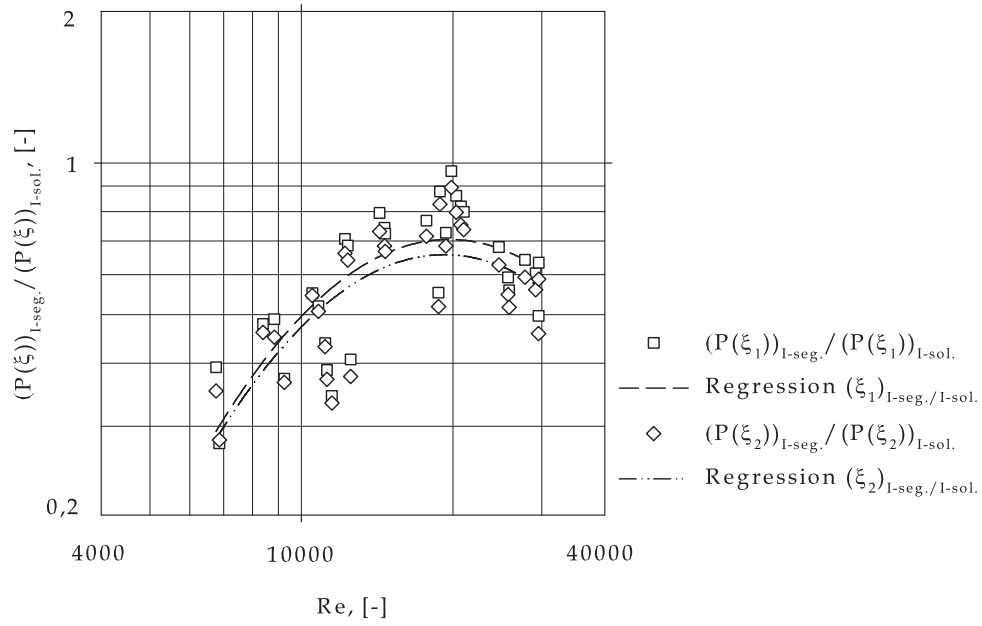
(a) Comparison of Seg./Sol. I-Shaped Fins



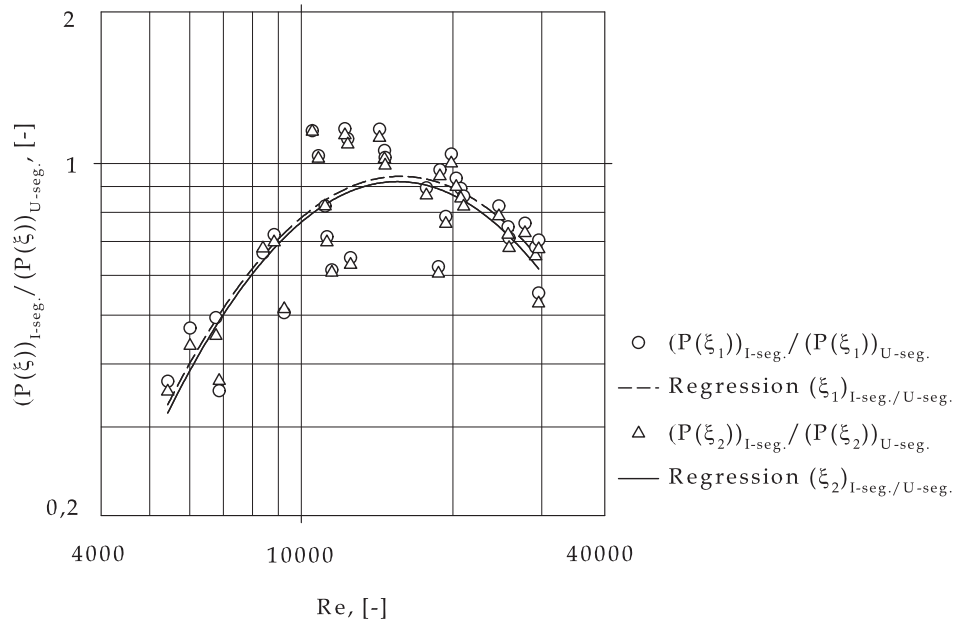
(b) Comparison of Seg. I/U-Shaped Fins

Figure 4.36.:  $(\alpha^* A^*) / (\alpha A)$  at equal  $(P^*/P)$  and  $(A^*/A)$

#### 4. Experimental and Numerical Results



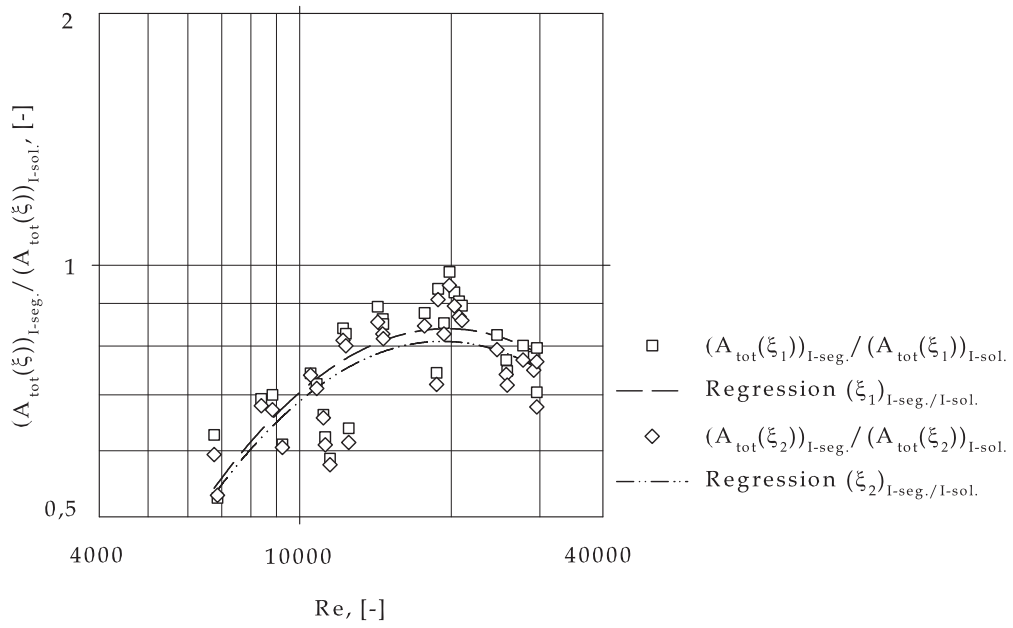
(a) Comparison of Seg./Sol. I-Shaped Fins



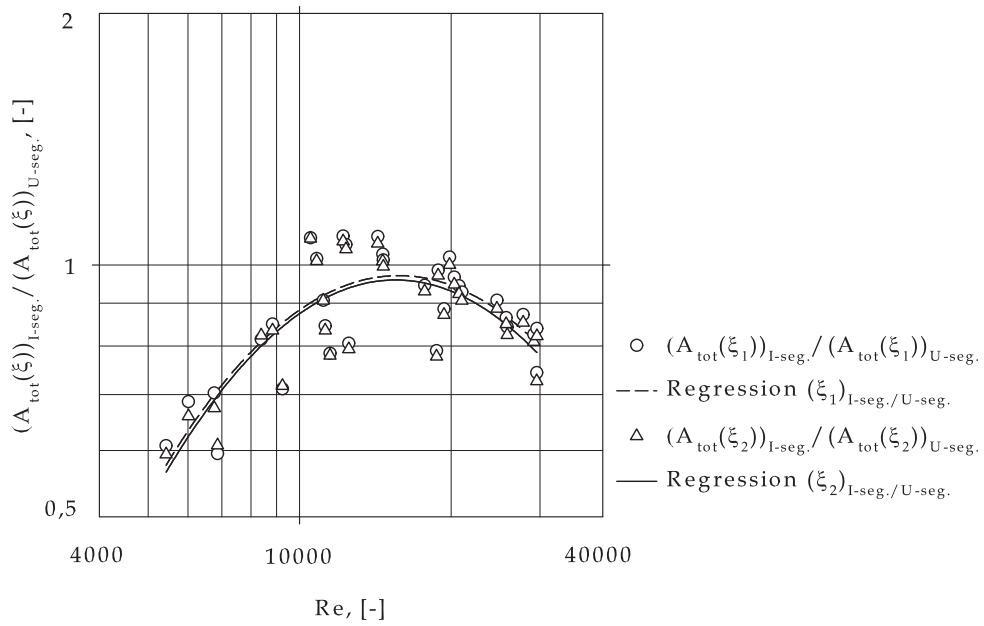
(b) Comparison of Seg. I/U-Shaped Fins

Figure 4.37.:  $(P^*/P)$  at equal  $(\alpha^* A^*)/(\alpha A)$  and  $(A^*/A)$

#### 4. Experimental and Numerical Results



(a) Comparison of Seg./Sol. I-Shaped Fins



(b) Comparison of Seg. I/U-Shaped Fins

Figure 4.38.:  $(A^*/A)$  at equal  $(\alpha^* A^*)/(\alpha A)$  and  $(P^*/P)$

#### 4. *Experimental and Numerical Results*

ing almost comparable same pressure drop. As the PEC shows, for  $Re < 10000$  and  $Re > 20000$  the installation size of the heat exchanger with I-shaped fins is superior (refer to Figure 4.38(b)). In the range of  $10000 < Re < 20000$  no improvement of the heat exchanger size is possible. This inverse result is due to the constant transverse and longitudinal pitch. As the finned-tubes have almost the same net free area within one tube row, only the packing density of the heat exchangers differs if heat exchanger volume is considered.

The applied PEC relation does not take into account variations in heat conduction between U-shaped and I-shaped fins as well as fin efficiency. However, in the range of  $10000 < Re < 20000$ , all compared segmented heat exchangers display very similar behavior; no advantage in terms of pumping power or heat exchanger surface area may be observed for this range. This may lead to the conclusion that fin height, next to other geometrical parameters, e.g. in combination with fin pitch or minimum net free area within a tube row, is apparently one of the most important factors for evaluating the performance of the investigated segmented finned-tube geometries.

## 4.6. Local Considerations of the Finned-Tube Bundle

In this section some local fluid flow and heat transfer phenomena of the analyzed circular/helical solid and segmented finned-surfaces will be discussed qualitatively. As some authors in literature remarked [58], [55], the investigation of flow patterns across a finned surface and local heat transfer from a finned-tube in cross-flow is rather complicated and a difficult task. The development of the hydrodynamic and thermal boundary layer is the most dominant factor in the conjugate heat transfer, as it occurs at the considered single-row finned-tube bundle. Strictly speaking, a comparison of different tube geometries (i.e. circular and helical) at equal inlet conditions causes different fluid flow behavior and thus different thermal properties. However, this consideration does not claim to include the complete basic research and in the case of applied science a similar trend will be identified and described.

### 4.6.1. Fluid Flow Behavior

The physical complexity of a finned-tube under cross-flow conditions is dominated by the three-dimensional boundary layer development and the subsequent flow separation effects. According to PRANDTL, the boundary layer attached on a flat plate can be subdivided into the internal layer where the viscosity has to be considered and the external layer where all viscous forces are small and thus be neglected; the fluid flow is considered ideal as it is assumed in the potential theory, [55], [68]. At the wall, i.e. fin surface, the no slip condition must be met. The boundary layer thickness is obviously thinner the higher the Reynolds number and the smaller the viscous forces are. Apart from the existence of the hydrodynamic boundary layer due to friction a convection boundary layer as a result of heat transport exist. Thus, the convective heat transfer occurs within the developed boundary layer and depends on its thickness. It may be concluded that the heat transfer declines with increasing boundary layer thickness.

Starting in flow direction from the leading part of the fin tube at the angle  $\Theta = 0^\circ$  related to the stagnation line, a boundary layer begins to grow. The fluid will be first accelerated and then decelerated streaming around the tube. If the fluid momentum is too weak to overcome the adverse pressure gradient, flow separation on the bare tube occurs and the boundary layer peels away from the tube surface. GRÖBER, ET. AL remarked, [21], that a turbulent boundary layer provides higher kinetic energy, thus a separation would be able to overcome the drag forces and detaches further downstream. If separation has occurred, the flow behind the separation line in the tailing zone of the tube consists of a wake with strong vortices.

From the leading part of the finned-tube a horseshoe vortex system develops, due to negative pressure gradient towards the fin surface. The boundary layer can not withstand this adverse pressure gradient and rolls to formate a horseshoe vortex, which is developed further on at both tube sides with rotating direction contrary towards the



#### 4. Experimental and Numerical Results

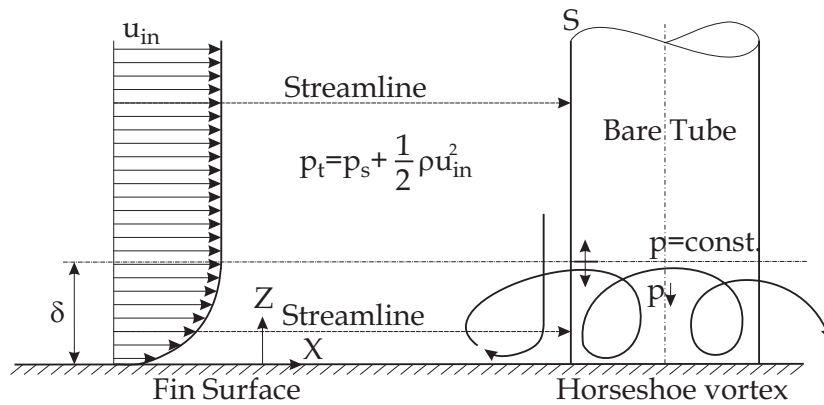


Figure 4.39.: Formation of Horseshoe Vortex at the Leading Part of the Tube

fin surface. This is schematically depicted in Figure 4.39. An increase in total heat transfer rate in front of the cylinders and low heat transfer coefficients in the wake region downstream of the finned-tube is involved. As remarked in [58] the high heat transfer at the leading part of the fins may be attributed to its sharp edges.

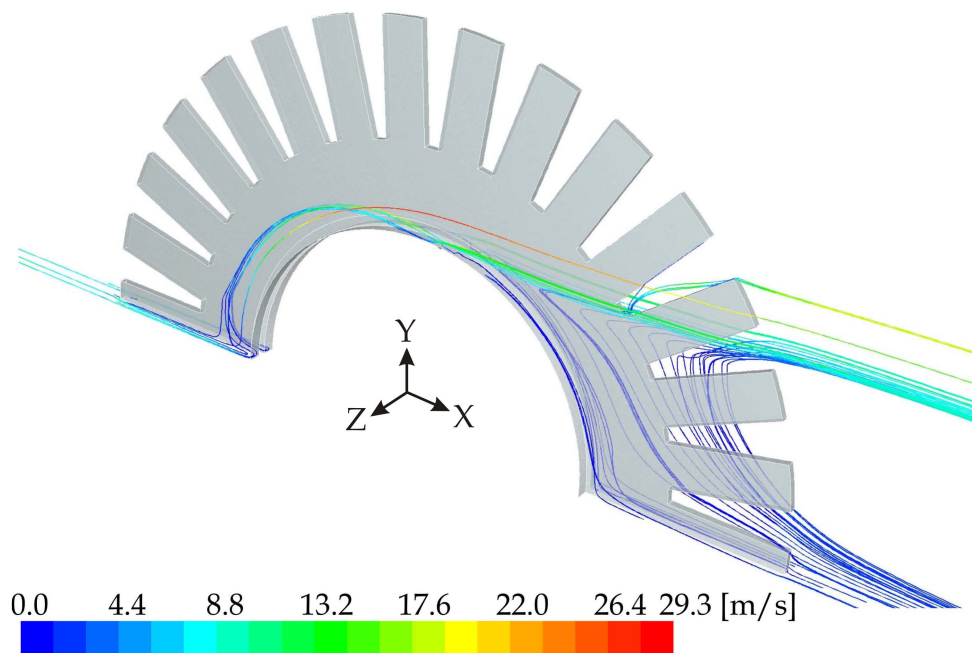


Figure 4.40.: Calculated Possible Pathlines with Local Velocity Upstream/Downstream above Circular Segmented Fin-Surface

In Figure 4.40 possible pathlines with local velocity upstream/downstream above

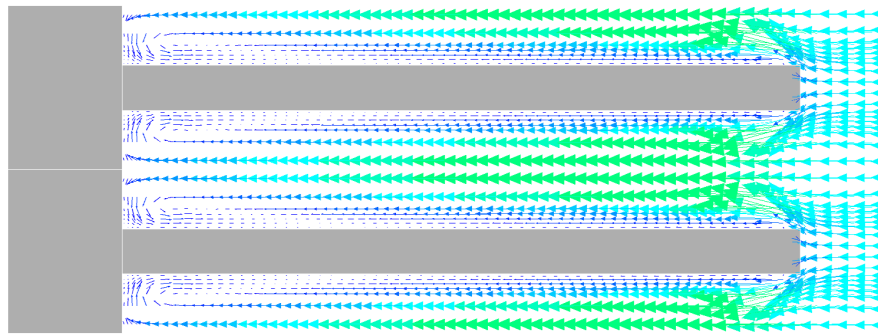
#### 4. Experimental and Numerical Results

circular segmented fin-surface are depicted schematically. As shown in the leading part of the fin tube, a horseshoe vortex system occurs curling towards the finned surface. These secondary flow mechanisms cause intermixtures and transport heat from the hot main stream flow to the cold fin and from the cold fin to the channel center.

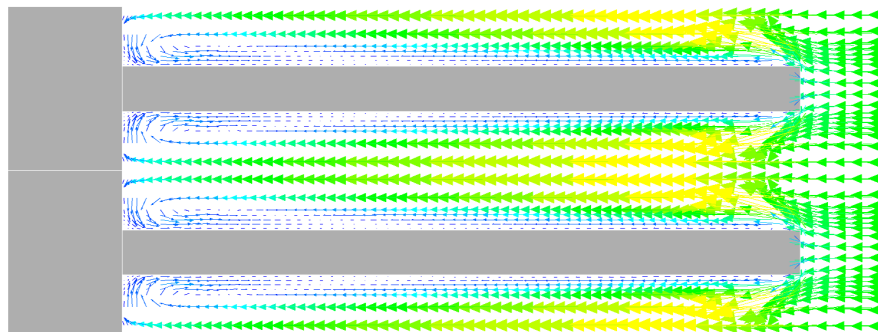
The local velocity distribution between adjacent circular solid fins at angle  $\Theta = 0^\circ$  in symmetry-plane is depicted in Figures 4.41(a) to 4.41(c). The inlet velocity is varied in between  $u_{in} = 3 \div 7 \text{ m/s}$ . At the fin tip a turbulent boundary layer starts to grow and as the fluid streams along the fin surface, the velocity reduces. A secondary flow mechanism is developed near the fin base of bare tube diameter.

In Figures 4.42(a) to 4.43(b) the difference between the local velocity distribution of adjacent circular segmented I-shaped and U-shaped fins is presented. Similar to the graphs shown above a boundary layer is developed starting from the fin tip. Generally, no considerable difference between the I-shaped fin compared to the U-shaped fin may be observed within the *CFD*-simulations. But carefulness by judging qualitatively has to be paid to the fact that the comparison is realized at different inlet velocities and thus a different flow field will occur.

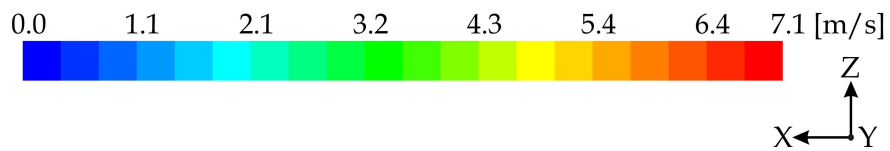
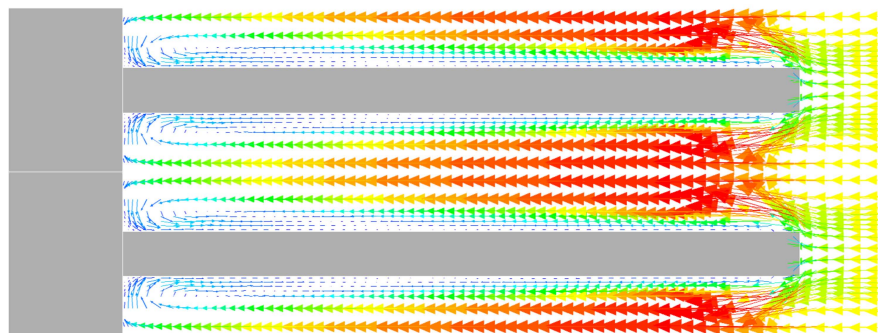
#### 4. Experimental and Numerical Results



(a) at  $u_{in} = 3 \text{ m/s}$ ,  $Re \approx 8900$



(b) at  $u_{in} = 5 \text{ m/s}$ ,  $Re \approx 14600$



(c) at  $u_{in} = 7 \text{ m/s}$ ,  $Re \approx 20200$

Figure 4.41.: Local Velocity Distribution in  $[m/s]$  between Adjacent Circular Solid Fins in Symmetry-Plane

#### 4. Experimental and Numerical Results

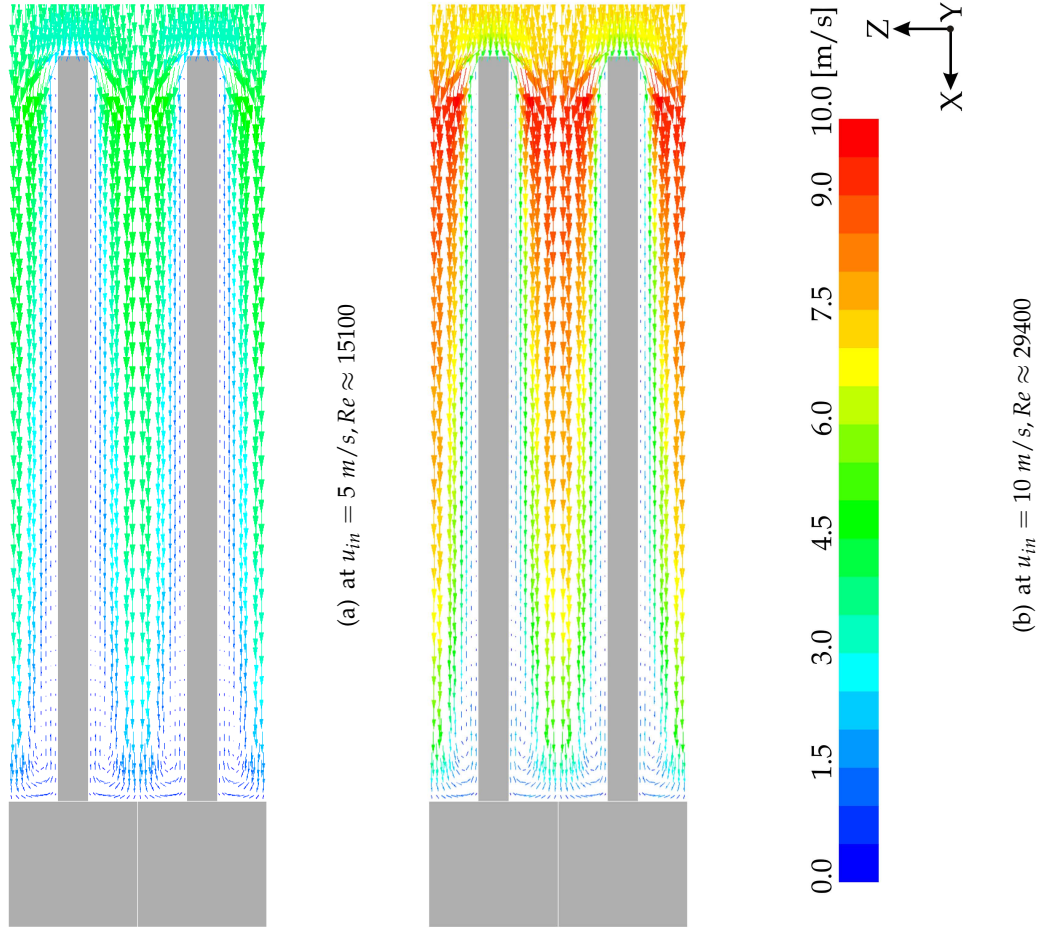


Figure 4.42.: Local Velocity Distribution in [m/s] between Adjacent Circular Segmented I-Shaped Fins in Symmetry-Plane

#### 4. Experimental and Numerical Results

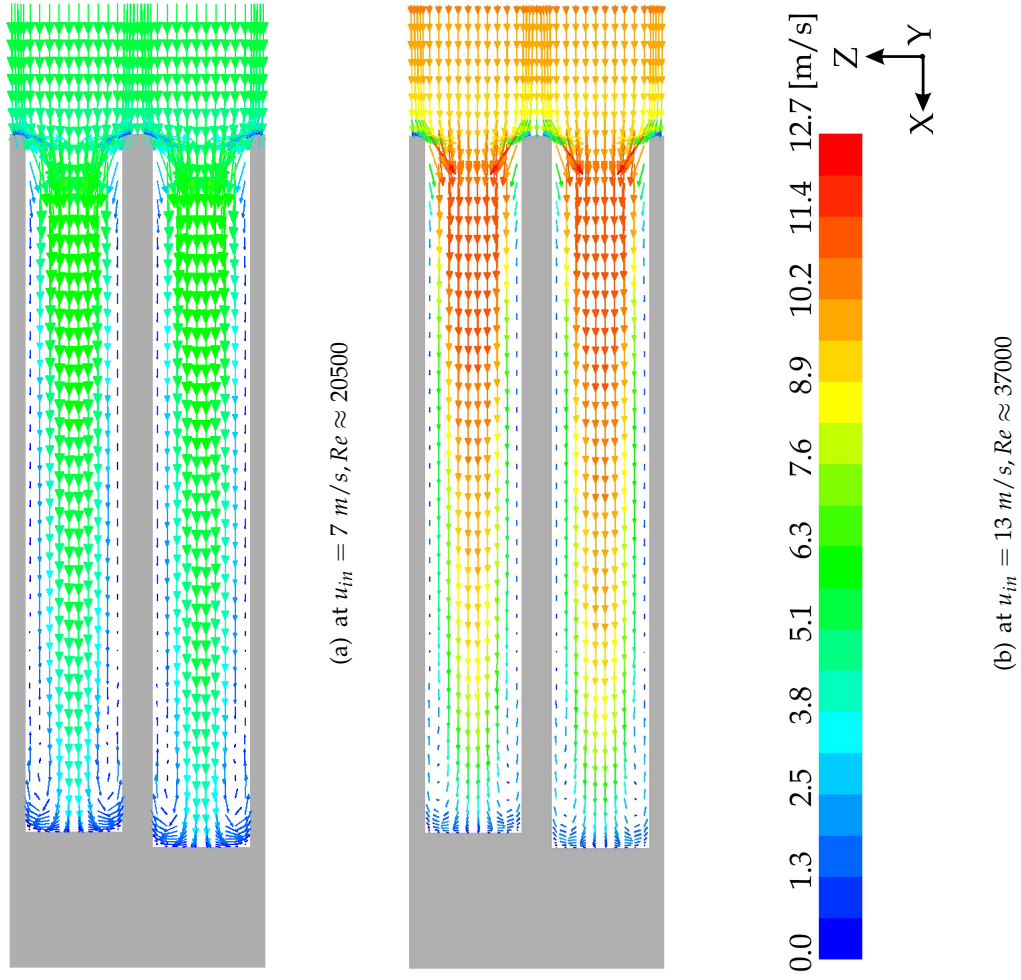


Figure 4.43.: Local Velocity Distribution in [m/s] between Adjacent Circular Segmented U-Shaped Fins in Symmetry-Plane

##### 4.6.2. Heat Transfer Behavior

A conjugate heat transfer problem is influenced mainly by the flow field. In this section the thermal boundary layer formation, the temperature distribution within the fin and across the fin surface, and the distribution of the heat transfer coefficient averaged circumferentially as well as radially will be discussed.

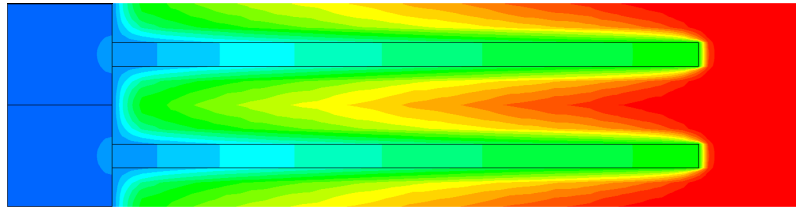
##### Thermal Boundary Layer and Temperature Distribution within the Fin

The formation of thermal boundary layers constrains flow interactions between the two adjacent fins. For this reason STASIULEVICIUS, [58] suggested at least two thicknesses of boundary layers as fin clearance. MON, [46], investigated numerically the influence of different fin clearances on the temperature distributions between the adjacent circular solid fins and found in the course of the validity in their study that the two boundary layers grow to touch each other at the narrowest fin clearance of 1.6 mm.

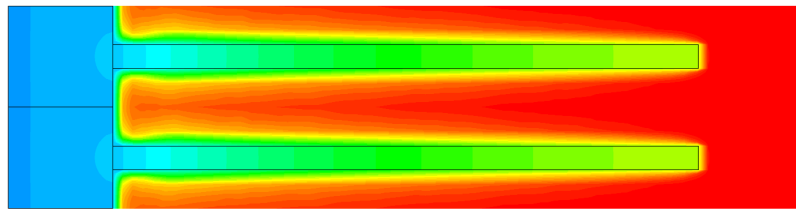
An examination of Figures 4.44(a) to 4.44(d) shows the development of the thermal boundary layer starting from the fin tip as evaluated from the *CFD*-calculation of the I-shaped segmented circular finned-tube. The fluid flow is in positive *X*-direction at constant angle  $\Theta = 0^\circ$ , related to the stagnation line. At  $Re = 4750$  the two boundary layers grow to touch each other. This causes a steep temperature gradient between fin base and fin tip and reduces the air-sided heat transfer coefficient. Similar results are obtained by MON, [46]. As interpreted from the graphs, starting from  $Re > 15100$  the main flow would be able to penetrate the bare tube surface. This effect reveals superior results with increasing Reynolds number. A comparison with results evaluated for U-shaped finned-tubes (Figures 4.45(a) to 4.45(d)) displays equal behavior. Starting from approximately  $Re = 12000$  the impact of horseshoe vortex systems influences the temperature gradient at the fin base, where the main flow of nearly inlet conditions with 480 K is able to heat up the bare tube surface. The upstream inlet temperature at the gas-side (dry air) and the free stream temperature at the internal tube-side are defined to be constant with an appropriate heat transfer coefficient of the adjacent fluid inside the tube. Thus, the wall temperature is obtained for a given free stream inlet temperature and material of the finned-section and varies for different inlet velocity ( $u_{in} = 1.3 \div 13 \text{ m/s}$ ).

As stated in [58], at thick-walled finned-tubes the radial temperature gradient is the controlling factor. Considering this fact, no remarkable difference between the U-shaped fin compared to the I-shaped fin as well as the wall of the tube may be observed within the *CFD*-simulations, although the comparison is realized at different inlet velocities and thus a different flow field occurs. However, in the course of this study the main fluid flow and thermal behavior will be mainly observed qualitatively applying an idealized calculation model and makes no claim of being fully detailed as it occurs under real industrial conditions.

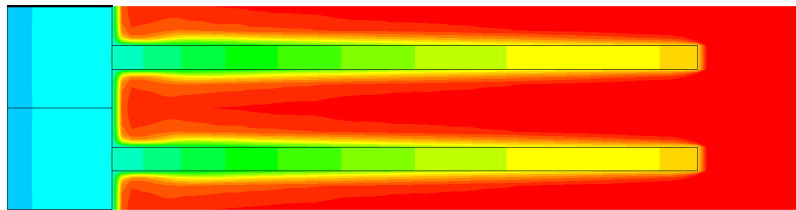
#### 4. Experimental and Numerical Results



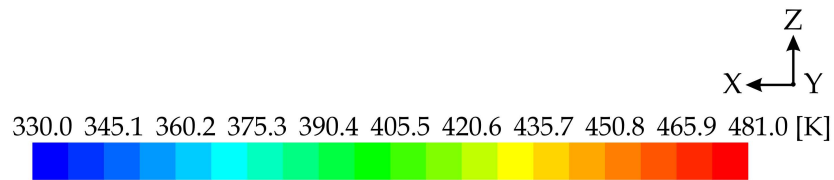
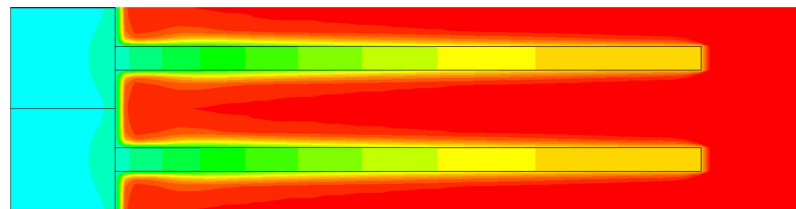
(a) at  $u_{in} = 1.5 \text{ m/s}$ ,  $Re \approx 4750$



(b) at  $u_{in} = 5 \text{ m/s}$ ,  $Re \approx 15100$



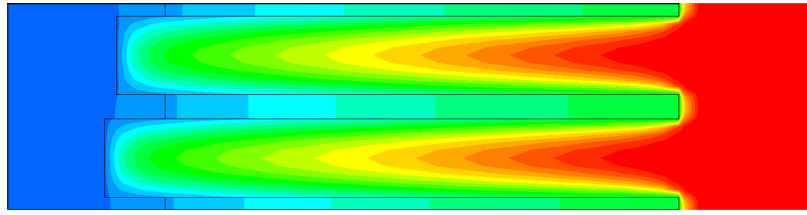
(c) at  $u_{in} = 10 \text{ m/s}$ ,  $Re \approx 29400$



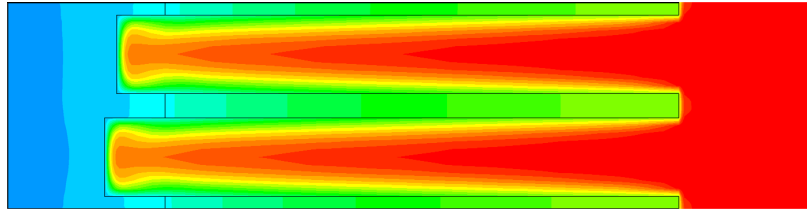
(d) at  $u_{in} = 13 \text{ m/s}$ ,  $Re \approx 37700$

Figure 4.44.: Contour of the Local Temperature Distribution of the Fin and between Adjacent Circular I-Shaped Segmented Fin-Surface in Symmetry-Plane

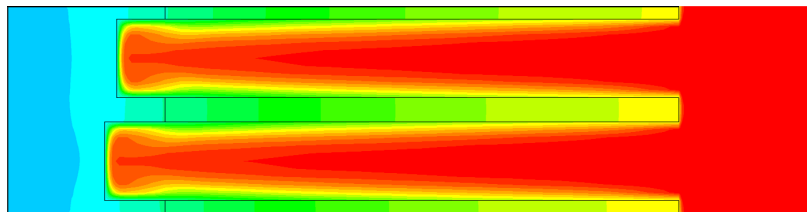
#### 4. Experimental and Numerical Results



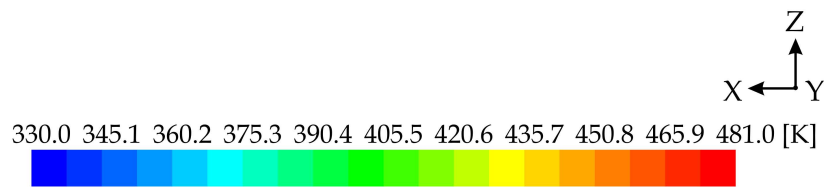
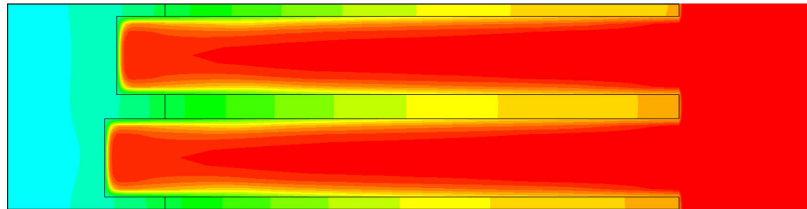
(a) at  $u_{in} = 1.3 \text{ m/s}$ ,  $Re \approx 4000$



(b) at  $u_{in} = 4 \text{ m/s}$ ,  $Re \approx 12000$



(c) at  $u_{in} = 7 \text{ m/s}$ ,  $Re \approx 20500$



(d) at  $u_{in} = 13 \text{ m/s}$ ,  $Re \approx 37000$

Figure 4.45.: Contour of the Local Temperature Distribution of the Fin and between Adjacent Circular U-Shaped Segmented Fin-Surface in Symmetry-Plane



### Temperature Distribution above the Fin Surface

Figures 4.46(a) to 4.46(c) present the contour of the local temperature distribution at the circular segmented finned-surface. The fluid flow is in positive X-direction at constant angle  $\Theta = 0^\circ$  related to the stagnation line<sup>17</sup>. The inlet velocity is varied in between  $u_{in} = 1.5 \text{ m/s}$  and  $u_{in} = 10 \text{ m/s}$ . As shown, the highest temperatures are located at the surface part of segments in between the transversally arranged tubes, near  $\Theta = 270^\circ$  (positive Y-direction), which corresponds to the narrowest flow passage. At high  $Re$ -numbers a steep temperature gradient occurs at the leading part of the fin tube as well as the tailing zone, while at low  $Re$ -numbers a more or less uniform temperature profile is found especially at the tailing zone of the tube, indicating a higher influence of conduction to the conjugate heat transfer problem. Generally, the lowest temperatures are located in the tailing part of the tube (downstream part of fin).

The results of the local temperature distribution at circular solid finned-tubes is presented in Figures 4.47(a) to 4.47(c). Contrary to the results of the segmented fins, the highest temperatures are found to be located near the leading point of the finned section. The inlet velocity is varied in between  $u_{in} = 3 \text{ m/s}$  and  $u_{in} = 7 \text{ m/s}$ . At high  $Re$ -numbers a steep temperature gradient occurs at the leading part of the fin tube as well as the tailing zone, but also at low  $Re$ -numbers a steeper temperature profile is calculated at the tailing zone of the solid fin than of the tube with segmented fins. The slight difference in the  $Re$ -numbers in between these two fin types at  $u_{in} = 5 \text{ m/s}$  can be explained by different inlet flow cross-sections. The evaluated results correspond to simulations presented by e.g. [46] and [58]. STASIULEVICIUS, [58], performed measurements applying the local heating method in a cooling process. They found a temperature maximum which is located in the tailing region of the tube (heat flows from base to the tip of the fin).

### Heat Transfer Coefficient Distribution above the Fin Surface

High temperature differences between wall and air (reference temperature) evaluate for high heat transfer coefficients at the air-side. According to individual authors, [46], [34], and [2] the local heat transfer coefficient reads

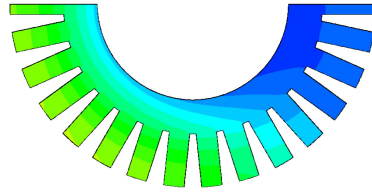
$$\alpha(x, y) = \frac{\dot{q}(x, y)}{T_{in} - T_{wall}(x, y)} = \frac{\lambda \frac{\partial T}{\partial z}|_{wall}}{T_{in} - T_{wall}(x, y)}. \quad (4.36)$$

In this work,  $T_{in}$  is chosen as the reference temperature. LEGKIV ET AL., [40], calculate the heat transfer coefficient from the average air temperature between inlet and outlet. MON evaluated the local  $Nu$ -number based on the inlet temperature of air<sup>18</sup>.

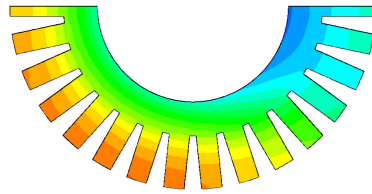
<sup>17</sup>Equal denotation may be found in [46], [32]

<sup>18</sup>Carefulness should be paid to all evaluations of the averaged local heat transfer coefficients, being valid for average values of air velocities; the calculations should be seen basically qualitative to give any idea about their distribution.

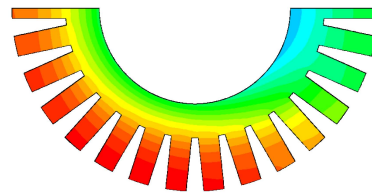
#### 4. Experimental and Numerical Results



(a) at  $u_{in} = 1.5 \text{ m/s}$ ,  $Re \approx 4750$



(b) at  $u_{in} = 5 \text{ m/s}$ ,  $Re \approx 15100$



(c) at  $u_{in} = 10 \text{ m/s}$ ,  $Re \approx 29400$



Figure 4.46.: Contour of the Local Temperature Distribution in [K] at the Circular Segmented Fin-Surface

#### 4. Experimental and Numerical Results

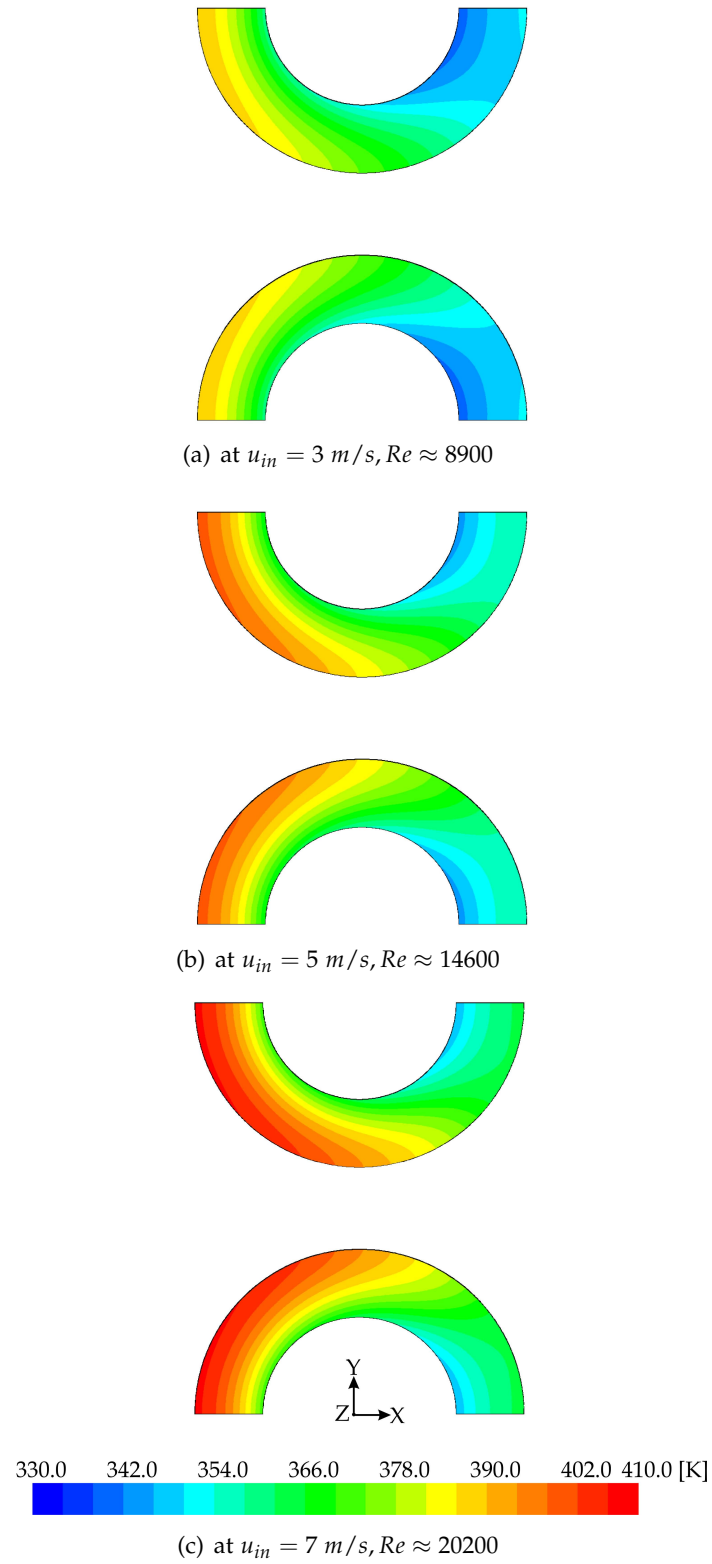


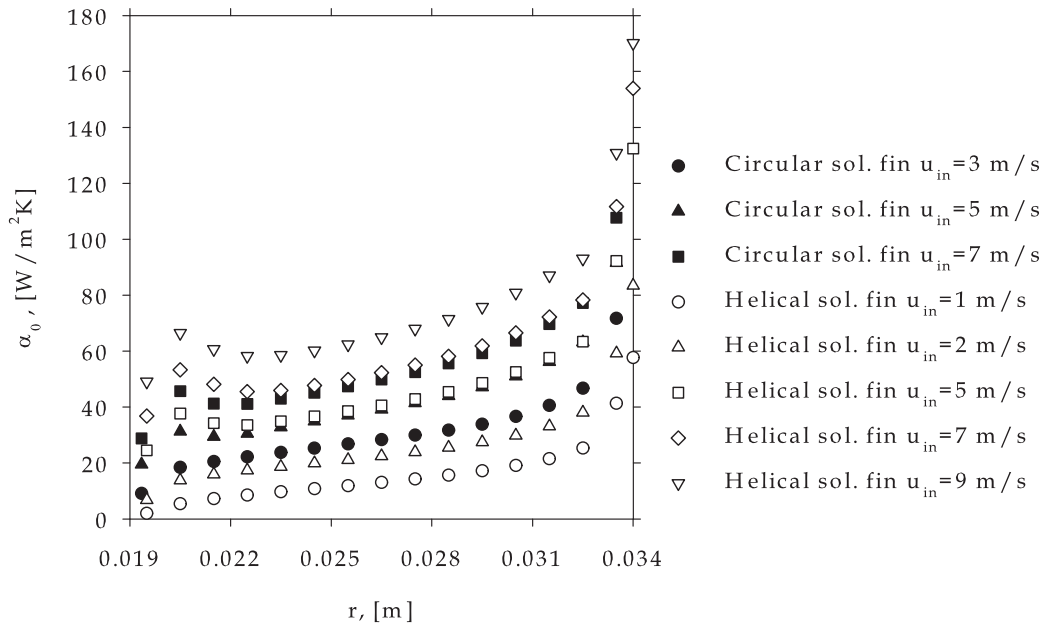
Figure 4.47.: Contour of the Local Temperature Distribution in [K] at the Circular Solid Fin-Surface

#### 4. Experimental and Numerical Results

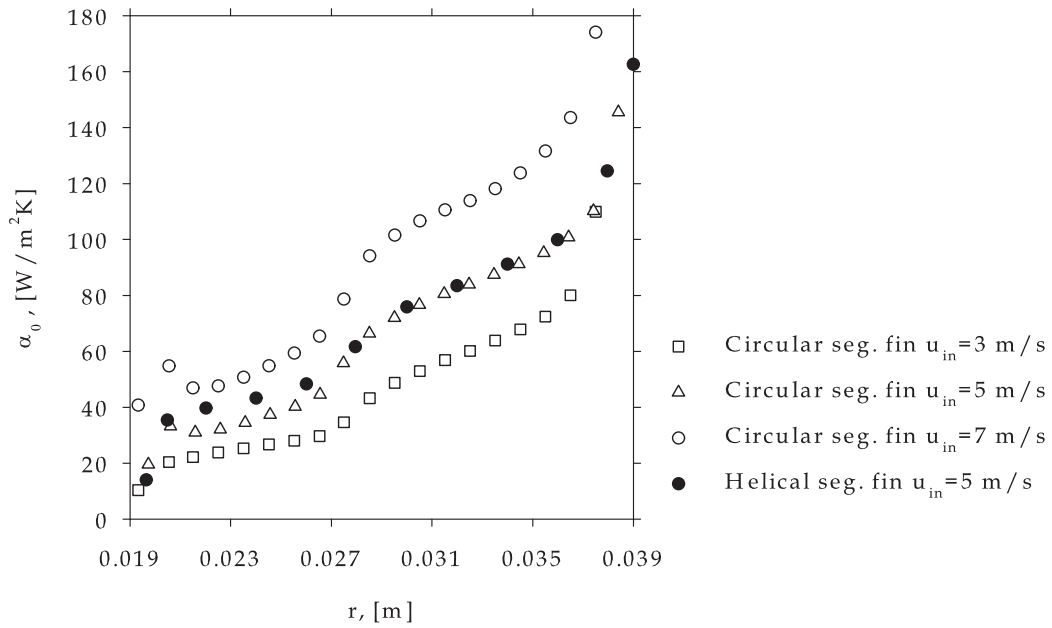
In Figures 4.48(a) and 4.48(b) the circumferentially averaged heat transfer coefficient at circular/helical solid as well as segmented fin surface is depicted. The convective boundary layer thickness increases as the fluid streams along the fin surface, thus the heat transfer coefficient at the fin base decreases. As in the literature review stated, LEGKIV ET AL., [40], reported that two heat transfer coefficient maxima occur at the solid fin surface, one at the fin tip and the other at the fin base. A slight increase at the fin base, especially at helical fins at high  $Re$ -numbers, may be also interpreted by precise inspection of Figure 4.48(a) and 4.48(b). This effect may be caused by the occurring of horseshoe vortex systems and seems to be also observed at segmented fins. At the fin tip a maximum of heat transfer coefficients occurs at both solid and segmented fins. This may be interpreted as follows: Due to no slip condition at the solid fin surface, a hydrodynamic boundary layer starts growing from the fin tip along the fin surface. The heat transfer coefficient may change along the region where the boundary layer thickens. Considering Figures 4.48(a) and 4.48(b) also a slight difference between circular and helical fin can be interpreted. The relation of the local heat transfer coefficient  $\alpha_0$  to the evaluated average value  $\bar{\alpha}_0$ , depicted in Figures 4.49(a) to 4.49(b), shows the difference between solid and segmented fins.  $\alpha_0/\bar{\alpha}_0 = 1$  is already reached in the first half of the fin height, while at solid tubes the compensation takes place in the second half of the fin height, starting from the bare tube diameter. The variation in heat transfer coefficient along the fin height is approximately  $200 \div 300\%$ , but attention has to be paid to the high heat transfer coefficients near the stagnation line at the finned tip section, evaluated from the *CFD*-simulations; compare with results obtained by [58].

In Figures 4.50(a) and 4.50(b) the radially averaged heat transfer coefficient at circular solid as well as segmented fin surface, evaluated for discrete angles ( $\Delta\Theta$ ), is depicted as a function of the angle  $\Theta$ . The orientation of  $\Theta$  is counter-clockwise. The parameter study of different  $Re$ -numbers (at the solid as well as the segmented fin surface) gives information about the distribution of the heat transfer coefficient.  $\alpha_0$  increases significantly with increasing  $Re$ -number. At  $\Theta \approx 70 \div 90^\circ$  a maximum is attained, further on the heat transfer drops off steeply and at  $\Theta \approx 135 \div 150^\circ$  it increases again slightly. STASIULEVICIUS, [58], ascribes this steep drop-off in heat transfer due to flow separation, where the position depends on the type of boundary layer. Qualitatively, the obtained results are stated in good agreement with literature, see e.g. [58] and [40]. The higher average heat transfer coefficient values of the "zig-zag" characteristics as displayed at the segmented fin surface include the radial part, starting at the fin-base and ending at its tip; the lower  $\alpha_0$ -values are for the radial part of the fin without the segment, refer to Figure 2.9. It has to be remarked finally that all *CFD* calculations are performed at steady state conditions, thus any insight into periodic wake effects can not be provided in the course of this work.

#### 4. Experimental and Numerical Results



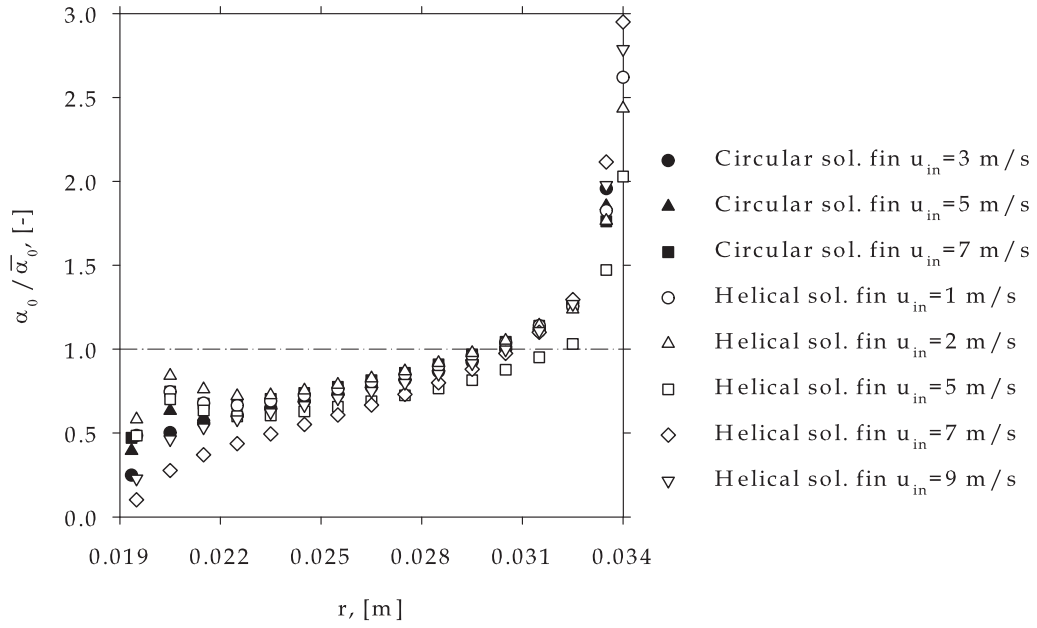
(a) at the Circular/Helical Solid Fin-Surface



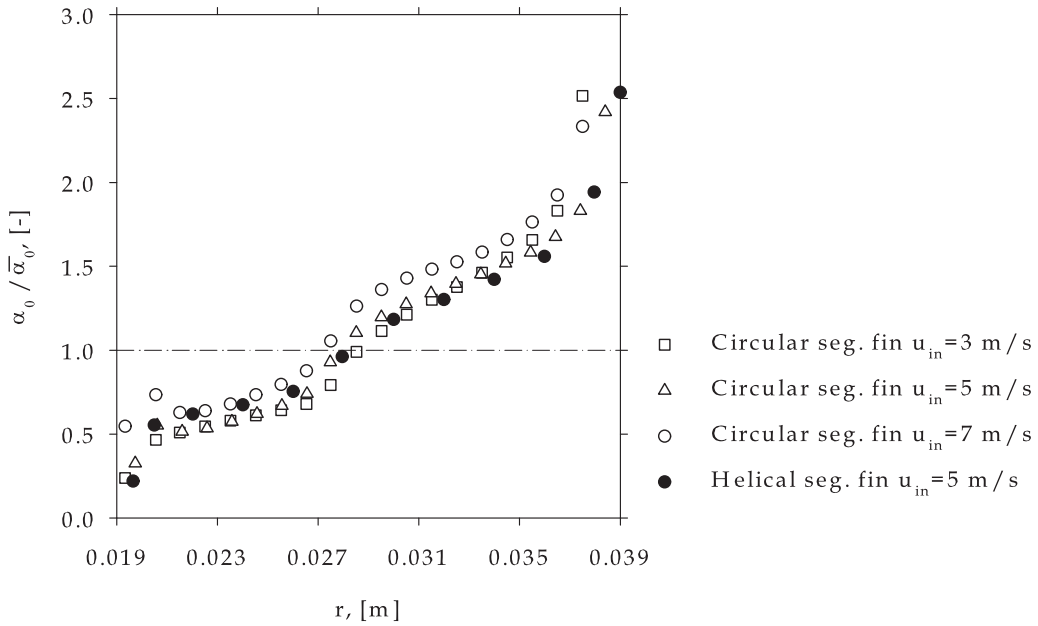
(b) at the Circular/Helical Segmented Fin-Surface

Figure 4.48.: Circumferentially Averaged Heat Transfer Coefficient

#### 4. Experimental and Numerical Results



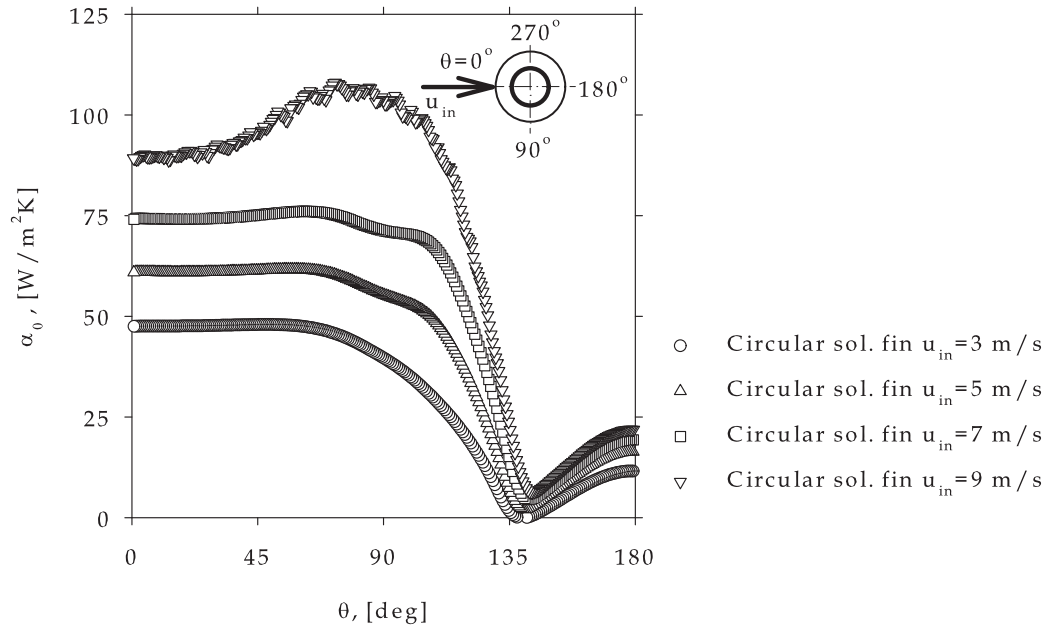
(a) at the Circular/Helical Solid Fin-Surface



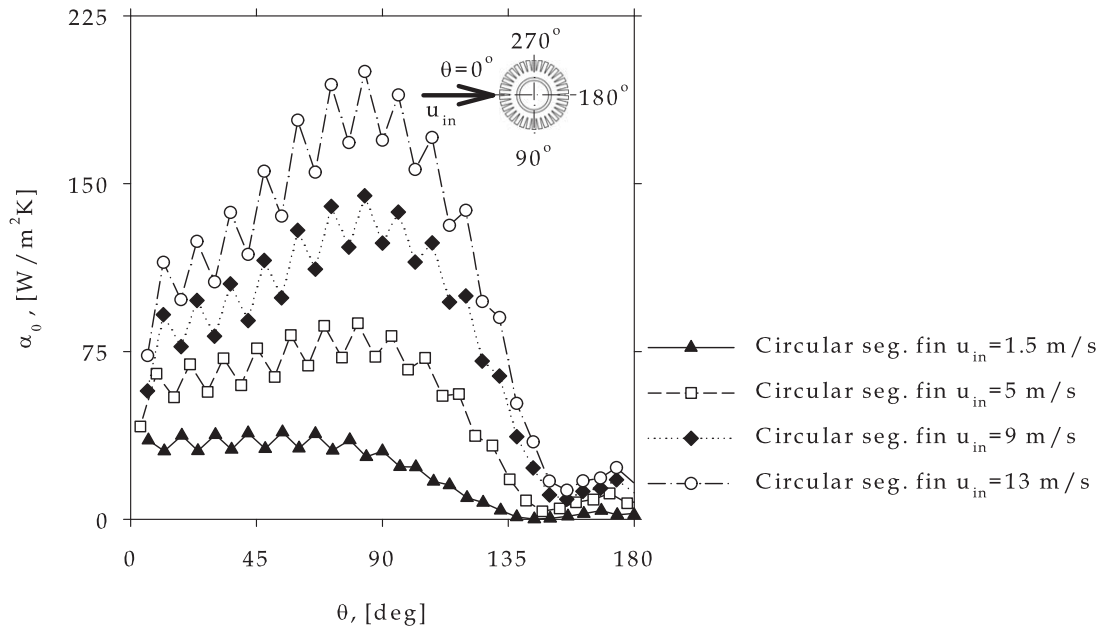
(b) at the Circular/Helical Segmented Fin-Surface

Figure 4.49.: Relative Circumferentially Averaged Heat Transfer Coefficient

#### 4. Experimental and Numerical Results



(a) at the Circular Solid Fin-Surface  $\Delta\Theta \approx 0.7^\circ$



(b) at the Circular Segmented Fin-Surface  $\Delta\Theta \approx 6^\circ$

Figure 4.50.: Radially Averaged Heat Transfer Coefficient at Discrete Angles ( $\Delta\Theta$ )

## 5. Summary and Conclusions

The enchanting charms of this sublime science reveal themselves in all their beauty only to those who have the courage to go deeply into it.

*Carl Friedrich Gauss*

★

Global and local heat transfer as well as pressure drop interactions across circularly and helically segmented finned-tube surfaces in cross-flow require extensive research, because a more complete understanding of local transport mechanisms may improve heat exchanger performance as well as provide the possibility of advanced design recommendations.

In this work experimental investigations in industrial scale at different finned-tube bundle configurations of equal transversal and longitudinal pitch in staggered formation were accomplished. In the course of the experimental investigations preliminary tests at solid and segmented finned-tubes as well as tests at the unloaded channel were performed, followed by measurements at 8, 6, 4, and 2 consecutively arranged finned-tube rows, measurements at 1 heated finned-tube row with 7 consecutively arranged unheated rows, measurements at 1 finned-tube row with/without a semi-tube installed at the channel-wall, as well as temperature dependence and stability tests. The Reynolds number was varied in the range between 4500 and 35000. A subsequently performed measurement validation was addressed to fulfill the energy balance of the used system boundaries. Furthermore, an uncertainty calculation was proceeded to give any association or insight to the size of the measured quantities. Additionally, global as well as local effects of conjugate heat transfer and fluid flow was investigated applying a three dimensional steady state numerical simulation. Five different models of a single row finned-tube heat exchanger with solid and segmented fins were developed. The fins with U-shape and I-shape are arranged circularly or helically on the bare tube in cross-flow. Especially any difference between segmented I-shape and U-shape fin surface as well as solid and serrated fins was analyzed. It was



## 5. Summary and Conclusions

intended to calibrate the CFD-calculations within the computational model boundaries with those calculated from the measurements at the test rig. Thus, any effects from global to local behavior of the thermal field as well as convective transport phenomena have been examined.

### Global Behavior

From an evaluation of the experimental results it was found that the difference between counter-flow and counter cross-flow in the formula for the calculation of the *LMTD* decreases with an increasing number of consecutively arranged tube rows. Thus, in this study in case of a single tube row due to small average mean error of 3%, the *LMTD* was calculated for all configurations using the equation for counter-flow heat exchangers.

As a result of the investigations new heat transfer coefficient and pressure drop coefficient correlations, applicable for helically U-shaped as well as I-shaped segmented finned-tubes within the stated range of validity, have been developed. A comparison of the proposed equation for the Nusselt number with the simulation as well as most measurement results are found to be accurate within about  $\pm 15\%$ ; for the equation of the pressure drop coefficient an uncertainty of  $\pm 20\%$  may be found. The performed uncertainty calculation of the total heat transfer measurements indicates that approximately 80% of the measurands have a relative uncertainty laying within  $\pm 15\%$  and it may be agreed that the relative uncertainties for the pressure drop coefficient, evaluated for the channel wall and channel center, for 80% of the measurands are  $\pm 20\%$ . The pressure drop correlation is developed for a 8 row deep tube bundle, since  $\xi_1$  at the channel wall increases for low *Re*-numbers at few tube rows. This effect may be attributed to bypass flow between tubes and channel i.e. top, bottom, and two side walls (necessary space for the double helix of the U-shaped finned-tube as well as insufficient alignment of the tubes), because this influence is reduced, as the number of consecutively arranged tubes increases.

Another result of these studies comprises an increase in heat transfer for finned-tube heat exchangers with different number of consecutive tube rows arranged in flow direction, which tend to be constant for 8 row deep heat exchangers. An average mean row correction factor, originally a function of the Reynolds number and the number of tube rows, was developed for a representative number of measured points within the *Re*-range of approximately  $7000 \leq Re \leq 30000$ . Between low  $Re \approx 7000$  and high  $Re \approx 30000$ , this reduction varies in the range of about  $\pm 15\%$ . The average mean heat transfer seems to increase degresively from row-to-row, i.e. first to second row about 13.3%, second to fourth row about 10.9%, and fourth to sixth row about 5.5%.

The correlation's ability is demonstrated using different literature case studies. A

## 5. Summary and Conclusions

comparison of the developed heat transfer correlation (Equation (4.15)) with available literature, which is explicitly defined to be valid for segmented fins, shows a relative deviation of approximately  $\pm 20\%$ . Good agreement may be found by a comparison with the traditional  $ESCOA_{TM}$ -correlation. Here the relative deviation ( $\approx 10\%$ ) is evaluated more or less constantly within the investigated  $Re$ -range. As a comparison with literature of solid finned-tubes indicates, an application of segmentation would expect much higher Nusselt numbers. In the course of the generation of the correlation it turned out that the influence of the exponents in the geometry functions is very small, thus a simplified ansatz, applying  $C_1$  as a constant for the consideration of the influence on geometrical parameters and tube bundle arrangement, was used. The difference between these two equations is roughly 5%. The calculated relative deviations of pressure drop coefficient data, evaluated for a single tube in cross-flow, are within about  $\pm 20\%$ . As presented, a comparison of the pressure drop correlation (Equation (4.26)) with literature tends to higher deviations, due to the fact of the improved power-law ansatz (Power (a,b,c)). Generally a comparison between the developed equation and literature attributes the same characteristics. The comparison between literature and simulation of the helically segmented finned-tubes pronounces a good agreement.

A comparison of the investigated fin tubes also revealed a decrease in heat transfer as well as fin efficiency with greater fin height. Thus, an optimal fin height may be determined and/or achieved, e.g. by using second law analysis or performance evaluation criteria. The application of second law analysis on the evaluated measured data produced high fluctuating values and indicated thus inapplicability for the measurement configuration. For this reason a performance evaluation criterion for single-phase flows was applied to characterize the efficiency of the various finned-tube bundles. When comparing segmented finned-tubes, three ranges may be identified:  $Re \leq 10000$ ,  $10000 \leq Re \leq 20000$ , and  $Re \leq 20000$ . Despite varying fin height and fin pitch in the two different geometries, no substantially differing tendencies may be observed when applying these equations especially at  $10000 \leq Re \leq 20000$ . A comparison of solid and segmented finned-tubes revealed a general increase in the air-side heat transfer coefficient within the investigated Reynolds range. Furthermore, the validated measured values for solid and segmented I-shaped finned-tubes displayed good agreement especially with the formula of  $ESCOA_{TM}$ .

The result of the comparison of all gathered heat transfer data from measurements, performed on a single U-segmented finned-tube row in cross-flow with a semi-tube installed at the channel wall, and the corresponding CFD calculations is found to be in excellent agreement with a small deviation. A qualitative and quantitative pressure drop coefficient comparison of the experiment at 8 tube rows (evaluated for a single tube row) with the CFD-calculation shows good agreement especially in the  $Re$ -range

## 5. Summary and Conclusions

of about  $6000 \leq Re \leq 20000$ . At higher Reynolds numbers than 20000 up to 50000, a diverging effect was observed. Generally, the calculated  $\zeta$  from the CFD-simulation of the helical fin-tube shows better agreement with measurement than the circular ones. A comparison of the heat transfer at a single solid finned-tube row shows a good congruence. However, in the whole  $Re$ -range, the CFD-calculation would predict slightly higher dimensionless heat transfer coefficients than the evaluated measured values and this effect is increased if the difference of  $F_{min}$  between simulation and measurement is considered, which corresponds to the pressure drop coefficient comparison. Generally, the simulation results tend to lower pressure drop coefficients than the measurement. Considering this fact of the relative difference of the minimum net free area between a tube row of about 13%, these results may found to be in a realistic agreement.

### Local Behavior

Apart from global transfer behavior, some local effects may be indicated in the course of the investigation. The boundary layer thickness at the finned surface obviously decreases with increasing Reynolds number and the heat transfer coefficient may change along the region where the boundary layer thickens. It may be concluded that the heat transfer declines with increasing boundary layer thickness.

As a result of an adverse pressure gradient, horseshoe vortex systems developed. These secondary flow mechanisms near the fin base and bare tube diameter were observed in the course of these studies within all different finned-tube models.

As the investigations of the local velocity distribution indicate, no considerable difference between the segmented I-shaped fin compared to the U-shaped fin may be observed.

At low  $Re$ -numbers two boundary layers between the two adjacent segmented fins grow to touch each other, which causes a steep temperature gradient and comprises low heat transfer. The simulations indicate that the main flow would be able to penetrate the bare tube surface starting from the mid  $Re$ -range. A comparison between U-shaped and I-shaped finned-tubes may display equal behavior.

As remarked in literature very high temperatures and heat transfer at the leading part of the fins are observed from an evaluation of possible solutions from the CFD-simulation.

The investigated temperatures across the circular segmented finned-surfaces indicate that the highest temperatures are located at the surface part of segments in between the transversally arranged tubes. Steep temperature gradients occur at high

## 5. Summary and Conclusions

*Re*-numbers, while at low *Re*-numbers a more or less uniform temperature profile may be found especially at the tailing zone of the tube. The evaluated results of circular solid finned-tubes show contrary behavior. The highest temperatures are found to be located near the leading point of the finned section.

As remarked in literature two heat transfer coefficient maxima at the fin tip and at the fin base may be interpreted by evaluating the circumferentially averaged heat transfer coefficient at circular/helical solid as well as segmented fin surface. The occurring maximum at the fin base may be attributed to horse-shoe vortex systems. A slight difference between circular and helical fin may also be interpreted.

From the evaluations a variation of the local heat transfer coefficient related to the evaluated average value along the fin height of approximately  $200 \div 300\%$  may be found. However, very high heat transfer coefficients near the stagnation line at the finned tip section are evaluated from the *CFD* simulations. This effect may be attributed to the used *CFD* turbulence model (e.g. stagnation point anomaly effects), although influences caused by flows with rapid rate of strains will have a positive impact imposed by the strain-dependent correction term in the RNG  $k - \epsilon$  turbulence model.

The parameter study indicates that the radially averaged heat transfer coefficient at circular solid as well as segmented fin surface increases significantly with increasing *Re*-number. At  $\Theta \approx 70 \div 90^\circ$  a maximum is attained; qualitatively the obtained results are stated in good agreement with literature.

### Concluding Remarks

Apart from many insufficient differences between the simulation model and the exact realistic application (inclination and deformation of the individual fin segments, especially chosen surface roughness, contact face between fin and tube, perfect arrangement of the tube in the channel, facing fin tip on fin tip in transversal direction, and no bypass effect as well as geometrical imperfectness) these studies prove to provide details, further insight, and knowledge of fluid flow and local heat transfer distribution within these complex flow passages, and are addressed to give a more complete understanding of the performance of heating surfaces applied in HRSG. Finally it may be suggested to investigate in a further study influences caused by periodic wake effects and their impact on local mass transfer in the course of unsteady *CFD* simulations.

## A. Test facility

The Figures A.1(b) to A.2 depicts some details of the investigated finned-tube as well as the test-channel.



(a) Fin Section

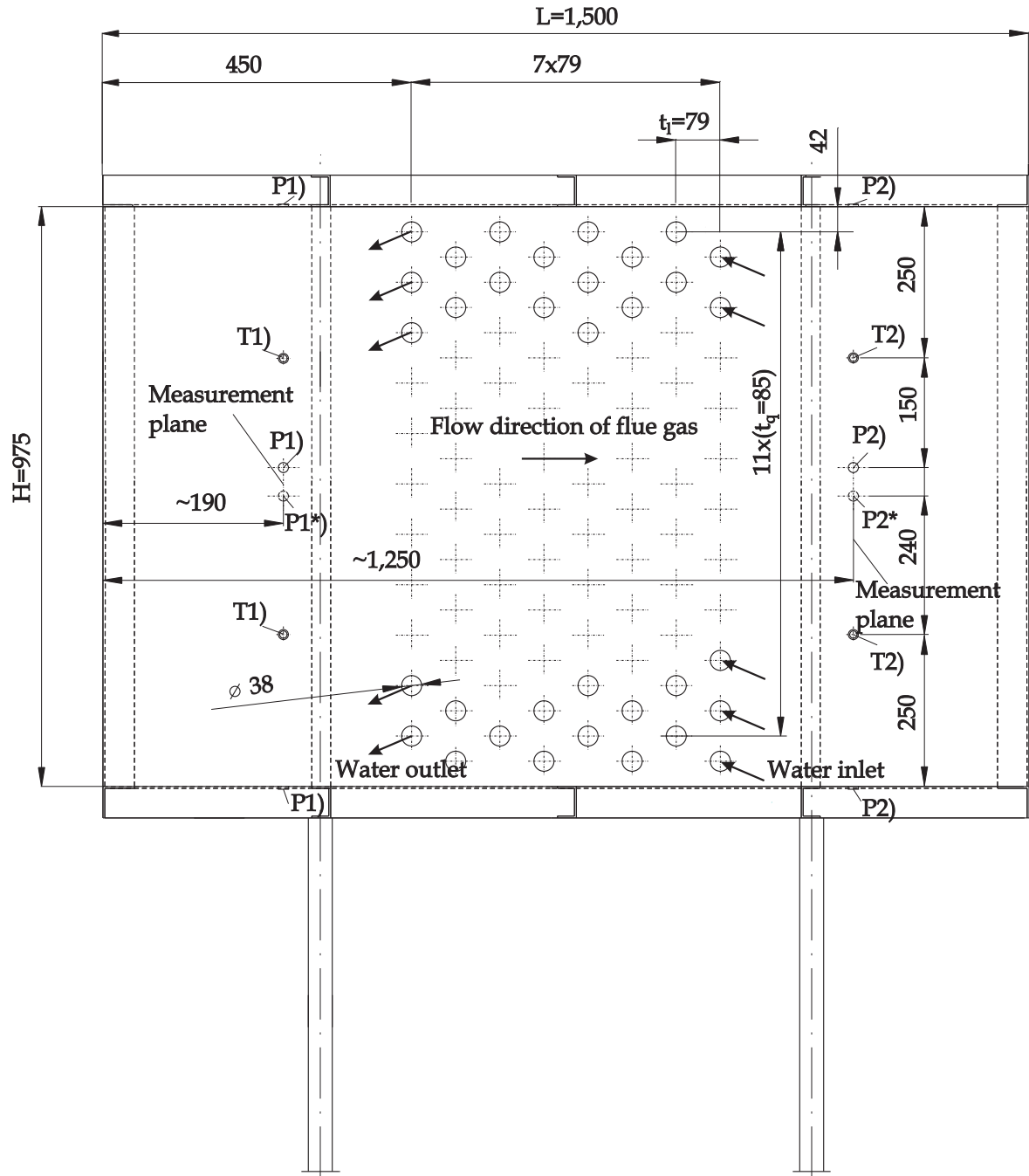


(b) Torsion of the Fins

(c) U-Shaped Fin

Figure A.1.: Finned-Tube

### A. Test facility



- |            |   |
|------------|---|
| P1*), P2*) | Borehole for installation of pitot-static probe                     |
| P1), P2)   | Borehole for static-pressure measurement in an closed circular pipe |
| T1), T2)   | Borhole for installation of thermocouple                            |

Figure A.2.: Sketch of the Test Section

## B. Thermo-Physical Properties

### B.1. Experiment

- **Finned-Tube Material**

For the calculation of the heat transfer coefficient, the following thermo-physical properties according to literature are used, [42]:

$$\lambda_{cs} = A + B\vartheta + B\vartheta^2 + C\vartheta^3 \quad (\text{B.1})$$

Geometry	Material	A $\left[\frac{\text{W}}{\text{mK}}\right]$	$10^2$ B $\left[\frac{\text{W}}{\text{mK}^2}\right]$	$10^5$ C $\left[\frac{\text{W}}{\text{mK}^3}\right]$
Fin	DC 01	58.4	−2.21	−2.33
Tube	St35.8	55.3	−3.35	−0.50

- **Fluid**

The thermo-physical properties of air and flue-gas i.e. specific heat capacity, thermal conductivity, and dynamic viscosity, are correlated with the knowledge of the flue-gas composition according to [9].

The *Pr*-Number, specific enthalpy and all thermo-physical properties of water i.e. thermal conductivity, density, and dynamic viscosity are calculated, according to [23]. The saturation vapor pressure is estimated using the ANTOINE-equation as follows:

$$p_{sat \text{ H}_2\text{O}} = \exp \left[ 19.016 - \left( \frac{4064.95}{\vartheta_a + 236.25} \right) \right].$$

### B.2. Simulation

The thermo-physical properties of dry-air (index *a*) are considered using the following polynomial functions, recalculated for [K], according to [9]. The coefficient are given in Table B.1.

$$\left. \begin{aligned} c_{p_a} &= b_0 + \frac{b_1}{2}T + \frac{b_2}{3}T^2 + \frac{b_3}{4}T^3 + \frac{b_4}{5}T^4 \\ \lambda_a &= b_0 + b_1T + b_2T^2 + b_3T^3 + b_4T^4 \\ \eta_a &= b_0 + b_1T + b_2T^2 + b_3T^3 + b_4T^4 \end{aligned} \right\} \quad (\text{B.2})$$

### B. Thermo-Physical Properties

For the tube and fin material carbon steel (index  $cs$ ) is considered with a density of  $\rho_s = 7850 \text{ kg/m}^3$  with the following thermo-physical properties, according to literature, [42]:

$$\left. \begin{aligned} c_{p_{cs}} &= b_0 + b_1 T + b_2 T^2 + b_3 T^3 \\ \lambda_{cs} &= b_0 + b_1 T + b_2 T^2 \end{aligned} \right\} \quad (\text{B.3})$$



Table B.1.: Thermo-Physical Properties of Dry-air and Carbon Steel

Property	$b_0$	$b_1$	$b_2$	$b_3$	$b_4$
$c_{p_a}$ [J/kgK]	1002.393253	-0.046759943	0.000190133	$-1.00609 \cdot 10^{-07}$	$1.86136 \cdot 10^{-11}$
$\lambda_a$ [W/mK]	-0.000674354	0.000105474	$-6.22996 \cdot 10^{-08}$	$3.17144 \cdot 10^{-11}$	$-6.9318 \cdot 10^{-15}$
$\eta_a$ [Ns/m <sup>2</sup> ]	$2.42331 \cdot 10^{-06}$	$6.18574 \cdot 10^{-08}$	$-3.08574 \cdot 10^{-11}$	$9.86185 \cdot 10^{-15}$	$-1.23091 \cdot 10^{-18}$
$c_{p_s}$ [J/kgK]	185.8537793	1.272598818	-0.0017157	0.00000091	
$\lambda_s$ [W/mK]	66.17504949	-0.03482879	0.0000233		

## C. Geometrical Data of Investigated I-Shaped Finned-Tubes

Table C.1.: Specifications of Finned-Tubes taken from FRASZ-Institute of Thermodynamics and Energy Conversion

Fin Geometry	Notation	I-shaped solid	I-shaped segmented
Bare tube diameter	$d_a$	38.0 mm	38.0 mm
Tube thickness	$s_t$	2.6 mm	4.0 mm
Number of fins per m	$n_R$	276	276
Average fin height	$h$	15.0 mm	15.5 mm
Average fin thickness	$s$	1.0 mm	1.0 mm
Average tube length	$L_t$	500 mm	500 mm
Average segment width	$b_s$		4.5 mm
Number of tubes in flow-direction	$N_R$	8	8, 4, 2
Number of tubes per row	$N_L$	11	11
Longitudinal tube pitch	$t_l$	79 mm	79 mm
Transversal tube pitch	$t_q$	85 mm	85 mm
Outside surface area for 8 tube rows	$A_{tot}$	67.06 m <sup>2</sup>	64.05 m <sup>2</sup>
Fin material		St4	St37.2
Tube material		St35.8	St35.8
Net free area of tube row	$F_{min}$	0.234 m <sup>2</sup>	0.2326 m <sup>2</sup>

# Bibliography

- [1] VDI-Wärmeatlas, 10. ed. Springer-Verlag, Berlin Heidelberg New York, 2006.
- [2] BAEHR, H., AND STEPHAN, K. *Wärme- und Stoffübertragung*, 4. ed. Springer-Verlag, Berlin Heidelberg New York, 2004.
- [3] BANTEL, M. *Grundlagen der Messtechnik*, 1. ed. Fachbuchverlag, Leipzig, 2000.
- [4] BREBER, G. Heat Transfer and Pressure Drop of Stud Finned Tubes. *The American Institute of Chemical Engineers Vol.87*, No.283 (1991), pp. 383–390.
- [5] BRIGGS, D., AND YOUNG, E. Convection Heat Transfer and Pressure Drop of Air Flowing across Triangular Pitch Banks of Finned Tubes. *Chemical Engineering Progress Symposium Series Vol.59*, No.41 (1963), pp. 1–10.
- [6] BROCKMANN, M. Druckverlust bei Strömungen quer zu Rippenrohren. Reihe 6 No.431, Fortschritt-Berichte VDI, 2000. Energietechnik.
- [7] DIN 1319. Grundlagen der Messtechnik. Tech. rep., DIN, Berlin, 1996. Teil 1 bis 4.
- [8] EN ISO 5167-1. Durchflußmessung von Fluiden mit Drosselgeräten. Tech. rep., Europäisches Komitee für Normung, Brüssel, 1995.
- [9] FDBR-HANDBUCH. *Wärme - und Strömungstechnik, Wärmeübertragung in Dampferzeugern und Wärmeaustauschern*, FDBR Fachbuchreihe ed. Fachverband Dampfkessel-, Behälter- und Rohrleitungsbau, Essen, 1980.
- [10] FLUENT INC. *Fluent 6.3.26 Users Guide*.
- [11] FLUENT INC. *Conduction Heat Transfer, in Modeling Heat Transfer using Fluent, Fluent v6.3*, 2006. pp. 1-38.
- [12] FLUENT INC. *Is My Solution Converged?*, 2006. <http://www.fluent.com/about/news/newsletters/01v10i2/a20.htm>.
- [13] FRASZ, F. Wärmeübertragung in Rippenrohrwärmeaustauschern, Wärmeaustauscher, Energieeinsparung durch Optimierung von Wärmeprozessen. *Vulkan-Verlag Essen Vol.2* (1994), pp. 70–76.

## Bibliography

- [14] FRASZ, F. *Principles of Finned-Tube Heat Exchanger Design for Enhanced Heat Transfer*. Heat and Mass Transfer, WSEAS-Press, 2008. Edited by Hofmann, R. and Ponweiser, K.
- [15] FRASZ, F., AND LINZER, W. Wärmeübergangsprobleme an querangeströmten Rippenrohrbündeln. *BWK Vol.44*, No.7/8 (1992), pp. 333–336.
- [16] GANAPATHY, V. *Industrial Boilers and Heat Recovery Steam Generators*. Marcel Dekker Inc., New York Basel, 2003.
- [17] GASTEIGER, G. *Ein Beitrag zur Ermittlung von strömungserregten Schwingungen in Rohrbündelwärmetauschern*. Dissertation, TU-Wien, 1983.
- [18] GATSKI, T., HUSSAINI, M., AND LUMLEY, J. *Simulation and Modeling of Turbulent Flows*. Oxford University Press Inc., New York, 1996.
- [19] GEISER, P. Numerische Berechnung und Messung der Transportvorgänge sowie integraler Kenngrößen in quer angeströmten Rippenrohrwärmeübertragern. Reihe 19, Fortschritt-Berichte VDI, 2000. Wärmetechnik/Kältetechnik.
- [20] GRÄNICH, H. *Messung beendet - was nun?*, 2. ed. Hochschulverlag, ETH Zürich, 1989.
- [21] GRÖBER, H., ERK, S., AND GRIGULL, U. *Die Grundgesetze der Wärmeübertragung*, (Neudruck) 3. ed. Springer-Verlag, Berlin Heidelberg New York, 1988.
- [22] HAAE, S. *Wärmeübertragung in Luftkühlern in Handbuch der Kältetechnik*, vol. B of *Wärmeaustauscher*. Springer-Verlag, Berlin Heidelberg New York, 1988.
- [23] HAAR, L., GALLAGHER, J., AND KELL, G. *NBS/NRC Wasserdampf Tafeln, Thermodynamische und Transportgrößen mit Coputerprogrammen für Dampf und Wasser in SI-Einheiten*. Springer-Verlag, Berlin Heidelberg New York, 1988.
- [24] HASHIZUME, K., E. A. Fin Efficiency of Serrated Fins. *Heat Transfer Engineering Vol.23* (2002), pp. 6–14.
- [25] HASHIZUME, K., AND TAKAHIRO, M. Fin efficiency of Serrated Fins: Part1. Analysis of Theoretical Fin Efficiency and Experimental Results. *Heat Transfer-Asian Research Vol.28*, No.6 (1999), pp. 528–540.
- [26] HE, F., AND CAO, W. Study of Theoretical Fin Efficiency of High Segmented Serrated Fin. *Proc. of Internat. Conf. Eng. Env.* (2003), pp. 877–882.
- [27] HEDH. *Heat Exchanger Design Handbook*. Hemisphere Publ. Corp., Washington New York London, 1987.

## Bibliography

- [28] HOFMANN, R., FRASZ, F., AND PONWEISER, K. Heat Transfer and Pressure Drop Performance Comparison of Finned-Tube Bundles in Forced Convection. *WSEAS Transactions on Heat and Mass Transfer Vol.2*, No.4 (2007), pp. 72–88.
- [29] HOFMANN, R., FRASZ, F., AND PONWEISER, K. Experimental Heat Transfer Investigation of Tube Row Effects at Air Side Heat Exchanger with Serrated Finned-Tubes. In *Thermal Engineering and Environment* (2008), pp. 193–201.
- [30] HOFMANN, R., FRASZ, F., AND PONWEISER, K. Performance Evaluation of Solid and Serrated Finned-Tube Bundles with Different Fin Geometries in Forced Convection. In *Proceedings of the Eurotherm* (2008), pp. 1–8.
- [31] HU, X., AND JACOBI, A. Local Heat Transfer Behavior and its Impact on a Single-Row, Annularly Finned Tube Heat Exchanger. *Journal of Heat Transfer Vol.115* (1993), pp. 66–74.
- [32] JANG, J., LAI, J., AND LIU, L. The Thermal-Hydraulic Characteristics of Staggered Circular Finned-Tube Heat Exchangers under Dry and Dehumidifying Conditions. *Int. J. Heat Transfer Vol.41* (1998), pp. 3321–3337.
- [33] JOARDAR, A., AND JACOBI, A. A Numerical Study of Flow and Heat Transfer Enhancement Using an Array of Delta-Winglet Vortex Generators in a Fin-and-Tube Heat Exchanger. *Journal of Heat Transfer Vol.129* (2007), pp. 1156–1167.
- [34] KAMINSKI, S. *Numerische Simulation der luftseitigen Strömungs- und Wärmetransportvorgänge in Lamellenrohr-Wärmeübertragern*. Freiburger Forschungshefte A 867, TU-Bergakademie, Freiberg, 2002.
- [35] KAWAGUCHI, K. Heat Transfer and Pressure Drop Characteristics of Finned Tube Banks in Forced Convection. *Journal of Enhanced Heat Transfer Vol.12*, No.1 (2005), pp. 1–20.
- [36] KEARNEY, S., AND JACOBI, A. Local Convective Behavior and Fin Efficiency in Shallow Banks of In-line and Staggered, Annularly Finned Tubes. *Journal of Heat Transfer Vol.118* (1996), pp. 317–326.
- [37] KONAKOV, P. Eine neue Formel für den Reibungskoeffizienten glatter Rohre. *Bericht der Akademie der Wissenschaften der UDSSR Vol.51*, No.7 (1954), pp. 503–506.
- [38] KUNTYSH, V., AND STENIN, N. Heat Transfer and Pressure Drop in Cross Flow through Mixed In-Line-Staggered Finned-Tube Bundles. *Thermal Engineering Vol.40*, No.2 (1993), pp. 126–129.
- [39] LEE, D., HA, M., BALACHANDAR, S., AND LEE, S. Numerical Simulations of Flow and Heat Transfer past a Circular Cylinder with a Periodic Array of Fins. *Physics of Fluids Vol.16*, No.5 (2004), pp. 1273–1286.

## Bibliography

- [40] LEGKIY, V., PAVLENKO, V., MAKAROV, A., AND ZHELUDOV, Y. Investigation of Local Heat Transfer in a Tube with Annular Fins in Transverse Air Flow. *Heat Transfer-Soviet Research Vol.6*, No.6 (1974), pp. 101–107.
- [41] MALINOVEC, M. Wärmeübertragung und Druckverlust in Glattrohren und Rohren mit eingesetzter Drahtwendel. Diplomarbeit, TU-Wien, 2001.
- [42] MANNESMANN. Physikalische Eigenschaften von Stählen und ihre Temperaturabhängigkeit. Stahleisen-Sonderbericht Heft 10, Verlag Stahleisen M.B.H, Düsseldorf, 1983.
- [43] MARTINEZ, E., VICENTE, W., SALINAS, M., AND SOTO, G. Single-Phase Experimental Analysis of Heat Transfer in Helically Finned Heat Exchanger. *Applied Thermal Engineering Vol.29* (2009), pp. 2205–2210.
- [44] MAYR-ROHRAUER, G. Mathematische Behandlung des Zusammenhanges zwischen Temperatur- und Wärmeübergangsverteilung auf Kreisrippen. Diplomarbeit, TU-Wien, 1996.
- [45] MIETH, H. Method for Heat Transfer Calculations of Helical-Wound Fin Tubes. *ASME 70-Pet-4, Pet. Mech. Engrg. & Pressure Vessels & Piping Conference* (1970), pp. 2–8.
- [46] MON, M. *Numerical Investigation of Air-Side Heat Transfer and Pressure Drop in Circular Finned-Tube Heat Exchangers*. Dissertation, TU-Bergakademie, Freiberg, 2003.
- [47] NIR, A. Heat Transfer and Friction Factor Correlations for Cross Flow Over Staggered Finned Tube Banks. *Heat Transfer Eng. Vol.12*, No.1 (1991), pp. 43–58.
- [48] ORSZAG, S., AND YAKHOT, V., E. A. Renormalization Group Modeling and Turbulence Simulations. *Near-Wall Turbulent Flows* (1993), pp. 1031–1046.
- [49] PATANKAR, S. *Numerical Heat Transfer and Fluid Flow*, McGraw-Hill Book Company ed. Hemisphere Publishing Corporation, 1981.
- [50] PONWEISER, K., LINZER, V., AND MALINOVEC, M. Performance Comparison Between Wire Coil and Twisted Tape Inserts. *Journal of Enhanced Heat Transfer Vol.11*, No.4 (2004), pp. 359–370.
- [51] PRANDTL, L., OSWATITSCH, K., AND WIEGHARDT, K. *Führer durch die Strömungslehre*, 9. ed. Vieweg Verlag, Braunschweig, 1990.
- [52] RABAS, T., AND ECKELS, P. Heat Transfer and Pressure Drop Performance of Segmented Extended Surface Tube Bundles. *AIChE-ASME Heat Transfer Conference* (Aug.11-13 1975), pp. 1–8. San Francisco, California.

## Bibliography

- [53] RANGAN, B., KRISHNAMURTHY, A., AND RAGHAVAN, V. Analysis of Flow and Heat Transfer at a Finned Tube in Cross Flow. *Proceedings, ASME Summer Heat Transfer Conference* (2003), pp. 1–6. Las Vegas.
- [54] REID, D., AND TABOREK, J. Selection Criteria for Plain and Segmented Finned Tubes for Heat Recovery Systems. *Transactions of the ASME Vol.116* (1994), pp. 406–410.
- [55] SCHLICHTING, H., AND GERSTEN, K. *Grenzschichttheorie*, 10. ed. Springer-Verlag, Berlin Heidelberg New York, 2005.
- [56] SCHMIDT, T. E. Der Wärmeübergang an Rippenrohre und die Berechnung von Rohrbündel-Wärmeaustauschern. *Kältetechnik Vol.15*, No.4 (1963), pp. 98–102.
- [57] SHETTY, S., AND MITCHEL, H., E. A. Heat Transfer Performance of Fintubes with Solid versus Segmented Fins. *Avances en Ingenieria Quimica Vol.8*, No.1 (1998), pp. 16–23.
- [58] STASIULEVIČIUS, J., AND SKRINSKA, A. *Heat Transfer of Finned Tube Bundles in Cross-flow*. Hemisphere Publ. Corp., Washington New York London, 1988. Edited by Žukauskas, A. and Hewitt, G.
- [59] STEPHAN, K., AND MITROVIĆ, J. Maßnahmen zur Intensivierung des Wärmeübergangs. *Chemie Ingenieur Technik Vol.56*, No.6 (1984), pp. 427–431.
- [60] STREIT, S. Messunsicherheit und Verträglichkeitsprüfungen: Beispiele und Vergleich mit herkömmlichen Verfahren. Tech. Rep. 1210, Fortschritt-Berichte VDI, 1995.
- [61] SZCZEPANIK, K., OOI, A., AYE, L., AND ROSENGARTEN, G. A Numerical Study of Heat Transfer from a Cylinder in Cross Flow. *15<sup>th</sup> Australasian Fluid Mechanics Conference* (2004), pp. 1–4. Sydney.
- [62] TAVOULARIS, S. *Measurement in Fluid Mechanics*. Cambridge University Press, New York, 2005.
- [63] TENNER, J., KLAUS, P., AND SCHULZE, E. Erfahrungen bei der Erstellung und dem Einsatz eines Datenvalidierungsmodells zur Prozessüberwachung und -optimierung im Kernkraftwerk Isar 2. *VGB Kraftwerkstechnik Vol.4* (1998), pp. 43–49.
- [64] TORRESI, M., SAPONARO, A., CAMPOREALE, S., AND FORTUNATO, B. CFD Analysis of the Flow through Tube Banks of HRSG. *Proceedings, ASME Turbo Expo: Power for Land, Sea and Air* (2008), pp. 1–11. Berlin.
- [65] TU, J., YEOH, G., AND LIU, C. *Computational Fluid Dynamics - A Practical Approach*. Butterworth-Heinemann, USA, 2008.

## Bibliography

- [66] VERSTEEG, H., AND MALALASEKERA, W. *An Introduction to Computational Fluid Dynamics - The Finite Volumen Method*, 2. ed. Pearson Education Ltd., Essex, 2007.
- [67] WAGNER, W. *Wärmeaustauscher*, 1. ed. Vogel-Fachbuch, Würzburg, 1993.
- [68] WAGNER, W. *Wärmeübertragung*, 5. ed. Vogel-Fachbuch, Würzburg, 1998.
- [69] WALCZYK, H., E. A. An Experimental Study of Convective Heat Transfer from Extruded Type Helical finned Tubes. *Chemical Engineering and Processing Vol.42* (2003), pp. 29–38.
- [70] WEBB, R. Air-Side Heat Transfer in Finned Tube Heat Exchangers. *Heat Transfer Engineering Vol.1*, No.3 (1980), pp. 33–49.
- [71] WEBB, R. *Principles of Enhanced Heat Transfer*. John Wiley & Sons, 1994.
- [72] WEIERMAN, C. Correlations Ease the Selection of Finned Tubes. *The Oil and Gas Journal Vol.74*, No.36 (1976), pp. 94–100.
- [73] WEIERMAN, C., TABOREK, J., AND MARNER, W. Comparison of the Performance of In-Line and Staggered Banks of Tubes With Segmented Fins. *The American Institute of Chem. Engineers Vol.74*, No.174 (1978), pp. 39–46.
- [74] WILCOX, D. *Turbulence Modeling for CFD*. DCW Industries, San Diego, 2006.
- [75] ZELLER, S. Datenerfassung eines Rippenrohrwärmeaustauschers. Diplomarbeit, TU-Wien, 2004.



# Curriculum Vitae

## Persönliche Daten

*Dipl.-Ing. René Hofmann*

*geboren am 8. Juli 1976 in Mödling/NÖ*

*Familienstatus: Verheiratet*

## Ausbildung und Berufsweg

1982-1990	Volksschule Möding, Privatschule Wien; Grundschulabschluss
1990-1995	HTL Maschinenbau-Betriebstechnik Mödling; Matura m. Ausz. bestanden
1995-2005	Diplomstudium Maschinenbau TU Wien; Graduierung Dipl.-Ing. m. Ausz.
1995-1996	Tutor am Institut für Maschinenlehre und Fördertechnik, TU Wien
1999	University of Nebraska at Omaha, USA; 1 Summer Term
1996-2002	Global Knowledge Network GmbH; Referenz: Ing. Harald Bischof
1998-2001	Ingersoll-Dresser-Pumps; Referenz: Dipl.-Ing. Dr.techn. Rossegger
2001	Gutwinski Umweltmanagement GmbH; Referenz: Dr. Thomas Gutwinski
2005-2006	Zivildienst, Österreichisches Ökologie Institut
Seit 2006	Projektassistent und Dr.-Studium am Institut für Thermodynamik und Energiewandlung, TU Wien

## Stipendien und Auszeichnungen

2006	Leistungsstipendium, Windhag-Stipendienstiftung für Niederösterreich.
25.-27.01.2008	Best Student Paper Award; WSEAS 5 <sup>th</sup> International Conference on Heat and Mass Transfer, Mexiko.